Technische Universität München

Astrophysical uncertainties of direct dark matter searches

Dissertation

by

Andreas Günter Rappelt

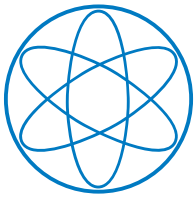

Physik Department, T30d
&
Collaborative Research Center SFB 1258
"Neutrinos and Dark Matter in Astro- and Particlephysics"

Technische Universität München

Physik Department T30d

Astrophysical uncertainties of direct dark matter searches

Andreas Günter Rappelt

Vollständiger Abdruck der von der Fakultät für Physik der Technischen Universität München zur Erlangung des akademischen Grades eines

Doktors der Naturwissenschaften

genehmigten Dissertation.

Vorsitzender:		Prof. Dr. Lothar Oberauer
Prüfer der Dissertation:	1.	Prof. Dr. Alejandro Ibarra
	2.	Prof. Dr. Björn Garbrecht

Die Dissertation wurde am 12.11.2019 bei der Technischen Universität München eingereicht und durch die Fakultät für Physik am 24.01.2020 angenommen.

Abstract

Although the first hints towards dark matter were discovered almost 100 years ago, little is known today about its properties. Also, dark matter has so far only been inferred through astronomical and cosmological observations. In this work, we therefore investigate the influence of astrophysical assumptions on the interpretation of direct searches for dark matter. For this, we assume that dark matter is a weakly interacting massive particle. First, we discuss the development of a new analysis method for direct dark matter searches. Starting from the decomposition of the dark matter velocity distribution into streams, we present a method that is completely independent of astrophysical assumptions. We extend this by using an effective theory for the interaction of dark matter with nucleons. This allows to analyze experiments with minimal assumptions on the particle physics of dark matter. Finally, we improve our method so that arbitrarily strong deviations from a reference velocity distribution can be considered. This allows us to bracket the influence of astrophysical uncertainties by parametrizing the deviation. We then use this method to study the dark matter interpretation of the annual modulation signal measured by the DAMA experiment. Furthermore, we calculate how the existence of dark matter sub-halos affects the expected signals. Using a state of the art sub-halo mass function calculated with a semi-analytic model, we consider sub-halos with masses larger than $10^{-5}\,M_{\odot}$. Thus, we extend existing works and calculate for the first time the effect of sub-halos on the annihilation of dark matter in the sun. Finally, this work is rounded off by an outlook and an introduction to the concepts of convex optimization.

Zusammenfassung

Obwohl erste Hinweise auf Dunkle Materie vor fast 100 Jahren entdeckt wurden, ist heute wenig über dessen Eigenschaften bekannt. Auch konnte Dunkle Materie bis jetzt nur durch astronomische und kosmologische Beobachtungen nachgewiesen werden. In dieser Arbeit untersuchen wir daher den Einfluss von astrophysikalischen Annahmen auf die Interpretation von direkten Suchen nach Dunkler Materie. Hierfür nehmen wir an, dass Dunkle Materie ein »weakly interacting massive particle« ist. Zuerst entwickeln wir eine neue Analysemethode für direkte Suchen nach Dunkler Materie. Ausgehend von der Zerlegung der Geschwindigkeitsverteilung von Dunkler Materie in Streams, präsentieren wir eine Analysemethode die vollkommen unabhängig von astrophysikalischen Annahmen ist. Wir erweitern diese, indem wir eine effektive Theorie für die Wechselwirkung von Dunkler Materie und Nukleonen benutzen. Dies ermöglicht es, Experimente mit minimalen Annahmen über die Teilchenphysik der Dunklen Materie zu analysieren. Schließlich verbessern wir unsere Methode damit auch beliebig starke Abweichungen von einer Referenzgeschwindigkeitsverteilung betrachtet werden können. Durch eine Parametrisierung der Abweichung lässt sich dann der Einfluss von astrophysikalischen Unsicherheiten eingrenzen. Anschließend verwenden wir diese Methode um die Interpretation des Modu-

lationssignals, welches vom DAMA Experiment gemessen wurde, durch Dunkle Materie zu untersuchen. Des Weiteren berechnen wir wie sich die Existenz von Dunkle Materie Sub-Halos auf die erwarteten Signale auswirkt. Die Verwendung einer modernen Sub-halo Massenfunktion, die mittels eines semi-analytischen Modells berechent wurde, erlaubt es uns Sub-halos mit Massen größer als $10^{-5}\,M_{\odot}$ zu berücksichtigen. Dadurch erweitern wir existierende Arbeiten und berechnen zum ersten Mal den Effekt von Sub-halos auf die Annihilation von Dunkler Materie in der Sonne. Diese Arbeit wird abgerundet von einem Ausblick sowie einer Einführung in die Konzepte der konvexen Optimierung.

This dissertation builds on the studies presented in

- A. Rappelt, *A halo independent comparison of direct dark matter searches*, Master's thesis, Technische Universität München, 2016

Publications in the context of this dissertation

- A. Ibarra and A. Rappelt, *Optimized velocity distributions for direct dark matter detection*, *JCAP* **1708** (2017), no. 08 039, [arXiv:1703.09168]
- R. Catena, A. Ibarra, A. Rappelt, and S. Wild, *Halo-independent comparison of direct detection experiments in the effective theory of dark matter-nucleon interactions*, *JCAP* **1807** (2018), no. 07 028, [arXiv:1801.08466]
- A. Ibarra, B. J. Kavanagh, and A. Rappelt, *Bracketing the impact of astrophysical uncertainties on local dark matter searches*, *JCAP* **1812** (2018), no. 12 018, [arXiv:1806.08714]
- A. Ibarra, B. J. Kavanagh, and A. Rappelt, *Impact of substructure on local dark matter searches*, arXiv:1908.00747

Contents

Chapter 1.

Introduction

Evidence for dark matter comes so far exclusively from indirect effects due to the gravitational interaction of dark matter with visible matter [6–9]. First discussions about an invisible component of matter present in the Milky Way date back to Kelvin [10], Öpik [11], Kapteyn [12] and Oort [13]. However, they concluded that there is at most as much invisible matter as there is visible. In the 1930s, first signs of a missing matter component emerged from the measurements of the velocity dispersion in the Coma cluster, from which Zwicky concluded that the mass to light ratio of the cluster is 500 [14]. This implies that a large fraction of the mass of the Coma cluster is invisible. Also in the 1930s, Oort investigated the motion of nearby stars and concluded that their trajectories could not be explained solely by the gravitational potential of the visible stars [13]. To this day, a large amount of evidence for dark matter has accumulated. This includes the famous result of Vera Rubin and collaborators [15], who measured the rotation curve of the Milky Way and found that it is flat for large distances from the galactic center, contradicting the expectations from visible matter. Other evidence arises from the observation of the merging cluster 1E0657-558 [16], which implies that the distribution of gravitating matter of this system does not coincide with the locations where visible matter is concentrated. Today, dark matter is an important ingredient in many physics models. For example, the ΛCDM model describes successfully the evolution of the Universe as a whole and explicitly assumes the existence of cold dark matter (CDM). The current state of research is that 84% of the mass-energy density of the Universe is in the form of dark matter [17]. In total, dark matter accounts for ∼25% of the energy density of the Universe as found by WMAP [18] and Planck [17].

Despite the overwhelming evidence for its existence, the particle physics properties of dark matter are not well known. One of the most pressing issues of modern particle physics is therefore to determine the fundamental properties of dark matter like its mass, spin and interactions with visible matter. In the successful Standard Model of Particle Physics (SM), none of the known particles is able to explain dark matter. Due to this, a wide range of models for dark matter have been proposed, featuring candidates with masses ranging over 50 orders of magnitude [19]. One of the most studied class of dark matter models is the weakly interacting massive particle (WIMP). In the broadest sense, it is a new particle with a mass of at least a few GeV up to tens of TeV which interacts weakly with SM particles. Here, weakly interacting means that the interaction strength between dark matter and SM particles is similar to the strength of the SM weak interac-

tion. WIMPs arise naturally from several theories that were introduced to solve different problems of particle physics. For example, supersymmetric models like the MSSM contain the neutralino that falls into the category of a weakly interacting massive particle [20]. However, the most compelling feature of WIMPs is thermal freeze-out [21] that provides a natural mechanism to explain the dark matter abundance in the Universe.

Due to these compelling theoretical arguments, many experiments quote the search for WIMP particles as a science case. Despite the huge experimental effort in the search for dark matter, no clear signal could be discovered until now. The dark matter interpretation of the annual modulation signal measured by the direct detection experiment DAMA [22, 23] is in conflict with almost all of the currently pursued direct detection experiments and dark matter searches utilizing neutrino telescopes. Furthermore, the excess in the antiproton data collected by AMS-02 [24] could hint towards dark matter but is discussed heavily in the literature [25–28] and no conclusion is reached yet. In spite of these controversies, a natural question to ask is how the interpretation of dark matter searches depends on assumptions about the astro- and particle physics nature of dark matter. For example, it is important to check whether the dark matter interpretation of the annual modulation signal reported by DAMA could be compatible with other direct detection experiments by relaxing some of the assumptions.

In this thesis, we investigate the astrophysical uncertainties arising in the interpretation of direct detection experiments and dark matter searches with neutrino telescopes as both discussed in chapter 3. We introduce the formalism necessary to describe the dark matter halo of the Milky Way in chapter 2. First, we develop in chapter 4 an analysis method that is completely independent of assumptions about the dark matter halo model. We show in chapter 5 that this method allows halo-independent analyses in terms of an effective theory for the interactions between dark matter and nucleons. This extended method addresses simultaneously the particle physics uncertainties on the concrete form of the dark matter-nucleon interaction as well as the astrophysical uncertainties on the local dark matter density and velocity distribution. In chapter 6, we further improve this method. This makes it possible to consider any deviations from the standard assumptions about the dark matter halo model in a statistically rigorous way. We then use this method in chapter 7 to study the dark matter interpretation of the DAMA annual modulation signal and its compatibility with null results of other experiments. After discussing this general method and its applications, we analyze a specific source of astrophysical uncertainties and determine in chapter 8 the impact of dark matter sub-halos on the interpretation of direct detection experiments and dark matter searches with neutrino telescopes. This extends previous works studying the impact of dark matter sub-halos on direct detection experiments by considering sub-halos as light as $10^{-5}\,M_{\odot}$ and by building probabilistic models. Finally, we present our conclusions in chapter 9. Appendices that cover the formalism of convex optimization and summarize the key figures of several dark matter searches complete this work.

Chapter 2.

Dark matter on astrophysical scales

2.1. Dark matter in the Universe

2.1.1. Evidence for dark matter in the Universe

Starting from the 1930s, a vast amount of evidence for dark matter in the Universe has accumulated. Here, we give a concise overview over some of the most striking evidence, while we refer to Refs. [6–9] for more detailed reviews on this subject.

In the early 1930s, Fritz Zwicky observed that there is evidence for a large amount of dark matter in the Coma cluster. While studying the redshifts of several galaxy clusters, he realized that eight galaxies in this cluster have large apparent velocities [29] as also found in Ref. [30]. He then applied the virial theorem to obtain the gravitating mass of the system from the velocity dispersion of the galaxies in the cluster. Comparing this to the luminosity of the Coma cluster, Zwicky determined the mass-to-light ratio M/L to be 500. He concluded that the Coma cluster hosts a large amount of invisible matter [14], which he referred to as dark matter. However, Zwicky's result relies on the Hubble parameter to relate the redshift and the distance. He assumed $H_0 = 558\,\mathrm{km\,s^{-1}\,Mpc^{-1}}$ as determined by [30] which is a factor 10 larger than the modern value of $H_0 = 67.4 \pm 0.5\,\mathrm{km\,s^{-1}\,Mpc^{-1}}$ [17]. Rescaling his result to the modern value reduces his estimate of the mass-to-light ratio by a factor $558/67.4 \approx 8.3$, the observation of the apparent velocities in the Coma cluster nevertheless suggests a large M/L and therefore dark matter.

One of the most famous evidence for dark matter comes from the flatness of the rotation curves at large distance to the galactic center. Starting in the 1970s, Rubin and collaborators pursued spectroscopic observations of several galaxies, mapping the velocities of the objects bound to them [15, 31, 32]. They found that the rotation curves $v(r)$ of those galaxies are flat far beyond the visible part of the galaxy. In the left plot of Fig. 1, we show the rotation curve of the galaxy NGC 6503 as determined in Ref. [33]. From Newton's law of gravity, one expects that the rotation curve follows $v(r) \propto \sqrt{M(r)/r}$ where $M(r)$ is the mass of the galaxy within a sphere with radius r. Assuming that galaxies host mostly visible matter, this would imply that $v(r) \propto \sqrt{1/r}$ beyond the visible part of the galaxy which is in contradiction to observations. Therefore, those galaxies must host an additional component of matter, extending far beyond the distribution of visible matter.

In 2006, Ref. [16] observed two merging galaxy clusters, collectively known as 1E0657-

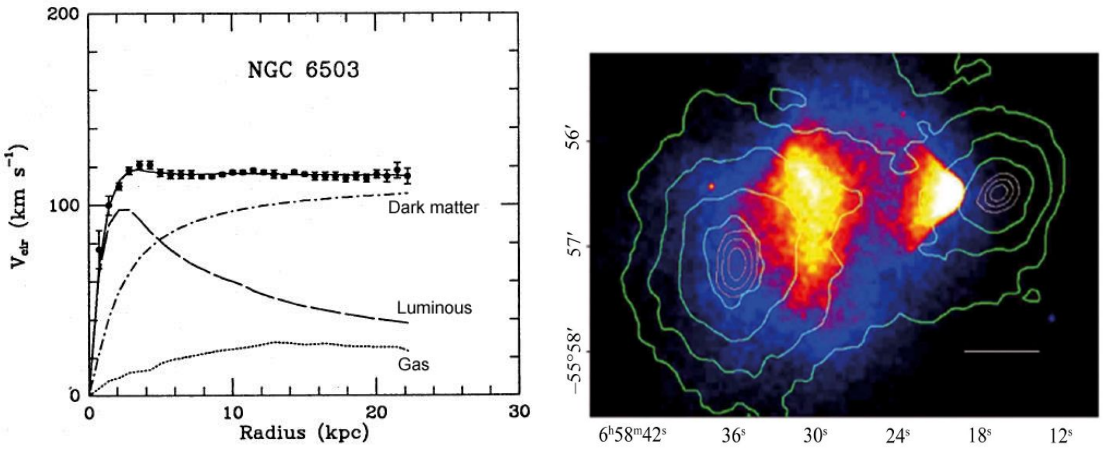

Figure 1.: Two famous examples of evidence for dark matter. In the left plot, we depict the rotation curve of the galaxy NGC 6503 as measured in Ref. [33]. This plot was adopted from Ref. [7] but was originally published in [33]. Furthermore, we show the merging cluster 1E0657-558 as observed by [16]. The color code indicates the temperature of the X-ray emitting gas while the green lines denote the gravitational potential. This plot was adopted from Ref. [16].

558 respectively "bullet cluster". As the clusters collided recently, the hot and X-ray emitting gas is located in the collision region while the stars and galaxies passed through each other. Although the majority of the baryonic mass of the clusters comes from the gas component, weak lensing surveys imply that the mass of the system is not centered in the collision region [16]. This discrepancy is also apparent from the right plot of Fig. 1 which shows the contour lines of the gravitational potential as green lines while X-ray observations are color coded. The plot shows that the locations of the highest mass density and the highest baryon density do not coincide. Therefore, an invisible mass component must be present that interacts only rarely and therefore traverses the opposing galaxy cluster. This observation also challenges theories of modified Newtonian dynamics, dubbed MOND [34,35], that aim to solve the dark matter problem by modifying the laws of gravity. Although the flatness of rotation curves can be explained by these theories, the bullet cluster requires an additional mass component that is hard to explain by a modification of gravity [36] although this is subject to discussion [37].

2.1.2. The total amount of dark matter in the Universe

Despite the compelling evidence for dark matter presented in the previous section, it is not possible to infer the total amount of dark matter in the Universe from those observations. An excellent probe for this is the cosmic microwave background (CMB), which we introduce concisely in the following but we refer to Refs. [38–40] for detailed reviews. Today, modern measurements of the CMB allow the precise determination of cosmological parameters of the ΛCDM model, the standard model of cosmology. This model describes successfully the evolution of the Universe from the Big Bang until present times and crucially relies on the existence of cold dark matter, abbreviated as CDM.

Gamow [41, 42] as well as Alpher and Hermann [43, 44] predicted the CMB in 1948 and almost 20 years later, in 1965, Penzias and Wilson were able to verify it [45]. At early times, the Universe was radiation dominated and the CMB photons were energetic enough to ionize hydrogen [40]. Therefore, the Universe consisted of a hot and charged plasma, which we refer to as the primordial plasma. As the CMB photons redshift due to the expansion of the Universe, they become less energetic. When the Universe was approximately $4 \cdot 10^5$ years old, they were no longer able to ionize hydrogen which lead to the formation of stable and neutral atoms. From then on, CMB photons decoupled from matter and were only subject to the redshift induced by the expansion of the Universe. Due to this, we observe today an almost perfect black-body spectrum of photons with a temperature of $T \simeq 2.73\,K$. There are, however, small fluctuations in the temperature and the polarization spectrum of CMB photons that were induced by acoustic oscillations in the primordial plasma, see Ref. [38] for a review on this topic. An overdensity in the primorial plasma gravitationally attracts matter which also increases the pressure due to photon-matter interactions. This gives rise to acoustic oscillations as those two forces act opposite to each other. As dark matter does not interact with photons but contributes to the gravitational potential, the power spectra of CMB photon temperature and polarization fluctuations depend crucially on the ratio dark matter to baryons. Under the assumption of the ΛCDM model, the latest measurements of the CMB conducted by Planck [17] found dark matter and baryon densities of

$$\Omega_{\mathrm{DM}}\, h^2 = 0.1200 \pm 0.0012 \tag{2.1}$$

$$\Omega_{\mathrm{b}}\, h^2 = 0.0224 \pm 0.0001\,, \tag{2.2}$$

which implies that 84.3% of the matter content in the Universe is dark matter. Here, Ω_X is the ratio of the energy density of the component X and the critical density of the Universe $\rho_{\mathrm{crit}} = 3\,H_0^2/8\pi\,G$, where G is the gravitational constant. Furthermore, h denotes the reduced Hubble constant which is defined as $h = H_0/100\,\mathrm{km\,s^{-1}\,Mpc^{-1}}$. The latest measurements of Planck [17] found $h = 0.674 \pm 0.005$.

Big Bang Nucleosynthesis (BBN) provides an alternative way to measure the baryonic density Ω_{b} by studying the production of light nuclei, see Ref. [46] for a detailed review. If the temperature of SM particles is much larger than the mass difference between protons and neutrons $T \gg m_{\mathrm{n}} - m_{\mathrm{p}}$, both particles are in equilibrium due to weak interactions. Once the Universe cooled down enough such that $T \lesssim 100\,\mathrm{keV}$ [40], neutrons decay into protons or fuse with them to produce light nuclei. In order to match the observed abundances of ^{2}H, ^{3}He, ^{4}He and ^{7}Li today, a baryon density in the Universe of

$$0.021 \leq \Omega_{\mathrm{b}}\, h^2 \leq 0.024 \quad \text{at } 95\% \text{ C.L.} \tag{2.3}$$

is needed [47]. Due to the good agreement with the measurement of the baryonic density using the CMB, we conclude that only a small fraction of the dark matter can be baryonic matter.

2.1.3. Structure formation

Dark matter plays a key role in explaining the structures observed in the Universe today like galaxies, galaxy clusters and larger objects. Weak fluctuations of the density in the early Universe provide the seed for the growth of such structures. Those inhomogeneities are probably due to quantum fluctuations and are directly visible in the CMB [17]. During inflation, the density fluctuations are blown up and finally gravitational interactions lead to the structures that we observe today. Following the recent review of Ref. [48], we give a quick overview over the formation of structure in the Universe. We describe the evolution of structure starting at the end of inflation where the density fluctuations $\delta\rho/\rho$ are predicted to be small and follow a nearly scale invariant power spectrum.

As long as the density perturbations are small, i.e. $\delta\rho/\rho \ll 1$, we are in the regime where linear perturbation theory can be applied. One important effect in this regime is the Mészáros effect [49]. It predicts that density perturbations on scales smaller than the horizon stagnate during radiation domination while those on scales larger than the horizon grow. As soon as matter dominates the energy density of the Universe, all perturbations grow at the same rate. This imprints two important scales into the power spectrum of density perturbations. The first one is the size of the horizon at matter-radiation equality, below which the power spectrum flattens. In addition to this, there is a scale that is set by the particle nature of dark matter and which imposes a cut-off. For thermal relics, this scale is set by free streaming and corresponds to the size of the horizon at the time when dark matter becomes non-relativistic [48]. This happens earlier for heavier dark matter and allows to group dark matter candidates into three different categories depending on their temperature today: cold ($m_{\mathrm{DM}} \sim 100\,\mathrm{GeV}$), warm ($m_{\mathrm{DM}} \sim 1\,\mathrm{keV}$) and hot dark matter ($m_{\mathrm{DM}} \sim 30\,\mathrm{eV}$) [48]. Another important effect in the linear regime is collisional damping that prevents the collapse of small structures and introduces a lower bound in the power spectrum of density fluctuations. For WIMPs, the decoupling from the photon-baryon plasma introduces a damping of small scale perturbations [50]. Another example for collisional damping is the interaction of dark matter with relativistic particles, for example photons or neutrinos [51, 52] respectively dark radiation [53, 54]. Those interactions give rise to a radiation pressure that counteracts the collapse of small density perturbations and introduces dark acoustic oscillations which are similar to baryonic acoustic oscillations. This imprints a characteristic scale that corresponds to the sound horizon at the time dark matter decouples from those relativistic particles. We conclude that the power spectrum of density perturbations crucially depends on the particle nature of dark matter. Recent observations of the large-scale distribution of galaxies [55, 56] and the Ly-α forest [57] constrain the power spectrum to be like cold dark matter for a co-moving wave number smaller than $k = 200\,\mathrm{h/Mpc}$.

As soon as the density contrast becomes sizable, i.e. $\delta\rho/\rho \sim 0.1$, perturbation theory brakes down as perturbations on different scales become coupled via gravity and can no longer be treated separately. In the literature, several methods were proposed to describe structure formation in the nonlinear regime, confer Ref. [48]. However, the most common approach are N-body simulations which follow the phase-space evolution of a set of N

particles that are drawn from an initial power spectrum. The initial state is derived in the linear regime [58, 59] using the Zel'dovic approximation [60] or the second-order Lagrangian perturbation theory [61]. From this, N-body simulations evolve the dark matter phase-space distribution $f(\vec{x}, \vec{v}, t)$ through time. In the case of cold dark matter, the collisionless Boltzmann equation and the Poisson equation describe the evolution of the gravitational field $\Phi(\vec{x})$

$$\frac{\mathrm{d}f}{\mathrm{d}t} = \frac{\partial f}{\partial t} + \sum_i v_i \frac{\partial f}{\partial x_i} + \sum_i \frac{\partial \Phi}{\partial x_i} \frac{\partial f}{\partial v_i} \tag{2.4}$$

$$\rho_{\mathrm{DM}}(\vec{x}, t) = \int f(\vec{x}, \vec{v}, t)\, \mathrm{d}^3 v \tag{2.5}$$

$$\nabla^2 \Phi(\vec{x}) = 4\pi\, G\, \rho_{\mathrm{DM}}(\vec{x})\,, \tag{2.6}$$

where G is the gravitational constant. Here, $\mathrm{d}/\mathrm{d}t$ is the Lagrangian derivative, ρ_{DM} is the dark matter density. N-body simulations solve this problem by discretizing the distribution function into N phase-space elements $\{\vec{x}_i, \vec{v}_i\}$ for $i = 1, \ldots, \mathrm{N}$. These phase-space regions represent the particles of the simulation. We note that these "particles" consist of a large amount of dark matter particles as $m_i/m_{\mathrm{DM}} \gg 1$, where m_i is the mass of the ith region. Therefore, the conclusions drawn from N-body simulations are always limited by the phase-space resolution. With this, the phase-space distribution function is evolved by tracing the dynamics of a system consisting of N particles subject to the potential imposed by the particle distribution in a self consistent way. This allows to determine the phase-space distribution of dark matter deep into the non-linear regime and study the properties of the Milky Way dark matter halo that are not accessible from observations.

2.2. Dark matter in the Milky Way

The phase-space distribution of dark matter in the Milky Way is a key ingredient for understanding dark matter in our Universe. Information about it can be extracted on all scales of the galaxy, ranging from the Milky Way as a whole down to stars in the solar neighborhood that could act as tracers of dark matter. In the following, we review the most popular models for both the velocity and density distribution of dark matter in our galaxy.

2.2.1. The dark matter density in the Milky Way

There are two main results that constrain the shape of the radial dark matter density profile of the Milky Way. First, the dark matter density profile can be extracted from N-body simulations by looking at simulated dark matter halos that have the same properties as the Milky Way. Furthermore, the profile must reproduce the observed rotation curve of the Milky Way.

The Navarro-Frenk-White (NFW) profile [62, 63] is motivated by dark matter only

N-body simulations and reads

$$\rho_{\rm NFW}(r) = \frac{\rho_s}{(r/r_s)\,(1+r/r_s)^2} \tag{2.7}$$

where $r_s \approx 20$ kpc is the scale radius of the Milky Way and ρ_s is the central density of the halo that acts as a normalization of the profile. A recent study [64] suggests $\rho_s \approx 0.5$ GeV/cm^3. As apparent from Fig. 2, the NFW profile increases strongly in the center of the halo while it decreases with r^{-3} for large radii.

A profile with similar features, confer Fig. 2, is the Einasto profile [65, 66] which was also determined from N-body simulations. It has the following form

$$\rho_{\rm Einasto}(r) = \rho_s \, \exp\left[-\frac{2}{\alpha}\left(\left(\frac{r}{r_s}\right)^{\alpha} + 1\right)\right], \tag{2.8}$$

where again $r_s \approx 20$ kpc is the scale radius and ρ_s is the central density. In addition to these two parameters, the Einasto profile is described by the shape parameter α. For the Milky Way dark matter halo, this shape parameter takes values between $0.12 \lesssim \alpha \lesssim 0.22$ [67] with best fit value $\alpha = 0.17$ [68, 69].

In contrast to the previously discussed profiles, the Burkert profile [70] was determined from the rotation curve of the Milky Way and describes well the dark matter density of dwarf galaxies. It is given by

$$\rho_{\rm Burkert}(r) = \frac{\rho_s}{\left(1+\frac{r}{r_s}\right)\left(1+\frac{r^2}{r_s^2}\right)}, \tag{2.9}$$

where $r_s \approx 10$ kpc is the scale radius for the Burkert profile and ρ_s is the central density. A recent study [64] points towards $\rho_s \approx 1.578$ GeV/cm^3. As apparent from Fig. 2, the Burkert profile does not rise in the center of the Milky Way halo but instead becomes flat, in contrast to the predictions of the NFW and the Einasto profile. Therefore, the density profiles extracted from N-body simulations and those determined from the rotation curve of the Milky Way predict a different behavior at the center of the halo. This is called the Core-Cusp problem and we refer to Ref. [71] for a detailed review.

In addition to the shape of the profile, another important quantity is the dark matter density in the solar neighborhood $\rho_{\rm loc}$. The canonical value for the local dark matter density is $0.3\,\text{GeV/cm}^3$ [72], which we indicate in Fig. 2 by a gray band assuming an uncertainty of $\pm 0.1\,\text{GeV/cm}^3$. Current measurements however suggest $\mathcal{O}(1)$ uncertainties [73] on $\rho_{\rm loc}$. There are two types of analyses to determine the local dark matter density. Global measurements model the whole mass distribution of the Milky Way from rotation curves and infer the dark matter density at the solar position from the resulting mass model. This method is prone to uncertainties in each component of the Milky Way mass model and depends on the assumptions made for the dark matter density profile. Recent studies [74–81] obtain that the local dark matter density is between 0.2 GeV/cm^3 and 0.4 GeV/cm^3. Local measurement rely instead on the motion of tracers in the solar neighborhood at distances smaller than 1 kpc from the Sun. In this case, the dominant

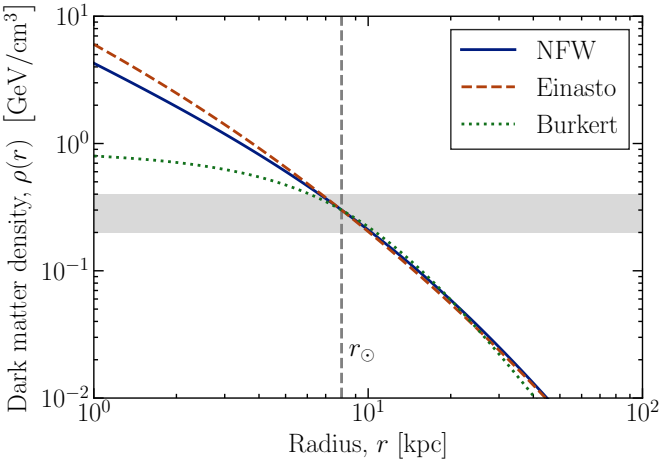

Figure 2.: The NFW [62, 63], the Einasto [65, 66] and the Burkert dark matter density profile [70]. In order to compare the shapes of the profiles, we choose the normalization in such a way that it predicts a dark matter density of $0.3\,\mathrm{GeV/cm^3}$ at the position of the sun, $r_\odot = 8$ kpc. We furthermore show the canonical value of the dark matter density with an uncertainty of $\pm 0.1\,\mathrm{GeV/cm^3}$ as gray shaded band and we indicate the position of the solar system with a gray dashed line.

uncertainties stem from the surface density of baryons and from the determination of the kinematic properties of the tracers. Latest local measurements [82–91] have a much larger spread, reaching from no hint towards dark matter to dark matter densities as large as $0.85\,\mathrm{GeV/cm^3}$.

2.2.2. The velocity distribution of dark matter particles in the Milky Way

There are several approaches to determine the velocity distribution of dark matter particles. As N-body simulations evolve the whole phase-space distribution of dark matter, it is possible to directly infer the velocity distribution. However, the simulated galaxy is only Milky Way like and does not explicitly contain the Solar System. The velocity distribution is then extracted by discretizing space into boxes and studying those boxes with the same distance to the galactic center as the Solar System. In order to illustrate this, we show the velocity distribution extracted from the Aquarius simulation [92] in Fig. 3. As the boxes are quite large, e.g. 2 kpc in Ref. [92], the extracted velocity distributions do not necessarily reflect distribution in the solar neighborhood but instead in a much larger volume. Another issue is the limited resolution of N-body simulations. As the traced particles consist of a large amount of real dark matter particles, only the average velocity of this bulk of dark matter particles is accessible via N-body simulations.

The velocity distribution can also be determined by using Eddington's result [93, 94]. For this, we assume spherical symmetry and a self-gravitating system, which implies that all particles are gravitationally bound to the halo and have energies per unit mass $\mathcal{E} > 0$. However, it is possible to generalize this to anisotropic halos [95]. As described

in Refs. [95–99], the dark matter density profile $\rho(\vec{r})$ can be used to infer the velocity distribution $f_{\vec{r}}(\vec{v})$ at the position $\vec{r}$ via

$$f_{\vec{r}}(\vec{v}) = \frac{\mathrm{F}(\vec{r},\vec{v})}{\rho(\vec{r})}\,, \tag{2.10}$$

where $\mathrm{F}(\vec{r},\vec{v})$ is the phase-space distribution. In the following, we assume that the halo is described by the relative gravitational potential $\Psi(r) = \Phi_0 - \Phi(r)$, where $\Phi(r)$ is the gravitational potential determined from Poisson's equation and Φ_0 is a constant. The density profile can then be written in terms of the density function $\mathrm{F}(\mathcal{E})$ [95]

$$\rho(r) = 4\pi\sqrt{2}\int_0^{\Psi(r)} \mathrm{d}\mathcal{E}\,\mathrm{F}(\mathcal{E})\sqrt{\Psi(r)-\mathcal{E}}\,, \tag{2.11}$$

where the density function depends solely via the energy per unit mass $\mathcal{E} = \Psi(r) - v^2$ on $\vec{r}$ and $\vec{v}$. Differentiating this equation with respect to Ψ, we obtain an Abel equation

$$\frac{\mathrm{d}\rho}{\mathrm{d}\Psi} = \sqrt{8}\pi\int_0^{\Psi} \mathrm{d}\mathcal{E}\frac{\mathrm{F}(\mathcal{E})}{\sqrt{\Psi-\mathcal{E}}}\,, \tag{2.12}$$

which can be inverted using Eddington's formula [93, 94]

$$\mathrm{F}(\mathcal{E}) = \frac{1}{\sqrt{8}\pi^2}\frac{\mathrm{d}}{\mathrm{d}\mathcal{E}}\int_0^{\mathcal{E}}\frac{\mathrm{d}\Psi}{\sqrt{\mathcal{E}-\Psi}}\frac{\mathrm{d}\rho}{\mathrm{d}\Psi}\,. \tag{2.13}$$

For a given density profile $\rho(r)$, this allows to self-consistently determine the density function $\mathrm{F}(\mathcal{E})$ and finally obtain the velocity distribution using Eq. (2.10). In Fig. 3, we show the velocity distribution obtained by Ref. [100] using this formalism. We note that the determination of the velocity distribution using this method heavily relies on the shape of the density profile and is prone to uncertainties of $\rho(r)$. This includes also the Core-Cusp controversy [71] discussed in the previous section.

Finally, it is possible to determine the velocity distribution from objects that are believed to trace the motion of dark matter in the Milky Way [101–103]. As suggested in Ref. [104], metal-poor[1] halo stars could be good tracers of dark matter which is supported by the ERIS simulation [106]. This is due to the fact that both dark matter and metal-poor stars are accreted to the Milky Way via mergers of satellites. In Fig. 3, we show the velocity distribution extracted in [103] from the combined data of *Gaia* [107,108] and SDSS [109]. If the accretion happened at early times ($z_{\mathrm{acc}} \gtrsim 3$), the kinematic properties today of the dark matter and metal-poor star components are similar as both are fully relaxed [103]. However, both components are not well correlated respectively displaced in the case of recent mergers. As described in Ref. [110], the dark matter component in the AURIGA [111] simulation is not well traced by stars if the galaxy was subject to a recent major merger. Another caveat of this method is that it is hard to take into account completely dark structures unless they are correlated to the motion of stars.

[1] Metal-poor stars are old [105] and have a low amount of iron compared to hydrogen [Fe/H].

2.2.3. The Standard Halo Model

The motivation for the Standard Halo Model (SHM) stems from the observation that the rotation curve of galaxies is flat in the outer regions, as apparent from the left plot of Fig. 1. This implies a constant rotation speed v_c and therefore

$$\frac{G\,M(r)\,m}{r^2} = \frac{m\,v_c^2}{r}\,, \tag{2.14}$$

where $M(r)$ is the mass of the Milky Way enclosed in a sphere of radius r and m is a small test mass. This relation does not hold in the inner region of the Milky Way as it is heavily influenced by baryons. In order to fulfill this equation, the density $\rho(r)$ has to be proportional to r^{-2} such that

$$M(r) = \int_0^r \mathrm{d}r'\, 4\pi r'^2\, \rho(r') \sim r\,. \tag{2.15}$$

The SHM therefore assumes that the dark matter density of the Milky Way is modeled by an isothermal sphere [112, 113]

$$\rho_{\mathrm{SHM}}(r) = \frac{\sigma_v^2}{2\pi\, G\, r^2}\,, \tag{2.16}$$

where σ_v is the velocity dispersion. Finally, the isothermal sphere implies a Maxwell-Boltzmann velocity distribution via Eddington's formula given in Eq. (2.10). The resulting velocity distribution reads [72, 112, 113]

$$f_{\mathrm{SHM}}(\vec{v}) = \frac{1}{(2\pi\sigma_v^2)^{3/2}\, N_{\mathrm{esc}}} \exp\left(-\frac{\vec{v}^2}{2\sigma_v^2}\right) \quad \text{for } v \leq v_{\mathrm{esc}}\,, \tag{2.17}$$

where the velocity dispersion of the Milky Way halo is roughly $\sigma_v \approx 156\,\mathrm{km\,s^{-1}}$ [72, 114, 115]. For the SHM, the velocity distribution is truncated at the escape velocity from the Milky Way. Here, we assume $v_{\mathrm{esc}} \simeq 544\,\mathrm{km/s}$ in concordance with the findings of Ref. [116]. In order to ensure that the velocity distribution is normalized, we have to introduce a normalization factor

$$N_{\mathrm{esc}} = \mathrm{erf}\left(\frac{v_{\mathrm{esc}}}{\sqrt{2}\sigma_v}\right) - \sqrt{\frac{2}{\pi}}\frac{v_{\mathrm{esc}}}{\sigma_v}\exp\left(-\frac{v_{\mathrm{esc}}^2}{2\sigma_v^2}\right)\,, \tag{2.18}$$

depending on the escape velocity v_{esc} and the velocity dispersion σ_v.

Despite being a good first approximation, it is unlikely that the SHM is realized in nature. As apparent from Eq. (2.15), the mass of the Milky Way would diverge for very large radii. Furthermore, the density profiles presented in section 2.2 are not proportional to r^{-2} and thus contradict the assumptions of the SHM. However, this implies that the velocity distribution also changes as it is related to the dark matter density profile, confer Eq. (2.10). In Fig.3, we show the SHM and compare it to the velocity distributions that are determined with the methods discussed in the previous section. As apparent from this plot, the SHM is not a good approximation to any of the other velocity distributions

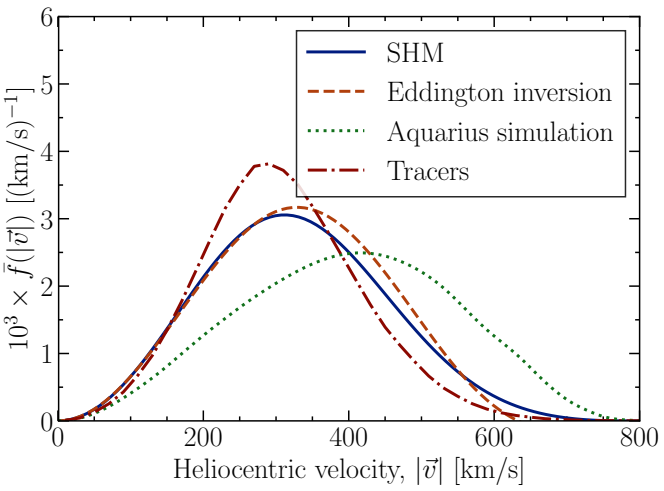

Figure 3.: The SHM as well as the velocity distributions determined from the Aquarius simulation [92], using Eddington inversion [100] and from tracers of dark matter [103]. In each case, the velocity distribution is given in the Sun's rest frame and averaged over angles.

as it predicts a different shape. It matches closest the results of Ref. [100] which also uses Eddington's result but assumes the NFW profile. The velocity distributions extracted from N-body simulations respectively from the motion of metal-poor stars show a much larger discrepancy. The Aquarius simulation [92] finds that the peak of the distribution is depleted while the high-velocity tail is enhanced. However, the opposite is reported in Ref. [103]. There, the peak of the distribution is shifted to lower velocities and is more pronounced than for the SHM while the high-velocity tail is suppressed. Despite the SHM being not a good fit to observations, also the current determinations of the velocity distributions disagree among each other. This leads us to conclude that there is currently no consensus on the velocity distribution of dark matter.

2.3. Dark matter substructure of the Milky Way

The paradigm of cold and collisionless dark matter predicts that small structures form first and then merge into larger structures [117, 118]. As a consequence of the hierarchical structure formation, the Milky Way halo is expected to host a large number of substructures. Indeed, recent analyses [102, 103] of the stellar kinematics measured by *Gaia* [107,108] show that a large fraction of the local dark matter halo of the Milky Way might be in substructure.

There are several types of substructures present in the Milky Way halo. One example of primary interest in this work are sub-halos, which are halo objects bound to larger halos. The largest known sub-halos of the Milky Way are the Large and the Small Magellanic Cloud as well as the known dwarf satellite galaxies. Those objects have masses of roughly $10^{11}\,M_\odot$ [119] respectively $10^7\,M_\odot$ [120]. In addition to these massive structures, there is a much larger fraction of light sub-halos which are not capable of accreting enough

matter to form stars and therefore remain dark [121–123]. Due to these observations, there has been a huge effort to determine the properties and the distribution of sub-halos in Milky Way-like galaxies, confer Refs. [124–135]. Another kind of substructure are stellar streams like Sagittarius [136–138], S1 [139], Ophiuchus [140], Orphan [141] or Cetus [141]. They are the debris of dwarf satellite galaxies that were disrupted by the Milky Way and are currently being accreted [142]. In addition to this, a recent study [143] of the *Gaia* [107, 108] data found a high-velocity stream counterrotating relative to the Sun. We conclude that stellar substructures play an important role in describing the dark matter halo.

2.3.1. Properties of dark matter sub-halos

In this work, we model the dark matter density of sub-halos with an NFW profile [62, 63]

$$\rho_{\rm sh}(r) = \begin{cases} \dfrac{\rho_s}{(r/r_s)\,(1+r/r_s)^2} & \text{for } r \leq r_t \\ 0 & \text{for } r > r_t\,, \end{cases} \tag{2.19}$$

where r_t is the truncation radius at which we set the profile to zero. For field halos [2], the truncation radius is identified with the virial radius $\mathrm{R_{vir}}$ [144–147], which is defined such that the mean density within a sphere of radius $\mathrm{R_{vir}}$ is $\Delta_c = 200$ times larger [148] than the critical density $\rho_{\rm crit} = 1.05371 \cdot 10^{-5}\, h^2\ \mathrm{GeV\,cm^{-3}}$. For sub-halos, the truncation radius is smaller than $\mathrm{R_{vir}}$ due to mass loss within the host halo [149] and is not related to the critical density. Here, a halo is described by its scale radius r_s and scale density ρ_s. The scale radius of a halo is related to the truncation radius via $r_s = r_t/c_V$, where c_V is the concentration parameter.

The mass of a halo is defined to be the mass enclosed by a sphere with radius r_t and is obtained by integrating the density profile in Eq. (2.19) up to r_t. This yields

$$M = \frac{4\pi}{3}\,\rho_s\, r_s^3\, f(c_V)\,, \tag{2.20}$$

where $f(c_V) = \ln(1+c_V) - c_V/(1+c_V)$. For field halos, we follow Ref. [150] and parametrize the distribution of the concentration parameter at current times by a log-normal distribution with mean value

$$\log_{10}(c_V) = 1.399 - (0.0257\, \log_{10}(M/M_\odot)) \cdot \left(1 + 0.00481(\log_{10}(M/M_\odot)^2)\right) \tag{2.21}$$

and scatter [131] $\sigma\left(\log_{10}(c_V)\right) = 0.06$. We refer to Refs. [151,152] for a detailed discussion of the concentration parameter of field halos. For field halos in the relevant mass range between $10^{-5}\, M_\odot$ and $10^{11}\, M_\odot$, c_V takes values between $c_V \simeq 9$ and $c_V \simeq 35$. Milky Way sub-halos in the same mass range have concentration parameters between $c_V \simeq 1$ and $c_V \simeq 35$ which suggests that sub-halos are denser and more concentrated than field halos, confer the results of Ref. [135]. By adopting a model for tidal stripping, the distribution

[2] Field halos are halo structures that are not bound to larger halos.

of the concentration parameter for sub-halos can be calculated.

The scale radius and scale density are related to the mass of the sub-halo M and concentration parameter c_V via

$$\rho_s = \frac{c_V\,\bar{\rho}}{3\,f(c_V)} \tag{2.22}$$

$$r_s = \left(\frac{M}{4\pi\,\rho_s\,f(c_V)}\right)^{1/3} = \left(\frac{3\,M}{4\pi\,c_V^3\,\bar{\rho}}\right)^{1/3}\,, \tag{2.23}$$

where $\bar{\rho}$ is the mean density inside a sub-halo. Assuming a Hubble constant $h \approx 0.68$ [153], the mean density inside a sub-halo is

$$\bar{\rho} = \Delta_c\,\rho_{\rm crit} \approx 9.745 \cdot 10^{-4}\ \mathrm{GeV\,cm^{-3}}\,. \tag{2.24}$$

Therefore, the density profile of a sub-halo is completely determined by its mass M and concentration c_V.

Assuming that the sub-halos of the Milky Way are fully virialized, we model the velocity distribution of dark matter particles bound to a sub-halo by a Maxwell-Boltzmann distribution with velocity dispersion $\sigma_{\rm sh}$

$$f_{\rm sh|sh}(\vec{v}) = \frac{1}{(2\pi\,\sigma_{\rm sh}^2)^{3/2}}\,\exp\left(-\frac{\vec{v}^2}{2\,\sigma_{\rm sh}^2}\right)\,. \tag{2.25}$$

The mean-squared velocity of those particles is given by

$$\langle|\vec{v}|^2\rangle = \int \mathrm{d}\vec{v}^3\,|\vec{v}|^2\,f_{\rm sh|sh}(\vec{v}) = 3\,\sigma_{\rm sh}^2\,. \tag{2.26}$$

We determine the velocity dispersion $\sigma_{\rm sh}^2$ by using the virial theorem which relates the kinetic energy T of the sub-halo to its potential energy U via

$$T = -\frac{1}{2}\,U\,. \tag{2.27}$$

The total kinetic energy of a sub-halo with mass M and mean-squared speed $\langle v^2\rangle$ is given by $T = \frac{1}{2}\,M\,\langle v^2\rangle$. Furthermore, we calculate the total gravitational energy of the sub-halo via

$$U = -4\pi G \int_0^R \frac{M_{\rm enc}(r)}{r} r^2 \rho_{\rm sh}(r)\mathrm{d}r\,. \tag{2.28}$$

Here, $M_{\rm enc}(r)$ is the mass of a sub-halo enclosed in a sphere with radius r and G is the gravitational constant. Adopting the NFW density profile from Eq. (2.19), we perform the integration and obtain

$$\begin{aligned} U &= -8\pi^2\,G\,\rho_s^2\,r_s^5\,\left[1 - 2\frac{\ln(c_V+1)}{(c_V+1)} - \frac{1}{(c_V+1)^2}\right] \\ &= -\left(\frac{\pi}{6}\right)^{1/3}\frac{G\,c_V}{f(c_V)^2}\bar{\rho}^{1/3}\,M^{5/3}\,\left[1 - 2\frac{\ln(c_V+1)}{(c_V+1)} - \frac{1}{(c_V+1)^2}\right]\,. \end{aligned} \tag{2.29}$$

We then apply the virial theorem and solve for the velocity dispersion. This yields

$$\sigma_{\rm sh}^2 = -\frac{U}{3M} = \frac{1}{3}\left(\frac{\pi}{6}\right)^{1/3}\frac{G\,c_V}{f(c_V)^2}\,\bar{\rho}^{1/3}\,M^{2/3}\left[1-2\frac{\ln(c_V+1)}{(c_V+1)}-\frac{1}{(c_V+1)^2}\right]. \tag{2.30}$$

In Fig. 4, we show the dependence of the velocity dispersion on the sub-halo mass as well as the band constructed from varying c_V within its 1σ range. From the negligibly thin

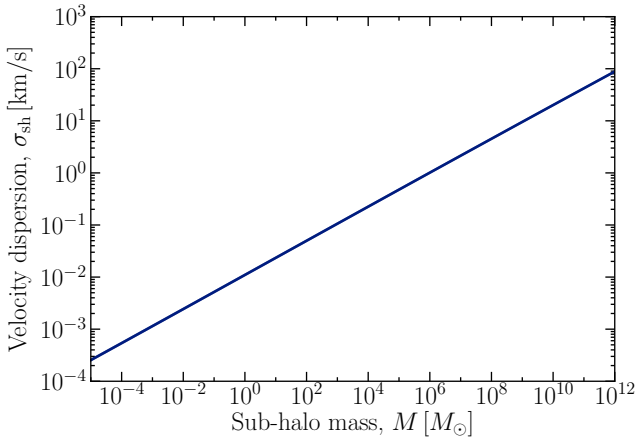

Figure 4.: Velocity dispersion as a function of the sub-halo mass. We assume that the sub-halos are fully virialized and that the velocity distribution of dark matter particles bound to sub-halos is described by a Maxwell-Boltzmann distribution. We furthermore plot the 1σ band in c_V which is negligibly thin.

band, we conclude that the dependence of $\sigma_{\rm sh}^2$ on the concentration parameter c_V is weak. The velocity dispersion is well approximated by

$$\sigma_{\rm sh} \approx 1.5\,{\rm km/s}\left(\frac{M}{10^6\,M_\odot}\right)^{\frac{1}{3}}, \tag{2.31}$$

where we assumed a generic value $c_V = 20$.

2.3.2. The distribution of sub-halos in the Milky Way

Following recent results from hydrodynamical N-body simulations that include baryonic effects [154], we model the spatial distribution of sub-halos within the Milky Way by an Einasto profile [65, 66]

$$\ln\left(n_{\rm sh}(r)/n_{-2}\right) = -\frac{\alpha}{2}\left[\left(\frac{r}{r_{-2}}\right)^{\alpha}-1\right]. \tag{2.32}$$

Here, r_{-2} is the radius at which the slope of the density profile $\ln\left(n_{\rm sh}(r)\right)$ equals -2. Furthermore, n_{-2} is the number of sub-halos within r_{-2} and α is a parameter. For r_{-2} and α, we follow Ref. [154] and adopt the values $r_{-2} = 0.817 \cdot {\rm R}_{\rm vir}^{\rm (MW)}$ and $\alpha = 0.854$. Here, ${\rm R}_{\rm vir}^{\rm (MW)} \simeq 200\,{\rm kpc}$ [155, 156] denotes the virial radius of the Milky Way. We calculate the normalization n_{-2} by demanding that $\int_{V_{\rm MW}} {\rm d}r^3\, n_{\rm sh}(r) = N_{\rm sh}$, where $N_{\rm sh}$ is the total

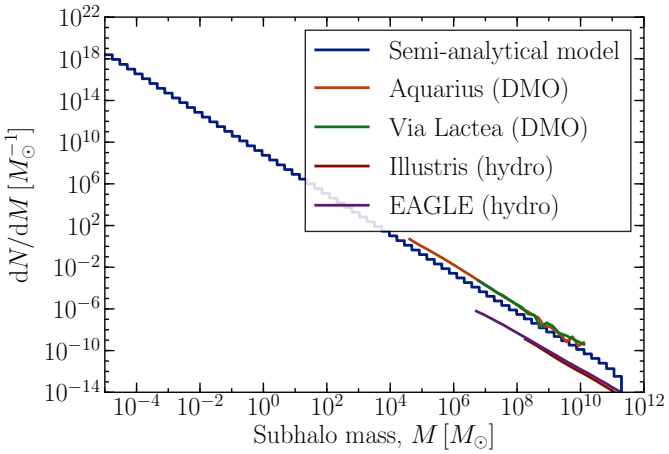

Figure 5.: The sub-halo mass function of the semi-analytical model from [135] as well as those extracted from simulations. Here, we show results from the Aquarius [126] and Via Lactea [157] dark matter only N-body simulations as well as from the Illustris and EAGLE hydrodynamical N-body simulations. For the latter, the sub-halo mass functions are taken from [158]. In the legend, we indicate those two simulation types by the labels DMO respectively hydro.

number of sub-halos.

For the velocity distribution of sub-halos in the Milky Way, we assume that it follows a Maxwell-Boltzmann distribution in the rest frame of the galaxy

$$f_{\mathrm{MB}}(\vec{v}) = \frac{1}{(2\pi\sigma_v^2)^{3/2}\, N_{\mathrm{esc}}} \exp\left(-\frac{\vec{v}^2}{2\sigma_v^2}\right) \quad \text{for } v \leq v_{\mathrm{esc}}\,, \tag{2.33}$$

where we assume $\sigma_v \approx 156\,\mathrm{km/s}$ and $v_{\mathrm{esc}} = 544\,\mathrm{km/s}$ as for the SHM. Furthermore, the normalization of the distribution N_{esc} depends on σ_v as well as v_{esc} and is given by Eq. (2.18).

In addition to the phase-space distribution of sub-halos in the Milky Way, another important key figure is the amount of sub-halos as a function of the sub-halo mass. This is described by the sub-halo mass function (ShMF) and is extracted from simulations by counting the number of sub-halos that fall in given bins of the sub-halo mass. The lower limit of the sub-halo mass function is given by the free streaming length of dark matter which restricts sub-halos to be heavier than $10^{-6}\,M_\odot$ [118] respectively $10^{-8}\,M_\odot$ [159]. Following Ref. [160], the minimal sub-halo mass that N-body simulations are able to resolve can be estimated from the particle mass by assuming that only sub-halos with at least 100 bound particles can be reliably detected. As shown in Fig. 5, current dark matter only N-body simulations resolve sub-halos heavier than $10^5\,M_\odot$. An exception to this is the semi-analytical model [135] which was built to trace sub-halos from infall until today including tidal stripping. Since it was tuned to a set of dedicated simulations probing sub-halo masses from $10^{-5}\,M_\odot$ to $10^{11}\,M_\odot$, this allows to cover the complete range of expected sub-halo masses. In Fig. 5, we compare this to sub-halo mass functions extracted from the dark matter only (DMO) N-body simulations Aquarius [126] and Via

Lactea [157] as well as to the sub-halo mass functions from the hydrodynamical (hydro) N-body simulations Illustris and EAGLE, both determined in [158]. We observe that the dark matter only N-body simulations agree well with the semi-analytical calculation from Ref. [135] while hydrodynamical N-body simulations predict a smaller number of sub-halos compared to the dark matter only case. As noted in Refs. [161–163], the amount of sub-halos is reduced in hydrodynamical N-body simulations. This conclusion however depends on the feedback model adopted in the simulation, confer [158].

There are claims that substructure could be depleted due to its interaction with the Milky Way disk [164, 165]. This effect would be strongest close to the galactic center and therefore alter the shape and normalization of the spatial distribution in Eq. (2.32) as well as the halo mass function, confer Fig. 5. However, the results of those calculations vary significantly from a 10% effect up to a 90% decrease in the expected amount of substructure. Since there is no common sense on the existence or magnitude of this effect, we do not take it into account here.

Chapter 3.

Detection of dark matter

3.1. Particle dark matter

Despite compelling evidence for dark matter from astrophysical observations, little is known about its particle physics properties. However, possible dark matter models have to fulfill several requirements in order to provide an explanation for the observations described in section 2.1.1. One necessary requirement is that dark matter is present in the Universe also at current times. Therefore, the model has to predict at least one particle that is stable or whose lifetime is larger than the age of the Universe. In addition to this, the electric charge of dark matter must be small or zero. Recent estimates of the dark matter charge place stringent limits of $|q| \lesssim 10^{-14}|e|\,(m_{\mathrm{DM}}/\mathrm{GeV})$ [166,167]. Finally, the model must be able to explain the observed dark matter density of $\Omega_{\mathrm{DM}}\,h^2 \simeq 0.12$, confer Eq. (2.1).

In addition to these requirements, dark matter models have to fulfill several constraints. First, baryonic dark matter candidates are disfavored due to the good agreement of the baryon density extracted from the CMB and BBN, confer the discussion in section 2.1.2. Second, each model is subject to various constraints on its interactions. Observations of the bullet cluster suggest that the self-interaction cross section of dark matter is bounded by $\sigma_{\mathrm{self}}/m_{\mathrm{DM}} < 2 \times 10^{-24}\,\mathrm{cm}^2/\mathrm{GeV}$. Otherwise, it is not possible to explain the observed separation between the interaction region and the region with the highest mass density, confer 2.1.1. Furthermore, interactions of dark matter with nuclei are constrained by various experimental searches for dark matter. This includes direct detection experiments and searches with neutrino telescopes that we both cover later in this chapter. Other constraints on the interactions of dark matter with SM particles come from indirect searches using γ-rays or cosmic rays as well as from colliders like the LHC.

With this in mind, the only known particles that could act as dark matter are SM neutrinos [6]. They are stable particles, electrically neutral, interact only weakly with SM particles and since the discovery of neutrino oscillations, it is established that they are massive. However, the relic density of SM neutrinos is given by [7]

$$\Omega_\nu\,h^2 = \sum_{i=1}^{3} \frac{m_i}{93\,\mathrm{eV}}\,, \tag{3.1}$$

where m_i is the mass of the i-th SM neutrino. Currently, the tritium β-decay experiment

KATRIN provides the best upper limits and restricts the SM neutrino mass to be $m_\nu < 1.1\,\mathrm{eV}$ at a confidence level of 90% [168]. By comparing the predictions of Eq. (3.1) to the measurements presented in Eq. (2.1), we conclude that SM neutrinos can contribute at most 29.6% to the dark matter density. Furthermore, structure formation is in conflict with the role of SM neutrinos as dark matter. Due to their low mass, SM neutrinos are highly relativistic particles and therefore an example of hot dark matter [169, 170]. In contrast to the "bottom up" procedure predicted by cold dark matter where small structures form first and then merge into larger ones, hot dark matter predicts a "top down" formation where large structures form first and then fracture into smaller ones. Using N-body simulations, Ref. [171] showed that SM neutrinos cannot explain dark matter in the Universe as it is not possible to explain the observed structures in the Universe.

As there is no good dark matter candidate in the SM, physics beyond the Standard Model is needed to explain dark matter. There is a huge number of proposed models that include dark matter candidates, sometimes motivated to solve other open problems in particle physics. Examples for this are supersymmetric models [20] that aim to solve the hierarchy problem, Kaluza-Klein models [172–174] that assume extra spacetime dimensions, sterile neutrinos [175] that could explain neutrino masses or axion dark matter models [176] that aim to solve the strong-CP problem. Instead of adopting a specific model, we focus in this work on the weakly interacting massive particle which represents a class of dark matter candidates. In the most general definition, a WIMP is a particle with a mass between a couple of GeV and several TeV that interacts weakly with SM particles. In order make the WIMP stable or have a lifetime longer than the age of the Universe, it is usually assumed that the WIMP is subject to a symmetry that prevents its decays, like R-parity in supersymmetric models.

There are several compelling arguments in favor of WIMP dark matter and in the remainder of this work, we explicitly assume that dark matter is a WIMP particle. First, it arises naturally in several theories of physics beyond the Standard Model. An example for a dark matter candidate that belongs to this category is the neutralino predicted by supersymmetric models [20]. Furthermore, WIMPs provide testable predictions that can be verified by experiments [177]. As discussed later in this work, searches for WIMP dark matter with various strategies are currently pursued. Finally, WIMP dark matter offers an intriguing way to explain the observed abundance of dark matter in the Universe via the freeze-out mechanism, see Refs. [178–181]. This mechanism relies on the assumption that dark matter and SM particles were in thermal and chemical equilibrium in the early Universe due to interactions of the form $\mathrm{DM\,DM} \leftrightarrow \mathrm{SM\,SM}$. As long as the interaction rate is larger than the expansion rate of the Universe, dark matter and the SM particles stay in equilibrium. At some point, the Universe expanded enough such that the annihilation rate of WIMP particles drops below the expansion rate of the Universe. WIMPs then decouple and their abundance is frozen-out. As discussed in Refs. [7, 21, 174, 182], the Boltzmann equation describes the time evolution of the particle number density of

WIMPs n

$$\frac{\mathrm{d}n}{\mathrm{d}t} + 3\,H\,n = -\langle\sigma v\rangle\,\left(n^2 - n_{\mathrm{eq}}^2\right)\,, \tag{3.2}$$

where $\langle\sigma v\rangle$ is the thermally averaged annihilation cross section of WIMPs, H is the Hubble constant and n_{eq} denotes the number density in thermal equilibrium. For heavy particles like WIMPs, the thermally averaged annihilation cross section can be expanded in terms of powers of v [7]

$$\langle\sigma v\rangle = a + b\,\langle v^2\rangle + \mathcal{O}(\langle v^4\rangle) \approx a + 6\,\frac{b}{x}\,, \tag{3.3}$$

where $x = m/T$ is the ratio of the mass of the WIMP particle and the temperature of the thermal bath. Assuming that the entropy after freeze-out is much larger than the entropy before, solving Eq. (3.2) yields the following dark matter density

$$\Omega_{\mathrm{WIMP}}\,h^2 = \frac{1.07\cdot 10^9\,\mathrm{GeV}^{-1}}{M_{\mathrm{PL}}}\,\frac{x_{\mathrm{F}}}{\sqrt{g^*}}\,\frac{1}{a + 3\,b/x_{\mathrm{F}}}\,, \tag{3.4}$$

where $x_{\mathrm{F}} = m/T_{\mathrm{F}}$ and T_{F} denotes the freeze-out temperature. Furthermore, g^* is the number of relativistic degrees of freedom at freeze-out. Using $g^* \approx 100$ [21] and $x_{\mathrm{F}} \approx 10$ [113], the dark matter density reads [20]

$$\Omega_{\mathrm{WIMP}}\,h^2 \approx \frac{3\cdot 10^{-27}\,\mathrm{cm/s}^{-1}}{\langle\sigma v\rangle}\,. \tag{3.5}$$

Assuming furthermore that WIMPs annihilate into lighter final states, the thermally averaged annihilation cross section is well approximated by $\langle\sigma v\rangle = \alpha^2/m^2$ [113]. Here, α is proportional to the square of the coupling constant and $\alpha \sim 0.01$ for a weakly interacting particle. This gives rise to exactly the correct dark matter abundance for a dark matter mass of $m_{\mathrm{DM}} \sim 100\,\mathrm{GeV}$, which is frequently referred to as the WIMP miracle. Interestingly, two of the defining properties of the WIMP, its weak interactions and the fact that it is massive, naturally give rise to the correct dark matter abundance. Despite this might be a pure coincidence, it serves as a motivation to study WIMPs as dark matter candidates.

3.2. Interactions of dark matter with nuclei

3.2.1. Spin-independent interactions

Spin-independent interactions between dark matter particles and nuclei are either due to scalar-scalar or vector-vector interactions. They are theoretically appealing since they arise naturally from several models, e.g supersymmetric models which feature a neutralino a lightest supersymmetric particle [20]. On the Lagrangian level, the following two terms

describe spin-independent interactions [112, 113]

$$\mathcal{L} \supset \alpha_{\mathrm{q}}^{\mathrm{S}}\, \bar{\chi}\chi\bar{\mathrm{q}}\mathrm{q} + \alpha_{\mathrm{q}}^{\mathrm{V}}\, \bar{\chi}\gamma^{\mu}\chi\bar{\mathrm{q}}\gamma_{\mu}\mathrm{q}\,, \tag{3.6}$$

where $\alpha_{\mathrm{q}}^{\mathrm{S}}$ and $\alpha_{\mathrm{q}}^{\mathrm{V}}$ are the scalar-scalar respectively vector-vector coupling constants for a specific quark species q. Furthermore, χ and q denote the dark matter field respectively the quark field.

In order to work on the nucleus level, dark matter parton interactions have to be related to interactions with nucleons first. The scalar-scalar couplings of dark matter to protons f^{p} respectively to neutrons f^{n} are given by [112]

$$\frac{f^{\mathrm{p}}}{m_{\mathrm{p}}} = \sum_{\mathrm{q}=u,d,s} \frac{\alpha_{\mathrm{q}}^{S}}{m_{\mathrm{q}}}\, f_{\mathrm{Tq}}^{\mathrm{p}} + \frac{2}{27}\, f_{\mathrm{TG}}^{\mathrm{p}} \sum_{\mathrm{q}=c,b,t} \frac{\alpha_{\mathrm{q}}^{S}}{m_{\mathrm{q}}}\,, \tag{3.7}$$

where a similar relation arises for neutrons [113]. Here, the factors $f_{\mathrm{Tq}}^{\mathrm{p,n}}$ model the contribution of the light quarks flavor q to the mass of the proton or the neutron. Furthermore, $f_{\mathrm{TG}}^{\mathrm{p,n}}$ is the interaction strength of dark matter with the gluon scalar density in the nucleon. Concretely, those factors are given by

$$\begin{aligned} m_{\mathrm{q}}\, f_{\mathrm{Tq}}^{\mathrm{p}} &\equiv \langle \mathrm{p}|\, m_{\mathrm{q}}\, \bar{\mathrm{q}}\mathrm{q}\, |\mathrm{p}\rangle \\ f_{\mathrm{TG}}^{\mathrm{p}} &= 1 - \sum_{\mathrm{q}=u,d,s} f_{\mathrm{Tq}}^{\mathrm{p}}\,, \end{aligned} \tag{3.8}$$

where we refer to Ref. [183] for numerical results. Finally, the differential WIMP-nucleus scattering cross section for scalar-scalar interactions reads

$$\frac{\mathrm{d}\sigma_{\mathrm{SI}}}{\mathrm{d}E_R} = \frac{\kappa\, m_T}{2\pi\, v^2}\, \left(Z\, f^{\mathrm{p}} + (A-Z)\, f^{\mathrm{n}}\right)^2\, F^2(E_R)\,, \tag{3.9}$$

where $F^2(E_R)$ is a form factor that parametrizes the dependence on the recoil energy and κ is a constant that arises from summing and averaging initial state respectively final state spins. Concretely, $\kappa = 4$ if WIMPs are Majorana particles and $\kappa = 1$ if they are Dirac particles [184]. Furthermore, A and Z denote the total number of nucleons respectively the number of protons in the nucleus and m_T is the mass of the nucleus.

In addition to this, the vector-vector interaction gives rise to a term that vanishes if dark matter is a Majorana particle but is non-zero for Dirac particles. This interaction yields the following differential WIMP-nucleus scattering cross section [112]

$$\frac{\mathrm{d}\sigma_{\mathrm{SI}}}{\mathrm{d}E_R} = \frac{2\, m_T}{\pi\, v^2}\, \frac{B_N^2}{256}\, F^2(E_R)\, \delta(\kappa - 1)\,, \tag{3.10}$$

where $F^2(E_R)$ is again the form factor for spin-independent interactions and $\delta(\kappa - 1)$ emphasizes that this term vanishes for Majorana particles. Here, the parameter B_N is given by

$$B_N = \alpha_u^V\, (A + Z) + \alpha_d^V\, (2A - Z)\,, \tag{3.11}$$

where α_u^V and α_d^V are the coupling constants for up-quarks respectively down-quarks as only valence quarks contribute to this term [112].

In the case of spin-independent dark matter-nucleus interactions, the form factor $F^2(E_R)$ is given by the Fourier transform of the nucleon density [185,186] due to the coherent nature of the interaction. Parametrized in terms of the momentum transfer $q = \sqrt{2\, m_T\, E_R}$, the form factor reads [185–187]

$$F^2(q) = \left(\frac{3\, j_1(q\, r_0)}{q\, r_0} \right)^2 \exp\left(-q^2\, s^2\right) \,, \tag{3.12}$$

which is referred to in the literature as Helm form factor. Here, j_1 is the spherical Bessel function for $n = 1$ and $s \simeq 1\,\text{fm}$ [112,113] is the thickness parameter of the nuclear surface. The parameter r_0 is related to the nuclear radius R_N and the thickness parameter s via

$$r_0 = \sqrt{R_N^2 - 5\, s^2} \,, \tag{3.13}$$

where $R_N \simeq 1.2\, A^{1/3}\,\text{fm}$ [112] depends on the number of nucleons A. The form factor is normalized to unity in the limit of zero momentum transfer $q \to 0$, as apparent from Eq. (3.12).

In general, the differential scattering cross section is given by

$$\frac{\mathrm{d}\sigma_{\text{SI}}}{\mathrm{d}E_R} = \frac{m_T\, \sigma_0^{\text{SI}}\, F^2(E_R)}{2\, \mu_T^2\, v^2} \,, \tag{3.14}$$

where σ_0^{SI} is the scattering cross section at zero momentum transfer and $F^2(E_R)$ is the nuclear form factor. Furthermore, $\mu_T = m_{\text{DM}}\, m_T/(m_{\text{DM}} + m_T)$ is the WIMP-nucleus reduced mass. Taking into account scalar-scalar as well as vector-vector interactions, σ_0^{SI} reads [112,115]

$$\sigma_0^{\text{SI}} = \frac{\kappa\, \mu_T^2}{4\pi} \left[(Z\, f^{\text{p}} + (A - Z)\, f^{\text{n}})^2 + \frac{B_N^2}{256}\, \delta(\kappa - 1) \right] \,, \tag{3.15}$$

where f^{p} and f^{n} paramterize the coupling strength of dark matter to protons respectively neutrons. For the usual assumption of equal coupling to protons and neutrons as well as assuming Majorana dark matter, the expression for the scattering cross section at zero momentum transfer simplifies to

$$\sigma_0^{\text{SI}} = \frac{\mu_T^2}{\pi}\, A^2\, (f^{\text{p}})^2 \,. \tag{3.16}$$

In order to compare the results of experiments using different target nuclei, the dark matter proton respectively the dark matter neutron cross section is used. It is related to the spin-independent scattering cross section at zero momentum transfer via [113,115,184]

$$\sigma_0^{\text{SI}} = \frac{\mu_T^2}{\mu_{\text{p,n}}^2}\, A^2\, \sigma_{\text{SI}}^{\text{p,n}} \,, \tag{3.17}$$

where $\mu_{\text{p,n}}$ and μ_T are the dark matter-nucleon respectively the dark matter-nucleus

reduced mass. With this, the differential scattering cross section can be expressed in terms of the interactions with nucleons

$$\frac{\mathrm{d}\sigma_{\mathrm{SI}}}{\mathrm{d}E_R} = \frac{m_T}{2\,\mu_{\mathrm{p,n}}^2\,v^2}\,A^2\,\sigma_{\mathrm{SI}}^{\mathrm{p,n}}\,F^2(E_R)\,, \tag{3.18}$$

where all information on the particle physics model of dark matter is encoded in the dark matter-nucleon cross section $\sigma_{\mathrm{SI}}^{\mathrm{p,n}}$.

As apparent from this expression, the scattering cross section scales with the squared number of nucleons A^2 for $f^{\mathrm{p}} \approx f^{\mathrm{n}}$. Since dark matter scatters coherently off the nucleus, the scattering cross section increases when increasing the number of nucleons. Popular target nuclei for direct detection experiments are therefore heavy elements like Xenon, Germanium or Iodine. However, the spin-independent scattering cross section might be suppressed due to destructive interference if the ratio of the interactions to protons and neutrons fulfills $f^{\mathrm{p}}/f^{\mathrm{n}} \approx -(A-Z)/Z$. As this ratio is different for each nucleus, it is important to have direct detection experiments with different targets in order to not miss the dark matter signal.

3.2.2. Spin-dependent interactions

Spin-dependent interactions arise for dark matter particles that interact with the quark axial current $\bar{\mathrm{q}}\gamma_\mu\gamma_5\mathrm{q}$. For Majorana or Dirac dark matter, the following term models spin-dependent interactions [112, 184]

$$\mathcal{L} \supset \alpha_{\mathrm{q}}^A\;(\bar{\chi}\gamma_\mu\gamma_5\chi)\;(\bar{\mathrm{q}}\gamma^\mu\gamma_5\mathrm{q})\;. \tag{3.19}$$

In order to relate this to the nucleus level, one constructs the nucleus matrix element which is given by [112]

$$\langle N|\,\bar{\mathrm{q}}\gamma^\mu\gamma_5\mathrm{q}\,|N\rangle = 2\lambda_{\mathrm{q}}^N\;\langle N|\,J_N^\mu\,|N\rangle\,, \tag{3.20}$$

where J_N^μ is the spin operator of the nucleus. The coefficients λ_{q}^N relate the quark axial current to the spin of the nucleus and are given by

$$\lambda_{\mathrm{q}}^N \simeq \frac{\Delta_{\mathrm{q}}^{(\mathrm{p})}\langle S_{\mathrm{p}}\rangle + \Delta_{\mathrm{q}}^{(\mathrm{n})}\langle S_{\mathrm{n}}\rangle}{J}\,, \tag{3.21}$$

where J is the total spin of the nucleus. Furthermore, $\langle S_{\mathrm{p,n}}\rangle$ are the expectation values of the spin of the proton group respectively the neutron group in the nucleus. They are determined from nuclear calculations as performed for example in Refs. [188–193]. Finally, the constants $\Delta_{\mathrm{q}}^{(\mathrm{p,n})}$ are extracted from the axial vector current in a nucleon and describe the amount of spin carried by quarks of the flavor q inside the proton respectively the neutron. Measurements of those quantities were performed in Refs. [194–197]. With these definitions, the Lagrangian reads

$$\mathcal{L} = 2\sqrt{2}\,G_F\,\Lambda\,(\bar{\chi}\gamma_\mu\gamma_5\chi)\;\langle N|\,J_N^\mu\,|N\rangle\;, \tag{3.22}$$

where G_F denotes Fermi's constant. It is convenient to define

$$\Lambda = \frac{a_\mathrm{p} \langle S_\mathrm{p} \rangle + a_\mathrm{n} \langle S_\mathrm{n} \rangle}{J} \,, \tag{3.23}$$

which weights the couplings of dark matter to protons respectively neutrons with the fraction of the spin that is carried by protons respectively neutrons and the total spin of the nucleus. The dark matter proton respectively neutron coupling constants are determined by adding up the contributions from all quarks

$$a_\mathrm{p} = \sum_{\mathrm{q}=u,d,s} \frac{\alpha_\mathrm{q}^A}{\sqrt{2}\, G_F} \, \Delta_\mathrm{q}^{(\mathrm{p})} \qquad\qquad a_\mathrm{n} = \sum_{\mathrm{q}=u,d,s} \frac{\alpha_\mathrm{q}^A}{\sqrt{2}\, G_F} \, \Delta_\mathrm{q}^{(\mathrm{n})} \,, \tag{3.24}$$

where the constants $\Delta_\mathrm{q}^{(\mathrm{p,n})}$ are related to the amount of spin carried by quarks of the flavor q.

Using the Lagrangian in Eq. (3.22), the differential WIMP-nucleus scattering cross section for a spin-$\frac{1}{2}$ dark matter particle and spin-dependent interaction is given by [184]

$$\frac{\mathrm{d}\sigma_\mathrm{SD}}{\mathrm{d}E_R} = \frac{4\,\kappa\, m_T}{\pi\, v^2} \, \Lambda^2 \, G_F^2 \, J(J+1) \, \frac{S_A(E_R)}{S_A(0)} \,, \tag{3.25}$$

where $\kappa = 4$ if dark matter is a Majorana particle and $\kappa = 1$ if it is a Dirac particle. We refer to [198] for a similar derivation of this quantity for a spin-1 dark matter particle. Here, $S_A(q)$ are nuclear structure functions that are determined numerically, confer [199–201]. For spin-dependent interactions, the scattering cross section at zero momentum transfer σ_0^SD is given by the following expression [202]

$$\sigma_0^\mathrm{SD} = \frac{8\,\kappa\, \mu_T^2\, G_F^2}{2\,J+1} \, S_A(0) \,, \tag{3.26}$$

where μ_T^2 is the dark matter-nucleus reduced mass. In order to compare experiments using different target nuclei, the results are cast in terms of the dark matter proton respectively neutron scattering cross section at zero momentum transfer. It can be derived from σ_0^SD via [202]

$$\sigma_\mathrm{SD}^\mathrm{p,n} = \frac{3\,\mu_\mathrm{p,n}^2\,(2J+1)}{4\pi\,\mu_T^2\, S_A(0)} \, \sigma_0^\mathrm{SD} \,, \tag{3.27}$$

where $\mu_\mathrm{p,n}$ is the dark matter proton respectively neutron reduced mass. Finally, the differential WIMP-nucleus scattering cross section can be rewritten in terms of $\sigma_\mathrm{p,n}^\mathrm{SD}$

$$\frac{\mathrm{d}\sigma_\mathrm{SD}}{\mathrm{d}E_R} = \frac{2\pi\, m_T}{3\,\mu_\mathrm{p,n}^2\, v^2\,(2J+1)} \, \sigma_\mathrm{SD}^\mathrm{p,n} \, S_A(E_R) \,, \tag{3.28}$$

where the whole dependence on particle physics is encoded in $\sigma_\mathrm{SD}^\mathrm{p,n}$.

In contrast to spin-independent dark matter-nucleus interactions, the spin-dependent scattering cross section does not increase with the number of nucleons A. Instead, the interaction strength scales with the spin of the nucleus. In order to test the spin-dependent

interactions between dark matter and nucleons, it is necessary to use nuclei for which either the protons or the neutrons contribute significantly to the total spin of the nucleus. Prime targets are for example Fluorine that has an unpaired proton which carries most of the spin of the nucleus. A further example is Xenon that has stable isotopes with an unpaired neutron which allows to effectively probe spin-dependent interactions with neutrons. Although the strength of spin-independent interactions usually exceeds those of spin-dependent ones, there are models for which the spin-independent interactions are suppressed [203]. Therefore, it is crucial to explore all possible interaction types.

3.2.3. Interactions of non-relativistic dark matter with nuclei

In addition to spin-independent and spin-dependent interactions, it is possible to construct a general, non-relativistic effective field theory for dark matter-nucleus interactions. In this work, we use the theory derived in Refs. [204–206] and adopt the form factors for direct detection experiments provided in [206]. Furthermore, we use the form factors relevant for nuclei present in the Sun which were determined in Ref. [207]. In the following discussion, we assume that dark matter has a spin of 0 or $\frac{1}{2}$. The calculation for spin-1 dark matter is similar, but we show only the final result for the sake of simplicity.

When constructing the most general and non-relativistic Hamiltonian for dark matter-nucleon interactions, energy and momentum conservation as well as Galilean invariance must be fulfilled. As detailed in [204–206], all operators in the Hamiltonian must be constructed from the following five operators

$$\mathbb{1}_{\mathrm{DM}} \qquad i\hat{\vec{q}} \qquad \hat{\vec{v}}^{\perp} \qquad \hat{\vec{S}}_{\mathrm{DM}} \qquad \hat{\vec{S}}_{N}\,. \tag{3.29}$$

These operators act on the two particle Hilbert space which is spanned by dark matter and nucleon states. Here, $\mathbb{1}_{\mathrm{DM}}$ and $\mathbb{1}_N$ are the identity matrices in this space and $\vec{v}^{\perp}$ is the relative transverse momentum satisfying $\vec{v}^{\perp} \cdot \vec{q} = 0$. In Tab. 1, we show the complete set of operators that can be constructed with those basis operators for dark matter particles with spin 0, $\frac{1}{2}$, 1. For all operators, the momentum transfer is divided by the mass of a nucleon $m_N = 0.9315\,\mathrm{GeV}$. In concordance with [204–206], we neglect operators $\mathcal{O}_2$ and $\mathcal{O}_{16}$. Operator $\mathcal{O}_2$ cannot arise at leading order in an effective field theory [205] and $\mathcal{O}_{16}$ is a linear combination of $\mathcal{O}_{12}$ and $\mathcal{O}_{15}$. The most general Hamiltonian density for non-relativistic scattering of dark matter particles with nucleons is given by

$$\hat{\mathcal{H}}_{\mathrm{N}}(\vec{r}) = \sum_{\tau=0}^{1} \sum_{k=1}^{18} c_k^{\tau}\, \hat{\mathcal{O}}_k(\vec{r})\, t^{\tau}\,. \tag{3.30}$$

Here, c_k^{τ} denotes the Wilson coefficient for the k-th operator and $t^{\tau}_{(i)}$ is a spin matrix with $t^0 = \mathbb{1}$ and $t^1 = \sigma_3$ the third Pauli matrix. The basis of isoscalar and isovector coupling is related the couplings to protons and neutrons via

$$c_k^{\mathrm{p}} = (c_k^0 + c_k^1)/2 \qquad c_k^{\mathrm{n}} = (c_k^0 - c_k^1)/2\,. \tag{3.31}$$

$\hat{\mathcal{O}}_1 = \mathbb{1}_{\mathrm{DM}}\mathbb{1}_N$	$\hat{\mathcal{O}}_{10} = i\hat{\vec{S}}_N \cdot \frac{\hat{\vec{q}}}{m_N}\mathbb{1}_{\mathrm{DM}}$
$\hat{\mathcal{O}}_3 = i\hat{\vec{S}}_N \cdot \left(\frac{\hat{\vec{q}}}{m_N} \times \hat{\vec{v}}^{\perp}\right)\mathbb{1}_{\mathrm{DM}}$	$\hat{\mathcal{O}}_{11} = i\hat{\vec{S}}_{\mathrm{DM}} \cdot \frac{\hat{\vec{q}}}{m_N}\mathbb{1}_N$
$\hat{\mathcal{O}}_4 = \hat{\vec{S}}_{\mathrm{DM}} \cdot \hat{\vec{S}}_N$	$\hat{\mathcal{O}}_{12} = \hat{\vec{S}}_{\mathrm{DM}} \cdot \left(\hat{\vec{S}}_N \times \hat{\vec{v}}^{\perp}\right)$
$\hat{\mathcal{O}}_5 = i\hat{\vec{S}}_{\mathrm{DM}} \cdot \left(\frac{\hat{\vec{q}}}{m_N} \times \hat{\vec{v}}^{\perp}\right)\mathbb{1}_N$	$\hat{\mathcal{O}}_{13} = i\left(\hat{\vec{S}}_{\mathrm{DM}} \cdot \hat{\vec{v}}^{\perp}\right)\left(\hat{\vec{S}}_N \cdot \frac{\hat{\vec{q}}}{m_N}\right)$
$\hat{\mathcal{O}}_6 = \left(\hat{\vec{S}}_{\mathrm{DM}} \cdot \frac{\hat{\vec{q}}}{m_N}\right)\left(\hat{\vec{S}}_N \cdot \frac{\hat{\vec{q}}}{m_N}\right)$	$\hat{\mathcal{O}}_{14} = i\left(\hat{\vec{S}}_{\mathrm{DM}} \cdot \frac{\hat{\vec{q}}}{m_N}\right)\left(\hat{\vec{S}}_N \cdot \hat{\vec{v}}^{\perp}\right)$
$\hat{\mathcal{O}}_7 = \hat{\vec{S}}_N \cdot \hat{\vec{v}}^{\perp}\mathbb{1}_{\mathrm{DM}}$	$\hat{\mathcal{O}}_{15} = -\left(\hat{\vec{S}}_{\mathrm{DM}} \cdot \frac{\hat{\vec{q}}}{m_N}\right)\left[\left(\hat{\vec{S}}_N \times \hat{\vec{v}}^{\perp}\right) \cdot \frac{\hat{\vec{q}}}{m_N}\right]$
$\hat{\mathcal{O}}_8 = \hat{\vec{S}}_{\mathrm{DM}} \cdot \hat{\vec{v}}^{\perp}\mathbb{1}_N$	$\hat{\mathcal{O}}_{17} = i\frac{\hat{\vec{q}}}{m_N} \cdot \mathcal{S} \cdot \hat{\vec{v}}^{\perp}\mathbb{1}_N$
$\hat{\mathcal{O}}_9 = i\hat{\vec{S}}_{\mathrm{DM}} \cdot \left(\hat{\vec{S}}_N \times \frac{\hat{\vec{q}}}{m_N}\right)$	$\hat{\mathcal{O}}_{18} = i\frac{\hat{\vec{q}}}{m_N} \cdot \mathcal{S} \cdot \hat{\vec{S}}_N$

Table 1.: Operators of the non-relativistic effective theory of dark matter-nucleon interactions [204, 205, 208]. Further details about the notation are provided in section 3.2.3. The matrices $\mathbb{1}_N$ and $\mathbb{1}_{\mathrm{DM}}$ denote the identity matrices in nucleus spin respectively dark matter spin space. Furthermore, the spin operators of nuclei and dark matter particles are denoted by $\hat{\vec{S}}_N$ and $\hat{\vec{S}}_{\mathrm{DM}}$. For spin-1 WIMPs, $\mathcal{S}$ denotes the symmetric combination of polarisation vectors. This table was adopted from Ref. [3].

This allows to relate the general non-relativistic effective field theory to the specific cases of spin-independent and spin-dependent interactions. As can be seen from comparing Eqs. (3.6) as well as (3.19) to the operators listed in Tab. 1 and using the identities presented in Ref. [205], the operators $\mathcal{O}_1$ and $\mathcal{O}_4$ correspond to the standard spin-independent respectively standard spin-dependent interactions. We note that $\mathcal{O}_1$ and $\mathcal{O}_4$ are the leading order operators of this effective field theory and therefore standard spin-independent and spin-dependent interactions could provide the most dominant effects in case they are non-zero.

In order to connect this to the signal expected in dark matter searches, one constructs the coupling to the nucleus. Following [204–206] and using the one-body approximation, the Hamiltonian density $\hat{\mathcal{H}}_{\mathrm{T}}(\vec{r})$ is used to model the interaction of dark matter particles with a nucleus. For this, the contributions of all A nucleons inside the nucleus are summed which yields

$$\hat{\mathcal{H}}_{\mathrm{T}}(\vec{r}) = \sum_{i=1}^{A}\sum_{\tau=0}^{1}\sum_{k=1}^{15} c_k^{\tau}\,\hat{\mathcal{O}}_k^{(i)}(\vec{r})\,t_{(i)}^{\tau}\,. \tag{3.32}$$

In order to relate to the operators in Tab. 1, it is useful to separate the motion of the center of mass of the nucleus and the motion of the ith nucleon with respect to it. In coordinate space, this induces the following separation [207]

$$\hat{\vec{q}} = -i\,\overleftarrow{\nabla}_{\vec{x}}\,\delta(\vec{x}-\vec{y}-\vec{r}) - i\,\delta(\vec{x}-\vec{y}-\vec{r})\,\vec{\nabla}_{\vec{x}} \tag{3.33}$$

$$\hat{\vec{v}}^{\perp} = \hat{\vec{v}}_N^{\perp} + \hat{\vec{v}}_T^{\perp}\,, \tag{3.34}$$

where $\nabla_{\vec{x}}$ acts on the wave function of the nucleus center of mass. The individual com-

ponents of the transverse momentum are given by

$$\hat{\vec{v}}_T^{\perp} = \delta(\vec{x} - \vec{y} - \vec{r}) \left(i \frac{\vec{\nabla}_{\vec{x}}}{m_T} - i \frac{\vec{\nabla}_{\vec{y}}}{m_{\mathrm{DM}}} \right) + \frac{\hat{\vec{q}}}{2\,\mu_T} \tag{3.35}$$

$$\hat{\vec{v}}_N^{\perp} = \frac{1}{2\,m_N} \left(i \overleftarrow{\nabla}_{\vec{r}}\, \delta(\vec{r} - \vec{r}_i) - i\, \delta(\vec{r} - \vec{r}_i)\, \vec{\nabla}_{\vec{r}} \right) . \tag{3.36}$$

Here, $\nabla_{\vec{y}}$ and $\nabla_{\vec{r}}$ act on the wave function of the dark matter particle respectively the constituent nucleon while m_T and μ_T are the mass respectively the reduced mass of the target nucleus. Furthermore, $\vec{r}$ and $\vec{r}_i$ denote the distance of the dark matter particle respectively of the ith nucleon to the nucleus center of mass. As apparent from this decomposition, the only part of $\hat{\vec{q}}$ and $\hat{\vec{v}}^{\perp}$ that depends on $\vec{r}_i$ is $\hat{\vec{v}}_N^{\perp}$. In order to separate the motion of the nucleons with respect to the nucleus center of mass, one categorizes the different dependencies on $\vec{r}_i$ in Eq. (3.32). As apparent from Eqs. (3.33) and (3.34) in combination with the operators shown in Tab. 1, there are only five different contributions possible

$$\begin{aligned}
\sum_{i=1}^{A} \mathbb{1}_i\, t_{(i)}^{\tau} = \sum_{i=1}^{A} \delta(\vec{r} - \vec{r}_i)\, t_{(i)}^{\tau} &\equiv \hat{\rho}_0^{\tau}(\vec{r}) \\
\sum_{i=1}^{A} \vec{\sigma}(i)\, \hat{\vec{v}}_N^{\perp}\, t_{(i)}^{\tau} &\equiv \hat{\rho}_{0A}^{\tau}(\vec{r}) \\
\sum_{i=1}^{A} \vec{\sigma}(i)\, \mathbb{1}_i\, t_{(i)}^{\tau} = \sum_{i=1}^{A} \vec{\sigma}(i)\, \delta(\vec{r} - \vec{r}_i)\, t_{(i)}^{\tau} &\equiv \hat{\vec{\rho}}_5^{\tau}(\vec{r}) \\
\sum_{i=1}^{A} \hat{\vec{v}}_N^{\perp} &\equiv \hat{\vec{\rho}}_M^{\tau}(\vec{r}) \\
\sum_{i=1}^{A} \vec{\sigma}(i) \times \hat{\vec{v}}_N^{\perp} &\equiv \hat{\vec{\rho}}_E^{\tau}(\vec{r}) \,,
\end{aligned} \tag{3.37}$$

where $\vec{\sigma}(i)$ is the vector of Pauli matrices that acts on the ith nucleon and $\mathbb{1}_i$ is equivalent to $\delta(\vec{r} - \vec{r}_i)$ in coordinate space [207]. Here, $\hat{\rho}_0^{\tau}(\vec{r})$ and $\hat{\rho}_{0A}^{\tau}(\vec{r})$ are the nuclear vector respectively nuclear axial charges. The operators $\hat{\vec{\rho}}_5^{\tau}(\vec{r})$, $\hat{\vec{\rho}}_M^{\tau}(\vec{r})$ and $\hat{\vec{\rho}}_E^{\tau}(\vec{r})$ denote the nuclear spin, nuclear convection and nuclear spin-velocity currents. Using these operators, the Hamiltonian density becomes a sum of those five contributions

$$\hat{\mathcal{H}}_{\mathrm{T}}(\vec{r}) = \sum_{\tau=0,1} \left(\hat{l}_0^{\tau}\, \hat{\rho}_0^{\tau}(\vec{r}) + \hat{l}_{0A}^{\tau}\, \hat{\rho}_{0A}^{\tau}(\vec{r}) + \hat{\vec{l}}_5^{\tau}\, \hat{\vec{\rho}}_5^{\tau}(\vec{r}) + \hat{\vec{l}}_M^{\tau}\, \hat{\vec{\rho}}_M^{\tau}(\vec{r}) + \hat{\vec{l}}_E^{\tau}\, \hat{\vec{\rho}}_E^{\tau}(\vec{r}) \right) . \tag{3.38}$$

In the case of dark matter particles with spin 0 or $\frac{1}{2}$, only operators $\mathcal{O}_1 - \mathcal{O}_{15}$ contribute. The operators $\hat{l}_k^{\tau}$ are then given by [206, 207]

$$\hat{l}_0^{\tau} = c_1^{\tau} + i \left(\frac{\hat{\vec{q}}}{m_N} \times \hat{\vec{v}}_T^{\perp} \right) \hat{\vec{S}}_{\mathrm{DM}}\, c_5^{\tau} + \hat{\vec{v}}_T^{\perp}\, \hat{\vec{S}}_{\mathrm{DM}}\, c_8^{\tau} + i \frac{\hat{\vec{q}}}{m_N}\, \hat{\vec{S}}_{\mathrm{DM}}\, c_{11}^{\tau}$$

$$
\begin{aligned}
\hat{l}^{\tau}_{0A} &= -\frac{1}{2}\left[c^{\tau}_{7} + i\frac{\hat{\vec{q}}}{m_N}\ \hat{\vec{S}}_{\mathrm{DM}}\ c^{\tau}_{14}\right] \\
\overset{\mathcal{T}}{\hat{l}}{}^{\tau}_{5} &= \frac{1}{2}\left[i\frac{\hat{\vec{q}}}{m_N}\times\hat{\vec{v}}^{\perp}_{T}\ c^{\tau}_{3} + \hat{\vec{S}}_{\mathrm{DM}}\ c^{\tau}_{4} + \frac{\hat{\vec{q}}}{m_N}\ \frac{\hat{\vec{q}}}{m_N}\ \hat{\vec{S}}_{\mathrm{DM}}\ c^{\tau}_{6} + \hat{\vec{v}}^{\perp}_{T}\ c^{\tau}_{7} + i\frac{\hat{\vec{q}}}{m_N}\times\hat{\vec{S}}_{\mathrm{DM}}\ c^{\tau}_{9} + i\frac{\hat{\vec{q}}}{m_N}\ c^{\tau}_{10}\right. \\
&\quad \left. + \hat{\vec{v}}^{\perp}_{T}\times\hat{\vec{S}}_{\mathrm{DM}}\ c^{\tau}_{12} + i\frac{\hat{\vec{q}}}{m_N}\hat{\vec{v}}^{\perp}_{T}\ \hat{\vec{S}}_{\mathrm{DM}}\ c^{\tau}_{13} + i\hat{\vec{v}}^{\perp}_{T}\frac{\hat{\vec{q}}}{m_N}\ \hat{\vec{S}}_{\mathrm{DM}}\ c^{\tau}_{14} + \frac{\hat{\vec{q}}}{m_N}\times\hat{\vec{v}}^{\perp}_{T}\ \frac{\hat{\vec{q}}}{m_N}\ \hat{\vec{S}}_{\mathrm{DM}}\ c^{\tau}_{15}\right] \\
\overset{\mathcal{T}}{\hat{l}}{}^{\tau}_{M} &= i\frac{\hat{\vec{q}}}{m_N}\times\hat{\vec{S}}_{\mathrm{DM}}\ c^{\tau}_{5} - \hat{\vec{S}}_{\mathrm{DM}}\ c^{\tau}_{8} \\
\overset{\mathcal{T}}{\hat{l}}{}^{\tau}_{E} &= \frac{1}{2}\left[\frac{\hat{\vec{q}}}{m_N}\ c^{\tau}_{3} + i\hat{\vec{S}}_{\mathrm{DM}}\ c^{\tau}_{12} - \frac{\hat{\vec{q}}}{m_N}\times\hat{\vec{S}}_{\mathrm{DM}}\ c^{\tau}_{13} - i\frac{\hat{\vec{q}}}{m_N}\frac{\hat{\vec{q}}}{m_N}\ \hat{\vec{S}}_{\mathrm{DM}}\ c^{\tau}_{15}\right] .
\end{aligned}
\tag{3.39}
$$

For spin-1 dark matter, the operators $\hat{l}^{\tau}_{k}$ look slightly different and we refer to Ref. [208] for explicit results. Integrating the Hamiltonian density $\hat{\mathcal{H}}_{\mathrm{T}}(\vec{r})$ over space coordinates finally yields the dark matter-nucleus interaction Hamiltonian H_{T}.

The transition matrix element between the initial state $|i\rangle$ and the final state $|f\rangle$ then reads

$$
\langle f|\, H_{\mathrm{T}}\, |i\rangle = (2\pi)^3\, \delta(\vec{k}'_{\mathrm{T}} + \vec{p}' - \vec{k}_{\mathrm{T}} - \vec{p})\, i\mathcal{M}_{\mathrm{NR}}\,. \tag{3.40}
$$

Here, $\vec{k}_{\mathrm{T}}$ and $\vec{p}$ are the momenta of the target nucleus respectively the dark matter particle. The matrix element can be calculated by performing a multipole expansion, confer [206, 207]. Using that nuclear ground states are eigenstates of P and CP to a very good approximation [205], some of the terms in the expansion vanish. In particular, none of the terms related to $\hat{l}^{\tau}_{0A}$ contribute. Furthermore, the charge $\hat{l}^{\tau}_{0}$ gives rise to the nuclear response operator M while the currents $\overset{\mathcal{T}}{\hat{l}}{}^{\tau}_{5}$, $\overset{\mathcal{T}}{\hat{l}}{}^{\tau}_{M}$ and $\overset{\mathcal{T}}{\hat{l}}{}^{\tau}_{E}$ induce the response operators Σ' and Σ'', Δ respectively $\tilde{\Phi}'$ and Φ''. In addition to this, the interference terms $\Phi'' M$ and $\Delta\Sigma'$ arise. We refer to Refs. [205–207] for explicit calculations of the response operators and the matrix element $\mathcal{M}_{NR}$.

Squaring the transition amplitude, summing over final spin states and averaging initial spin states, the transition probability is given by [206, 207]

$$
\begin{aligned}
P_{\mathrm{tot}}(v^2, q^2) &\equiv \frac{1}{2j_{\mathrm{DM}}+1}\frac{1}{2J+1}\sum_{\mathrm{spins}}|\mathcal{M}_{NR}|^2 \\
&= \frac{4\pi}{2J+1}\sum_{\tau=0,1}\sum_{\tau'=0,1}\left\{\sum_{k=M,\,\Sigma'',\,\Sigma'} R^{\tau\tau'}_{k}\left(v^{\perp 2}_{T}, \frac{q^2}{m^2_N}\right)\ W^{\tau\tau'}_{k}(y)\right. \\
&\quad \left. + \frac{q^2}{m^2_N}\sum_{k=\Phi'',\,\Phi'' M,\,\tilde{\Phi}',\,\Delta,\,\Delta\Sigma'} R^{\tau\tau'}_{k}\left(v^{\perp 2}_{T}, \frac{q^2}{m^2_N}\right)\ W^{\tau\tau'}_{k}(y)\right\}
\end{aligned}
\tag{3.41}
$$

where j_{DM} and J are the spin of the dark matter particle respectively the spin of the nucleus. The velocity of the dark matter particle with respect to the nucleus is denoted by v. Furthermore, the squared transverse velocity of the dark matter particle with

respect to the nucleus reads

$$\vec{v}_T^{\perp 2} = v^2 - \frac{q^2}{4\,\mu_T^2} \tag{3.42}$$

where μ_T is the dark matter-nucleus reduced mass. The transition probability P_{tot} depends on the form factors $W^{\tau\tau'}(y)$ which are functions of the dimensionless variable $y = (b\,q/2)^2$. Here, $b = \sqrt{41.467/(45\,A^{-1/3} - 25\,A^{-2/3})}\,\text{fm}$ and q is the momentum transfer. In this work, we adopt the fit polynomials for the form factors from Refs. [205, 207]. In the case of Ref. [207], the form factors were computed using the `Mathematica` script provided by [206]. The response functions $R_k^{\tau\tau'}\left(v_T^{\perp 2}, \frac{q^2}{m_N^2}\right)$ are quadratic functions of the Wilson coefficients and are given in Refs. [206, 207] for dark matter particles with spin-0 respectively spin-$\frac{1}{2}$. In the case of spin-1 dark matter, the response functions are given in Ref. [208]. In appendix A, we explicitly state the response functions including contributions from all operators listed in Tab. 1. Finally, the differential WIMP-nucleus scattering cross section off the nucleus T is obtained from the transition probability P_{tot}

$$\frac{\mathrm{d}\sigma}{\mathrm{d}E_R}\left(v^2, q^2\right) = \frac{m_T}{2\pi v^2}\,P_{\text{tot}}\left(v^2, q^2\right)\,, \tag{3.43}$$

where m_T is again the mass of the target nucleus.

In this work, we additionally take into account long-range interactions between dark matter particles and nuclei. To do this, the Wilson coefficients c_k^τ are replaced by the linear combination $c_k^\tau + \tilde{c}_k^\tau\, m_N^2/q^2$ where c_k^τ and $\tilde{c}_k^\tau$ may vary independently from each other. These additional coupling constants $\tilde{c}_k^\tau$ increase the total number of Wilson coefficients from 32 to 64. With this, several dark matter-nucleus interactions that arise from specific models can be represented. Examples are anapole dark matter [205] and millicharged dark matter [209–211] that both arise from models including dark photons in addition to a dark sector. A further example is magnetic dipole dark matter [211–213] that models the interactions of dark matter with the SM via electromagnetic interactions. Notable exceptions are models where the mediator has masses between 1 MeV and 100 MeV as well as models that predict inelastic scatterings. Furthermore, this formalism cannot be used to incorporate the effects of meson exchange in nuclei [214]. However, we expect the effects of this to be negligible in the mass range relevant for this work, confer [215].

3.3. Direct dark matter searches

3.3.1. Direct detection experiments

The goal of direct detection experiments is to detect dark matter particles via nuclear recoils in the target material. If enough energy is transferred onto the nucleus, several signatures can be used to search for dark matter. Those include scintillation light, ionization electrons or phonons. However, those signals can be faked easily by SM particles or swamped by the thermal motion of target particles in the detector. Therefore, sophisticated shielding and stable operation under cryogenic conditions are among the

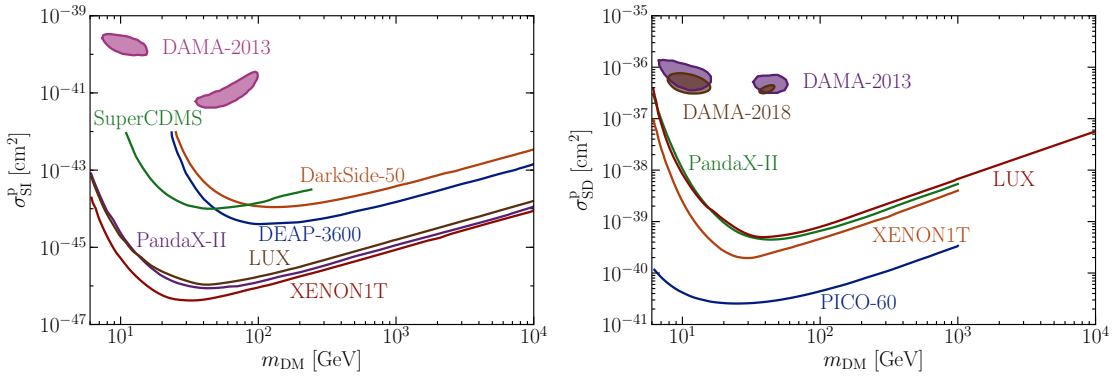

Figure 6.: This figure shows the upper limits on the spin-independent (left) and spin-dependent (right) scattering cross sections derived from several direct detection experiments. Concretely, we depict the upper limits of XENON1T [221, 230], PandaX-II [219,231], LUX [202,216], DEAP-3600 [223], DarkSide-50 [224] and SuperCDMS [227] and PICO-60 [232]. Furthermore, we include the preferred regions in parameter space reconstructed from the DAMA data released in 2013 [22] and 2018 [23]. Here, we adopt the results for the 2013 data set from Refs. [233,234] and for the 2018 data set from Ref. [235]. We note that the latter does not provide preferred regions in the case of spin-independent interactions as the fit to the data is bad.

major challenges experimental collaborations face when building and operating a direct detection experiment.

As discussed in section 3.2, the scattering cross section depends on the target nucleus. Therefore, experimental collaborations currently use several different target materials to avoid being blind to the dark matter signal due to an accidental destructive interference in the interaction of dark matter and a specific target element. Also, using different target materials allows to better understand and quantify the background. Among the most popular targets are xenon that is used by the LUX [202, 216], PandaX [217–219] and XENON1T [220, 221] collaborations. Further common targets include argon, used by the DEAP [222, 223] and DarkSide-50 [224] collaborations, as well as germanium and silicon that is employed by the CDMS collaboration [225–227]. For light dark matter searches, the CRESST [228, 229] collaboration uses a $CaWO_3$ target that allows to probe recoil energies in the eV range. The PICO collaboration [232, 236, 237] uses a C_3F_8 target in order probe spin-dependent interactions. In Fig. 6, we show a compilation of the current status of the dark matter searches with those experiments for spin-independent and spin-dependent interactions.

The expected rate of dark matter scatterings off the nucleus T_i in the detector, confer [112], is given by

$$\frac{\mathrm{d}R_i}{\mathrm{d}E_R} = \frac{\xi_i\,\rho_{\mathrm{loc}}}{m_{\mathrm{DM}}\,m_{T_i}} \int_{v^{(\mathrm{D})}\geq v^{(\mathrm{DD})}_{\mathrm{min,i}}(E_R)} \mathrm{d}^3 v^{(\mathrm{D})}\, \frac{f\left(\vec{v}^{(\mathrm{D})}+\vec{v}_{\mathrm{obs}}(t)\right)}{v^{(\mathrm{D})}}\, \frac{\mathrm{d}\sigma_i}{\mathrm{d}E_R}(v^{(\mathrm{D})}, E_R)\,, \tag{3.44}$$

where $\vec{v}^{(\mathrm{D})}$ is the velocity of the dark matter particle in the rest frame of the detector and

$\vec{v}_{\rm obs}$ is the velocity of the observer with respect to the Galactic rest frame, for which we adopt the parametrization derived in Ref. [238]. It can be decomposed into the velocity of the Sun with respect to the Galactic rest frame as well as the velocity of the Earth with respect to the Sun which yields

$$\vec{v}_{\rm obs} = \vec{v}_{\odot} + \vec{v}_{\oplus} = \vec{v}_{\rm LSR} + \vec{v}_{\odot,\rm pec} + \vec{v}_{\oplus}\,. \tag{3.45}$$

Here, $\vec{v}_{\rm LSR} = (0, v_c, 0)$ is the motion of the local standard of rest (LSR) and $v_c \approx 220\,\mathrm{km/s}$ [114] is the local circular speed. Furthermore, $\vec{v}_{\odot,\rm pec} = (11.1, 12.24, 7.25)\,\mathrm{km/s}$ [239] is the Sun's peculiar motion. In order to transfer the amount of energy E_R onto the nucleus, a dark matter particle must have a velocity larger than

$$v_{{\rm min},i}^{\rm (DD)}(E_R) = \sqrt{m_{T_i} E_R/(2\mu_{T_i}^2)}\,, \tag{3.46}$$

where $\mu_{T_i} = m_{\rm DM} m_{T_i}/(m_{\rm DM} + m_{T_i})$ is the dark matter-nucleus reduced mass. The differential scattering cross section $\mathrm{d}\sigma_i/\mathrm{d}E_R$ is discussed in detail in section 3.2 and we adopt the interactions described there. The total scattering rate is then given by

$$R = \int_0^\infty \sum_i \epsilon_i(E_R)\,\frac{\mathrm{d}R_i}{\mathrm{d}E_R}\,\mathrm{d}E_R\,, \tag{3.47}$$

where the efficiency $\epsilon_i(E_R)$ is the energy dependent probability to detect a recoil off the nucleus T_i. Finally, the expected number of events is given by $N_{\rm expected} = R\,\mathrm{T}\,\mathrm{M}_{\rm det}$, where T denotes the exposure time $\mathrm{M}_{\rm det}$ the target mass of the experiment.

Furthermore, direct detection experiments are able to search for the annual modulation of the recoil rate caused by to the motion of the Earth around the Sun. Due to the changing alignment of the Sun's velocity and the Earth's velocity over the course of the year, the recoil rate is expected to vary during the year. Specifically for the SHM, the minimum and maximum are expected at June 1st and December 1st. Given that the exposure time of the direct detection experiment is long enough, this signal can be detected [240] without the need for an excellent background suppression as processes that could mimic dark matter-nucleus interactions are expected to be time-independent. Although several searches for an annual modulation signal were performed by experimental collaborations with various targets, the most prominent target for this search is NaI. This is due to the annual modulation signal observed by the DAMA experiment [22, 23]. As the reconstructed dark matter parameters are in severe tension with the results from other dark matter searches, confer Figs. 6 and 7, several collaborations formed in order to test this signal with an NaI target in an model independent way. Among the currently pursued or planned experiments are Anais [241], Cosine-100 [242,243], COSINUS [244], DM-Ice [245] and Sabre [246]. Although first results do not support the claim of an annual modulation signal, those experiments cannot preclude the dark matter interpretation of the DAMA signal in a model independent way yet.

Motivated by the time dependence of the signal for the SHM, we define the modulation amplitude in the interval $[E_{\rm min}, E_{\rm max}]$ by the difference of the recoil rates at June 1st and

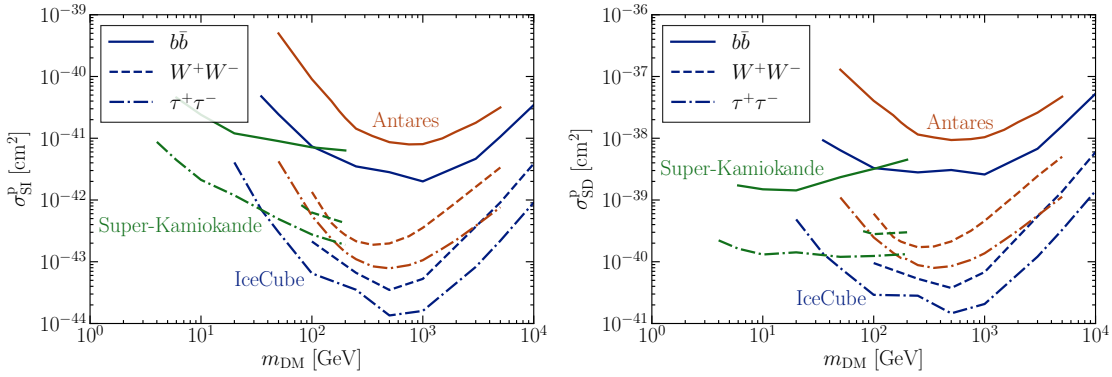

Figure 7.: Upper limits on the spin-independent (left) and spin-dependent (right) scattering cross sections of several neutrino telescopes. Concretely, we depict the upper limits derived by the IceCube [250], Antares [251] and Super-Kamiokande [252] collaborations. In each case, we include the limits for annihilation into $b\bar{b}$, W^+W^- and $\tau^+\tau^-$.

at December 1st [247]

$$S_m^{[E_{\mathrm{min}},E_{\mathrm{max}}]} = \frac{1}{E_{\mathrm{max}} - E_{\mathrm{min}}} \cdot \frac{1}{2} \cdot \left(R_{[E_{\mathrm{min}},E_{\mathrm{max}}]}\Big|_{\text{June 1st}} - R_{[E_{\mathrm{min}},E_{\mathrm{max}}]}\Big|_{\text{Dec 1st}} \right) . \tag{3.48}$$

Here, $R_{[E_{\mathrm{min}},E_{\mathrm{max}}]}$ denotes the event rate expected in the energy bin $[E_{\mathrm{min}}, E_{\mathrm{max}}]$ as a function of time.

3.3.2. Neutrino telescope experiments

Dark matter particles traversing a celestial body lose energy when scattering off particles bound to the body. If the energy loss is large enough, the dark matter particles get gravitationally bound and sink to the core where they generate an overdensity of dark matter particles. If the overdensity is large enough and the annihilation of dark matter into SM particles gives rise to neutrinos, the neutrino signal from the Sun is enhanced and could be observable by neutrino telescopes on Earth [248].

Following the derivation of the capture rate by Ref. [249], we start by computing the number of captured particles by a thin spherical shell of radius r and thickness $\mathrm{d}r$. For this, we denote the escape velocity from the surface of the shell by $v_{\mathrm{esc}}(r)$, the velocity of the dark matter particle infinitely far away from the shell by $v^{(\mathrm{S})}$ and the velocity at the surface of the shell by $w(r) \equiv \left(\left(v^{(\mathrm{S})}\right)^2 + v_{\mathrm{esc}}^2(r) \right)^{1/2}$. Assuming that the velocity of dark matter particles infinitely far away from the shell is $f\left(\vec{v}^{(\mathrm{S})} + \vec{v}_\odot\right) \mathrm{d}^3 v^{(\mathrm{S})}$, the flux of dark matter particles inward across the surface of the shell is given by [253]

$$\frac{1}{4} f\left(\vec{v}^{(\mathrm{S})} + \vec{v}_\odot\right) v^{(\mathrm{S})} \, \mathrm{d}^3 v^{(\mathrm{S})} \, \mathrm{d}\cos^2(\theta) \, , \tag{3.49}$$

where $0 \leq \theta \leq \pi/2$ parametrizes the angle with respect to the radial direction. Performing a variable transformation [249] of $(v^{(\mathrm{S})}, \theta)$ to $(v^{(\mathrm{S})}, J^2)$ where J is the angular momentum per unit mass and integrating over the surface of the shell, the total number of particles

entering the shell reads

$$\frac{\pi}{v^{(\mathrm{S})}} f\left(\vec{v}^{(\mathrm{S})} + \vec{v}_{\odot}\right) \mathrm{d}^3 v^{(\mathrm{S})} \, \mathrm{d}J^2 \,. \tag{3.50}$$

A dark matter particle that gets captured has to lose enough energy such that its velocity after scattering is smaller than the escape velocity at the position of scattering $v_{\mathrm{esc}}(r)$. For dark matter particles with mass m_{DM}, the rate of those scatterings per unit time at distance r from the center of the celestial body is given by [249]:

$$\Omega^{-}_{v_{\mathrm{esc}}(r)}(w(r)) = \sum_i \eta_i(r)\, w\, \Theta\left(\frac{\mu_i}{\mu_{+,i}^2} - \frac{v^2}{w^2}\right) \int_{E_k\, v^2/w^2}^{E_k\, \mu_i/\mu_{+,i}^2} \mathrm{d}E_R \frac{\mathrm{d}\sigma_i}{\mathrm{d}E_R}(w^2, q^2) \,, \tag{3.51}$$

where the sum extends over all nuclei present in the Sun. Furthermore, the definitions $\mu_i = m_{\mathrm{DM}}/m_{T_i}$, $\mu_{+,i}^2 = (\mu_i \pm 1)/2$ and $E_k = m_{\mathrm{DM}}\, w^2/2$ were introduced. If the dark matter particle is too fast, capture is kinematically impossible with one single scattering. As we do not consider multi-scattering here, the maximal velocity for capture is given by

$$v_{\mathrm{max},i}^{(\mathrm{NT})}(r) = 2\, v_{\mathrm{esc}}(r) \sqrt{m_{\mathrm{DM}} m_{T_i}} / \left|m_{\mathrm{DM}} - m_{T_i}\right| \,, \tag{3.52}$$

which depends on the masses m_{T_i} of the nuclei present in the Sun. In this work, we use the solar composition given in the model AGSS09 [254] from which we extract the number density profile $\eta_i(r)$ for each nuclear species in the Sun. For the differential scattering cross section $\mathrm{d}\sigma_i/\mathrm{d}E_R$, we study the interactions discussed in section 3.2. With this, the probability that a dark matter particle loses enough energy to become gravitationally captured reads

$$\Omega^{-}_{v_{\mathrm{esc}}(r)}(w(r)) \frac{\mathrm{d}l}{w(r)} \,, \tag{3.53}$$

where $\mathrm{d}l/w$ is the time the particle spends in the material of the shell. As the dark matter particle traverses the shell twice or not at all, a factor 2 has to be introduced as well as a θ-function which models the requirement that the dark matter particle must have an angular momentum J smaller than $r\, w$ in order to hit the sphere. Therefore, the time inside the shell material is given by [249]

$$\frac{\mathrm{d}l}{w} = \frac{1}{w} \sqrt{1 - \left(\frac{J}{r\, w}\right)^2} \, \mathrm{d}r\, 2\, \theta(r\, w - J) \,. \tag{3.54}$$

Multiplying the total number of particles entering the shell given in Eq. (3.50) by the probability per unit time to lose enough energy to become gravitationally captured, see Eq. (3.53), we obtain the number of particles captured per unit time and per unit velocity by integrating all angular momenta. This reads [249]

$$4\pi\, r^2 \mathrm{d}r\, \frac{f\left(\vec{v}^{(\mathrm{S})} + \vec{v}_{\odot}\right) \mathrm{d}v^{(\mathrm{S})}}{v^{(\mathrm{S})}}\, w\, \Omega^{-}_{v_{\mathrm{esc}}(r)}(w(r)) \,. \tag{3.55}$$

By integrating the velocity and dividing by the volume, the differential capture rate per volume is given by [249]

$$\frac{\mathrm{d}C}{\mathrm{d}V} = \int_0^\infty \mathrm{d}^3 v^{(\mathrm{S})} \, \frac{f\left(\vec{v}^{(\mathrm{S})} + \vec{v}_\odot\right)}{v^{(\mathrm{S})}} \, w \, \Omega^-_{v_{\mathrm{esc}}}(w) \,. \tag{3.56}$$

Assuming that the Sun is spherically symmetric, the angular parts of the volume integral can be performed analytically. Applying the Heaviside Θ function, the capture rate of dark matter particles in the Sun reads [249, 255]

$$C = \sum_i \int_0^{R_\odot} 4\pi \, r^2 \, \mathrm{d}r \, \eta_i(r) \, \frac{\rho_{\mathrm{loc}}}{m_{\mathrm{DM}}} \int_{v^{(\mathrm{S})} \leq v^{(\mathrm{Sun})}_{\mathrm{max},i}(r)} \mathrm{d}^3 v^{(\mathrm{S})} \, \frac{f\left(\vec{v}^{(\mathrm{S})} + \vec{v}_\odot\right)}{v^{(\mathrm{S})}} \, w^2(r) \int_{m_{\mathrm{DM}}\left(v^{(\mathrm{S})}\right)^2/2}^{2\mu^2_{T_i} w^2(r)/m_{T_i}} \mathrm{d}E_R \, \frac{\mathrm{d}\sigma_i}{\mathrm{d}E_R}(w(r), E_R) \,. \tag{3.57}$$

Here, $v^{(\mathrm{S})}$ is the velocity of the dark matter particle in the rest frame of the Sun infinitely far away from the Sun.

We determine the number $N(t)$ of dark matter particles captured in the Sun at time t from the differential equation [256]

$$\frac{\mathrm{d}N}{\mathrm{d}t} = C - C_E \, N - C_A \, N^2 \,, \tag{3.58}$$

where C_E is the evaporation rate of dark matter particles bound to the Sun. As evaporation requires a significant momentum transfer onto the dark matter particle, this is most effective for light dark matter particles or those matching the mass of a nucleus in the sun, i.e. $m_{\mathrm{DM}} \simeq m_{T_i}$ [256, 257]. Recent studies [257–261] found that this is only relevant for dark matter particles lighter than 1 to 4 GeV for the dark matter-nucleus scattering cross sections that are probed by current and future experiments. Therefore, we neglect this process in the following as neutrino telescope are currently not sensitive to dark matter particles that are this light [250–252]. Furthermore, the constant C_A [249, 256] depends on the dark matter mass and parametrizes the strength of the pair-annihilation processes. We calculate C_A following [256] by expressing the annihilation constant in terms of the thermally averaged annihilation cross section $\langle \sigma v \rangle$

$$C_A = \frac{V_2}{V_1^2} \, \langle \sigma v \rangle \,. \tag{3.59}$$

Following Ref. [256], the effective volumes V_j are given by

$$V_j = \int \mathrm{d}r^3 \left(\frac{n(\vec{r})}{n_0}\right)^j = 4\pi \int_0^{R_\odot} r^2 \, \exp\left(\frac{j \, m_{\mathrm{DM}} \, \Phi(r)}{T_{\mathrm{DM}}(r)}\right) \mathrm{d}r \,, \tag{3.60}$$

where $n(r) = n_0 \, \exp\left(j \, m_{\mathrm{DM}} \, \Phi(r)/T_{\mathrm{DM}}(r)\right)$ is the spatial density of dark matter in the Sun and n_0 is the density at $r = 0$. Furthermore, $T_{\mathrm{DM}}(r)$ is the temperature of the WIMP component, which we calculate following [261]. An analytical approximation for

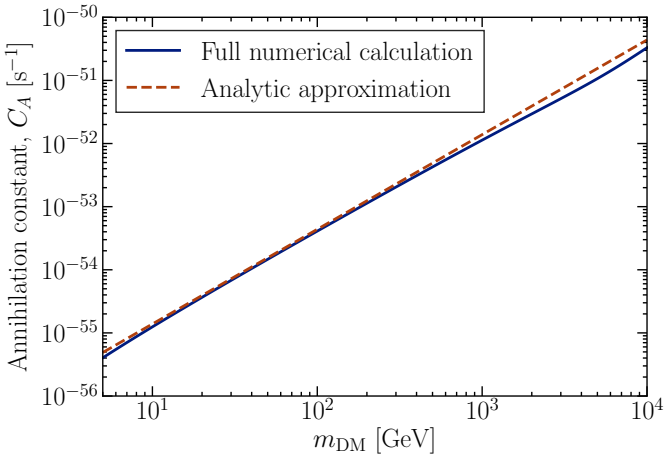

Figure 8.: Dependence of the annihilation constant C_A on the dark matter mass. For the numerical calculation, we follow the procedure outlined in Ref. [256] with a dark matter temperature determined as derived in Ref. [261]. For the analytic upper limit on the annihilation coefficient, we adopt the formula derived in [256] assuming that the neutrino temperature equals the core temperature of the Sun from the model AGSS09 [254].

the effective volumes of the Sun is provided in [256]. Finally, the gravitational potential $\Phi(r)$ is defined as

$$\Phi(r) = \int_0^r \frac{\mathrm{G}\, M(r')}{r'^2}\, \mathrm{d}r' \,. \tag{3.61}$$

This allows to determine the constant C_A self consistently from a given star model. Furthermore, Ref. [256] provides an analytic formula to compute an upper limit to the annihilation constant C_A for the Sun:

$$C_A = 5.1 \cdot 10^{-57} \left(\frac{T_{\mathrm{DM}}}{1.4 \cdot 10^7\,\mathrm{K}}\right) \cdot \left(\frac{m_{\mathrm{DM}}}{\mathrm{GeV}}\right) \cdot \left(\frac{\langle\sigma v\rangle}{3 \cdot 10^{-26}\,\mathrm{cm}^3/s}\right)\ s^{-1} \,. \tag{3.62}$$

In Fig. 8, we show a comparison of this analytic formula with the full calculation assuming the solar model AGSS09 [254]. We find that the analytic formula is accurate over a large range of dark matter masses between 10 GeV and 1000 GeV with minor deviations outside this region.

Neglecting evaporation, Eq. (3.58) can be solved analytically and the number of dark matter particles bound to the Sun is given by

$$N(t) = \sqrt{\frac{C}{C_A}} \tanh\left(\frac{t}{\tau}\right) \,, \tag{3.63}$$

where the equilibration time is defined as $\tau = 1/\sqrt{C\,C_A}$ and describes the time after which capture and annihilation processes are in equilibrium. We depict the dependence of τ on the dark matter mass in Fig. 9. From this plot, we conclude that equilibrium is achieved for the cross sections that are currently probed by neutrino telescopes, confer

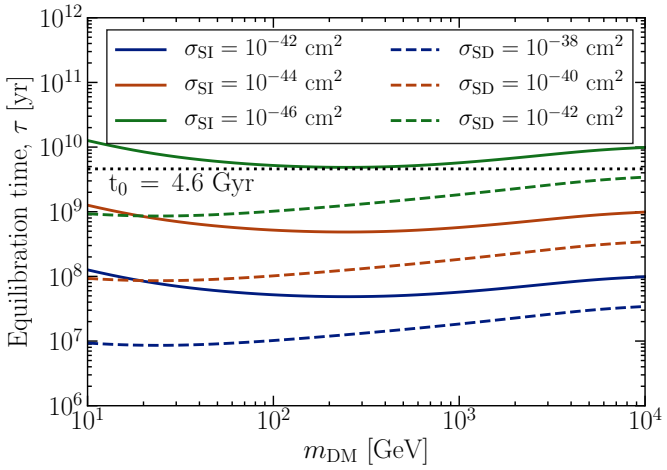

Figure 9.: Dependence of the equilibration time τ on the dark matter mass for several values of the spin-independent and the spin-dependent scattering cross sections. Furthermore, we indicate the age of the sun by a black dotted line.

also Fig. 7. However, if the sensitivity of neutrino telescopes increases by a factor of ~ 100, cross sections can be tested for which capture and annihilation processes are not in equilibrium.

Following Ref. [256], the annihilation rate of dark matter particles in the Sun reads

$$\Gamma_A = \frac{1}{2} \int \mathrm{d}r^3 \, n(r)^2 \, \langle \sigma v \rangle \tag{3.64}$$

This can be simplified by using the definition of the effective volume from Eq. (3.60) and by noting that the number of dark matter particles captured by the Sun is given by $V_1^2 \, n_0^2$. Using Eq. (3.63), the annihilation rate today reads

$$\Gamma_A = \frac{1}{2} \, C_A \, N(t_0)^2 = \frac{1}{2} \, C \, \tanh \left(\frac{t_0}{\tau} \right)^2 , \tag{3.65}$$

where $t_0 = 4.6\,\mathrm{Gyr}$ is the age of the Sun. As first suggested in Refs. [262, 263], the annihilation of dark matter in the Sun could be detected by neutrino telescopes if the final state of the annihilation process includes neutrinos or particles whose decay chain contains neutrinos. Once the annihilation process is fixed, the expected flux at the neutrino telescope on Earth can be calculated by taking into account the propagation of the neutrinos through the Sun and finally to the Earth. The calculation of the neutrino spectra at Earth for various annihilation channels is described in Ref. [264], which also provides the public code `WimpSim` [264] that is included in the `DarkSUSY` [265] code. In this work, we use this code to relate dark matter annihilation rate in the sun to the neutrino flux at Earth.

Chapter 4.

A halo-independent comparison of direct dark matter searches

The content of this section was published in Refs. [2] while the basis of the following discussion was also published in Ref. [1]. In the following, we clearly indicate the relevant publication for each section.

As discussed in chapter 2, astrophysics plays a major role when interpreting direct dark matter searches, see Refs. [72, 115, 266] for reviews of the associated uncertainties. The largest uncertainties stem from the fact that the velocity distribution of dark matter particles is unknown as well as from the local dark matter matter density as discussed in sections 2.2.1 respectively 2.2.2. In order to interpret the outcome of direct dark matter searches, one usually assumes the Standard Halo Model, see section 2.2 for a detailed discussion. Using more sophisticated models than an isothermal sphere to infer the velocity distribution from observations, Refs. [100, 102–104, 267, 268] showed that the deviations from the SHM are expected to be non-negligible.

In the following, we construct an analysis framework to interpret direct dark matter searches with minimal assumptions on the halo model. This extends and builds upon previous studies that performed halo-independent analyses [269–293]. Since the local dark matter density enters linearly in the signals under consideration, confer Eqs. (3.47) (3.57) and (3.48), those uncertainties can be incorporated trivially by rescaling the expected outcome of the experiment. Therefore, we present our results multiplied by the factor $\rho_{\mathrm{loc},\,0.3} \equiv \rho_{\mathrm{loc}}/(0.3\ \mathrm{GeV/cm^3})$ which indicates the uncertainty in the local dark matter density. In the following, we focus on the impact of the velocity distribution on the conclusions drawn from direct dark matter searches.

4.1. Optimizing the velocity distribution of dark matter particles

We note that the following content was published in [2] while a related discussion was also published in Ref. [1]. We aim to optimize the outcome $N^{(A)}$ of experiment A such that constraints from $p+q$ other experiments are met. This includes upper limits $N^{(B_\alpha)} \leq N^{(B_\alpha)}_{\mathrm{max}}$ with $\alpha = 1, \ldots, p$ and lower limits $N^{(B_\alpha)} \geq N^{(B_\alpha)}_{\mathrm{min}}$ for $\alpha = p+1, \ldots, p+q$ from experiments B_α. Concretely, the outcomes $N^{(A)}, N^{(B_\alpha)}$ can be the recoil rate or the annual modulation amplitude at a direct detection experiment respectively the capture

rate of dark matter particles in the Sun.

In order to find the optimal velocity distribution, we rewrite it in a mathematically equivalent way using δ-functions

$$f(\vec{v}) = \int_{v_0 \leq v_{\rm esc}} \mathrm{d}v_0^3 \, f(\vec{v}_0) \, \delta(\vec{v} - \vec{v}_0) \,, \tag{4.1}$$

where $v_0 = |\vec{v}_0|$ denotes the absolute value of the velocity. We interpret this as a superposition of streams with a fixed velocity $\vec{v}_0$ and weight $f(\vec{v}_0)$. Each stream gives rise to an experimental outcome $N_{\vec{v}_0}$ which can be calculated by assuming the velocity distribution $f(\vec{v}) = \delta(\vec{v} - \vec{v}_0)$. By taking into account the contributions from each stream, we calculate the experimental outcome expected from the full velocity distribution $f(\vec{v})$ as

$$N = \int_{v_0 \leq v_{\rm esc}} \mathrm{d}v_0^3 \, f(\vec{v}_0) \, N_{\vec{v}_0} \,. \tag{4.2}$$

With this, we formulate the problem of finding an upper limit on the outcome $N^{(A)}$ subject to constraints from other experiments as an optimization problem with the velocity distribution f as primal variable

$$\begin{aligned}
\text{optimize} \quad & \mathcal{F}[f] \equiv \int d^3 v_0 \; f(\vec{v}_0) \; N_{\vec{v}_0}^{(A)} \,, \\
\text{subject to} \quad & \int d^3 v_0 \; f(\vec{v}_0) = 1 \,, \\
\text{and} \quad & \int d^3 v_0 \; f(\vec{v}_0) \; N_{\vec{v}_0}^{(B_\alpha)} \leq N_{\rm max}^{(B_\alpha)}, \quad \alpha = 1, ..., p \,, \\
\text{and} \quad & \int d^3 v_0 \; f(\vec{v}_0) \; N_{\vec{v}_0}^{(B_\alpha)} \geq N_{\rm min}^{(B_\alpha)}, \quad \alpha = p+1, ..., p+q \,, \\
\text{and} \quad & f(\vec{v}_0) \geq 0 \,.
\end{aligned} \tag{4.3}$$

Here, we denote the objective function by $\mathcal{F}[f]$ to emphasize that it is a functional of the velocity distribution. However, this optimization problem cannot be solved as the velocity distribution enters linearly. This can be seen from the Lagrangian

$$\begin{aligned}
L = & \int d^3 v_0 \; f(\vec{v}_0) \; N_{\vec{v}_0}^{(A)} + \lambda \left(\int d^3 v_0 \; f(\vec{v}_0) - 1 \right) + \\
& \sum_{\alpha=1}^{p} \eta_\alpha \left(\int d^3 v_0 \; f(\vec{v}_0) \; N_{\vec{v}_0}^{(B_\alpha)} - N_{\rm max}^{(B_\alpha)} + s_\alpha \right) - \\
& \sum_{\alpha=p+1}^{p+q} \eta_\alpha \left(\int d^3 v_0 \; f(\vec{v}_0) \; N_{\vec{v}_0}^{(B_\alpha)} - N_{\rm min}^{(B_\alpha)} - s_\alpha \right) \,,
\end{aligned} \tag{4.4}$$

where λ, η_α are Lagrangian multipliers and s_α are slack variables. The Karush-Kuhn-Tucker conditions [294, 295] can be calculated by setting the first derivatives of the Lagrangian to zero, confer the discussion in appendix B.1. As every term of L is linear in $f(\vec{v})$, we conclude that no information can be extracted from those conditions.

However, we can solve this problem by transforming it into a linear programming prob-

lem, see the discussion in appendix B.3. Therefore, we discretize the velocity distribution into n streams with velocity $\vec{v}_i$ for $i = 1, \ldots, n$. This yields

$$f(\vec{v}) = \sum_{i=1}^{n} \Delta v_i^3 \, f(\vec{v}_i) \; \delta(\vec{v} - \vec{v}_i) \equiv \sum_{i=1}^{n} c_{\vec{v}_i} \; \delta(\vec{v} - \vec{v}_i) \, , \tag{4.5}$$

where Δv_i^3 is the integration weight from discretizing the integral and $f(\vec{v}_i)$ is the velocity distribution to be optimized, evaluated at the velocity $\vec{v}_i$. The decomposition into a finite number of streams is justified by the Fenchel-Eggleston theorem [296, 297] as well as Choquet's theorem [298]. We note that the decomposition into streams was first suggested in Refs. [281, 285]. In the following, we define $c_{\vec{v}_i} \equiv \Delta v_i^3 \, f(\vec{v}_i)$ as the weight of the stream $\delta(\vec{v} - \vec{v}_i)$. With this, we write the optimization problem as

$$\begin{aligned}
\text{optimize} \quad & F(c_{\vec{v}_1} ..., c_{\vec{v}_n}) = \sum_{i=1}^{n} c_{\vec{v}_i} N_{\vec{v}_i}^{(A)} \, , \\
\text{subject to} \quad & \sum_{i=1}^{n} c_{\vec{v}_i} = 1 \, , \\
\text{and} \quad & \sum_{i=1}^{n} c_{\vec{v}_i} N_{\vec{v}_i}^{(B_\alpha)} \leq N_{\max}^{(B_\alpha)}, \quad \alpha = 1, ..., p \, , \\
\text{and} \quad & (-1) \cdot \sum_{i=1}^{n} c_{\vec{v}_i} N_{\vec{v}_i}^{(B_\alpha)} \leq (-1) \cdot N_{\min}^{(B_\alpha)}, \quad \alpha = p+1, ..., p+q \, , \\
\text{and} \quad & - c_{\vec{v}_i} \leq 0, \quad i = 1...n \, ,
\end{aligned} \tag{4.6}$$

where the objective function $F(c_{\vec{v}_1} ..., c_{\vec{v}_n})$ is now a function of the weights $c_{\vec{v}_i}$. We give the optimization problem in Eq. (4.6) in the standard form of linear programming, see appendix B.3, by multiplying lower limit inequalities by a factor of (-1). We then solve those problems using the linear programming solvers from `Mathematica` [299] or `CVXOPT` [300]. In the limit of an infinitely large number of streams $n \to \infty$, the solution converges to the optimal function $f(\vec{v})$.

From Eq. (B.30), we read off that this specific linear programming problem has a number of non-zero coefficients $c_{\vec{v}_i}$ between 1 and $1 + p + q$ depending on how many constraints are saturated. We use this to gain analytic insight into the structure of the optimal solution. Here, we restrict ourselves to the particular case of one experiment that we wish to optimize and one constraint from another experiment. In this case, the linear programming problem is given by

$$\begin{aligned}
\text{minimize} \quad & R(\{a_{\vec{v}_i}\}) = \sum_{i=1}^{n} a_{\vec{v}_i}^2 R_{\vec{v}_i} \, , \\
\text{subject to} \quad & \sum_{i=1}^{n} a_{\vec{v}_i}^2 = 1 \, , \\
\text{and} \quad & C(\{a_{\vec{v}_i}\}) = \sum_{i=1}^{n} a_{\vec{v}_i}^2 C_{\vec{v}_i} \leq C_{\max} \, ,
\end{aligned} \tag{4.7}$$

where we assumed the particular case of optimizing the signal at a direct detection experiment, which measures the recoil rate R, such that constraints on the capture rate of dark matter in the Sun are met. Here, we choose the primal variables $a_{\vec{v}_i}^2 \equiv c_{\vec{v}_i}$ which ensures that $c_{\vec{v}_i}$ is positive without including a constraint. We solve this problem by minimizing the Lagrangian

$$L(\{a_{\vec{v}_i}\},\{\vec{v}_i\},s,\lambda,\eta) = \sum_{i=1}^{n} a_{\vec{v}_i}^2 R_{\vec{v}_i} - \lambda\left(\sum_{i=1}^{n} a_{\vec{v}_i}^2 - 1\right) - \eta\left(\sum_{i=1}^{n} a_{\vec{v}_i}^2 C_{\vec{v}_i} + s^2 - C_{\max}\right) , \tag{4.8}$$

where we introduce two Lagrangian multipliers $\lambda > 0$ and $\eta > 0$ as well as the slack variable $s^2 > 0$. We use the latter to convert the inequality constraint of Eq. (4.7) into an equality constraint. From this, we derive the optimal configuration of the variables by calculating the Karush-Kuhn-Tucker conditions

$$\frac{\partial L}{\partial a_{\vec{v}_p}} = 2\, a_{\vec{v}_p}\left[R_{\vec{v}_p} - \lambda - \eta C_{\vec{v}_p}\right] = 0, \quad p = 1,\ldots,n\,, \tag{4.9}$$

$$\frac{\partial L}{\partial \vec{v}_p} = a_{v_i}^2\left[\frac{\partial R_{\vec{v}_p}}{\partial \vec{v}_p} - \eta\frac{\partial C_{\vec{v}_p}}{\partial \vec{v}_p}\right] = 0, \quad p = 1,\ldots,n\,, \tag{4.10}$$

$$\frac{\partial L}{\partial s} = 2\,\eta\, s = 0\,, \tag{4.11}$$

$$\frac{\partial L}{\partial \lambda} = \sum_{i=1}^{n} a_{\vec{v}_i}^2 - 1 = 0\,, \tag{4.12}$$

$$\frac{\partial L}{\partial \eta} = \sum_{i=1}^{n} a_{\vec{v}_i}^2\, C_{\vec{v}_i} + s^2 - C_{\max} = 0\,. \tag{4.13}$$

In order to fulfill this system of equations, we require $\eta = 0$ or $s = 0$. The solution $s = 0$ corresponds to the case that the upper limit on C is saturated while $\eta = 0$ indicates that the constraint is not fulfilled.

For the case that the constraint on C is not fulfilled, i.e. $\eta = 0$, we obtain the condition

$$\frac{\partial R_{\vec{v}}}{\partial \vec{v}}\Big|_{\vec{v}=\vec{v}_1} = 0 \tag{4.14}$$

from the derivative of the Lagrangian with respect to the velocities of the streams. This implies that the optimal velocity distribution consists of streams that are placed at the position of the extreme points of the scattering rate. Using furthermore the derivative of the Lagrangian with respect to the primal variables $a_{\vec{v}_i}$

$$a_{\vec{v}_p}[R_{\vec{v}_p} - \lambda] = 0, \quad p = 1,\ldots,n\,, \tag{4.15}$$

we conclude that there is only one stream with a non-zero weight fulfilling the condition $R_{\vec{v}_i} = \lambda$. In the case that there are multiple extreme points, it suffices to pick one of them as all of those points are equivalent. Finally, we conclude from the derivative with respect to λ that this stream must have a weight $a_{\vec{v}_i} = 1$ and therefore $c_{\vec{v}_i} = 1$. In the case that the constraint on the capture rate is not fulfilled, we conclude that the optimized velocity

distribution is given by

$$f(\vec{v}) = \delta(\vec{v} - \vec{v}_1) \qquad \text{with} \qquad \left.\frac{\partial R_{\vec{v}}}{\partial \vec{v}}\right|_{\vec{v}=\vec{v}_1} = 0\,. \tag{4.16}$$

For the specific case that the minimum of the scattering rate is sought-after, the stream velocity is $\vec{v} = 0$ as this leads to recoil energies below the threshold of the experiment $R_{\vec{v}=0} = 0$.

In the case that the constraint on the capture rate is saturated, we conclude that there are two streams since the equation

$$a_{\vec{v}_p}[R_{\vec{v}_p} - \lambda - \eta C_{\vec{v}_p}] = 0, \quad p = 1, \ldots, n \tag{4.17}$$

has exactly two solutions, confer the discussion in appendix B.3. In the following, we denote the velocities of the two streams by v_1 and v_2. From the two equations in Eq. (4.17) for which the weights are non-zero, we derive the Lagrangian multipliers

$$\lambda = \frac{C_{\vec{v}_1} R_{\vec{v}_2} - C_{\vec{v}_2} R_{\vec{v}_1}}{C_{\vec{v}_1} - C_{\vec{v}_2}}\,, \qquad \eta = \frac{R_{\vec{v}_1} - R_{\vec{v}_2}}{C_{\vec{v}_1} - C_{\vec{v}_2}}\,. \tag{4.18}$$

Furthermore, we determine the weights from the derivatives of the Lagrangian with respect to the Lagrangian multipliers. This yields

$$a^2_{\vec{v}_1} = \frac{C_{\max} - C_{\vec{v}_2}}{C_{\vec{v}_1} - C_{\vec{v}_2}}\,, \qquad a^2_{\vec{v}_2} = \frac{C_{\vec{v}_1} - C_{\max}}{C_{\vec{v}_1} - C_{\vec{v}_2}}\,. \tag{4.19}$$

Finally, we derive the velocities of the two streams from the derivatives of the Lagrangian with respect to the stream velocities, confer Eq. (4.9), using the expression for η. The resulting equations read

$$\frac{\partial R_{\vec{v}_1}}{\partial \vec{v}_1} = \left(\frac{R_{\vec{v}_1} - R_{\vec{v}_2}}{C_{\vec{v}_1} - C_{\vec{v}_2}}\right) \frac{\partial C_{\vec{v}_1}}{\partial \vec{v}_1}\,, \tag{4.20}$$

$$\frac{\partial R_{\vec{v}_2}}{\partial \vec{v}_2} = \left(\frac{R_{\vec{v}_1} - R_{\vec{v}_2}}{C_{\vec{v}_1} - C_{\vec{v}_2}}\right) \frac{\partial C_{\vec{v}_2}}{\partial \vec{v}_2}\,. \tag{4.21}$$

From solving this set of coupled equations, we obtain the velocities of the streams. However, the number of coupled equations depends on the number of constraints and increases with the number of constraints that are saturated. This makes it very hard to solve this set of equations analytically for more than one inequality constraint in Eq. (4.6).

4.2. Applications

Here, we present halo-independent analyses for several applications to direct dark matter searches and we implement the experiments as detailed in appendix C. We note that examples for the application of this method to signal claims are discussed in chapter 5 and chapter 7.

4.2.1. Upper limits on the cross section from null results

For this application, we minimize the outcome of experiment A subject to the upper limits on the outcomes of experiments B_α with $\alpha = 1, \ldots, p$. For a fixed scattering cross section and dark matter mass, we calculate the minimal outcome of experiment A that is allowed by varying the velocity distribution. We consider a pair of parameters $(m_{\rm DM}, \sigma)$ to be ruled out if

$$\begin{aligned} & \min\{N^{(A)}\}(\sigma, \mathrm{m_{DM}}) \;\geq\; N^{(A)}_{\rm max}\,, \\ \text{subject to} \quad & N^{(B_\alpha)} \leq N^{(B_\alpha)}_{\rm u.l.} \quad \text{for } \alpha = 1, \ldots, p\,, \\ & \int f(\vec{v})\, \mathrm{d}^3 v = 1\,. \end{aligned} \tag{4.22}$$

With this, we calculate halo-independent upper limits on the scattering cross section as a function of the dark matter mass from the combination of $p + 1$ experiments that do not claim a signal.

To illustrate this application, we calculate the halo-independent upper limits by combining results from one direct detection experiment and one neutrino telescope. For this, we discretize the velocity integrals and introduce 775 streams. As apparent from the discussion of those experiments in sections 3.3.1 and 3.3.2, direct detection experiments are sensitive to velocities larger than $v^{\rm (DD)}_{\rm min}$ while neutrino telescopes probe velocities smaller than $v^{\rm (NT)}_{\rm max}$. As long as $v^{\rm (DD)}_{\rm min} < v^{\rm (NT)}_{\rm max}$, the combination of a direct detection experiment and a neutrino telescope covers the whole velocity space. If this is not the case, the halo-independent upper limit vanishes as a stream with velocity $v^{\rm (NT)}_{\rm max} < v < v^{\rm (DD)}_{\rm min}$ cannot be detected by neither the direct detection experiment nor the neutrino telescope. The complementarity of these two detection techniques was highlighted in Refs. [2, 4, 98, 285, 301, 302].

In Fig. 10, we show the combined halo-independent analysis using the upper limits on the annihilation rate from IceCube [250] and Super-Kamiokande [252] for annihilation into W^+W^- ($\tau^+\tau^-$ for $m_{\rm DM} < M_W$) as well as using the null results from PandaX Run 8 [217] and Run 9 [218] for spin-independent interactions and PICO-60 [237] for spin-dependent interactions. Here, we assume equilibrium between capture and annihilation as the combined upper limits shown in Fig. 10 are in regions where equilibrium is achieved, confer Fig. 9. Since the capture of dark matter in the Sun does not depend on the characteristics of the neutrino telescope, we use the strongest upper limit on the annihilation rate available. In addition to this, we show the halo-independent upper limits derived from only neutrino telescope data.

This methods yields remarkably strong limits reaching down to $\sigma^{\rm p}_{\rm SI} \simeq 10^{-44}\,\mathrm{cm}^2$ and $\sigma^{\rm p}_{\rm SD} \simeq 10^{-40}\,\mathrm{cm}^2$ when combining direct detection experiments and neutrino telescopes. For the combined analysis of PICO and IceCube, the limits presented here are compatible with the combined analysis performed jointly by both collaborations [293]. Here, we assume a dark matter density of 0.3 GeV/cm^3 and choose the angle between the velocity of the Sun and the Earth such that the limits are most conservative. As apparent from

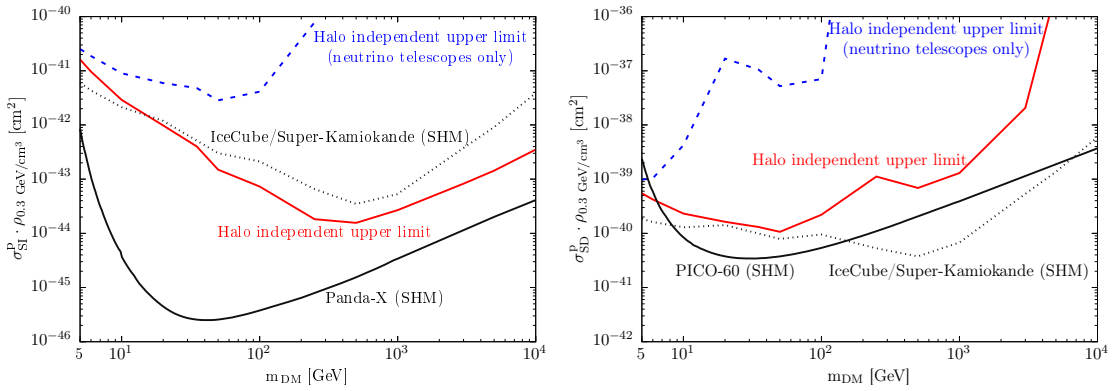

Figure 10.: Combined halo-independent upper limits on the scattering cross section assuming a local dark matter density of $\rho = 0.3$ GeV/cm^3. We depict limits on spin-independent interactions in the left plot. For this, we use the dark matter search results from PandaX Run 8 and Run 9. The right plot shows the halo-independent upper limits for spin-dependent interactions using results from the direct detection experiment PICO-60. In both plots, we combine the results of the direct detection experiment under consideration and the neutrino telescopes IceCube as well as Super-Kamiokande. We additionally show halo-independent upper limits derived from neutrino telescopes only. In each case, we use limits on the annihilation rate in the Sun derived by assuming that dark matter annihilates solely into W^+W^- ($\tau^+\tau^-$ for $m_{\rm DM} < m_W$). As a comparison, we show the upper limits of the individual experiments derived from the Standard Halo Model as black solid and dotted lines. These plots were taken from Ref. [2].

Fig. 10, it is not always possible to derive halo-independent upper limits on the cross section due to the fact that $v^{(\rm NT)}_{{\rm max},i}$ is small for heavy dark matter, confer Eq. (3.52). Observing furthermore that the minimal velocity needed to leave a detectable signature increases for heavy dark matter, see Eq. (3.46), we conclude that $v^{(\rm NT)}_{\rm max} < v^{(\rm DD)}_{\rm min}$ for very heavy dark matter. In this regime, the limit vanishes as the minimum of the objective function is achieved for streams with velocity $v^{(\rm NT)}_{\rm max} < v < v^{(\rm DD)}_{\rm min}$ as those streams can neither be detected by direct detection experiments nor by neutrino telescopes. The dark matter mass above which this happens depends on the experiments under consideration and the nuclei present in the target. For the combination of PandaX and IceCube, dark matter must be heavier than $\sim 165\,$TeV, while for PICO-60 and IceCube the threshold is at $m_{\rm DM} \sim 4.5\,$TeV.

For dark matter masses smaller than $\sim 200\,$GeV, we are able to set halo-independent upper limits on the scattering cross section solely from IceCube and Super-Kamiokande. This is possible as the maximal velocity that can lead to capture in the Sun is larger than the escape velocity from the Milky Way for those masses. Therefore, neutrino telescopes alone probe the whole velocity space. As apparent from the discussion in section 4.1, the optimal velocity distribution consists of one stream that is placed at $v = v_{\rm esc}$ as the capture rate is a monotonically decreasing function of the stream velocity.

4.2.2. Prospects for future experiments

In this section, we study the sensitivity of proposed experiments to a dark matter signal. For this, the results from existing experiments are a valuable input when studying the detection prospects. This additional information allows to determine the part of the dark matter parameter space ($m_{\rm DM}$, σ) where the limits could be or will be refined. Therefore, we consider the future experiment A as well experiments B_α that set upper limits. Assuming the minimal number of events $N_{\rm det}^{(A)}$ that is necessary to establish a signal at experiment A, we identify the region in parameter space that cannot be probed by this experiment regardless of the velocity distribution via the condition

$$\max\{N^{(A)}\}(m_{\rm DM},\sigma) < N_{\rm det}^{(A)}\,. \tag{4.23}$$

Concretely, we maximize the outcome of experiment A subject to constraints from experiments B_α with $\alpha = 1,\ldots,p$. The region in parameter space that will be probed by some velocity distributions is defined as

$$\max\{N^{(A)}\}(m_{\rm DM},\sigma) \geq N_{\rm det}^{(A)}\,. \tag{4.24}$$

In this region, it is possible to have a signal larger than the detection threshold depending on the velocity distribution. Finally, we define the region in parameter space that can be probed regardless of the velocity distribution. It consists of points $(m_{\rm DM},\sigma)$ satisfying

$$\min\{N^{(A)}\}(m_{\rm DM},\sigma) \geq N_{\rm det}^{(A)}\,, \tag{4.25}$$

i.e. points for which a dark matter signal will be detected by the experiment regardless of the velocity distribution. In addition to these three regions, there is a fourth one for which a signal is excluded by the experiments B_α in a halo-independent way.

Here, we asses the detection prospects of the proposed LUX-ZEPLIN (LZ) [303] experiment. We solve the optimization problems by discretizing the velocity integrals into 775 streams and modeling the constraints as in the previous sections. We identify the regions in parameter space that can be probed by LZ using the null results from SuperCDMS [226] and PICO-60 [237] as constraints for spin-independent respectively spin-dependent interactions. In contrast to the previous sections, we do not use the null results of xenon-based direct detection experiments as we need experiments with different characteristics for a meaningful halo-independent forecast. Therefore, we use the results of SuperCDMS which employs a germanium target. In addition to constraints from direct detection experiments, we include the null results of IceCube [250] and Super-Kamiokande [252] into the analysis considering annihilation of dark matter solely into W^+W^- ($\tau^+\tau^-$ for $m_{\rm DM} < m_W$). As in the previous sections of this chapter, we assume equilibrium between capture and annihilation processes as equilibration is given for the relevant cross sections. Finally, we fix the time-dependent velocity of the Earth such that the optimized recoil rate at LZ is smallest (largest) which allows us to identify the regions that will be tested (remain untested) in the most conservative way. Further details on the experiments under consideration can

be found in appendix C.

In Fig. 11, we show the detection prospects of LZ for constraints from direct detection experiments (upper row), neutrino telescopes (middle row) as well as for direct detection experiments and neutrino telescopes combined. We study spin independent (left column) and spin-dependent interactions (right column). Furthermore, we assume that the number of events necessary to claim a signal at LZ is one, i.e. $N_{\rm det}^{\rm (LZ)} = 1$. In the plots of Fig. 11, we denote the domain which is not accessible by LZ in white. This consists of parameters for which the maximal number of events at LZ is smaller than the detection threshold. We show in light red the region that is testable for some velocity distributions. For parameters in this region, there exist velocity distributions for which the expected number of recoil events is larger than $N_{\rm det}^{\rm (LZ)}$. Furthermore, the dark red domain in Fig. 11 corresponds to the points in parameter space which are for sure testable as even the minimal number of events at LZ exceeds $N_{\rm det}^{\rm (LZ)}$. Finally, we show the region in parameter space that is already ruled out by the constraints in gray. In addition to those regions, we depict the projected sensitivity derived by the LZ collaboration [303] assuming the SHM. For a local dark matter density of $\rho_{\rm loc} = 0.3\,{\rm GeV/cm^3}$ and a dark matter mass of 1 TeV, we find that LZ will be able to probe $\sigma_{\rm SI}^{\rm p} \gtrsim 3 \cdot 10^{-45}\,{\rm cm^2}$ as well as $\sigma_{\rm SD}^{\rm p} \gtrsim 3 \cdot 10^{-40}\,{\rm cm^2}$ regardless of the velocity distribution. Furthermore, cross sections smaller than $\sigma_{\rm SI}^{\rm p} \lesssim 2 \cdot 10^{-47}\,{\rm cm^2}$ and $\sigma_{\rm SD}^{\rm p} \lesssim 2 \cdot 10^{-42}\,{\rm cm^2}$ will escape detection for all velocity distributions and dark matter masses between 5 GeV and 10 TeV.

In the following, we motivate the contours shown in Fig. 11 analytically. In the region that cannot be accessed by LZ, the cross section is small and therefore none of the constraints is active. Due to this, the optimized velocity distribution consists of one single stream $f(v) = \delta(v - v_0)$, where v_0 either fulfills the condition $\partial R/\partial v_0 = 0$ or is located at the boundary of the velocity space. The region in parameter space which is fully testable with LZ, i.e. for which $\min\{R^{\rm (LZ)}\}(m_{\rm DM}, \sigma) \geq N_{\rm det}^{\rm (LZ)}$ holds, does not exist when considering constraints from direct detection experiments only. The optimized velocity distribution in this case is a single stream with a speed smaller than the velocity threshold of each experiment and cannot be probed by direct detection experiments. As a stream with a small velocity would violate the bounds from neutrino telescopes, there can be a region in parameter space that is fully testable with LZ or already excluded in a halo-independent way from the results of other experiments. As discussed in section 4.1 and depicted in Fig. 10, this region exists only in the case that constraints from neutrino telescopes are considered.

4.3. Discussion and summary

In this Chapter, we introduced a method to analyze results from direct detection experiments and neutrino telescopes without specifying the velocity distribution. For this method, we calculate the minimal/maximal expected outcome of an experiment subject to constraints from other local dark matter searches. We do this by decomposing the velocity distribution into a sum of weighted streams. Using the fact that the velocity distribution

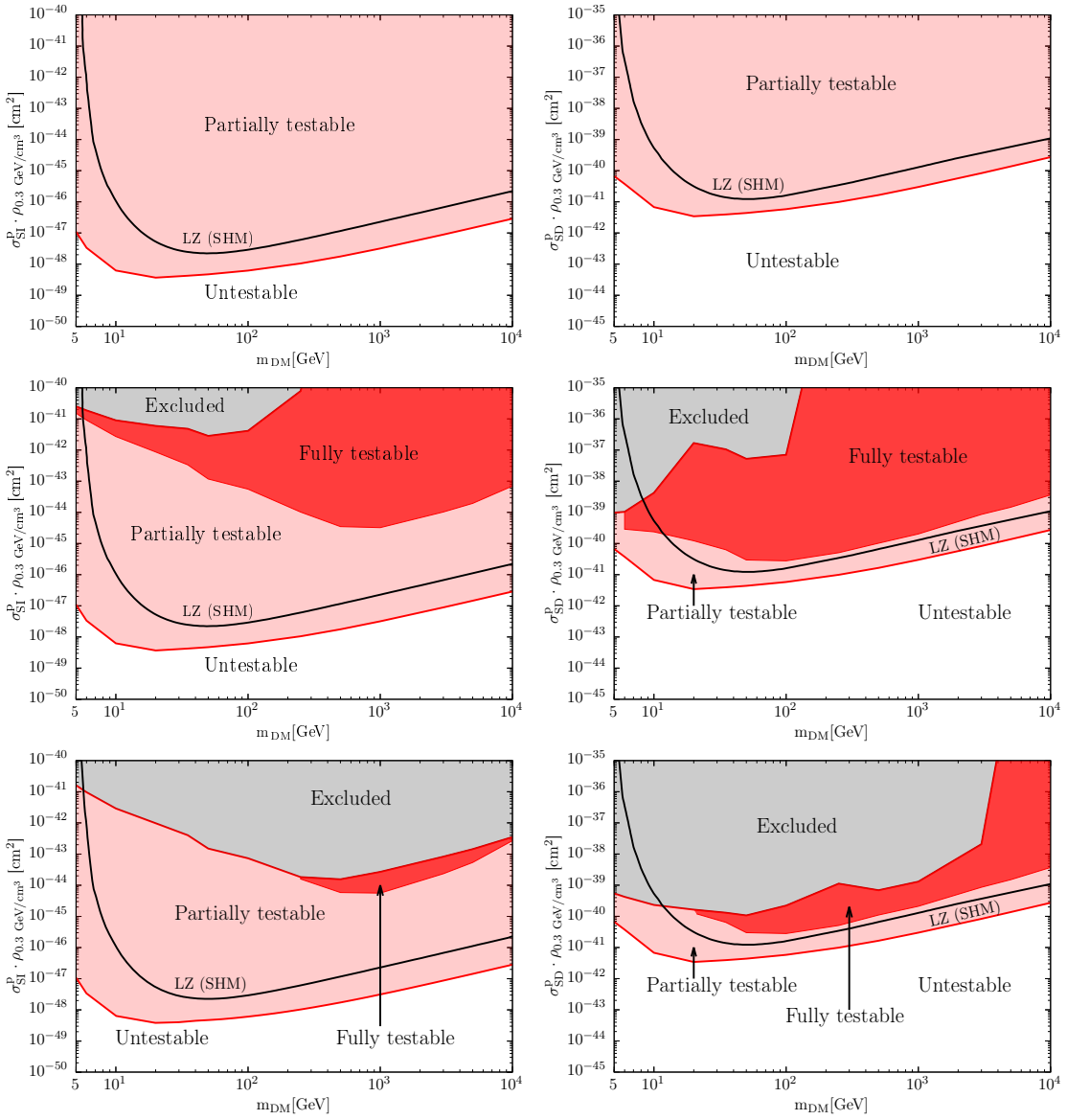

Figure 11.: Detection prospects of LZ assuming spin-independent (left) as well as spin-dependent interactions (right). In the upper row, we depict the detection prospects of LZ compatible with null results from SuperCDMS and PICO-60. In the middle row, we show the same but using constraints from the neutrino telescopes IceCube and Super-Kamiokande for annihilation into W^+W^- ($\tau^+\tau^-$ for $m_{\rm DM} < m_W$). Finally, the bottom row contains plots for the detection prospects of LZ given combined constraints from direct detection experiments and neutrino telescopes. In each plot, we include the projected sensitivity assuming the SHM as derived by the LZ collaboration [303]. These plots were taken from Ref. [2].

enters linearly into the number of events expected at a direct detection experiment and the capture rate of dark matter particles in the Sun, we decompose those observables into sums which depend linearly on the weights. Finally, we use linear programming techniques to optimize the outcome of an experiments subject to constraints. For p constraints from experiments, we found that the optimal velocity distribution consists of $p+1-r$ streams, where r is the number of constraints that are not saturated.

We applied the method to two different types of analyses. First, we derived halo-independent upper limits on the scattering cross section from the combination of direct detection experiments and neutrino telescopes. The combination of those two experimental techniques leads to the strongest limits as the whole velocity space can be probed. For the particular case of annihilation into W^+W^- ($\tau^+\tau^-$ for $m_{\rm DM} < m_W$), we computed the halo-independent upper limits from the combination of direct detection experiments and neutrino telescopes. From this, we obtained remarkably strong limits excluding $\sigma^{\rm p}_{\rm SI} \gtrsim 3 \cdot 10^{-44}\,{\rm cm}^2$ and $\sigma^{\rm p}_{\rm SD} \gtrsim 10^{-40}\,{\rm cm}^2$ in a halo-independent way for a dark matter mass of 1 TeV and a local dark matter density of $\rho_{\rm loc} = 0.3\,{\rm GeV/cm}^3$.

We investigated furthermore the detection prospects of future experiments given null results from other experiments. Concretely, we studied the sensitivity of the planned experiment LZ in light of the current dark matter searches performed by SuperCDMS and PICO-60 as well as by the neutrino telescopes IceCube and Super-Kamiokande. For the latter, we assumed that dark matter annihilates solely into W^+W^- ($\tau^+\tau^-$ for $m_{\rm DM} < m_W$). We found that LZ will probe $\sigma^{\rm p}_{\rm SI} \gtrsim 3{\cdot}10^{-45}\,{\rm cm}^2$ and $\sigma^{\rm p}_{\rm SD} \gtrsim 3{\cdot}10^{-40}\,{\rm cm}^2$ regardless of the velocity distribution for a dark matter mass of 1 TeV and a local dark matter density of $\rho_{\rm loc} = 0.3\,{\rm GeV/cm}^3$. In contrast, scattering cross sections smaller than $\sigma^{\rm p}_{\rm SI} \lesssim 2{\cdot}10^{-47}\,{\rm cm}^2$ and $\sigma^{\rm p}_{\rm SD} \lesssim 2 \cdot 10^{-42}\,{\rm cm}^2$ will not be probed for any velocity distribution and dark matter masses between 5 GeV and 10 TeV.

However, this method has two disadvantages. Despite the fact that our results are strict in the mathematical sense, they are too conservative as it is unlikely that the velocity distribution in the solar neighborhood saturates such a mathematically optimal distribution. This is also supported by the velocity distributions extracted from astrophysical observations or from N-body simulations, confer Fig. 3. Our method therefore finds the most extreme outcome of an analysis. Furthermore, this method does not properly include the propagation of errors. As a consequence of this, the confidence level of our results is not clear in the case of a combined analysis. However, our results are conservative as the confidence level of a combined analysis is higher than the confidence level of the individual bounds. This motivates to improve this method, see chapter 6.

Chapter 5.

A halo-independent analysis in the effective theory of dark matter-nucleon interactions

The content of this chapter was published in Ref. [3]. As this was done before the latest data from XENON1T [221] were released, we used the results from 2017 [220] which in the following will be referred to as XENON1T-2017.

We propose in this chapter a method to confront, in a halo-independent way, a putative dark matter signal with the null results from other direct detection experiments in an effective theory of dark matter-nucleon interactions, including possible interferences. The method then allows to check the compatibility of different experiments despite our ignorance of the local dark matter velocity distribution and with only minor assumptions on the characteristics of the dark matter-nucleon interaction. This extends previous works that can either treat the uncertainties arising from the local dark matter density and velocity distribution [2, 4, 269–293] or the uncertainties from the concrete form of the dark matter-nucleon interaction [3].

As an application of this method, we examine the compatibility of the tentative detection of a dark matter signal by the silicon detectors of the CDMS-II experiment (CMDS-Si) [225] with the null results from XENON1T-2017 [220] and PICO-60 [237] experiments. This putative dark matter signal consists of three candidate events that were collected over the full exposure of the detectors. The parameters necessary to explain those events with dark matter are in strong tension with null results from other experiments when assuming the spin-independent or the spin-dependent interaction as well as the SHM. Until today, there is no satisfactory explanation of this signal as no new sources of background could be identified and the probability that the signal is due to a statistical fluctuation of the known background is smaller than 5.4% [225]. The question therefore arises whether the CDMS-Si signal can be reconciled with null search experiments by considering other types of dark matter-nucleon interactions and/or by being agnostic about the local velocity distribution of dark matter particles.

5.1. Optimizing the interaction of dark matter with nuclei

We adopt the non-relativistic effective field theory discussed in section 3.2.3 in order to account for the fact that the concrete form of the dark matter-nucleon interaction is unknown. In this framework, the expected outcome of an experiment for a fixed velocity distribution $f(\vec{v})$ is given by

$$N_{f(\vec{v})}\left(\vec{c}\right) = \vec{c}^{T}\mathbb{N}_{f(\vec{v})}\vec{c}, \tag{5.1}$$

where $\vec{c}$ is the vector of Wilson coefficients corresponding to the operators shown in Tab. 1. Furthermore, $\mathbb{N}_{f(\vec{v})}$ is a symmetric matrix that depends on the velocity distribution and the details of the experiment under consideration.

We determine the maximal signal at an experiment $\mathcal{E}_0$ subject to null results from p other experiments $\mathcal{E}_1, \ldots, \mathcal{E}_p$ by solving the following optimization problem for a fixed velocity distribution

$$\begin{aligned} & \max_{\vec{c}} \left[N_{f(\vec{v})}^{(\mathcal{E}_0)}\left(\vec{c}\right) \right], \\ \text{subject to} \quad & N_{f(\vec{v})}^{(\mathcal{E}_1)}(\vec{c}) \leq N_{\text{u.l.}}^{(\mathcal{E}_1)}, \\ & \vdots \\ & N_{f(\vec{v})}^{(\mathcal{E}_p)}(\vec{c}) \leq N_{\text{u.l.}}^{(\mathcal{E}_p)}. \end{aligned} \tag{5.2}$$

This is a convex optimization problem[1] as both the objective function as well as the constraints are quadratic in the Wilson coefficients. We solve this following the procedure outlined in Refs. [3, 304] and we assume for simplicity that there are constraints from two experiments. However, this discussion can be extended in a straight forward way to an arbitrary number of constraints. As the constraints are quadratic, each of them corresponds to the interior of an ellipse in $\dim(\vec{c})$ dimensions. We illustrate this in Fig. 12 for a two dimensional slice of the parameter space. All vectors $\vec{c}$ that are within a colored ellipse are allowed by the constraint from the corresponding experiment and the feasible set is therefore the intersection of all colored ellipses. The contours of the objective function are also shown in Fig. 12 for three different cases labeled by $N_3 < N_2 < N_1$. Geometrically, they correspond to surfaces of ellipses as the objective function is also quadratic. Concretely, a number of events at CDMS-Si equal to N_3 is allowed but not optimal while N_1 is forbidden as its contour does not touch the feasible region. Finally, the maximum is given by the largest dashed ellipse that intersects the feasible region and is denoted by N_2. We check whether the ellipse surface parametrized by the condition $\vec{c}^{T}\mathbb{N}_{f(\vec{v})}^{(\mathcal{E}_0)}\vec{c} = N_{f(\vec{v})}^{(\mathcal{E}_0)}\left(\vec{c}\right)$ intersects the feasible region by finding real parameters $\zeta^{(\mathcal{E}_1)}$ and

[1] More specifically, a second order cone problem, confer the discussion in appendix B.4.

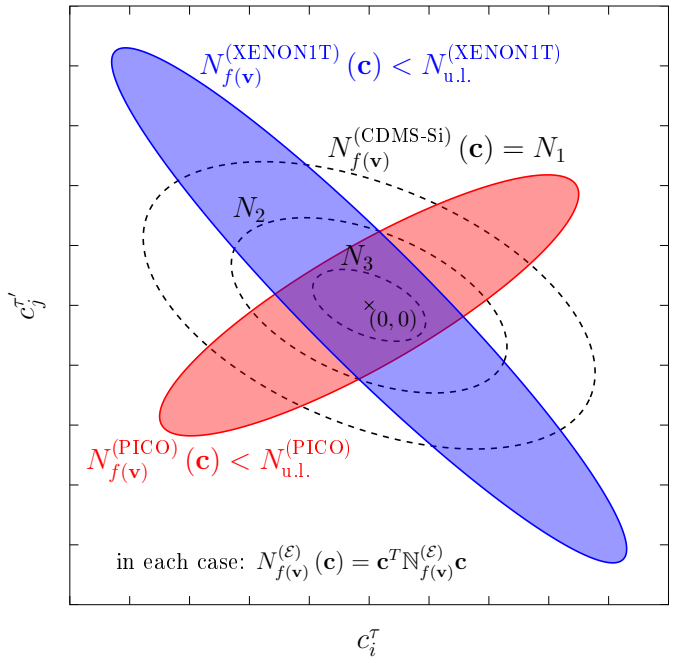

Figure 12.: Visualization of the proposed method. We depict upper limit constraints from XENON1T (blue) and PICO-60 (red) as colored ellipses. The black dashed ellipses denote the contours of the objective function labeled by the expected number of scattering events at CDMS-Si with $N_3 < N_2 < N_1$. We note that the depicted ellipses are not based on real data. This figure was initially published in Ref. [304] but taken from Ref. [3].

$\zeta^{(\mathcal{E}_2)}$ such that [3, 304]

$$i)\ \zeta^{(\mathcal{E}_1)} + \zeta^{(\mathcal{E}_2)} < 1 \quad \text{and} \tag{5.3}$$

$$ii)\ \left(\zeta^{(\mathcal{E}_1)} \frac{\mathbb{N}_{f(\vec{v})}^{(\mathcal{E}_1)}}{N_{\mathrm{u.l.}}^{(\mathcal{E}_1)}} + \zeta^{(\mathcal{E}_2)} \frac{\mathbb{N}_{f(\vec{v})}^{(\mathcal{E}_2)}}{N_{\mathrm{u.l.}}^{(\mathcal{E}_2)}} \right) - \frac{\mathbb{N}_{f(\vec{v})}^{(\mathcal{E}_0)}}{N_{f(\vec{v})}^{(\mathcal{E}_0)}} \text{ is a positive definite matrix.} \tag{5.4}$$

We then increase $N_{f(\vec{v})}^{(\mathcal{E}_0)}$ until it is not possible to find those real parameters. We implement this algorithm using the `feasp` solver of `MATLAB` [305] respectively the `conelp` solver of `CVXOPT` [300].

For a completely halo-independent analysis in the context of the effective theory of dark matter-nucleon interactions, the optimization problem is then given by

$$\begin{aligned} & \max_{f(\vec{v})} \max_{\vec{c}} \left[N_{f(\vec{v})}^{(\mathcal{E}_0)}(\vec{c}) \right] , \\ \text{subject to} \quad & N_{f(\vec{v})}^{(\mathcal{E}_1)}(\vec{c}) \leq N_{\mathrm{u.l.}}^{(\mathcal{E}_1)} , \\ & \vdots \\ & N_{f(\vec{v})}^{(\mathcal{E}_p)}(\vec{c}) \leq N_{\mathrm{u.l.}}^{(\mathcal{E}_p)} , \\ & \int f(\vec{v})\, \mathrm{d}^3 v = 1 , \end{aligned} \tag{5.5}$$

where we assume p constraints from experiments. Fixing again $p = 2$, we conclude from section 4.1 that there are between 1 and 3 streams with non-zero weights, depending on the number of constraints that are saturated. When maximizing the objective function and since the normalization of the Wilson coefficients is not fixed, we are able to write the optimal velocity distribution in terms of at most two streams, as proven by an explicit calculation in appendix D. Therefore, we write the optimal velocity distribution as

$$f_{\alpha,\vec{v}_1,\vec{v}_2}(\vec{v}) = \alpha\,\delta(\vec{v}-\vec{v}_1) + (1-\alpha)\delta(\vec{v}-\vec{v}_2)\,, \tag{5.6}$$

where we have two streams with velocity $\vec{v}_1$ and $\vec{v}_2$ as well as weights α and $1-\alpha$. We then find the maximum by scanning the parameters α, $\vec{v}_1$ as well as $\vec{v}_2$ and calculating $N_{f(\vec{v})}^{(\mathcal{E}_0)}(\vec{c})$ for each velocity distribution. We note that the complexity of this increases significantly when increasing the number of constraints from experiments. In practice however, this is not a problem as the number of different target elements is limited and so is the number of reasonable constraints.

5.2. Confronting the CDMS-Si signal to null results

We analyze the signal at the silicon detectors of the CDMS-II experiment (CDMS-Si) that found three events with an exposure of 140.2 kg×day [225]. However, the experiments XENON1T-2017 and the PICO-60 found no evidence for dark matter despite much larger exposures of $3.35 \cdot 10^4$ kg×day [220] and 1167 kg×day [237]. Assuming spin-independent or spin-dependent scattering, the dark matter interpretation of the CDMS-Si excess is disfavored by the results of XENON1T-2017 and PICO-60. It is however important to note that these three experiments have different target materials, whose responses could be dramatically affected by the nature of the DM-nucleon interaction. Furthermore, the typical energy transferred onto the nucleus, and thus also the detectability of the scattering events, depends crucially on the local dark matter velocity distribution. We therefore investigate whether the CDMS-Si signal can be reconciled with null search experiments by considering other types of dark matter-nucleon interactions and/or by being agnostic about the local velocity distribution of dark matter particles. The optimization problem relevant for this analysis reads

$$\begin{aligned} & \max_{f(\vec{v})} \max_{\vec{c}} \left[N_{f(\vec{v})}^{(\text{CDMS-Si})}(\vec{c}) \right] , \\ \text{subject to} \quad & N_{f(\vec{v})}^{(\text{XENON1T})}(\vec{c}) \leq N_{\text{u.l.}}^{(\text{XENON1T})} , \\ & N_{f(\vec{v})}^{(\text{PICO-60})}(\vec{c}) \leq N_{\text{u.l.}}^{(\text{PICO-60})} , \\ & \int f(\vec{v})\,\mathrm{d}^3 v = 1\,. \end{aligned} \tag{5.7}$$

where $\vec{c}$ denotes the vector of Wilson coefficients corresponding to the operators described in Tab. 1. Furthermore, $N_{\text{u.l.}}^{(\text{XENON1T})}$ and $N_{\text{u.l.}}^{(\text{PICO-60})}$ are the 95% CL upper limits on the number of events at XENON1T-2017 and PICO-60.

In Fig. 13, we show the maximal number of events at CDMS-Si compatible with the null

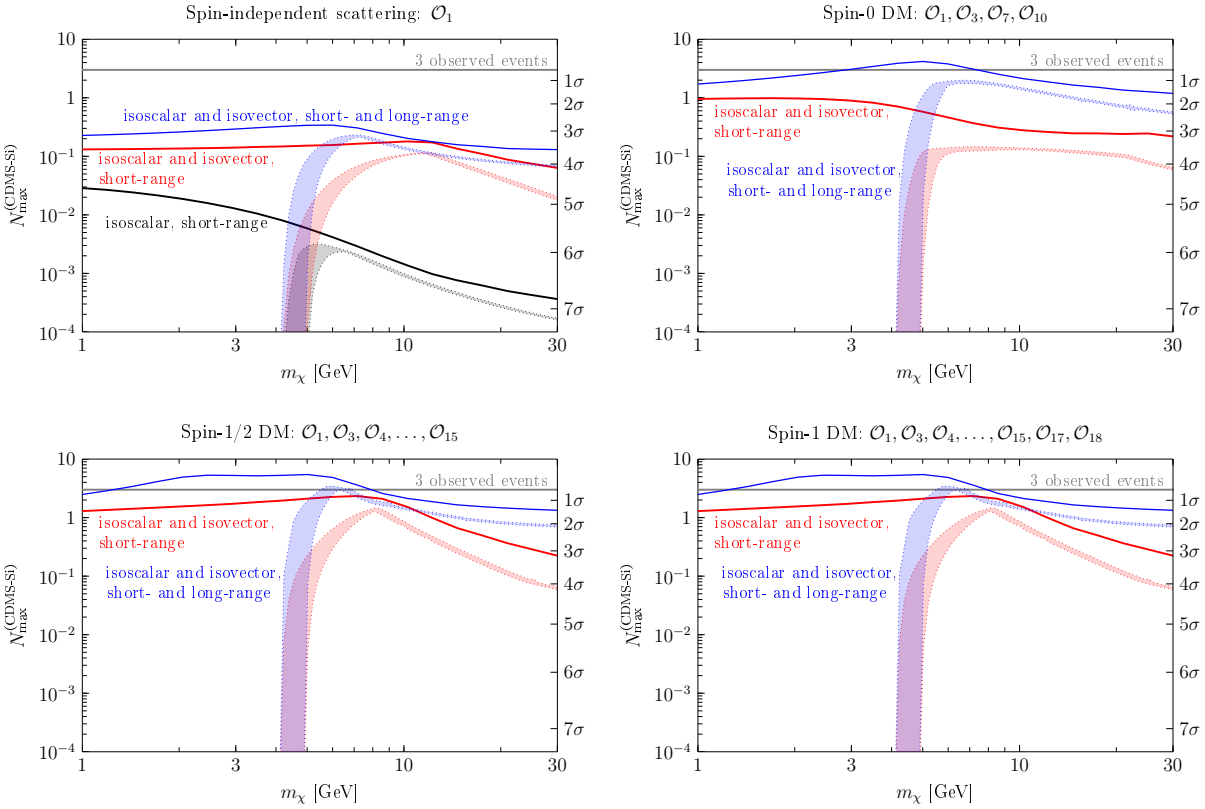

Figure 13.: Maximal number of events at CDMS-Si compatible with null results from XENON1T-2017 and PICO-60. In each panel we show different sets of operators used in our analysis. We include results for spin-independent interactions (top left) as well as for the complete set of operators allowed for spin-0 (top right), spin-1/2 (bottom left) and spin-1 dark matter (bottom right). In each panel, we denote results for short-range interactions by red lines while those additionally assuming long-range interactions are indicated by blue lines. In case of spin-independent interactions, we also show results for isoscalar, short-range interactions as black lines. In each plot, we furthermore depict the maximal number of events at CDMS-Si compatible with the constraints calculated by assuming the SHM. We indicate those by colored bands with the same color code as before. These plots were taken from [3].

results from XENON1T-2017 and PICO-60. In the upper left panel, we depict results for spin-independent interactions only. The upper right, bottom left and bottom right panels correspond to plots for spin-0, spin-1/2 and spin-1 dark matter. We denote results using only short-range interactions in red while those assuming also long-range interactions are shown in blue. For spin-independent scattering, we additionally depict the results for isoscalar short-range interactions. We furthermore show the maximal number of events at CDMS-Si with optimized Wilson coefficients but for the particluar case of the SHM. The colored bands correspond to uncertainties of the SHM constructed by varying the most probable speed v_0 between 220 and 240 km/s as well as considering escape velocities v_{esc} between 492 and 587 km/s. In each panel of Fig. 13, we show the significance with which the dark matter interpretation of the CDMS-Si excess is excluded. We define this quantity

as the number of standard deviations that correspond to the probability of observing three or more events when expecting only $N_{\max}^{(\text{CDMS-Si})}$ events and we assume zero background events for definiteness. The significance of exclusion would however decrease if one or more of the observed events could be credited to background.

When assuming the SHM, the maximal number of events at CDMS-Si is zero for dark matter masses smaller than 4 GeV as apparent from Fig. 13. This is due to the fact that the velocity distribution has a cutoff at v_{esc} which can be translated into a maximal recoil energy for a given dark matter mass. For light dark matter with $m_{\text{DM}} \lesssim 4\,\text{GeV}$, this energy is smaller than the energy threshold of the CDMS-Si experiment. For the halo-independent analysis, we do not impose a cutoff at v_{esc} but instead consider only particles slower than 3000 km/s. We motivate this by the fact that faster dark matter particles are in conflict with the assumption of cold dark matter and cannot be explained even when considering highly non-standard galactic dynamics. Therefore, the expected number of events at CDMS-Si is greater than zero even for $m_{\text{DM}} \leq 4$ GeV.

As already observed in previous studies, see e.g. Ref. [306], the excess at CDMS-Si is in tension with results from XENON1T-2017 and PICO-60 when assuming a spin-independent, isoscalar and short-ranged interaction as well the SHM. For this particular setup, we expect at most $3 \cdot 10^{-3}$ events. As apparent from the black band in the top left plot of Fig. 13, this excludes the dark matter hypothesis with $\sim 6\sigma$ confidence. The expected number of events increases to 0.1 when additionally assuming isovector interactions and finally reaches 0.2 events when including isoscalar and isovector as well as short and long-range interactions. When furthermore using the optimal velocity distribution, the maximum number of events at CDMS-Si increases to $\sim 0.03, 0.2$ respectively 0.3 events. Therefore, we conclude that for spin-independent scattering mediated by the operator $\mathcal{O}_1$, the dark matter interpretation of the CDMS-Si excess is excluded by the null results of XENON1T-2017 and PICO-60 with at least $\sim 3\sigma$ confidence.

We find the tension between the experiments is alleviated significantly for arbitrary interactions of spin-0, spin-1/2 and spin-1 dark matter. When assuming the SHM, the maximal number of events at CDMS-Si for spin-0 dark matter is ~ 2 events which is only in mild tension with the experimental results. For spin-1/2 and spin-1 dark matter, we even find that the experiments can be reconciled but only for dark matter masses of ~ 6 GeV. This however is only possible when considering the full set of operators, i.e. those corresponding to isoscalar and isovector as well as short and long-range interactions. When additionally considering arbitrary velocity distributions, the experiments are compatible in a much larger dark matter mass range. This region extends from slightly above 1 GeV up to 8 GeV for a dark matter particle with spin-1/2 or spin-1. For spin-0 dark matter, we find that the experiments can be reconciled for dark matter masses between 3 GeV and 7 GeV. In addition to this, we studied the effect of smearing the optimal velocity distribution by a Gaussian with a variance of up to 50 km/s. We find that the conclusions do not change significantly.

As apparent from Fig. 13, the maximal number of events at CDMS-Si is ~ 5.4 for arbitrary interactions and velocity distributions when including the constraints from

XENON1T-2017 and PICO-60. If the exposure of both experiments increases by a factor of ~ 20, the signal at CDMS-Si will either be confirmed or ruled out with more than 3σ significance in a halo-independent way for the effective theory of dark matter-nucleon interactions.

5.3. Discussion and Summary

In this chapter, we have extended the method presented in chapter 4 that allows to check whether a putative dark matter signal at a direct detection experiment is compatible with the null results from other experiments. The extended method addresses simultaneously the particle physics uncertainties on the concrete form of the dark matter-nucleon interaction as well as the astrophysical uncertainties on the local dark matter density and velocity distribution. For the former, we consider an arbitrarily large set of operators inducing scattering, which possibly interfere with each other. The method then allows to study whether that set of operators is capable of reproducing all experimental results for a given velocity distribution. For the latter, we determined analytically, using the results of chapter 4, a parametrization of the velocity distribution that yields the largest scattering rate compatible with the null results from other experiments. We found that it is parametrized by a superposition of streams which allows us to obtain the optimal velocity distribution by scanning over a small number of parameters.

We illustrated our method by confronting the dark matter interpretation of the CDMS-Si excess to the null results of XENON1T-2017 and PICO-60. We found that it is not possible to explain this excess in terms of the spin-independent interaction, even when allowing for isovector and/or long-range interactions and regardless of the velocity distribution. When allowing for a larger set of operators that induce scattering of dark matter with nuclei, the constraints from null results of other experiments get relaxed. For general spin-0, spin-1/2 or spin-1 dark matter, we found configurations of the velocity distribution and the dark matter-nucleon interactions that reconcile the experiments. However, the next generation of dark matter experiments will either confirm the CDMS-Si excess or rule it out in a halo-independent way regardless of the concrete form of the dark matter-nucleon interaction.

Chapter 6.

An improved method to asses the impact of astrophysical uncertainties on direct dark matter searches

The content of this chapter was published in [4]. In the following, we explicitly indicate additional information that was not published.

As already mentioned in section 4.3, the method presented in chapter 4 has two shortcomings. First, it is not possible to derive solid statistical conclusions. For a long time, it was not possible to perform a halo-independent analysis in a statistically solid framework, see Refs. [269–280, 282, 283, 285, 287, 291, 293]. Recently, there has been interest in resolving this issue, leading to a series of works [284, 286, 289] that discuss how to extract the best fit velocity integral $\eta(v_{\min}) = \int_{v_{\min}} \mathrm{d}v^3 \, f(v)/v$ from the results of direct detection experiments. Furthermore, several approaches were introduced to perform analyses independent of astrophysical assumptions with a well defined statistical meaning. With the methods proposed in Refs. [281, 290, 292, 307–309], it is possible to extract parameters of a velocity distributions in a statistically rigorous way. Another application [288] is the extraction of the time-independent dark matter signal at DAMA compatible with the annual modulation signal. Furthermore, Refs. [301, 310, 311] showed that information about the dark matter mass can be inferred from a signal at a direct detection experiment without assumptions on the velocity distribution.

Second, with the method presented in the previous chapter it is only possible to perform a fully halo-independent analysis which leads to a velocity distribution consisting of a finite number of streams. Those extremely fine tuned solutions are the mathematically optimal velocity distributions, however it is unlikely to find such contrived distributions in nature. In fact, there are several hints that there is a significant smooth contribution to the velocity distribution. Among those are the results of chapter 8 as well as the findings of numerical simulations [92, 312–320] and attempts to reconstruct the local dark matter velocity distribution [100–104, 143, 321, 322]. Therefore, it is more realistic to optimize perturbations on top of a smooth distribution. However, halo-independent analyses are a valuable tool to asses the worst case scenario.

In this chapter, we extend the method derived in the previous chapter to do both, taking into account deviations from reference distributions as well as deriving statistically rigorous results. We start by defining a measure of the distances between functions in

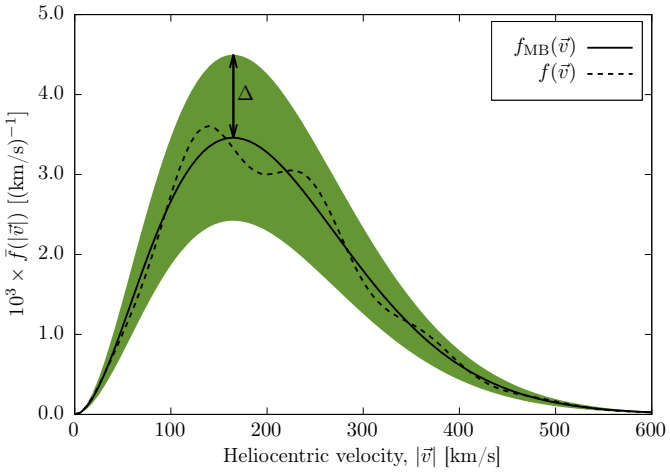

Figure 14.: Sketch of the constraint $\mathrm{D}_{f|f_{\rm MB}}(\vec{v}) \leq \Delta$. We denote the reference velocity distribution $f_{\rm MB}(\vec{v})$ with a black solid line while we show an example of the velocity distribution $f(\vec{v})$ as black dashed line. Furthermore, we show the band around the reference velocity distribution for which the distance is smaller than Δ in dark green.

order to quantify deviation from a reference velocity distribution by a number Δ. We then reformulate the optimization problems from the previous chapter in order to capture the correct statistical treatment of the experiments under consideration. Finally, we minimize the appropriate p-value respectively likelihood subject to the constraint that the velocity distribution deviates at most a factor Δ from the reference distribution. By adjusting this parameter, we are able to smoothly interpolate between fixing the velocity distribution to the reference distribution and a fully halo-independent analysis.

6.1. Optimization with constraints on the velocity distribution

In the following, we investigate how the conclusions drawn from direct dark matter searches change if we take into account deviations from the SHM velocity distribution. Therefore, we define the distance of the velocity distribution $f(\vec{v})$ to the reference distribution $f_{\rm MB}(\vec{v})$ as

$$\mathrm{D}_{f|f_{\rm MB}}(\vec{v}) = \left| \frac{f(\vec{v}) - f_{\rm MB}(\vec{v})}{f_{\rm MB}(\vec{v})} \right| , \tag{6.1}$$

where the parameter Δ parametrizes the deviation and $f(\vec{v})$ as well as $f_{\rm MB}(\vec{v})$ are non-negative. In the following, we assume that $f_{\rm MB}(\vec{v})$ is a Maxwell-Boltzmann distribution as for the SHM. The difference between $f(\vec{v})$ and the reference velocity distribution $f_{\rm MB}(\vec{v})$ is at most Δ if

$$\mathrm{D}_{f|f_{\rm MB}}(\vec{v}) \leq \Delta \quad \forall\, \vec{v}\,. \tag{6.2}$$

We sketch this constraint in Fig. 14 where we show in dark green the band around the reference velocity for which the distance is smaller than Δ. As apparent from Eq. (6.1), the velocity distribution is allowed to vanish in parts of the velocity space if $\Delta \geq 1$. If $\Delta < 1$, the velocity distribution is non-vanishing over the whole range of velocities. With this, we bracket the uncertainties due to the velocity distribution. For a given Δ, we calculate the most conservative as well as the most aggressive outcome. We then conclude that all velocity distributions that differ at most by a factor Δ from the reference distribution give rise to results bounded by these upper and lower limits.

Here, we assume that the experiments are described by the p-value derived from the cumulative Poisson probability distribution P_{Poisson}. Given the observed number of signal events N_{obs} as well as the number of background events N_{BG}, the p-value is given by

$$p_{\text{tot}}(N_{\text{sig}}) = P_{\text{Poisson}}(k \leq N_{\text{obs}} | N_{\text{sig}} + N_{\text{BG}}) \,, \tag{6.3}$$

where N_{sig} is the number of events expected from a given dark matter model. We then optimize the p-value requiring that the velocity distribution is normalized, non-negative and deviates at most Δ from the reference velocity distribution. The corresponding optimization problem in standard form reads

$$\begin{aligned} \text{Optimize:} \quad & \log p\,(m_{\text{DM}}, \sigma) \\ \text{Subject to:} \quad & \left| \frac{f(\vec{v}) - f_{\text{MB}}(\vec{v})}{f_{\text{MB}}(\vec{v})} \right| \leq \Delta \\ & \int \mathrm{d}^3 v \, f(\vec{v}) = 1 \\ & -f(\vec{v}) \leq 0 \,. \end{aligned} \tag{6.4}$$

With this, we determine the most conservative outcome from

$$\max_{f(\vec{v})} \{\log p_{\text{tot}}\}\,(m_{\text{DM}}, \sigma) \geq \log(1-\alpha) \,, \tag{6.5}$$

and the best possible outcome from

$$\min_{f(\vec{v})} \{\log p_{\text{tot}}\}\,(m_{\text{DM}}, \sigma) \geq \log(1-\alpha) \,. \tag{6.6}$$

Here, α is the confidence level which we set to 90% in the following. In order to perform this computation, we decompose the velocity distribution into a set of streams as defined in Eq. (4.5). For this particular analysis, we discretize the velocity space into 3000 streams in the interval $[0, v_{\text{max}}]$. Here, v_{max} is the largest possible velocity of a dark matter particle in the rest frame of the detector which we calculate from the escape velocity from the Milky Way $v_{\text{esc}} = 544\,\text{km/s}$ [116]. With this decomposition, the optimization problem

reads

$$\begin{aligned} \text{Optimize:} \quad & \log p\left(\{c_{\vec{v}_i}\}, m_{\mathrm{DM}}, \sigma\right) \\ \text{Subject to:} \quad & c_{\vec{v}_i} \leq (\Delta+1) f_{\mathrm{MB}}(\vec{v}_i) \quad \forall\, i \\ & c_{\vec{v}_i} \geq \max\Big\{0, (1-\Delta)\Big\} f_{\mathrm{MB}}(\vec{v}_i) \quad \forall\, i \\ & \sum_i c_{\vec{v}_i} = 1\,. \end{aligned} \tag{6.7}$$

We note that this formalism is completely general and does not rely on the statistical method used to describe the experiments under consideration. However, it is very hard, sometimes even impossible, to solve this problem with standard techniques like Monte Carlo methods for a large number of variables $c_{\vec{v}_i}$ as required for the accurate modeling of a function. In the case that the objective function is at most quadratic and convex, one can apply the methods of convex optimization which are summarized in appendix B. Those algorithms quickly solve those problems even for large number of streams, which allows to tackle even problems for which the velocity distribution is described in three dimensions. Here, we use the interior-point algorithms provided by the `CVXOPT` [300, 323] package to efficiently solve the optimization problems discussed in this chapter.

In addition to the astrophysical uncertainties due to the shape of the velocity distribution, there are several other sources of uncertainties. A major astrophysical uncertainty stems from the local dark matter density as discussed in section 2.2.1. As it enters linearly into the computation of the expected signals in direct dark matter searches, a deviation from the canonical value of 0.3 GeV/cm^3 leads to a rescaling of the signal. As in chapter 4, we highlight this by multiplying our results with the factor $\rho_{\mathrm{loc},\,0.3} \equiv \rho_{\mathrm{loc}}/(0.3\ \mathrm{GeV/cm^3})$. In addition to this, we take into account the uncertainties of the reference velocity distribution when determining the best and the worst possible outcome. Concretely, we assume the SHM velocity distribution, confer Eq. (2.17), described by the velocity of the Sun $v_\odot$ with respect to the galaxy and the escape velocity from the Milky Way v_{esc}. We vary those parameters in the range 220-240 km/s [324,325] in the case of $v_\odot$ as well as between 499 km/s and 608 km/s for v_{esc} [116]. We note that when building specific models for the Milky Way, the parameters $v_\odot, v_{\mathrm{esc}}$ and ρ_{loc} are correlated, confer Ref. [268]. However, we stay agnostic about specific Milky Way models and vary the parameters individually in their corresponding ranges as this leads to conservative results. Finally, when analyzing results from direct detection experiments, we take into account the time-dependent velocity of the Earth with respect to the Sun. When solving the optimization problem in Eq. (6.7), we use the point in time that results in the largest maximum respectively the smallest minimum of the objective function.

6.2. Applications

As demonstrated in the remainder of this chapter, many problems related to local dark matter searches can be expressed or well approximated by quadratic functions and therefore be solved efficiently. To this end, we apply our improved formalism to the following

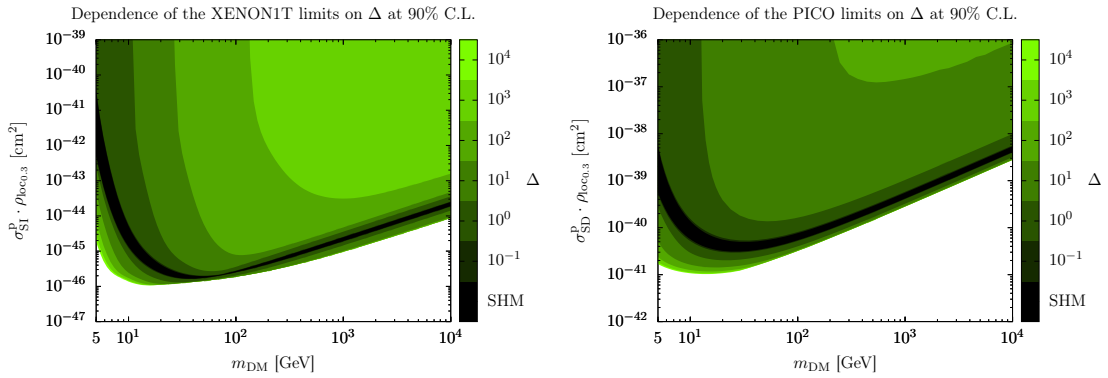

Figure 15.: Most conservative and most aggressive 90% C.L. upper limits for the null results of XENON1T-2017 (left) and PICO-60 (right) assuming spin-independent (left) respectively spin-dependent interactions (right). In both plots, we highlight the impact of deviations from the SHM by including upper limits for various choices of Δ between 0 and 10^4. These plots were taken from Ref. [4].

problems. First, we bracket the impact of uncertainties in the velocity distribution on upper limits from direct detection experiments, neutrino telescopes as well as combined limits using both. Furthermore, we investigate how astrophysical uncertainties affect the reconstruction of dark matter parameters from a putative signal. With this, we are able to find the allowed region in parameter space as a function of Δ.

6.2.1. Impact on limits from direct detection experiments

We start by deriving the most conservative and most aggressive upper limits on the interaction cross section between dark matter and nuclei. Concretely, we use the null results from the XENON1T experiment as published in 2017 [220] (which we denote by XENON1T-2017 in the following) for spin-independent interactions as well as the results from PICO-60 [237] for spin-dependent interactions. As the number of observed events is in both cases zero, we write the p-value for N_{sig} predicted events given an expected background of N_{BG} as

$$\log(p) = -(N_{\mathrm{BG}} + N_{\mathrm{sig}})\,, \tag{6.8}$$

where we neglect uncertainties of the background. In the specific case of XENON1T-2017 and PICO-60, the background is given by $N_{\mathrm{BG}} = 0.36$ respectively $N_{\mathrm{BG}} = 0.331$. In order to calculate the expected dark matter signal, we use the efficiency to detect nuclear recoils from [326, 327] in the case of XENON1T-2017 and from [236] for PICO-60. For further details on those experiments, we refer to appendix C.

In Fig. 15, we show the most conservative as well as the most aggressive upper limits for several values of Δ between 0 and 10^4. We note that neither the most aggressive nor the most conservative upper limit changes for $\Delta > 10^4$. In all cases, we vary the velocity of the Sun in the galactic rest frame $v_\odot$ and the escape velocity from the Milky Way v_{esc}

within 220-240 km/s respectively 499-608 km/s. When allowing the velocity distribution to vary freely, i.e. for very large Δ, we find that the most conservative upper limits vanish. This is to be expected from the results presented in section 4.2 and the optimized velocity distribution corresponds to one stream placed below the detection threshold of the experiment. Furthermore, we find that the impact of astrophysical uncertainties is strongest for small dark matter masses as only fast dark matter particles are able to cause detectable recoils in this case. Due to this, even small changes in the high velocity tail of the distribution can degrade the most conservative exclusion limits significantly for light dark matter particles. For the most aggressive upper limit, we find that the exclusion strength increases by at most an order of magnitude compared to the most stringent SHM limit. This is due to the fact that the most probable speed of the SHM is close to the velocity that leads to the largest scattering rate at direct detection experiments for the dark matter masses considered here. Specifically for the upper limits derived from XENON1T-2017, we find that the most aggressive, halo-independent upper limit is only marginally stronger than the limit derived from the SHM for $m_{\mathrm{DM}} \simeq 100$ GeV. The reason for this is that the mean velocity of the SHM and the velocity of the optimal stream coincide for those dark matter masses. For lighter or heavier dark matter particles, both velocities differ notably and the upper limits can be strengthened by approximately an order of magnitude again.

With our method, it is also possible to obtain the optimized velocity distributions. Extending the content published in Ref. [4], we depict the most conservative and the most aggressive upper limits for XENON1T-2017 in Fig. 16. In both plots, we show the optimized distributions for the same values of Δ that were used in Fig. 15. As discussed in Ref. [4], it is also possible to determine the optimal velocity distribution for the most aggressive upper limit analytically

$$\begin{aligned} f_{\mathrm{R}_{\mathrm{max}}}(v) =& f_{\mathrm{MB}}(v) \Big[(1+\Delta)\Theta(v-v_1)\Theta(v_2-v) \\ &+ (1-\Delta)\Theta(1-\Delta)\Big(1-\Theta(v-v_2)\Theta(v_1-v)\Big)\Big] . \end{aligned} \tag{6.9}$$

Here, the velocities v_1 and v_2 with $v_1 < v_2$ can be calculated for a given dark matter mass and Δ. We find that the high and low velocity tails of the optimized distribution are depleted while the number of dark matter particles with $v_1 < v < v_2$ is increased with respect to the SHM. This is also apparent from the right plot of Fig. 16. We furthermore observe that the support of the function $f_{\mathrm{R}_{\mathrm{max}}}(v)$ decreases as we are able to rewrite the normalization condition $\int \mathrm{d}v\, f_{\mathrm{R}_{\mathrm{max}}}(v) = 1$ into

$$\int_{v_1}^{v_2} \mathrm{d}v\, f_{\mathrm{MB}}(v) \simeq \frac{1}{\Delta} , \tag{6.10}$$

for $\Delta \geq 1$. For very large Δ, the support goes to zero and the optimized velocity distribution finally becomes a stream with a velocity such that the recoil rate is maximized. This is to be expected from the results of section 4.2 as the constraint on the velocity distribution from Eq. (6.1) becomes irrelevant for $\Delta \to \infty$.

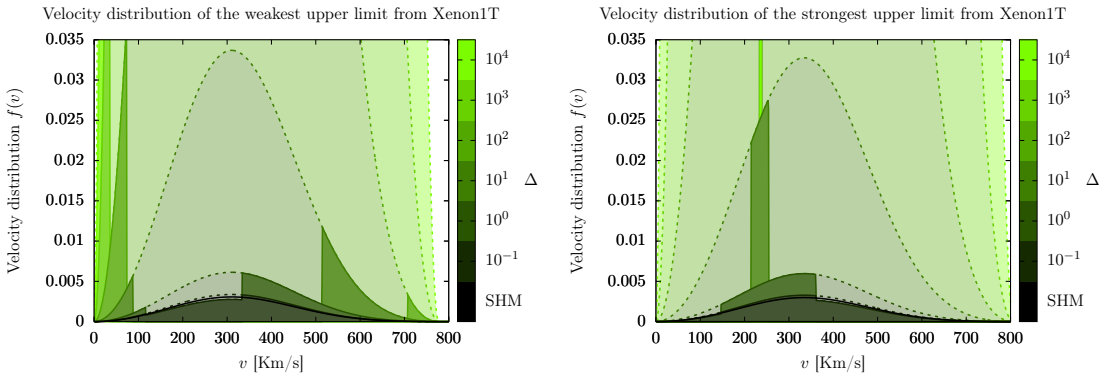

Figure 16.: Optimized velocity distributions for the most conservative (left) and most aggressive (right) upper limits derived from XENON1T-2017 for a dark matter mass of 100 GeV. We indicate the possible deviations from the SHM as light colored regions for each value of Δ. Furthermore, we show the optimized velocity distributions as dark shaded region. In both plots, we depict the optimized velocity distributions for the same values of Δ as in Fig. 15.

In contrast to the most aggressive upper limits, the most conservative upper limits deviate significantly from the SHM and even vanish for $\Delta \to \infty$. The velocity distribution that gives the weakest upper limit reads

$$f_{\mathrm{R}_{\mathrm{min}}}(v) = f_{\mathrm{MB}}(v)\Big[(1+\Delta)\Big(\Theta(v_1' - v) + \Theta(v - v_2')\Big) + (1-\Delta)\Theta(1-\Delta)\Big(\Theta(v - v_1') + \Theta(v_2' - v) - 1\Big)\Big]\,, \tag{6.11}$$

where the velocities of the streams v_1', v_2' are labeled such that $v_1' < v_2'$. As for the most aggressive upper limits, those velocities can be calculated given the dark matter mass and Δ. The features of this solution are opposite to those in Eq. (6.9). The low and high velocity tails are more populated than for the SHM while the number of particles with velocities $v_1' < v < v_2'$ is decreased. This gives rise to the smallest signal as direct detection experiments are most sensitive between v_1' and v_2'. The normalization condition for $\Delta \gg 1$ reads

$$\int_0^{v_1'} \mathrm{d}v f_{\mathrm{MB}} + \int_{v_2'}^{v_{\mathrm{max}}} \mathrm{d}v f_{\mathrm{MB}} \simeq \frac{1}{\Delta}\,, \tag{6.12}$$

which again implies that the support of $f_{\mathrm{R}_{\mathrm{min}}}(v)$ decreases as $\Delta \to \infty$. Therefore, the solution converges to streams when $\Delta \to \infty$. In this limit, we furthermore find that v_2' exceeds the escape velocity while $v_1' \to 0$. This implies that the optimized velocity distribution consists of one stream below the threshold of the experiment. Therefore, the dark matter-nucleon scattering cross section is unconstrained for large values of Δ. As a result, we find that the most conservative upper limit can vary between the upper limit derived from the SHM and being completely unconstrained.

6.2.2. Impact on limits from neutrino telescopes

In this section, we illustrate the impact of astrophysical uncertainties on the upper limits derived from neutrino telescopes. We use the 3 year data sample of the neutrino flux at IceCube from the direction of the Sun reported in Ref. [250]. It consists of the DeepCore (DC) and the IceCube (IC) sample which we use for dark matter masses below respectively above 100 GeV. Those samples are given in several bins of the angle Ψ which is defined as the angle between the reconstructed track of the event and the direction of the Sun. As the uncertainties of the direction reconstruction increase for small energies, we take into account all seven angular bins for the analysis of the low energy DC sample. Conversely, we use the three bins with the smallest angles Ψ from the direction of the Sun for the IC sample.

We construct the p-value by modeling IceCube as a counting experiment with a single bin both for the DC and the IC sample. We take into account background uncertainties by summing those in quadrature for each bin in Ψ and then taking the 1σ downward fluctuation of the background. The number of observed events and the expected number of background events are then

$$\begin{aligned} \text{DeepCore (7 bins):} \qquad & N_{\text{obs}} = 427 \qquad N_{\text{BG}}(-1\sigma) = 414\,, \\ \text{IceCube (3 bins):} \qquad & N_{\text{obs}} = 926 \qquad N_{\text{BG}}(-1\sigma) = 931\,. \end{aligned} \tag{6.13}$$

We obtain the p-value with the cumulative Poisson probability distribution

$$p_A(N_{\text{sig}}) = P(k \leq N_{\text{obs}} | N_{\text{BG}} + N_{\text{sig}})\,, \tag{6.14}$$

where $A = \text{DC}, \text{IC}$. For a confidence level of 90%, we obtain an upper limit on the number of signal events of $N_{\text{sig}}^{90\%} = 35.0$ for IceCube and $N_{\text{sig}}^{90\%} = 39.9$ for DeepCore, which is in good agreement with the upper limits reported in [250]. With this, we set conservative upper limits on the dark matter-nucleon cross section without the need for an event-by-event likelihood. We note that a counts based analysis of IceCube leads to stronger limits for small dark matter masses and weaker limits for heavy dark matter in comparison to a likelihood based analysis, see Ref. [328]. As we are interested in at most quadratic objective functions, we approximate the logarithm of the p-value with second order polynomials. Concretely, we use the following polynomials

$$\begin{aligned} \log(p_{\text{DC}}) &= -0.319 - 0.0155\, N_{\text{sig}} - 0.0008\, N_{\text{sig}}^2\,, \\ \log(p_{\text{IC}}) &= -0.823 - 0.0276\, N_{\text{sig}} - 0.0004\, N_{\text{sig}}^2\,. \end{aligned} \tag{6.15}$$

We find that those fitting functions deviate at most 10% from the full p-value for $N_{\text{sig}} \in [0, 10]$, decreasing to 1% for $N_{\text{sig}} \in [10, 100]$. Finally, we relate the number of signal events and the capture rate following Ref. [250] in order to stay as close to the full analysis of the IceCube collaboration as possible. We note that Ref. [250] explicitly assumes equilibrium of capture and annihilation which is expected for the currently probed scattering cross sections. However, Fig. 9 suggests that this should be taken into account for future results

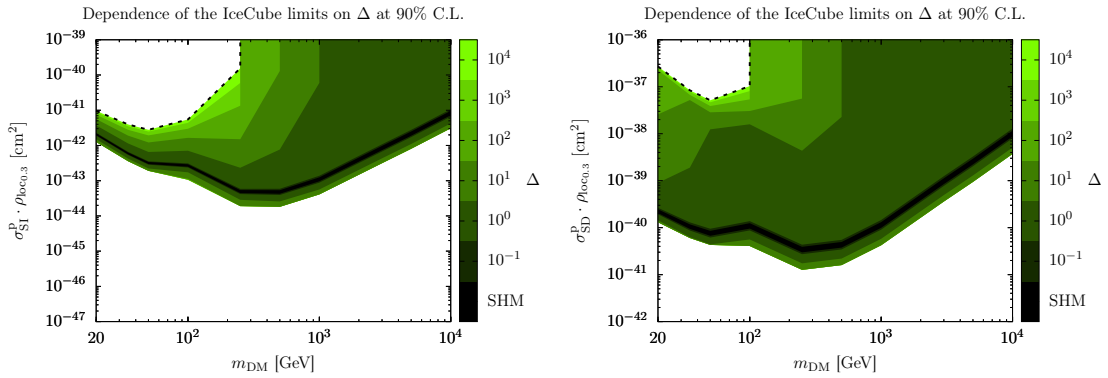

Figure 17.: Most conservative and most aggressive upper limits from neutrino telescopes for spin-independent (left) as well as spin-dependent interactions (right). Here, we assume annihilation into W^+W^- ($\tau^+\tau^-$ for $m_{\mathrm{DM}} < m_W$). In both plots, we show the most aggressive and most conservative upper limits for several choices of the parameter Δ that quantifies the deviation from the SHM. These plots were taken from Ref. [4].

of IceCube.

In Fig. 17, we show the 90% C.L. upper limits on the spin-independent and spin-dependent scattering cross sections derived from the null results of IceCube assuming annihilation into W^+W^- ($\tau^+\tau^-$ for $m_{\mathrm{DM}} < m_W$). We indicate the impact of astrophysical uncertainties by considering deviations of the SHM between $\Delta = 0$ (SHM limits) and $\Delta = 10^4$ (halo-independent limits), where we again observe that the limits do not change for $\Delta > 10^4$. We find that the most aggressive upper limits are at most an order of magnitude stronger than the limits derived from the SHM. In concordance with the results from chapter 4, the most conservative upper limits remain finite for $\Delta \to \infty$ assuming dark matter particles lighter than 250 GeV for spin-independent interactions respectively 100 GeV for spin-dependent interactions. For heavy dark matter, the most conservative upper limits vanish for large Δ. As the maximal velocity for which capture in the Sun is possible is small in this case, no dark matter particles can be captured for a velocity distribution that predicts only fast particles. This, in turn, implies vanishing most conservative upper limits on the interaction cross section from IceCube.

The optimized velocity distribution that leads to the most aggressive upper limits on the scattering cross section can be parametrized as

$$f_{C_{\mathrm{max}}}(v) = f_{\mathrm{MB}}(v)\Big[(1+\Delta)\Theta(v_1 - v) + (1-\Delta)\Theta(1-\Delta)\Theta(v - v_1)\Big]\,, \tag{6.16}$$

where we are able to calculate the velocity v_1 given Δ and the dark matter mass. In addition to the content published in Ref. [4], we show those optimized distributions in the right plot of Fig. 18 for spin-independent interactions. The shape of these velocity distributions is a consequence of the fact that the capture rate decreases monotonically with increasing velocity of the stream. Therefore, the capture rate is maximized when the low velocity tail is as populated as possible which is depicted in the right plot of Fig. 18.

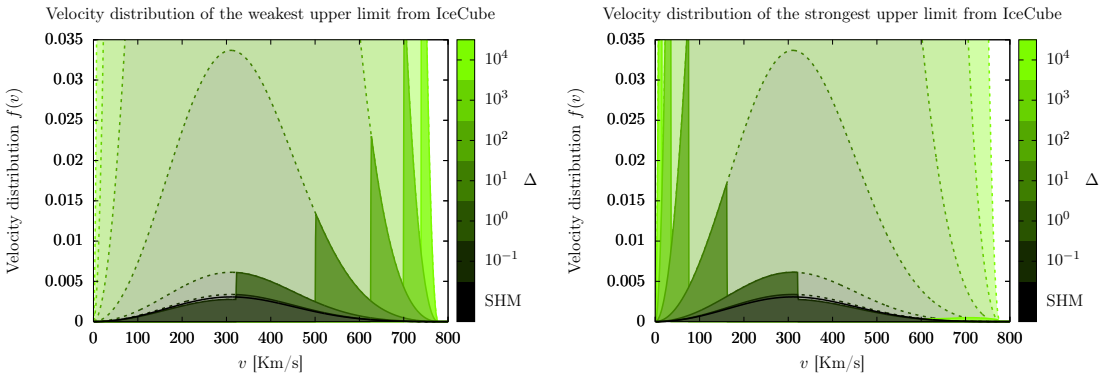

Figure 18.: Optimized velocity distributions for the most conservative (left) and the most aggressive upper limits (right) on the scattering cross section for a dark matter mass of 100 GeV. We derive those distributions from the null results of IceCube assuming spin-independent interactions. For each value of Δ, we indicate the largest possible deviations from the SHM as light colored regions. Furthermore, we highlight the optimized velocity distributions as dark shaded region. In both plots, we depict the optimized velocity distributions for the same values of Δ as in Fig. 17.

With this observation, we are able to calculate the velocity v_1 from the normalization condition, which can be rearranged into

$$\int_0^{v_1} f_{\rm MB}(v)\,\mathrm{d}v = \frac{1-(1-\Delta)\Theta(1-\Delta)}{1+\Delta-(1-\Delta)\Theta(1-\Delta)}\,. \tag{6.17}$$

When Δ increases, the value of v_1 decreases as $f_{\rm MB}(v)$ is a non-negative function. Therefore, $f_{C_{\rm max}}(v)$ converges to a δ-function at $v=0$ for large Δ which is in concordance with the findings in section 4.2.

On the other hand, the optimized velocity distribution leading to the most conservative upper limit reads

$$f_{C_{\rm min}}(v) = f_{\rm MB}(v)\Big[(1+\Delta)\Theta(v-v_1') + (1-\Delta)\Theta(1-\Delta)\Theta(v_1'-v)\Big]\,, \tag{6.18}$$

which maximally populates the high velocity tail as the capture rate decreases monotonically with increasing velocity of the stream. This is shown in the left plot of Fig. 18 for the specific case of spin-independent interactions. Again, we are able to calculate v' from the normalization condition

$$\int_{v_1'}^{v_{\rm esc}} f_{\rm MB}(v)\,\mathrm{d}v = \frac{1-(1-\Delta)\Theta(1-\Delta)}{1+\Delta-(1-\Delta)\Theta(1-\Delta)}\,. \tag{6.19}$$

Increasing the deviation from the SHM, the velocity v_1' increases as the right side of the equation is proportional to Δ^{-1} for large deviations. In the limit $\Delta\to\infty$, we obtain a δ-function at $v=v_{\rm esc}$ as expected from the results of the halo-independent analysis presented in section 4.2. For heavy dark matter, this leads to vanishing most conservative upper limits as the maximal velocity for which capture is kinematically possible in the

Sun decreases with the dark matter mass, confer Eq. (3.52).

6.2.3. Impact on limits from direct detection experiments and neutrino telescopes

Several works highlighted the complementarity of direct detection experiments and neutrino telescopes for constraining the dark matter-nucleon cross section, see Refs. [2, 4, 98, 285, 301, 302] and section 4.2 for a discussion of this in terms of a halo-independent analysis. Here, the complementarity is evident from the optimized velocity distributions shown in Figs. 16 and 18. For the most conservative upper limit and for $\Delta \to \infty$, we find $f_{\mathrm{R}_{\min}}(v) = \delta(v)$ for direct detection experiments while $f_{C_{\min}}(v) = \delta(v - v_{\mathrm{esc}})$ for neutrino telescopes. Conversely, the velocity distributions for the most aggressive upper limit converge to $f_{\mathrm{R}_{\max}}(v) = \delta(v - v_1)$ with $v_1 > 0$ for direct detection experiments and to $f_{C_{\max}}(v) = \delta(v)$ for neutrino telescopes. Given the completely different features for both detection techniques, we expect that the optimized distributions for the combined upper limits are non-trivial unless one detection technique is far more sensitive than the other. But even in this case, the fact that direct detection experiments and neutrino telescopes probe together the whole velocity space is enough to prevent that upper limits vanish in the limit $\Delta \to \infty$.

We obtain the most conservative and the most aggressive limits following Eq. (6.7). The total p-value for different experiments is given by

$$\log p_{\mathrm{tot}} = \sum_{k \in \mathrm{expts}} \log p_k \,, \tag{6.20}$$

where each individual contribution $\log p_k$ is at most quadratic in the recoil rate or the capture rate. We then apply the techniques described in section 6.1 to solve the optimization problem.

In Fig. 19, we show the most conservative and the most aggressive upper limits on the spin-independent respectively on the spin-dependent scattering cross section as a function of Δ. For the former, we use the null results from XENON1T-2017 [220] and IceCube [250] while for the latter we combine PICO-60 [237] and IceCube. In both cases, we use the IC and the DC sample to construct the p-value for IceCube as outlined in section 6.1. As for direct detection experiments and neutrino telescopes individually, the most aggressive upper limits are at most an order of magnitude stronger than the upper limits derived from the SHM. Remarkably, the most conservative upper limits are also not too different to the limits derived from the SHM. For spin-independent interactions, the upper limits are bounded over the whole mass range considered here even in the limit $\Delta \to \infty$. This is also true for spin-dependent interactions but only for dark matter masses smaller than 3 TeV. For heavier dark matter, the maximal velocity for which capture in the Sun is possible, confer Eq. (3.52), is smaller than the minimal velocity that is necessary to induce a detectable recoil at PICO-60. Therefore, a velocity distribution that is non-zero only in this gap evades constraints from IceCube and from PICO-60 simultaneously. Due to this, it is not possible to derive a most conservative upper limit in this specific case. However,

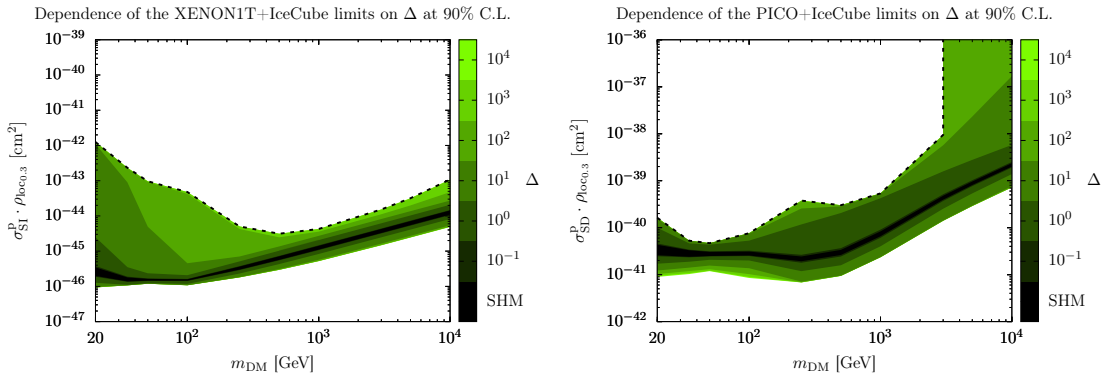

Figure 19.: Most conservative and most aggressive upper limits assuming spin-independent (left) respectively spin-dependent interactions (right). We combine the null results from IceCube and XENON1T-2017 for spin-independent interactions respectively IceCube and PICO-60 for spin-dependent interactions. In both plots, we show the most aggressive and the most conservative limit for several choices of the parameter Δ that quantifies the deviation from the SHM. Here, we explicitly assume annihilation into W^+W^- ($\tau^+\tau^-$ for $m_{\mathrm{DM}} < m_W$). These plots were taken from Ref. [4].

we note that the limits for $\Delta \to \infty$ can be significantly weaker than the SHM limits if one experiment is much more sensitive to the interaction under investigation.

Extending the content published in Ref. [4], we depict the optimized velocity distributions for the combined limits from direct detection experiments and neutrino telescopes in Fig. 20. Here, we study the specific case of WIMPs with a mass of 100 GeV and constraints on the spin-independent scattering cross section from XENON1T-2017 and IceCube. Comparing this to Fig. 15, we observe that the optimized distributions are very similar to those that give the most aggressive respectively the most conservative limit at XENON1T-2017. This is to be expected as direct detection experiments are more sensitive to spin-independent interactions than neutrino telescopes. However, the most conservative upper limits do not vanish in the limit $\Delta \to \infty$ as IceCube is sensitive to this region. Due to the complementarity of direct detection experiments and neutrino telescopes, the velocity distribution that minimizes the recoil rate leads to a large capture rate. This is also apparent from the comparison of Figs. 15, 17 and 19 as the most conservative combined upper limit for $m_{\mathrm{DM}} = 100$ GeV is several orders of magnitude weaker than the upper limit derived from XENON1T-2017 but still stronger than the upper limit from IceCube. For the most aggressive limit, the optimized velocity distribution maximizes the signal at XENON1T-2017. Since IceCube is also sensitive to this region in velocity space, the combined limits are stronger than those derived from XENON1T-2017 alone, compare Fig. 15 and Fig. 19.

6.2.4. Parameter reconstruction for general velocity distributions

In the following, we study the impact of astrophysical uncertainties on the reconstruction of dark matter properties in case of a future signal. Henceforth, we consider the

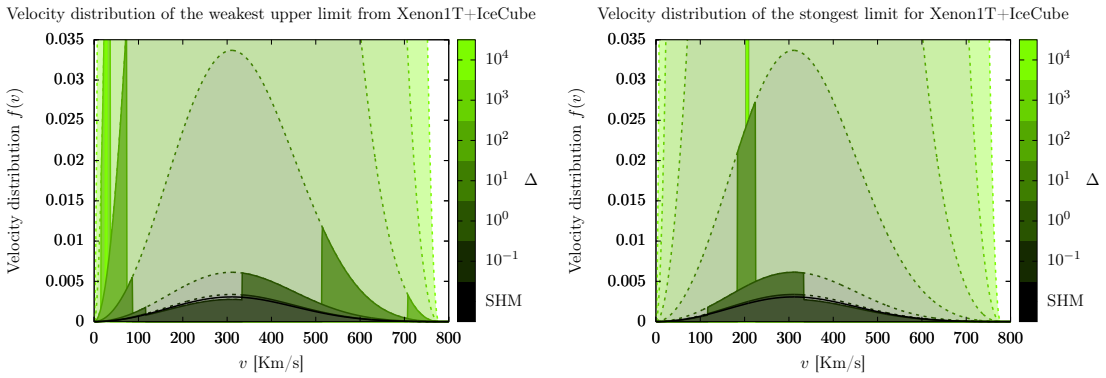

Figure 20.: Optimized velocity distributions for the most conservative (left) and the most aggressive upper limits (right) on the scattering cross section for a dark matter mass of 100 GeV. We assume spin-independent interactions and the null results of XENON1T-2017 as well as IceCube. Furthermore, we indicate the largest possible deviations from the SHM as light colored regions for each value of Δ. We highlight the optimized velocity distributions as dark shaded region. In both plots, we depict the optimized velocity distributions for the same values of Δ as in Fig. 19.

XENON1T detector and construct an approximate likelihood for a total exposure of 730 days. We assume that the current target mass of 1042 kg stays constant over two years of exposure and we assume that the detector is sensitive to nuclear recoil energies between 3 keV and 70 keV. We conservatively assume that the detector does not undergo a major upgrade and that the nuclear recoil detection efficiency is given by [326, 327] over the whole exposure time. In order to reconstruct dark matter properties from a number of counts, we introduce $N_{\text{bins}} = 4$ bins which we define in such a way that each bin contains at least 5 events for a given dark matter mass and scattering cross section. We estimate that the uncertainty in the signal rate in each bin is given by $\sigma_i = \sqrt{N_{\text{obs}}^{(i)}}$. Note that we do not include backgrounds or systematic uncertainties here as we do not have access to the relevant information. In case of a signal, those information could be provided by the experimental collaboration which would allow us to include those uncertainties. Here, we describe XENON1T by an approximate Gaussian likelihood

$$\log \mathcal{L}_{\text{Xe}} = -\frac{1}{2} \sum_{i}^{N_{\text{bins}}} \frac{\left(N_{\text{sig}}^{(i)} - N_{\text{obs}}^{(i)}\right)^2}{\sigma_i^2}\,, \tag{6.21}$$

where N_{obs} is the observed number of events. Furthermore, N_{sig} is the number of dark matter events for a given velocity distribution $f(\vec{v})$, dark matter mass m_{DM} and scattering cross section σ.

In order to infer the median significance for discovery, we construct the so-called "Asimov data set" [329] by setting $N_{\text{obs}}^{(i)} = N_{\text{sig}}^{(i)}$ for a benchmark dark matter mass and scattering cross section. This procedure is based on the Wald equation [330]. Concretely, we generate the data set for $m_{\text{DM}} = 50$ GeV and $\sigma_{\text{SI}}^{\text{p}} = 1.5 \times 10^{-46}\,\text{cm}^2$ as well as as-

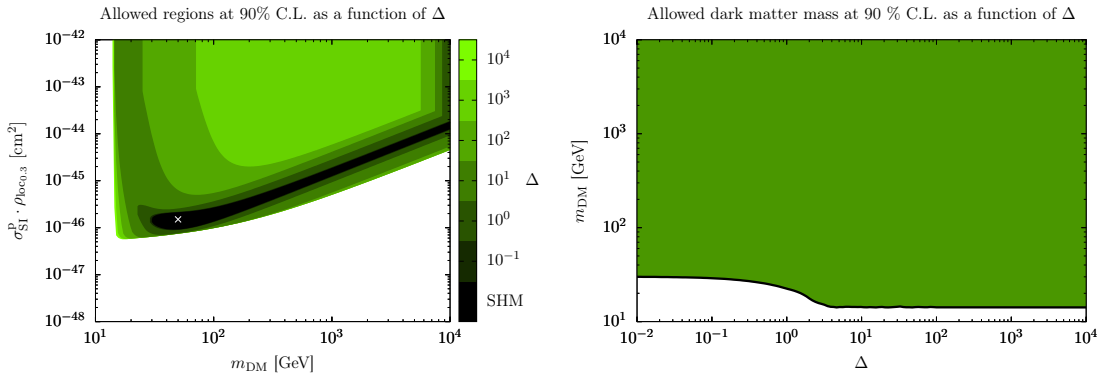

Figure 21.: Reconstruction of a putative signal after two years of XENON1T exposure. The left plot shows the allowed region in the $(m_{\rm DM}, \sigma^{\rm p}_{\rm SI})$ parameter space for various values of Δ. We indicate with a white cross the true dark matter parameters of $m_{\rm DM} = 50$ GeV and $\sigma^{\rm p}_{\rm SI} = 1.5 \times 10^{-46}\,{\rm cm}^2$. Furthermore, the right plot shows the allowed dark matter masses as a function of Δ. These plots were taken from Ref. [4].

suming the SHM. For this specific benchmark point, we expect 34 dark matter events at XENON1T over the final exposure. We note that this approach could be extended to benchmark-free forecasting methods, for example the technique presented in Ref. [211].

As the likelihood in Eq. (6.21) is quadratic in $N_{\rm sig}$, it is at most quadratic in the velocity distribution and can therefore be optimized with the routines of convex optimization. We then maximize the likelihood with respect to the velocity distribution for several choices of Δ. With this, we construct allowed regions in parameter space by profiling over all velocity distributions that deviate by at most Δ from the SHM. The allowed region consists of all points in parameter space $(m_{\rm DM}, \sigma^{\rm p}_{\rm SI})$ that satisfy [329, 331]

$$\max_{f(\vec{v})} \left\{ \log \mathrm{L}(m_{\rm DM}, \sigma^{\rm p}_{\rm SI}) \right\} > \log \mathrm{L}_{\rm max} - \frac{1}{2}\chi^2_{\gamma\%}\,, \tag{6.22}$$

where $\log \mathrm{L}_{\rm max}$ is the maximum of the likelihood over all dark matter masses, scattering cross sections and velocity distributions. Furthermore, $\chi^2_{\gamma\%}$ is the critical χ^2 value for two degrees of freedom. As we are interested in contours with a confidence level of 90%, we set $\chi^2_{\gamma\%} \approx 4.605$.

In the left plot of Fig. 21, we depict the allowed region in parameter space reconstructed from the putative signal. As in the discussions in the previous sections, the allowed region for $\Delta \to \infty$ extends to arbitrary large cross sections but has a finite lower limit. For very large cross sections, the signal can be reproduced by modifying the velocity distribution in such a way that most of the dark matter particles are too slow to be detected by XENON1T. Similar conclusions can also be found in Ref. [310]. In addition to this, the dark matter mass is bounded from below. Regardless of the deviation from the SHM, dark matter particles lighter than 14 GeV cannot reproduce the putative signal. For dark matter masses between 100 GeV and 5000 GeV, XENON1T probes a large part of the relevant velocity space. Therefore, large deviations from the SHM are needed to hide a

significant fraction of the velocity distribution below the threshold as apparent from the right plot of Fig. 21. Concretely, deviations as large as $\Delta \gtrsim 10^3$ are necessary for those dark matter masses in order to make large cross sections compatible with the observed signal.

In the right plot of Fig. 21, we furthermore show the allowed dark matter masses as a function of the distance Δ to the SHM. Assuming the SHM velocity distribution, the putative signal can be reproduced for dark matter masses larger than ~ 25 GeV for some dark matter-nucleus cross section. If the velocity distribution is completely free to vary, the signal can be reproduced for dark matter masses larger than $m_{\mathrm{DM}} \gtrsim 10$ GeV. For smaller dark matter masses, the shape of the signal for a 50 GeV WIMP is sufficiently distinct to any predicted spectrum derived from arbitrary velocity distributions. Especially for light dark matter, the signal at large recoil energies is hard to reproduce even for very large deviations from the SHM.

In the left plot of Fig. 22 we show the allowed region of dark matter masses and interaction cross sections that reproduce the putative signal and do not violate the constraints from IceCube. For this analysis, we describe IceCube by a single bin likelihood

$$\log \mathcal{L}_{\mathrm{IC}} = -\frac{1}{2} \frac{(N_{\mathrm{sig}} + N_{\mathrm{BG}} - N_{\mathrm{obs}})^2}{\sigma^2} \,, \tag{6.23}$$

where we adopt the observed number of events N_{obs}, the background events N_{BG} and uncertainties σ as described in (6.13). We obtain the total likelihood by summing the individual parts, i.e. $\log \mathcal{L}_{\mathrm{Xe}}$ and $\log \mathcal{L}_{\mathrm{IC}}$. The current sensitivity of IceCube is not enough to probe the signal of a dark matter particle with a mass of 50 GeV and a spin-independent scattering cross section of $1.5 \times 10^{-46}\,\mathrm{cm}^2$ assuming the SHM. However, IceCube provides useful constraints as it tests some extreme velocity distributions that are able to reproduce the putative signal. When additionally using the constraints from IceCube, the allowed region is bounded from above for $\sigma_{\mathrm{SI}}^{\mathrm{p}}$ even in the limit $\Delta \to \infty$ as apparent from the left plot of Fig. 22. This is due to the fact that the solutions that reproduce the putative signal for large cross sections predict a large fraction of slow dark matter particles. As the maximal velocity for which capture in the Sun is possible is small for dark matter particles with masses larger than 5 TeV, the spin-independent scattering cross section is not bounded from above for those masses. At intermediate masses between 500 GeV and 5 TeV however, it can be well reconstructed and is constrained to be within roughly a narrow band.

In the right plot of Fig. 22, we show the allowed dark matter masses compatible with the putative signal and the constraints from IceCube. For small deviations from the SHM, i.e. $\Delta \lesssim 0.1$, the dark matter mass is constrained to be between 30 GeV and 300 GeV. For $\mathcal{O}(1)$ distortions however, the dark matter mass range for which the putative signal can be reproduced gradually broadens. When finally imposing no constraints on the velocity distribution, we find that dark matter masses larger than ~ 20 GeV are allowed for some scattering cross section.

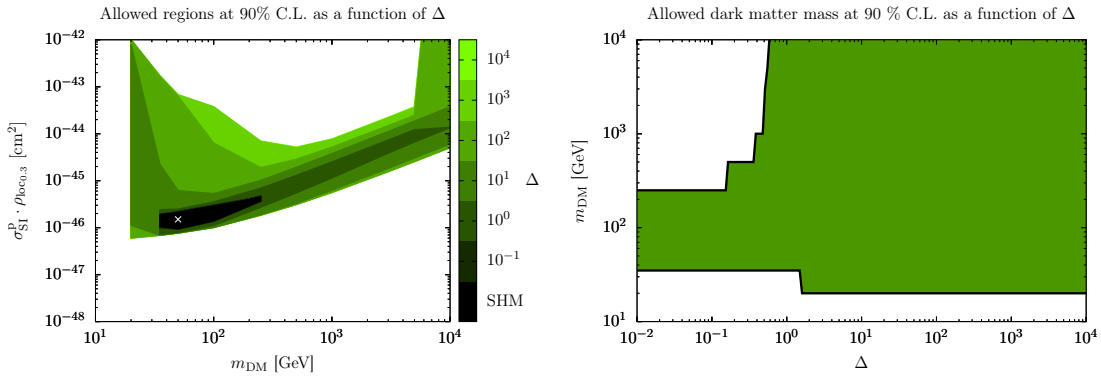

Figure 22.: Reconstruction of a putative signal at XENON1T after two years exposure including constraints from IceCube. In the left plot, we depict the allowed region in the $(m_{\rm DM}, \sigma^{\rm p}_{\rm SI})$ parameter space for various values of Δ. We indicate with a white cross the true dark matter parameters of $m_{\rm DM} = 50$ GeV and $\sigma^{\rm p}_{\rm SI} = 1.5 \times 10^{-46}\,{\rm cm}^2$. The right plot shows the reconstructed range of dark matter masses compatible with the signal at XENON1T and the constraints from IceCube as a function of Δ. These plots were taken from Ref. [4].

6.3. Discussion and summary

In this chapter, we improved the method presented in chapter 4 in order to analyze direct dark matter searches in a statistically rigorous way. Furthermore, the updated method allows us to bracket the astrophysical uncertainties as a function of the distance to some reference velocity distribution and to reduce the bias in the reconstruction of dark matter parameters from a future signal. Concretely, we used the SHM as reference in the analyses presented in this chapter. We parametrized the deviation by a single parameter Δ with values between 0 and ∞. Fixing $\Delta = 0$ corresponds to an analysis in terms of the reference velocity distribution while a large value of Δ gives rise to an analysis that is completely agnostic of the velocity distribution. We recovered the halo-independent method presented in chapter 4 in the limit $\Delta \to \infty$ and concluded that it is contained in the more general method derived in this chapter. Uncertainties of the local dark matter density were included by rescaling the results. As an additional feature, it is possible to extract the optimal velocity distribution of the problem under consideration with the updated method.

As in chapter 4, the approach which was presented in this chapter relies on the decomposition of the velocity distribution into streams. This requires only minimal assumptions on the velocity distribution and can be applied to arbitrary types of analyses. The optimization problems which we encountered here are challenging to solve with standard approaches like Monte Carlo parameter scans due to the large amount of free parameters that were necessary to model the velocity distribution. Instead, we used convex optimization techniques that allow to solve large scale optimization problems efficiently. Concretely, we restricted the types of analyses to convex problems that are at most quadratic in the velocity distribution. As we showed in this chapter, rare event searches

can be modeled or approximated in many cases by such convex optimization problems. In the case of a signal, a likelihood that is at most quadratic in the velocity distribution is justified as soon as the Gaussian limit is approached. If the problem cannot be modeled by a quadratic function, the results of this method can be used as an initial guess for computationally more expensive but exact methods like [301] to determine the dark matter mass.

We illustrated various applications of this method in the previous sections. We bracketed the impact of astrophysical uncertainties on upper limits derived from direct detection experiments respectively neutrino telescopes. Furthermore, we calculated combined upper limits from both experimental techniques, derived in statistically rigorous way. Finally, we reconstructed a putative signal at XENON1T with minimal assumptions on the velocity distribution. For each application, we performed the analyses for deviations from the SHM ranging between $\Delta = 0$ and $\Delta \to \infty$.

From those applications, we derived several key conclusions. For direct detection experiments, the upper limits on the scattering cross section can be improved by at most an order of magnitude when being completely agnostic of the velocity distribution. In contrast to this, we found that the upper limits can be weakened infinitely for $\Delta \to \infty$ by populating only the low velocity tail of the distribution that is inaccessible due to the finite detection threshold of the experiment. Furthermore, we investigated the impact of astrophysical uncertainties on the upper limits derived from the null results of neutrino telescopes. We found that the sensitivity can be improved by a factor $\lesssim 10$ when adjusting the velocity distribution in such a way that the expected neutrino flux from the Sun is maximized. In contrast to the upper limits derived from direct detection experiments, we observed that the most conservative upper limits derived from neutrino telescopes do not vanish for $\Delta \to \infty$ if the dark matter particle is lighter than several hundreds of GeV. In this case, the upper limits are at most a factor of 1000 weaker compared to those derived from the SHM. For heavy dark matter, the maximal velocity that leads to capture in the Sun is smaller than the escape velocity. Therefore, the most conservative upper limit vanishes in this case as the optimized velocity distribution predicts only dark matter particles that are too fast to be captured in the Sun. When combining limits from direct detection experiments and neutrino telescope in a statistically rigorous way, we observed that the upper limits remain finite for all but the largest dark matter masses considered here. Concretely, we found that the most conservative and the most aggressive combined upper limits only differ by less than two orders of magnitude for dark matter masses between 100 GeV and 1 TeV. For very heavy dark matter, the combined upper limits can vanish again as those dark matter particles cannot be captured in the Sun unless they are very slow.

Finally, astrophysical uncertainties play an important role when analyzing a dark matter signal. In the case of a signal in a direct detection experiment, we found that uncertainties in the velocity distribution severely reduce the precision of the reconstruction. In addition to this, the interaction cross section cannot be constrained from above when being completely agnostic of the shape of the velocity distribution. However, including

upper limits from neutrino telescopes in the analysis allowed us to extract an upper bound on the cross section. We furthermore found that the mass of the dark matter particle can be well reconstructed for deviations $\Delta \lesssim 1$ from the SHM and including null results from neutrino telescopes.

Chapter 7.

Analysis of the annual modulation signal measured by DAMA

The content of this section was published in Ref. [2] and we explicitly indicate additional information that was not published. The following discussion is also based on results from Ref. [1].

In contrast to the standard approach of direct detection experiments to measure the total number of recoil events, the DAMA collaboration [22,23,332] searches for the annual modulation of the recoil rate that is due to motion of the Earth around the Sun. The advantage of this approach is that the background is expected to be time-independent which reduces the need for an excellent background reduction. In addition to its uncommon detection technique, DAMA is also unique in the sense that it observes a signal that is in concordance with the expectations from dark matter. Concretely, the DAMA collaboration observed an annual modulation of the recoil rate over 14 years which corresponds to a significance of more than $9\,\sigma$ [22, 23] for a modulation signal. This signal is present in two data sets released in 2013 [22] (DAMA-2013) and 2018 [23] (DAMA-2018).

From Figs. 6 and 7 we observe that the dark matter interpretation of the DAMA signal, assuming the SHM, is in tension with both direct detection experiments and neutrino telescopes for spin-independent as well as spin-dependent interactions. Furthermore, it was shown in Ref. [304] that the same conclusion holds for arbitrary dark matter-nucleon interactions described by the effective theory of Refs. [204–206]. As those conclusions are only valid when assuming the SHM, we analyze in this chapter the annual modulation signal at DAMA with minimal assumptions on the halo model. We do this in two different ways. First, we confront the annual modulation signal to null results from other direct dark matter searches in a halo-independent way. From this analysis, we obtain the regions in parameter space for which the annual modulation signal cannot be explained by dark matter regardless of the velocity distribution. Second, we reconstruct the dark matter mass and scattering cross section from the annual modulation signal in a halo-independent way. Comparing this to the results assuming the SHM allows us to determine the impact of astrophysical uncertainties on the parameter reconstruction from the DAMA data.

7.1. Confronting the DAMA-2013 annual modulation signal to null results

In this section, we confront the annual modulation signal observed by DAMA-2013 [22] to several other experiments for spin-independent and spin-dependent interactions. Concretely, we use the measured annual modulation amplitude in the energy bins [2.0, 2.5], [2.5, 3.0] and [3.0, 3.5] keV of $(1.75 \pm 0.37) \times 10^{-2}$, $(2.51 \pm 0.40) \times 10^{-2}$ and $(2.16 \pm 0.40) \times 10^{-2}$ day^{-1} kg^{-1} keV^{-1} and model the modulation amplitude as described in Eq. (3.48). We adopt the quenching factors $Q_{\rm Na} = 0.30$ and $Q_{\rm I} = 0.09$ as measured by the DAMA collaboration [333] but we note that there are claims that the quenching factors are energy dependent, see Refs. [334]. Furthermore, we include the effect of channeling and dechanneling as described in [335] and we adopt the largest channeling fraction. This lowers the DAMA-2013 detection threshold and the analysis is therefore conservative in ruling out parameter space.

As the annual modulation signal at DAMA-2013 is present in multiple energy bins, we optimize the outcome of a null experiment A such that the signal is reproduced in the p energy bins $N_{\rm min}^{(B_\alpha)} \leq N^{(B_\alpha)} \leq N_{\rm max}^{(B_\alpha)}$, where $\alpha = 1, \ldots, p$. In addition to this, we consider q additional experiments reporting upper limits $N^{(B_\alpha)} \leq N_{\rm max}^{(B_\alpha)}$ for $\alpha = p{+}1, \ldots, p{+}q$. For a given dark matter mass $m_{\rm DM}$ and scattering cross section σ, we calculate the minimum of the outcome of experiment A subject to those constraints. We conclude that the signal claim is incompatible with the null results from other experiments in a halo-independent way if

$$\min\{N^{(A)}\}(m_{\rm DM}, \sigma) \geq N_{\rm max}^{(A)} \,. \tag{7.1}$$

This problem has $p + q$ upper limit constraints and p lower limit constraints as well as one equality constraint from the normalization of the velocity distribution. However, p upper or lower limit constraints are not saturated as upper and lower limits cannot be fulfilled simultaneously. From Eq. (B.30), we conclude that there are at most $p + q + 1$ and at least 1 streams.

In Fig. 23, we show the allowed regions in parameter space when confronting the DAMA-2013 signal to one null experiment in a halo-independent way. The corresponding optimization problem reads

$$\begin{aligned}
&\min_{f(\vec{v})} \left[N_{f(\vec{v})}^{(A)} \left(m_{\rm DM}, \sigma\right) \right] , \\
\text{subject to} \quad & S_{\rm l.l.}^{(\text{DAMA}_{[2.0,2.5]})} \leq S_{f(\vec{v})}^{(\text{DAMA}_{[2.0,2.5]})}(m_{\rm DM}, \sigma) \leq S_{\rm u.l.}^{(\text{DAMA}_{[2.0,2.5]})} , \\
& S_{\rm l.l.}^{(\text{DAMA}_{[2.5,3.0]})} \leq S_{f(\vec{v})}^{(\text{DAMA}_{[2.5,3.0]})}(m_{\rm DM}, \sigma) \leq S_{\rm u.l.}^{(\text{DAMA}_{[2.5,3.0]})} , \\
& S_{\rm l.l.}^{(\text{DAMA}_{[3.0,3.5]})} \leq S_{f(\vec{v})}^{(\text{DAMA}_{[3.0,3.5]})}(m_{\rm DM}, \sigma) \leq S_{\rm u.l.}^{(\text{DAMA}_{[3.0,3.5]})} , \\
& \int f(\vec{v})\, \mathrm{d}^3 v = 1 \,,
\end{aligned} \tag{7.2}$$

where we consider the modulation signal in the three lowest DAMA-2013 bins. Here, we

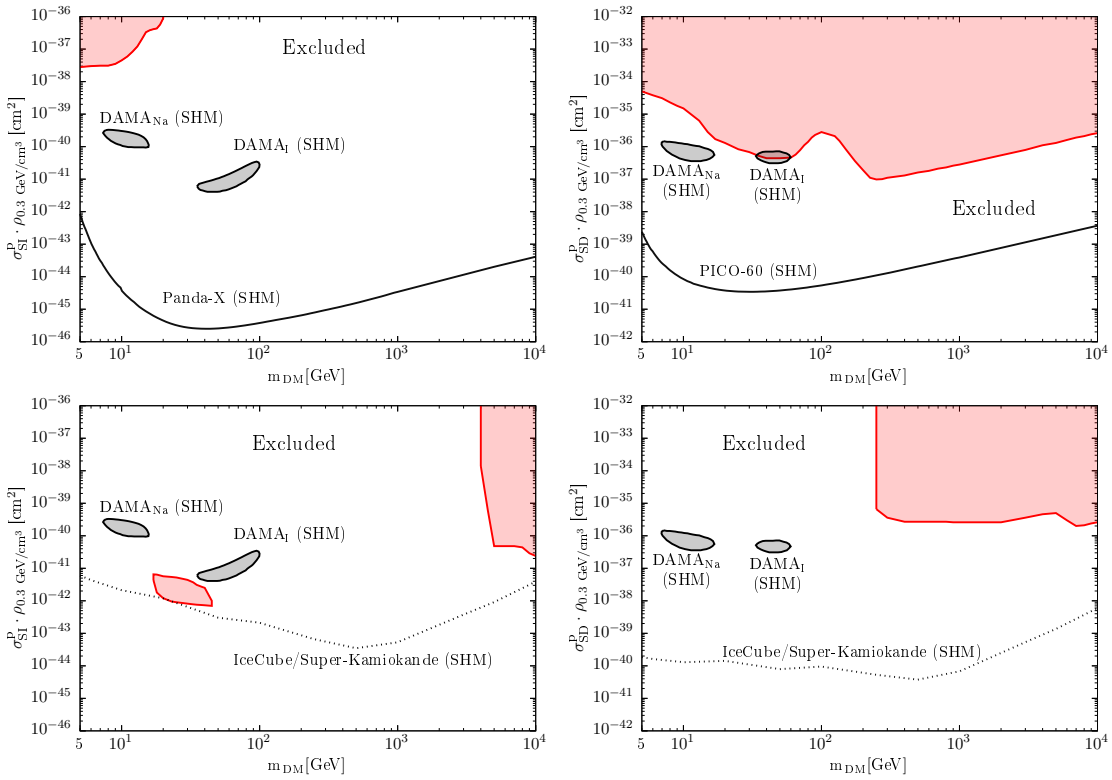

Figure 23.: In this figure, we confront the DAMA-2013 signal to various null results. The left column depicts the allowed region for spin-independent interactions from the combined analysis of DAMA-2013 and PandaX (upper plot) as well as for DAMA-2013 and the neutrino telescopes IceCube and Super-Kamiokande (lower plot). The same is shown in the right column but for spin-dependent interactions. Here, we use null results from PICO-60 (upper plot) and neutrino telescopes (lower plot). The region in parameter space for which the DAMA-2013 signal is compatible with the corresponding null result in a halo-independent way is shown in color. Furthermore, we depict the best fit regions for the DAMA-2013 signal derived from the SHM as gray shaded region [233, 234]. We denote the upper limits of the null experiments derived from the SHM by solid respectively dotted black lines.

use constraints from the direct detection experiments PandaX [217,218] and PICO-60 [237] as well as from the neutrino telescopes IceCube [250] and Super-Kamiokande [252]. To solve this optimization problem, we discretize the velocity integrals and introduce 100000 streams. In Fig. 23, we additionally show the upper limits placed by the null experiments assuming the SHM as well as the regions favored by DAMA-2013 for spin-independent [233] and spin-dependent interactions [234]. For the direct detection experiments, we properly model the motion of the Earth around the Sun during the exposure time of the experiment. We parametrize the motion of the Earth following Ref. [238] and we discretize the path of the Earth in time intervals of two weeks. In Fig. 23, we denote the region of parameter space for which the DAMA-2013 signal is incompatible with one of the null results as white region. We observe that direct detection experiments (upper plots) probe and exclude the DAMA-2013 signal for large dark matter masses while neutrino

telescopes exclude the parameter space for light dark matter. This is due to the fact that neutrino telescopes cannot probe fast moving, heavy dark matter while direct detection experiments are less sensitive to slow and light dark matter.

When assuming the SHM, PandaX respectively PICO-60 exclude the preferred regions in parameter space inferred from the DAMA-2013 signal by more than four orders of magnitude. However, we find that parts of the parameter space cannot be excluded in a halo-independent way. This conclusion heavily relies on the fact that we take into account the channeling effect [335]. Neglecting it, we find no region in parameter space for which the signal is compatible with PandaX or PICO-60 constraints. Using constraints from PandaX Run 8 [217] and Run 9 [218], we are able to exclude the DAMA-2013 signal in the whole parameter space except for a region at low masses, i.e. $m_{\rm DM} \leq 20\,\text{GeV}$, and large cross sections $\sigma_{\rm SI} \geq 10^{-38}\,\text{cm}^2$. For PICO-60 however, we find a much larger region in parameter space that cannot be excluded in a halo-independent way. This is due to the fact that the energy threshold to detect nuclear recoils in PICO-60 is much higher than for DAMA-2013. Therefore, it is easier to find streams that cannot be detected by PICO-60 but are visible in DAMA-2013.

As apparent from Eq. (B.30) and the previous discussion, we expect between four and one streams for the combined analysis of one direct detection experiment and the DAMA-2013 signal in three energy bins. In Tab. 2, we show some examples of optimal velocity distributions that reconcile DAMA-2013 with null results from direct detection experiments. For the analysis of the DAMA-2013 modulation signal confronted to PandaX, we show the velocity distribution that minimizes the expected number of events for the benchmark parameters $m_{\rm DM} = 10\,\text{GeV}$ and $\sigma_{\rm SI} = 10^{-37}\,\text{cm}^2$. In the spin-dependent case, we tabulate the velocity distribution that minimizes the number of events expected at PICO-60 for $m_{\rm DM} = 3000\,\text{GeV}$ and $\sigma_{\rm SD} = 10^{-34}\,\text{cm}^2$. The optimal stream configuration for the combined analysis of PandaX and DAMA-2013 consists of three streams with similar absolute values of the velocities. As discussed in general above, the channeling effect [335] plays a crucial role for this solution as it lowers the velocity that is necessary to induce a detectable recoil in DAMA-2013. The streams are placed such that they are below or close to the PandaX threshold of $v_{\rm min}^{(\rm PandaX)} = 259.6\,\text{km/s}$ which yields a tiny signal. However, those streams give rise to the correct modulation amplitude as the threshold to induce a nuclear recoil that is detected in the highest energy bin is $v_{\rm min}^{(\rm DAMA_{[3.0,3.5]})} = 143.9\,\text{km/s}$. The velocity distribution that minimizes the outcome at PICO-60 has similar features. As tabulated in Tab. 2, it consists of four streams below the threshold of $v_{\rm min}^{(\rm PICO\text{-}60)} = 120.0\,\text{km/s}$. Those streams have velocities between 95 km/s and 118 km/s. Thus, no signal is expected at PICO-60. As before, the streams reproduce the correct modulation amplitude at DAMA-2013 as the velocity threshold of the highest energy bin $v_{\rm min}^{(\rm DAMA_{[3.0,3.5]})} = 20.3\,\text{km/s}$ is smaller than the velocities of the streams. For both examples discussed above, the optimal velocity distribution consists of streams close to the threshold of the null experiment. Therefore, even a small width of the stream might spoil the solution and exceed the upper limits placed by PandaX or PICO-60. More precisely, the solutions presented in Tab. 2 are in tension with PandaX and PICO-60 if the

	stream 1	stream 2	stream 3	stream 4
$c_{\vec{v}_i}$	0.54	0.28	0.18	–
$\vec{v}_i$ [km/s]	$(-10, -123, 191)$	$(100, -167, -161)$	$(56, 119, -183)$	–
$\lvert\vec{v}_{i,\max}^{(\text{PandaX})}\rvert$ [km/s]	257.1	264.3	255.1	–
$\lvert\vec{v}_{i,\text{June}}^{(\text{DAMA})}\rvert$ [km/s]	256.1	245.0	195.7	–
$\lvert\vec{v}_{i,\text{Dec}}^{(\text{DAMA})}\rvert$ [km/s]	198.8	263.2	255.1	–
$c_{\vec{v}_i}$	0.35	0.34	0.17	0.14
$\vec{v}_i$ [km/s]	$(-91, 10, 20)$	$(-1, 100, 2)$	$(35, 46, -52)$	$(-37, -62, 74)$
$\lvert\vec{v}_{i,\max}^{(\text{PICO-60})}\rvert$ [km/s]	112.4	117.5	107.3	94.1
$\lvert\vec{v}_{i,\text{June}}^{(\text{DAMA})}\rvert$ [km/s]	109.9	89.6	49.0	133.0
$\lvert\vec{v}_{i,\text{Dec}}^{(\text{DAMA})}\rvert$ [km/s]	85.9	117.3	107.0	74.1

Table 2.: Examples for optimized velocity distributions assuming constraints from direct detection experiments. We tabulate solutions that reconcile the DAMA-2013 modulation signal in the three lowest energy DAMA-2013 bins and null results from PandaX for the benchmark point $m_{\text{DM}} = 10\,\text{GeV}$ and $\sigma_{\text{SI}} = 10^{-37}\,\text{cm}^2$. For spin-dependent interactions, we use constraints from PICO-60 for $m_{\text{DM}} = 3000\,\text{GeV}$ and $\sigma_{\text{SD}} = 10^{-34}\,\text{cm}^2$. We show the velocities of the streams $\vec{v}_i$ in the galactic rest frame and the corresponding weights $c_{\vec{v}_i}$. Furthermore, we include the velocities of the streams in the rest frame of the Earth and integrated over the exposure time of PandaX respectively PICO-60. Finally, we depict the stream configuration at June and December in the rest frame of the Earth, where the minimum and the maximum of the DAMA-2013 signal is expected. This table was taken from Ref. [2].

streams are smeared by Gaussians with widths larger than $\Delta v = 1.7\,\text{km/s}$ respectively $\Delta v = 1.6\,\text{km/s}$.

As shown in Fig. 23, we find a lower limit of the cross section that is necessary to reconcile the DAMA-2013 signal with upper limits from direct detection experiments. However, there is no upper limit on the cross section. In order to see this, we study the optimized distribution shown in Tab. 2 for the combined analysis of DAMA-2013 and PandaX. The optimized stream configuration consists of three streams placed at velocities close to 260 km/s. An increase in the cross section can be balanced by decreasing the normalization of the weights by the same factor. In order to fulfill the constraint that the velocity distribution has to be normalized, we introduce an additional stream below the threshold of all experiments. This stream does not contribute to any of the experiments and we choose the weight in such a way that the normalization condition is fulfilled. Therefore, it is always possible to find a velocity distribution that reconciles DAMA-2013 and a direct detection experiment for a larger cross section.

In the bottom row of Fig. 23, we show the region in parameter space for which the DAMA-2013 signal cannot be reconciled with results from neutrino telescopes. Here, we use the limits derived from IceCube and Super-Kamiokande assuming annihilation into W^+W^- ($\tau^+\tau^-$ for $m_{\text{DM}} < m_W$). As for the constraints from direct detection ex-

	stream 1	stream 2	stream 3	stream 4
$c_{\vec{v}_i}$	0.56	0.44	6×10^{-5}	–
$\vec{v}_i$ [km/s]	$(120, -623, -357)$	$(110, -643, -337)$	$(110, 177, -297)$	–
$\lvert\vec{v}_i^{\,(\mathrm{Sun})}\rvert$ [km/s]	728.0	734.2	362.8	–
$\lvert\vec{v}_{i,\mathrm{June}}^{\,(\mathrm{DAMA})}\rvert$ [km/s]	728.0	735.4	333.0	–
$\lvert\vec{v}_{i,\mathrm{Dec}}^{\,(\mathrm{DAMA})}\rvert$ [km/s]	734.2	729.1	392.6	–
$c_{\vec{v}_i}$	0.51	0.47	0.02	
$\vec{v}_i$ [km/s]	$(70, 107, -167)$	$(-60, -113, 173)$	$(-50, -103, 143)$	–
$\lvert\vec{v}_i^{\,(\mathrm{Sun})}\rvert$ [km/s]	210.3	215.2	183.2	–
$\lvert\vec{v}_{i,\mathrm{June}}^{\,(\mathrm{DAMA})}\rvert$ [km/s]	180.5	244.9	212.9	–
$\lvert\vec{v}_{i,\mathrm{June}}^{\,(\mathrm{DAMA})}\rvert$ [km/s]	240.1	185.4	153.5	–

Table 3.: Examples for optimized velocity distributions assuming constraints from neutrino telescopes. We tabulate solutions that reconcile the DAMA-2013 modulation signal in the three lowest energy bins and null results from the neutrino telescopes IceCube as well as Super-Kamiokande. Concretely, we assume annihilation into W^+W^- ($\tau^+\tau^-$ for $m_{\mathrm{DM}} < m_W$). We use the benchmark points $m_{\mathrm{DM}} = 10\,\mathrm{GeV}$ and $\sigma_{\mathrm{SI}} = 10^{-37}\,\mathrm{cm}^2$ for spin-independent interactions as well as $m_{\mathrm{DM}} = 3000\,\mathrm{GeV}$ and $\sigma_{\mathrm{SD}} = 10^{-34}\,\mathrm{cm}^2$ for spin-dependent interactions. We show the velocities of the streams $\vec{v}_i$ in the galactic rest frame and the corresponding weights $c_{\vec{v}_i}$. Furthermore, we include the velocities of the streams in the rest frame of the Sun. Finally, we depict the stream configuration at June and December in the rest frame of the Earth, where the minimum and the maximum of the DAMA-2013 signal is expected. This plot was taken from Ref. [2].

periments, we find the optimized velocity distribution in the case of spin-independent and spin-dependent scattering. We show in white the region in parameter space where the DAMA-2013 signal is in tension with the upper limits on the annihilation rate from neutrino telescopes. Conversely, the region in parameter space where DAMA-2013 can be reconciled with neutrino telescopes is colored. For spin-independent as well as for spin-dependent interactions, we find a region at large dark matter masses and large cross sections that cannot be ruled out in a halo-independent way. For the former interaction type, we find the region at $m_{\mathrm{DM}} \gtrsim 4\,\mathrm{TeV}$ and for the latter at $m_{\mathrm{DM}} \gtrsim 250\,\mathrm{GeV}$. Furthermore, we observe an allowed region for spin-independent interactions at dark matter masses between 20 GeV and 40 GeV as well as for cross sections between $10^{-42}\,\mathrm{cm}^2$ and $10^{-41}\,\mathrm{cm}^2$.

The optimized velocity distributions that minimize the tension between the DAMA-2013 signal and upper limits from neutrino telescopes consist of one to four streams, confer Eq. (B.30). In Tab. 3, we show the stream configuration for the same benchmark points as in Tab. 2, i.e. $m_{\mathrm{DM}} = 10\,\mathrm{GeV}$ and $\sigma_{\mathrm{SI}} = 10^{-37}\,\mathrm{cm}^2$ as well as $m_{\mathrm{DM}} = 3000\,\mathrm{GeV}$ and $\sigma_{\mathrm{SD}} = 10^{-34}\,\mathrm{cm}^2$. In the case of spin-independent interactions, the optimal stream configuration consists of three streams of which two are placed at very large velocities.

The remaining stream has a small weight $c_{\vec{v}_3} \sim \mathcal{O}(10^{-5})$ and therefore barely contributes. More precisely, all streams contribute to the first three DAMA-2013 bins in June as well in December as they have velocities larger than $v_{\rm min}^{(\rm DAMA_{[3.0,3.5]})} = 143.9\,\rm km/s$. For spin-dependent interactions however, the optimal velocity distribution consists of three streams with velocities between 180 km/s and 220 km/s. As apparent from Eq. (3.52), the maximal velocity for which capture in the Sun is kinematically possible decreases for heavy dark matter. Therefore, the capture rate from those streams is small. In contrast, all streams contribute to the scattering rate at DAMA-2013 and therefore reproduce the modulation signal.

For the regions in parameter space where DAMA-2013 can be reconciled with upper limits from neutrino telescopes, we do not find that they extend to arbitrary large cross sections. In contrast to constraints from direct detection experiments, increasing the cross section cannot be compensated by a stream below the detection threshold of DAMA-2013. This would yield a large capture rate and therefore a large annihilation rate inside the Sun as the capture rate is largest for slow dark matter particles. Therefore, the regions in which the DAMA-2013 data set is compatible with neutrino telescopes in a halo-independent way have an upper and a lower bound on the cross section.

As apparent from the optimal velocity distributions shown in Tab. 2 and Tab. 3, the optimal stream configurations are very different when considering constraints from direct detection experiments compared to constraints from neutrino telescopes. For the former, the velocity distribution must be small at large velocities in order to avoid a large scattering rate at the direct detection experiment. For neutrino telescopes however, the reverse is preferred as streams with low velocities lead to a large capture rate in the Sun. It is therefore interesting to study whether there exist velocity distributions that can reconcile the DAMA-2013 signal with constraints from direct detection experiments and neutrino telescopes.

In Fig. 24, we show the minimal number of events at PandaX and PICO-60 with the constraints that the DAMA-2013 modulation amplitude is reproduced in the three energy bins under consideration as well as that the upper limit from neutrino telescopes is not violated. We find that the DAMA-2013 signal cannot be reconciled with the null results from PandaX and the neutrino telescopes IceCube and Super-Kamiokande assuming spin-independent dark matter-nucleus interactions. For dark matter masses between 5 GeV and 10 TeV, the minimal number of events expected at PandaX is $\mathcal{O}(10^3)$ which is much larger than the 90 % upper limit from PandaX $\mathcal{N}_{\rm u.l.}^{\rm PandaX} = 6.7$. For very large dark matter masses $m_{\rm DM} \gg 10\,\rm TeV$, we find a velocity distribution that reconciles the experiments. This is due to the fact that neutrino telescopes do not probe this region. However, such heavy dark matter particles are in tension with the unitarity limit for thermally produced dark matter [336]. For spin-dependent interactions, we find velocity distributions that reconcile DAMA-2013 with the null results from PICO-60 and neutrino telescopes. Those solutions exist for dark matter particles heavier than $\sim 4.5\,\rm TeV$ for which the limits from neutrino telescopes can be evaded due to $v_{\rm max}^{(\rm NT)}$ decreasing with increasing dark matter mass, confer Eq. (3.52). However, the optimal stream configurations are fine tuned and

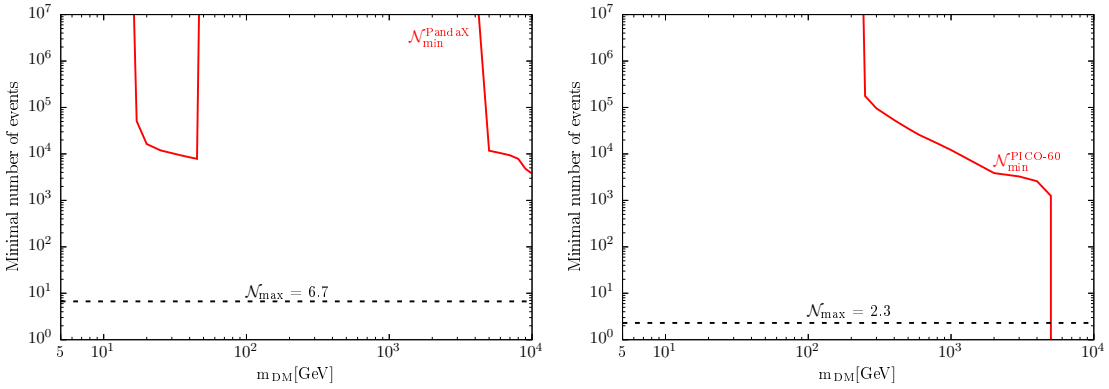

Figure 24.: In this figure, we show the DAMA-2013 signal confronted to null results from direct detection experiments and neutrino telescopes. In the left plot, we assume spin-independent interactions and constraints from PandaX as well as IceCube and Super-Kamiokande. We depict the minimal number of events at PandaX that is compatible with the DAMA-2013 signal and the upper limits from neutrino telescopes as a solid line. We additionally include the upper limit from PandaX on the number of nuclear recoil events as a dashed line. In the right plot, we assume spin-dependent interactions and constraints from PICO-60 as well as IceCube and Super-Kamiokande. We indicate the minimal number of events at PICO-60 by a solid line and the upper limit on the number of events by a dashed line. These plots were taken from [2].

even a small width of the streams spoils the solutions. Concretely, we find that smearing the streams with Gaussian distributions with a width of $\sigma_v \gtrsim 1.7\,\mathrm{km/s}$ is enough to spoil the solutions.

We note that the analysis presented in this section is conservative and some of the allowed parameters might be excluded in a more detailed analysis. The DAMA collaboration observes a signal that is well fit by a cosine modulation with maximum in June and minimum in December, compare [22, 23]. Our optimized solutions consist of only few streams, therefore the time dependence of the recoil rate can be different from a cosine function, see Ref. [240]. Another caveat is that the annual modulation amplitude in Eq. (3.48) predicts the minimum of the recoil rate to be in winter and the maximum to be in summer. For streams however, the absolute minima and maxima might occur at other times of the year. Therefore, we expect that the region in parameter space for which the DAMA-2013 signal is compatible with null searches shrinks further if we constrain the shape of the modulation signal.

7.2. Halo-independent analysis of the DAMA data

Here, we study the DAMA data released in 2018 [23] that features two additional low energy bins compared to DAMA-2013. As we show later in this section, the modulation signal in those additional two bins is hard to reproduce for spin-independent interactions assuming the SHM, confer also Ref. [235]. Instead of repeating the analysis presented in the previous section, we reconstruct both the dark matter mass and the interaction

cross section from the annual modulation signal. We do this once assuming the SHM and once in a fully halo-independent way, which allows us to check whether the tension for spin-independent interactions can be alleviated when being agnostic about the velocity distribution. Furthermore, this gives hints on the impact of astrophysical uncertainties on the interpretation of the DAMA-2018 signal. In contrast to the previous discussion in this chapter, the following analysis was not published previous to this work.

7.2.1. Statistical modeling of DAMA-2018

In order to determine the most likely parameters to reproduce the DAMA-2018 data, we adopt a maximum likelihood method. In the following, we focus on spin-independent as well as spin-dependent interactions. However, the same formalism can be applied to other interaction types. We base our analysis on the maximum likelihood ratio

$$\frac{\mathrm{L}(m_{\mathrm{DM}}, \sigma \mid \mathrm{S}_{m,\mathrm{obs}})}{\mathrm{L}(\hat{m}_{\mathrm{DM}}, \hat{\sigma} \mid \mathrm{S}_{m,\mathrm{obs}})}, \tag{7.3}$$

where the quantities with hats denote the maximum likelihood estimators. Furthermore, $\mathrm{S}_{m,\mathrm{obs}}$ are the observed modulation amplitudes in the DAMA-2018 data set in the energy bins under consideration. A pair of parameters $(m_{\mathrm{DM}}, \sigma)$ is allowed at a confidence level α if

$$2\ln\left(\mathrm{L}(m_{\mathrm{DM}}, \sigma \mid \mathrm{S}_{m,\mathrm{obs}})\right) \geq 2\ln(\mathrm{L}_{\mathrm{max}}) - 2\ln(\Delta\mathrm{L}_{\alpha}) \tag{7.4}$$

where $\mathrm{L}_{\mathrm{max}} = \mathrm{L}(\mathrm{S}_m \mid \hat{m}_{\mathrm{DM}}, \hat{\sigma})$ is the global maximum of the likelihood and $\Delta\mathrm{L}_{\alpha}$ is determined by the confidence level. In order to find the allowed region in parameter space, we first determine the global maximum of the likelihood. We then scan the parameter space and evaluate Eq. (7.3) for each point to check whether it is allowed.

Following Ref. [247], we assume that the DAMA-2018 data are normally distributed in each bin. With this, the condition of Eq. (7.4) can be rewritten in terms of the chi-square distribution

$$\chi^2(m_{\mathrm{DM}}, \sigma \mid \mathrm{S}_{m,\mathrm{obs}}) \leq \chi^2_{\mathrm{min}} + \Delta\chi^2_{\alpha}\,, \tag{7.5}$$

where χ^2_{min} denotes the global minimum and $\Delta\chi^2_{\alpha}$ depends on the confidence level α. The chi-square distribution is a quadratic function depending on the observed and the predicted modulation amplitude as well as the uncertainty of the amplitude

$$\chi^2_{\mathrm{DAMA}}(m_{\mathrm{DM}}, \sigma \mid \mathrm{S}_{m,\mathrm{obs}}) = \sum_{\mathrm{bins}} \frac{\left(\mathrm{S}_m^{(\mathrm{bin})}(m_{\mathrm{DM}}, \sigma) - \mathrm{S}_{m,\mathrm{obs}}^{(\mathrm{bin})}\right)^2}{\sigma^2_{\mathrm{bin}}}\,, \tag{7.6}$$

where $\mathrm{S}_{m,\mathrm{obs}}$ denotes the modulation amplitude observed in the DAMA-2018 data.

This can be expanded in terms of streams by using the fact that the velocity distribution

enters linearly when computing the modulation amplitude

$$\mathrm{S}_m^{(\mathrm{bin})}(m_{\mathrm{DM}},\sigma) = \sum_i \mathrm{S}_{\vec{v}_i}^{(\mathrm{bin})}(m_{\mathrm{DM}},\sigma)\; c_{\vec{v}_i}\,, \tag{7.7}$$

where the stream response functions $\mathrm{S}_{\vec{v}_i}^{(\mathrm{bin})}$ can be calculated from Eq. (3.48) using the decomposition into streams given in Eq. (4.2). Using this expansion for the chi-squared distribution describing the DAMA-2018 data given in Eq. (7.6), we obtain a quadratic polynomial in the primal variables $c_{\vec{v}_i}$

$$\chi^2_{\mathrm{DAMA}}(m_{\mathrm{DM}},\sigma \mid \mathrm{S}_{m,\mathrm{obs}}) = \sum_{\mathrm{bins}} \frac{1}{\sigma^2_{\mathrm{bin}}} \left(\left(\mathrm{S}_{m,\mathrm{obs}}^{(\mathrm{bin})}\right)^2 - 2\,\mathrm{S}_{m,\mathrm{obs}}^{(\mathrm{bin})} \sum_i \mathrm{S}_{\vec{v}_i}^{(\mathrm{bin})}(m_{\mathrm{DM}},\sigma)\, c_{\vec{v}_i} + \sum_{i,j} \mathrm{S}_{\vec{v}_i}^{(\mathrm{bin})}(m_{\mathrm{DM}},\sigma)\, \mathrm{S}_{\vec{v}_j}^{(\mathrm{bin})}(m_{\mathrm{DM}},\sigma)\, c_{\vec{v}_i}\, c_{\vec{v}_j} \right)\,. \tag{7.8}$$

This allows us to write the maximum likelihood ratio of Eq. (7.3) as a quadratic optimization problem with linear constraints

$$\begin{aligned} \text{minimize:} \quad & \chi^2_{\mathrm{DAMA}}(m_{\mathrm{DM}},\sigma \mid \{c_{\vec{v}_i}\}) \\ \text{subject to:} \quad & c_{\vec{v}_i} \geq 0 \qquad \forall\, i \\ & \sum_i c_{\vec{v}_i} \;=\; 1\,. \end{aligned} \tag{7.9}$$

This problem is equivalent to a second order cone problem and we solve it for each pair of parameters (m_{DM},σ) using the routines provided by the `Python` module `CVXOPT` [300].

7.2.2. Reconstructing dark matter properties from DAMA-2018

In order to find the allowed region in parameter space when assuming the SHM, we proceed as described in the previous section and directly use Eq. (7.5). For the halo-independent analysis however, we minimize the chi-square distribution with respect to the velocity distribution for each dark matter mass and scattering cross section. A point in parameter space is compatible with the annual modulation signal if it fulfills

$$\min_{f(\vec{v})}\{\chi^2_{\mathrm{DAMA}}(m_{\mathrm{DM}},\sigma \mid \mathrm{S}_{m,\mathrm{obs}})\} \leq \chi^2_{\mathrm{DAMA,min}} + \Delta\chi^2_\alpha\,, \tag{7.10}$$

where $\chi^2_{\mathrm{DAMA,min}}$ is the minimum of the chi-square distribution with respect to the dark matter mass, cross section and velocity distribution.

In Fig. 25, we show the results for an analysis assuming the SHM (top panel) as well as a fully halo-independent analysis (lower panel). We show the contours corresponding to a confidence level of 90% respectively 99% which are derived using Eq. (7.5) or Eq. (7.10). Furthermore, we mark the best fit point, i.e. where the minimum of the chi-square distribution is attained, by a star and give the concrete values in the lower left corner of the plot. If the global minimum of the chi-square distribution is degenerate, we do not

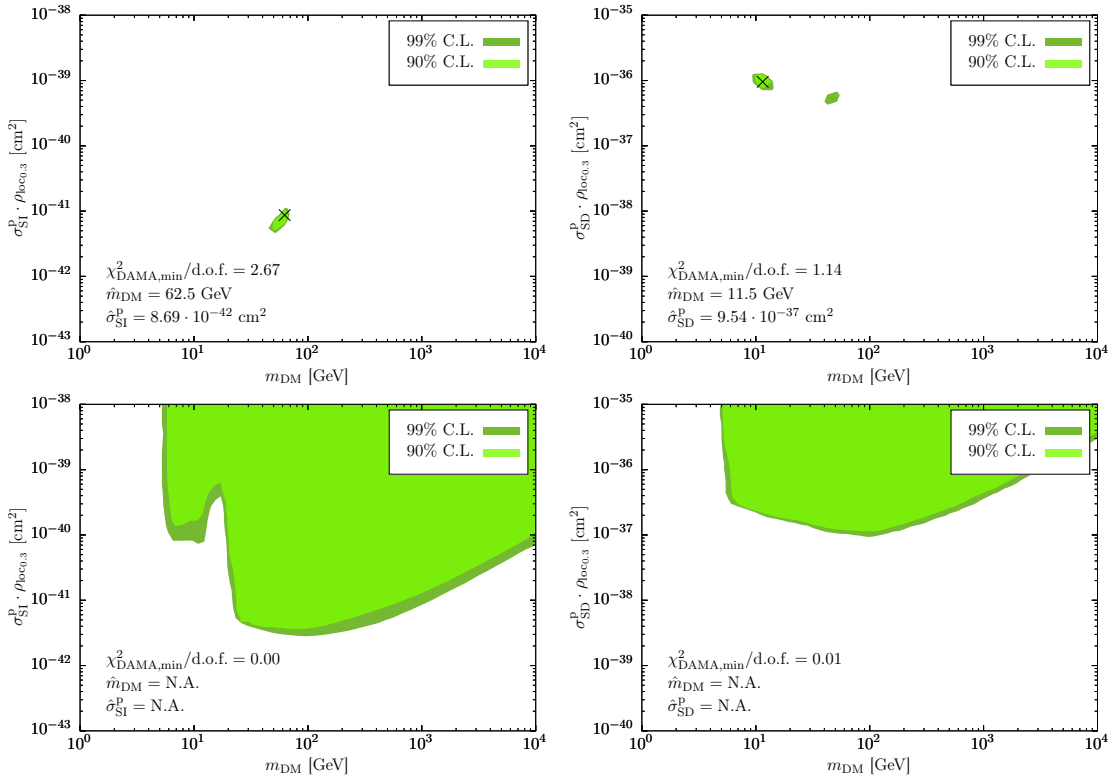

Figure 25.: Regions in parameter space that are compatible with the DAMA-2018 modulation signal at a confidence level of 90% respectively 99%. Shown are the regions when assuming the SHM (upper row) and when being agnostic about the velocity distribution (lower row). In each case, we study spin-independent (left) and spin-dependent interactions (right).

indicate the best fit point and neither give a best fit dark matter mass nor the best fit scattering cross section.

When assuming the SHM, spin-independent interactions provide a bad fit to the DAMA-2018 data. Concretely, the best fit point has a reduced chi-square of 2.67 which is equivalent to a p-value of 0.0067. We note that this observation coincides with the findings of Refs. [235, 291]. The bad fit is due to the fact that the lowest two energy bins of the DAMA-2018 data are incompatible with the signal shape expected from spin-independent interactions. However, the data set from 2018 [23] has a lower energy threshold compared to the 2013 data set which does therefore not contain the problematic bins. Thus, spin-independent interactions provide an acceptable fit to the DAMA-2013 data set as found by Ref. [247]. In contrast to this, spin-dependent interactions reproduce the DAMA-2018 signal reasonably well when assuming the SHM. In this case, we find a minimal reduced chi-square of 1.14 which yields an acceptable fit. We obtain two allowed regions at dark matter masses of approximately 10 GeV respectively ~ 50 GeV. They are very small and are located approximately at the same interaction cross section of $\sigma^{\text{p}}_{\text{SD}} \sim 10^{-36}\,\text{cm}^2$. This leads to very strong predictions that are in conflict with the results of other direct dark matter searches that constrain spin-dependent interactions, confer Figs. 6 and 7.

In order to asses the impact of the velocity distribution on the parameter reconstruction

from the DAMA-2018 signal, we minimize the chi-square distribution with respect to the velocity distribution for each dark matter mass and scattering cross section. For spin-independent interactions, we find that the modulation signal can be perfectly reproduced for a large number of dark matter masses and scattering cross sections. Furthermore, the allowed region in parameter space at a confidence level of 90% respectively 99% increases significantly. We conclude that the spin-independent scattering cross section has to be larger than $\sim 2 \cdot 10^{-42}\,\mathrm{cm}^2$ and the dark matter mass has to be larger than 5 GeV in order to reproduce the DAMA-2018 signal. For spin-dependent interactions, we obtain similar results. Being agnostic about the velocity distribution again leads to perfect fits for a large region in parameter space. For an arbitrary velocity distribution, we find that the correct modulation signal can only be reproduced for a spin-dependent scattering cross section larger than $\sim 10^{-37}\,\mathrm{cm}^2$ and for dark matter particles heavier than 5 GeV. As in the analysis presented in section 7.1, the reconstructed regions in parameter space are not bounded from above neither for the spin-independent nor for the spin-dependent scattering cross section. This is again due to the fact that increasing the scattering cross section can be compensated by adding a stream below the detection threshold of DAMA-2018. We note that the lower bound on the allowed dark matter masses is due to kinematics and the energy threshold $E_{\mathrm{th}} \sim 3$ keV of DAMA-2018.

For both types of interactions, the smallest possible cross section is still in conflict with the upper limits derived from the SHM. However, this does not imply that the modulation signal is excluded by the results of other direct dark matter searches as the optimized velocity distribution could significantly degrade the upper limits. This is also apparent from Figs. 15 and 17. In order to check whether the DAMA-2018 signal is compatible with other experiments, we need to perform a combined halo-independent analysis similar to section 7.1. The computational effort of such an analysis is tremendous as the chi-square distribution has to be modeled in general by a symmetric $N^3 \times N^3$ matrix where N is the number of discrete velocities for a single spatial dimension. For 100 discrete velocities per spatial dimension, the resulting matrix has $N^3\,(N^3+1)/2 \approx 10^{12}$ independent entries. This analysis is beyond the scope of this work, as each spatial dimension has to be discretized into several hundreds of discrete velocities in order to model the velocity distribution accurately.

7.3. Discussion and summary

In this chapter, we analyzed the dark matter interpretation of the DAMA annual modulation signal. First, we confronted the DAMA-2013 signal to null results from other dark matter experiments. Concretely, we used constraints from direct detection experiments as well as from neutrino telescopes, assuming annihilation into W^+W^- ($\tau^+\tau^-$ for $m_{\mathrm{DM}} < m_W$). For constraints from one individual dark matter search, we found velocity distributions that are able to reproduce the modulation signal in the three lowest energy bins of the DAMA-2013 data set. When considering combined constraints from direct detection experiments and neutrino telescopes, we observed that the DAMA-2013 signal

can only be reconciled for dark matter masses larger than 165 TeV for spin-independent interactions and for $m_{\mathrm{DM}} \gtrsim 4.5$ TeV assuming spin-dependent interactions. We stress that those solutions arise only when assuming the channeling effect that allows to detect nuclear recoils below the energy threshold at DAMA. We furthermore note that the optimized distributions are fine tuned as smearing the streams with Gaussians with a width of $\sigma_v \gtrsim 1.7\,\mathrm{km/s}$ spoils the solutions.

Using the DAMA-2018 data set, we observed that uncertainties in the velocity distribution significantly affect the reconstruction of parameters. When assuming the SHM, we obtained small regions in parameter space that are compatible with the modulation signal. For general velocity distributions however, these regions increase significantly and it is only possible to extract the smallest dark matter mass and scattering cross section that could reproduce the modulation signal. Concretely, we found that the spin-independent scattering cross section has to be larger than $\sim 2 \cdot 10^{-42}\,\mathrm{cm}^2$ and the dark matter particle has to be heavier than ~ 5 GeV. For spin-dependent interactions, we obtained the same lower bound on the dark matter mass while the spin-dependent scattering cross section has to be larger than $\sim 10^{-37}\,\mathrm{cm}^2$. We note that the lower bound on the dark matter mass is due to kinematics and the energy threshold $E_{\mathrm{th}} \sim 3$ keV of DAMA-2018.

Chapter 8.

Impact of sub-halos on direct dark matter searches

The content of this chapter was published in Ref. [5] unless explicitly stated otherwise.

As a consequence of structure formation, the Milky Way halo contains a large variety of substructure. Dark matter sub-halos for example are expected to have masses ranging from $10^{-6}\,M_\odot$ to $\sim 10^{11}\,M_\odot$, confer Fig. 26. Due to this large spread, substructure affects the Milky Way on all scales and can leave characteristic imprints.

On scales of our Solar System, the Milky Way halo could be affected by individual substructures. By studying the motion of stars in the solar neighborhood mapped by *Gaia* [107, 108], Ref. [102] showed that the surrounding of the Solar System is largely influenced by a non-virialized component. This additional component could originate from the tidal disruption of a massive satellite [102]. Other examples of substructures that could influence the dark matter halo in the solar neighborhood are stellar streams like Sagittarius [136–138] or S1 [139]. If the Earth is currently affected by one of these structures, the signal at direct detection experiments could be enhanced. The impact of known substructure in the proximity of the Sun was investigated for the Sagittarius stream in [138] and for the S1 stream in [139]. Furthermore, the sub-halos predicted by N-body simulations were used to estimate the effect on direct detection experiments [337–341].

As dark matter substructure is expected to exist in a huge variety of masses and sizes, it might not only have impact on the solar neighborhood but also leave detectable signatures on galactic scales. One possible effect is an enhancement of the γ-ray signal from the Milky Way halo due to the presence of sub-halos [342–347]. Since some dwarf spheroidal galaxies host a large amount of dark matter and have large concentration parameters, the annihilation rate of dark matter particles could be significantly enhanced in these structures. Therefore, several studies [348–355] investigated the γ-ray signal originating from the direction of known dwarf spheroidal galaxies. This signal might even be boosted by smaller subsub-halos that are bound to dwarf spheroidal galaxies [135]. Neutrinos from dark matter annihilations in those structures are currently impossible to detect as the signal is too faint due to the large distance between the dwarf spheroidal galaxy and the Earth as well as due to the small interaction cross section of neutrinos. Another signature of dark matter sub-halos are gaps or similar features [356–360] in stellar streams that can be detected by a high precision astrometric survey like *Gaia* [107, 108]. Those features arise due to the gravitational perturbations induced by a sub-halo that passes

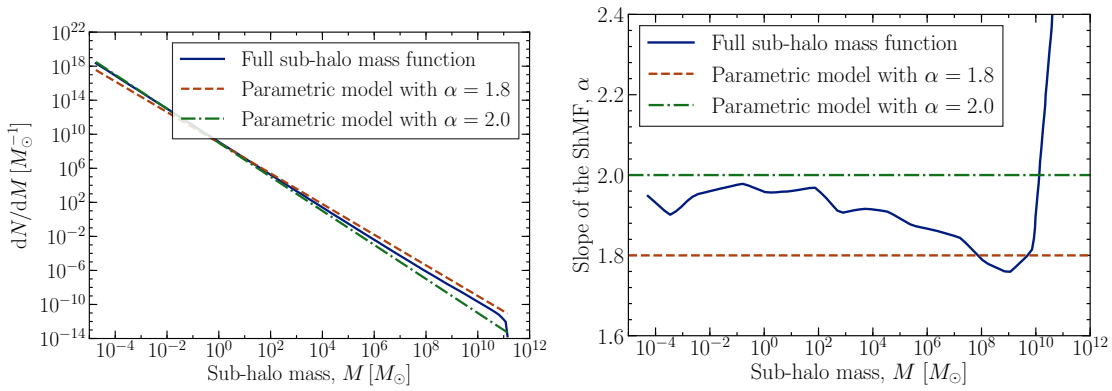

Figure 26.: The left plot shows the sub-halo mass functions from the semi-analytical model of Ref. [135] and from two parametric models with $\alpha = 1.8$ and $\alpha = 2.0$. The right plot depicts the parameter α of the sub-halo mass function for the three models shown in the left plot. The plots were taken from [5].

close to the stream. Furthermore, the signal of high energy neutrinos originating from dark matter annihilations in the Sun could be affected by sub-halos [361]. As discussed in detail in section 3.3.2, this annihilation signal depends on the amount of dark matter the Sun captures over time. As the Sun traverses the Milky Way, encounters with sub-halos lead to an increased capture rate during passage of the sub-halo. This, in turn, could affect the neutrino signal from the Sun today as the relaxation into equilibrium is extended over time.

In the following, we investigate a specific source of astrophysical uncertainties and determine the impact of dark matter sub-halos on direct detection experiments and neutrino telescopes. We extend previous works studying the enhancement of the dark matter signal at direct detection experiments by taking into account sub-halos as light as $10^{-5}\,M_\odot$, whereas previous studies [337–341] were restricted to the resolution of N-body simulations which is at best $10^5\,M_\odot$. Furthermore, we quantify the enhancement of the neutrino signal from dark matter annihilation in the Sun by tracing the number of dark matter particles captured by the Sun over the whole lifetime.

In addition to the properties and the distribution of dark matter sub-halos that were introduced in section 2.3, we adopt the semi-analytical sub-halo mass function from [135]. We furthermore investigate more general sub-halo mass functions that are parametrized via

$$\frac{\mathrm{d}N}{\mathrm{d}M} = A \cdot M^{-\alpha}, \tag{8.1}$$

where A is the normalization and α is the exponent of the power law. We determine A by fitting the parametric model to the sub-halo mass function from [135]. In the left plot of Fig. 26, we compare the parametric models for $\alpha = 1.8$ and $\alpha = 2.0$ to the full sub-halo mass function calculated in [135]. From this, we observe that the parametric model with $\alpha = 1.8$ ($\alpha = 2.0$) predicts the most heavy (light) sub-halos as well as the least light (heavy) sub-halos. Those two parametric models are therefore ideally suited

to study the impact of uncertainties in the sub-halo mass function. We furthermore show the power law index α extracted from the results of Ref. [135] in the right plot of Fig. 26. It is obtained by fitting the sub-halo mass function of [135] in mass bins to the parametric model in Eq. (8.1). As apparent from this plot, $\alpha = 1.8$ and $\alpha = 2.0$ are good estimators for the lowest and the largest values of α. In order to be consistent with the sub-halo mass function, we use the distributions of the sub-halo properties ρ_s, r_s and r_t that were kindly provided by the authors of Ref. [135] via private communications.

We are interested in signatures of dark matter from a smooth background as well as from sub-halos. For the smooth background halo, we adopt the SHM with a local dark matter density $\rho_{\mathrm{SHM}}^{\mathrm{loc}}$ and a velocity distribution $f_{\mathrm{SHM}}(\vec{v})$ as shown in Eq. (2.17). We furthermore describe sub-halos as detailed in section 2.3.1 but we work in the rest frame of the Sun respectively the Earth. Therefore, we have to take into account the relative velocity $\vec{v}_{\mathrm{rel}}$ of the sub-halo and the respective celestial body. In the specific case of the Sun, the relative velocity is given by $\vec{v}_{\mathrm{rel}} = \vec{v}_{\odot} - \vec{v}_{\mathrm{sh}}$, where $\vec{v}_{\odot}$ and $\vec{v}_{\mathrm{sh}}$ are the velocities of the Sun respectively the sub-halo in the Galactic rest frame. This leads to a time-dependent dark matter density $\rho_{\mathrm{sh}}^{\mathrm{loc}}[r(t)]$ at the position of the Sun, where $r(t)$ is the distance of the detector to the sub-halo center that changes as the Sun traverses the sub-halo. We obtain the velocity distribution of dark matter particles bound to the sub-halo in the rest frame of the respective celestial body via a Galileo transformation of Eq. (2.25)

$$f_{\mathrm{sh}|\vec{v}_{\mathrm{sh}}}(\vec{v}) = \frac{1}{(2\pi\sigma_{\mathrm{sh}}^2)^{3/2}} \exp\left[-\frac{|\vec{v}+\vec{v}_{\mathrm{rel}}|^2}{2\sigma_{\mathrm{sh}}^2}\right] . \tag{8.2}$$

Since we assume that the velocities of the sub-halos follow a Maxwell-Boltzmann distribution, we conclude that the speed of the sub-halo is much larger than its velocity dispersion σ_{sh} for all but the heaviest sub-halos, see Fig. 4. Therefore, the dark matter particles bound to the sub-halo behave effectively as a stream of dark matter particles with velocity $\vec{v}_{\mathrm{rel}}$

$$f_{\mathrm{sh}|\vec{v}_{\mathrm{sh}}}(\vec{v}) \simeq \delta(\vec{v}+\vec{v}_{\mathrm{rel}}) . \tag{8.3}$$

With this, we can finally calculate the flux of dark matter particles at the position of the Sun or the Earth. It has two components, one from the smooth Milky Way dark matter halo which is described by the time-independent quantities $\rho_{\mathrm{SHM}}^{\mathrm{loc}}$ and $f_{\mathrm{SHM}}(\vec{v})$ as well as a component from dark matter sub-halos that is characterized by the time-dependent dark matter density $\rho_{\mathrm{sh}}^{\mathrm{loc}}[r(t)]$ and velocity distribution $f_{\mathrm{sh},\vec{v}_{\mathrm{sh}}}(\vec{v})$. The flux is given by

$$F(\vec{v},t) = v\left(\frac{\rho_{\mathrm{SHM}}^{\mathrm{loc}}}{m_{\mathrm{DM}}} f_{\mathrm{SHM}}(\vec{v}) + \frac{\rho_{\mathrm{sh}}^{\mathrm{loc}}[r(t)]}{m_{\mathrm{DM}}} f_{\mathrm{sh}|\vec{v}_{\mathrm{sh}}}(\vec{v})\right) , \tag{8.4}$$

where v is the velocity of the dark matter particle in the rest frame of the Sun or the Earth.

8.1. Impact of sub-halos on direct detection experiments

As described in detail in section 3.3.1, the signal of dark matter at a direct detection experiment is characterized by the number of scattering events N during the exposure of the experiment. Here, we write the scattering rate of dark matter particles in terms of the flux $F(\vec{v}, t)$, confer Eq. (8.4), in order to include the contribution of the smooth Milky Way halo as well as the sub-halos. The scattering rate at current times t_0 then reads

$$R = \sum_i \int_0^\infty \mathrm{d}E_R \, \epsilon_i(E_R) \, \frac{\xi_i}{m_{T_i}} \int_{v \geq v_{\mathrm{min},i}^{(E_R)}} \mathrm{d}^3 v \, F(\vec{v} + \vec{v}_\oplus, t_0) \, \frac{\mathrm{d}\sigma_i}{\mathrm{d}E_R}(v, E_R) \,, \tag{8.5}$$

where m_{T_i} and ξ_i are the mass respectively the mass fraction of a nucleus T_i. Furthermore ϵ_i is the probability to detect a nuclear recoil off the target nucleus i and $\frac{\mathrm{d}\sigma_i}{\mathrm{d}E_R}$ is the differential WIMP-nucleus scattering cross section of a dark matter particle with the nucleus T_i. Finally, $\vec{v}_\oplus$ denotes the velocity of the Earth in the galactic rest frame and the minimal velocity of a dark matter particle that is necessary to observe a detectable recoil in the detector is given by $v_{\mathrm{min},i}^{(\mathrm{D})}(E_R) = \sqrt{m_{T_i} \, E_R / (2 \, \mu_{T_i}^2)}$.

As we assume that the dark matter particles bound to a sub-halo behave effectively as a stream, we show in Fig. 27 the scattering rate due to such a stream normalized to the scattering rate R_{SHM} expected from the smooth background halo as a function of the velocity with respect to Earth $\vec{v}_{\mathrm{rel}}$. For this, we denote the scattering rate of a stream with velocity distribution $\delta(\vec{v} + \vec{v}_{\mathrm{rel}})$ and dark matter density $\rho_{\mathrm{SHM}}^{\mathrm{loc}}$ by $R^{\rho_{\mathrm{SHM}}^{\mathrm{loc}}}_{\delta(\vec{v}+\vec{v}_{\mathrm{rel}})}$. For dark matter masses greater than 100 GeV, the scattering rate for large velocities is smaller than expected from the SHM while it is enhanced for small velocities. For light dark matter however, the enhancement occurs for fast streams while the scattering rate is zero for slow streams. This is due to fact that the detection threshold is very important for light dark matter. If the particles in the stream are to slow, the energy transfer is too small to cause an observable recoil in the detector. For large velocities however, the enhancement is large as most of the velocities probed by the SHM do not contribute to the scattering rate.

With this, we investigate the case that the Earth currently traverses a sub-halo with mass M and concentration parameter c_V that moves with a relative velocity $\vec{v}_{\mathrm{sh}}$ in the galactic rest frame. We calculate the recoil rate at a direct detection experiment from Eq. (8.5) by specifying the properties of the sub-halo. The increment of the scattering rate with respect to the expectation from the SHM is given by

$$\mathcal{I}_R \equiv \frac{R}{R_{\mathrm{SHM}}} - 1 \simeq \frac{\rho_{\mathrm{sh}}^{\mathrm{loc}}[r(t)]}{\rho_{\mathrm{SHM}}^{\mathrm{sh}}} \, \frac{R^{\rho_{\mathrm{SHM}}^{\mathrm{loc}}}_{\delta(\vec{v}+\vec{v}_{\mathrm{rel}})}}{R_{\mathrm{SHM}}} \,, \tag{8.6}$$

where we assume that the velocity distribution of dark matter particles bound to the sub-halo is approximately a stream, confer Eq. (8.3), with velocity $\vec{v}_{\mathrm{rel}} = \vec{v}_\oplus - \vec{v}_{\mathrm{sh}}$ and $\vec{v}_\oplus$ is the velocity of the Earth in the rest frame of the galaxy. We show the contours of $\mathcal{I}_R$ in Fig. 28. Here, $\rho_{\mathrm{sh}}^{\mathrm{loc}}[r(t)]$ is the density of dark matter particles bound to the sub-halo as a function of the current distance $r(t_0)$ of the Earth to the center of the sub-halo. We find

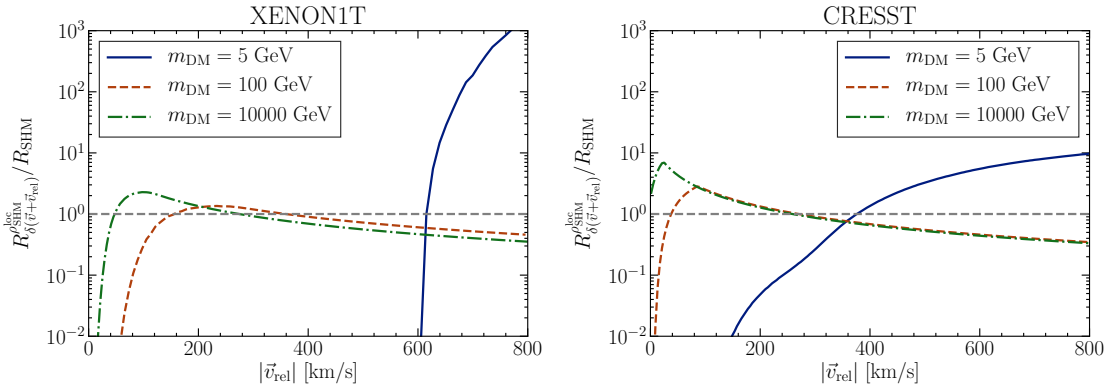

Figure 27.: Scattering rate for a stream in the case of XENON1T [221] (left) and CRESST [228] (right). We assume that the stream has a velocity $|\vec{v}_{\rm rel}|$ in the rest frame of the detector and a local dark matter density $\rho^{\rm loc}_{\rm SHM}$. In both cases, we use the `DDCalc` [326, 327] package to compute the detector responses. A gray dashed line separates the plot into two regions, where the scattering rate is enhanced (suppressed) with respect to the SHM in the upper (lower) part of the plot. These plots were taken from [5].

that the increment increases if the contribution of the sub-halo to the local dark matter density, i.e. $\rho^{\rm loc}_{\rm sh}[r(t)]/\rho^{\rm sh}_{\rm SHM}$, is large. Additionally, a velocity distribution that is more favorable to detect dark matter recoils than the SHM increases $\mathcal{I}_R$.

In the following, we calculate the probability that the Earth currently traverses a sub-halo and obtain the increment $\mathcal{I}_R$ due to the sub-halo. The probability that a sub-halo with mass M and concentration c_V contributes currently with a dark matter density $\tilde{\rho}$ to the local dark matter density at Earth is given by

$$P(\tilde{\rho}, M, c_V) = P(D, M, c_V) \left[\frac{\mathrm{d}\,\tilde{\rho}(D, M, c_V)}{\mathrm{d}D}\right]^{-1} \qquad \text{for } D < R_{\rm vir}(M, c_V)\,, \tag{8.7}$$

where $P(D, M, c_V)$ is the probability to find the center of a sub-halo with mass M and concentration c_V at distance D from Earth. We calculate this probability by multiplying the probability $P(M)$ to find a sub-halo with mass M with the conditional probability $P(c_V|M)$ to observe a concentration parameter c_V given a sub-halo mass M. Finally, we multiply this by the probability that the Earth is located at distance D from a sub-halo center, given that the sub-halo has mass M and concentration parameter c_V. In total, we obtain

$$P(D, M, c_V) = P(M)\, P(c_V|M)\, P(D|M, c_V)\,. \tag{8.8}$$

We calculate the probability to find a sub-halo with mass M from the sub-halo mass functions shown in Fig. 26. This probability is given by the sub-halo mass function divided by the total number of sub-halos $N_{\rm sh}$ in the Milky Way, i.e.

$$P(M) = \frac{1}{N_{\rm sh}} \frac{\mathrm{d}N}{\mathrm{d}M}\,. \tag{8.9}$$

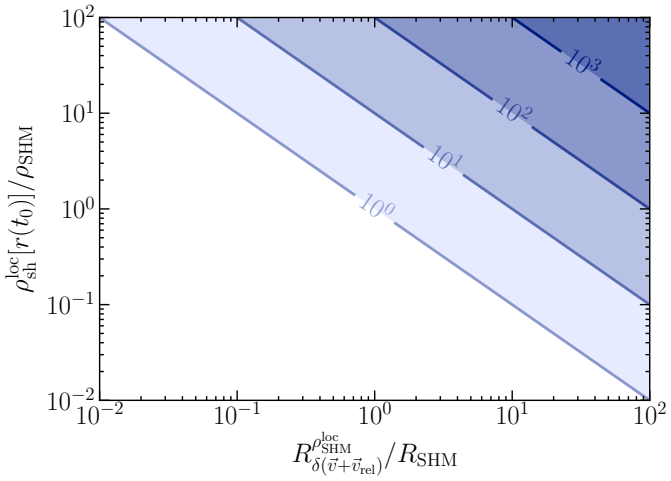

Figure 28.: Increment of the scattering rate from one single sub-halo encounter as a function of the ratios $R^{\rho_{\rm SHM}^{\rm loc}}_{\delta(\vec{v}+\vec{v}_{\rm rel})}/\rho_{\rm SHM}^{\rm loc}$ and $\rho_{\rm sh}^{\rm loc}[r(t)]/\rho_{\rm SHM}^{\rm sh}$. A white region indicates the parameters for which $\mathcal{I}_R < 1$ while colored regions indicate larger increments. This plot was taken from Ref. [5].

Furthermore, we calculate the conditional probability $P(c_V|M)$ from the supplementary data kindly provided by the authors of Ref. [135]. With this, we obtain the probability of the Earth currently being located at distance D from a sub-halo center given M and c_V

$$P(D|M,c_V) \equiv \frac{1}{N_{\rm sh}}\frac{{\rm d}N_{\rm sh}(D)}{{\rm d}D} = \frac{4\pi D^2 \bar{n}_{\rm sh}(D)}{N_{\rm sh}} \qquad \text{for } D < R_{\rm vir}(M,c_V)\,, \tag{8.10}$$

where ${\rm d}N_{\rm sh}(D)$ is the number of sub-halos in a spherical shell with radius D and thickness ${\rm d}D$. Therefore, we write ${\rm d}N_{\rm sh}(D) = 4\pi D^2 \bar{n}_{\rm sh}(D){\rm d}D$ with the average density of sub-halos $\bar{n}_{\rm sh}(D)$ at distance D

$$\bar{n}_{\rm sh}(D) = \frac{1}{2}\int_{-1}^{1} n_{\rm sh}[r(D,\psi)]\,{\rm d}\cos(\psi)\,. \tag{8.11}$$

Here, $n_{\rm sh}(r)$ is the number density of sub-halos as a function of the distance of the Earth to the Galactic Center $r(D,\psi) = \sqrt{D^2 + r_\oplus^2 - 2\,r_\oplus\,D\,\cos(\psi)}$. Furthermore, $r_\oplus \approx r_\odot$ denotes the distance of the Earth to the Galactic Center and ψ is the angular separation between the Sun and the Galactic Center. Concretely, we assume that the spacial distribution of sub-halos does neither depend on the mass M nor on the concentration parameter c_V of the sub-halo. This is motivated by the hydrodynamical N-body simulation conducted in Ref. [154], which suggests that baryonic disruption affects heavy sub-halos at small distances from the galactic center. However, the spatial distribution of sub-halos depends only mildly on sub-halo properties at larger distances from the galactic center which is relevant for this work.

We calculate the probability that one sub-halo contributes a dark matter density $\tilde{\rho}$ to the local dark matter density at Earth by marginalizing the sub-halo mass M and the

concentration parameter c_V in Eq. (8.7):

$$P_{\text{single}}(\tilde{\rho}) = \int_{M_{\text{min}}}^{M_{\text{max}}} \mathrm{d}M \int_{c_{V,\text{min}}}^{c_{V,\text{max}}} \mathrm{d}c_V \, P(\tilde{\rho}, M, c_V) \,. \tag{8.12}$$

We restrict the integration of the mass in Eq. (8.12) to sub-halos heavier than $10^{-6}\, M_\odot$ and lighter than $10^{12}\, M_\odot$ as dictated by the sub-halo mass function. The integration over c_V ranges from 0 to ∞, however concentration parameters outside the interval $[1, 35]$ are heavily suppressed. We show this probability distribution in the left plot of Fig. 29 for

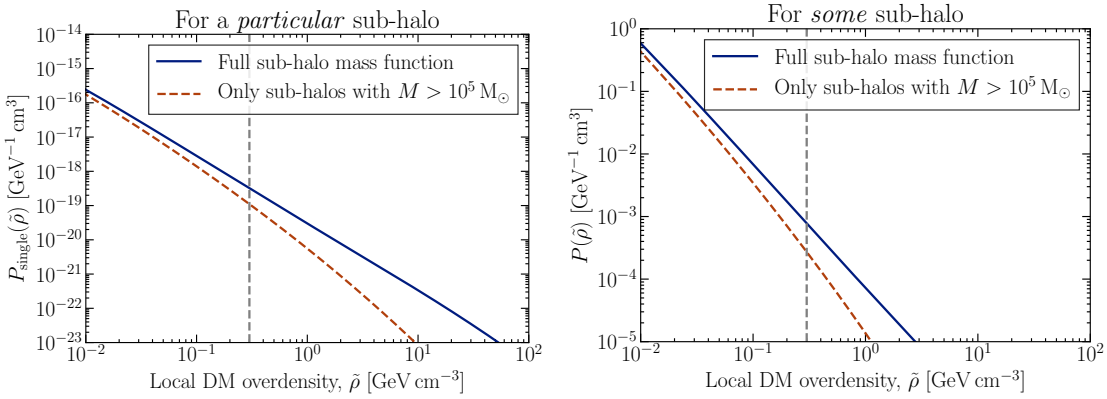

Figure 29.: Probability of a contribution $\tilde{\rho}$ to the local dark matter density at the position of the Earth from a single sub-halo (left) and from some sub-halo (right) in the Milky Way. In both plots, we indicate $\mathcal{O}(1)$ overdensities by a gray dashed line. Both plots show the probability distributions under consideration for both the full sub-halo mass function from [135] as well as for the same sub-halo mass function restricted to sub-halos heavier than $10^5\, M_\odot$. In both plots, the probability distribution at large $\tilde{\rho}$ is suppressed when only heavy sub-halos are considered. These plots were taken from Ref. [5].

the sub-halo mass function from [135]. The probability that a single sub-halo contributes significantly to the local dark matter density at Earth is negligible, as evident from the plot. This is to be expected as the volume of an individual sub-halo is small in comparison with the Milky Way. Indeed, we find that the total probability P_{single} to observe any contribution from a single sub-halo to the local dark matter density at the position of the Earth from Eq. (8.12) is negligible

$$P_{\text{single}} = \int \mathrm{d}\rho \, P_{\text{single}}(\rho) \approx 5 \cdot 10^{-17} \,. \tag{8.13}$$

As shown in the left plot of Fig. 29, those conclusions do not change when only considering sub-halos heavier than $10^5\, M_\odot$.

As the number of sub-halos bound to the Milky Way is large, it is likely that some sub-halo contributes to the local dark matter density. The probability that the Earth is immersed by any single sub-halo is given by

$$P_1 = N_{\text{sh}}\, P_{\text{single}}\, (1 - P_{\text{single}})^{N_{\text{sh}}-1} \approx N_{\text{sh}}\, P_{\text{single}}\, (1 - P_{\text{single}})^{N_{\text{sh}}} \sim 12\% \,. \tag{8.14}$$

Furthermore, the probability that the Earth is currently located within two sub-halos simultaneously is given by

$$P_2 = \binom{N_{\rm sh}}{2} (P_{\rm single})^2 (1 - P_{\rm single})^{N_{\rm sh}-2} \approx \frac{1}{2}(N_{\rm sh}\, P_{\rm single})^2\, P_0 = 0.7\%\,, \tag{8.15}$$

and it is even more unlikely that three or more sub-halos contribute to the local dark matter density in the Solar System at the same time. Therefore, we neglect the possibility that the Earth is located within multiple sub-halos at the same time. We then calculate the probability $P(\tilde{\rho})$ that some sub-halo contributes with $\tilde{\rho}$ to the local dark matter density by rescaling the probability distribution in Eq. (8.12) such that

$$\int \mathrm{d}\rho\, P(\rho) = A \int \mathrm{d}\rho\, P_{\rm single}(\rho) = P_1\,, \tag{8.16}$$

where A is a constant. From this, we obtain the probability distribution $P(\tilde{\rho})$ as

$$P(\tilde{\rho}) = \frac{P_1}{P_{\rm single}}\, P_{\rm single}(\tilde{\rho}), \tag{8.17}$$

which is shown in the right plot of Fig. 29 for the sub-halo mass function from [135]. As depicted in the plot, there is a probability of 0.1 % to find an overdensity $\tilde{\rho}$ that is equal to the dark matter density expected from the smooth background halo. Larger contributions are more unlikely, e.g. for an overdensity as large as $10\,\rho^{\rm loc}_{\rm SHM}$ we find a probability of 10^{-3} %. In Fig. 29, we also show the probability distributions derived from the sub-halo mass function of [135] when neglecting contributions from sub-halos lighter than $10^5\,M_\odot$. This is approximately the resolution of current N-body simulations. As apparent from the plot, neglecting light sub-halos decreases the probability to have large overdensities $\tilde{\rho}$ in the solar neighborhood. This is to be expected as a large overdensity is either due to the Earth passing through a heavy sub-halo or a passage close to the center of a sub-halo. The first possibility is well approximated by considering only sub-halos with masses larger than $10^5\,M_\odot$. However, taking into account the full sub-halo mass function results in a significantly larger probability of observing a passage close to the center of a sub-halo. Concretely, neglecting light sub-halos decreases the probability to find $\tilde{\rho}$ as large as $\rho^{\rm loc}_{\rm SHM}$ by a factor of approximately 3. Larger overdensities like $10\ \rho^{\rm loc}_{\rm SHM}$ are suppressed by a factor of ~ 10.

Having calculated the velocity distribution of a dark matter particle bound to a sub-halo as well as the probability distribution for $\tilde{\rho}$, we determine the increment $\mathcal{I}_R$ of the scattering rate due to a sub-halo. More concretely, we consider the experiments XENON1T [221] and CRESST [228] as they offer an interesting comparison between an experiment with a large exposure and an experiment with a low detection threshold. In Fig. 30, we show plots of the probability distributions of $\mathcal{I}_R$ for both experiments and for dark matter masses of 5 GeV, 100 GeV and 10000 GeV. For all dark matter masses and both experiments, we find that there is a probability $\lesssim 7 \cdot 10^{-4}$ for increasing the scattering rate by an $\mathcal{O}(1)$ factor. In order to quantify the impact of the sub-halo mass

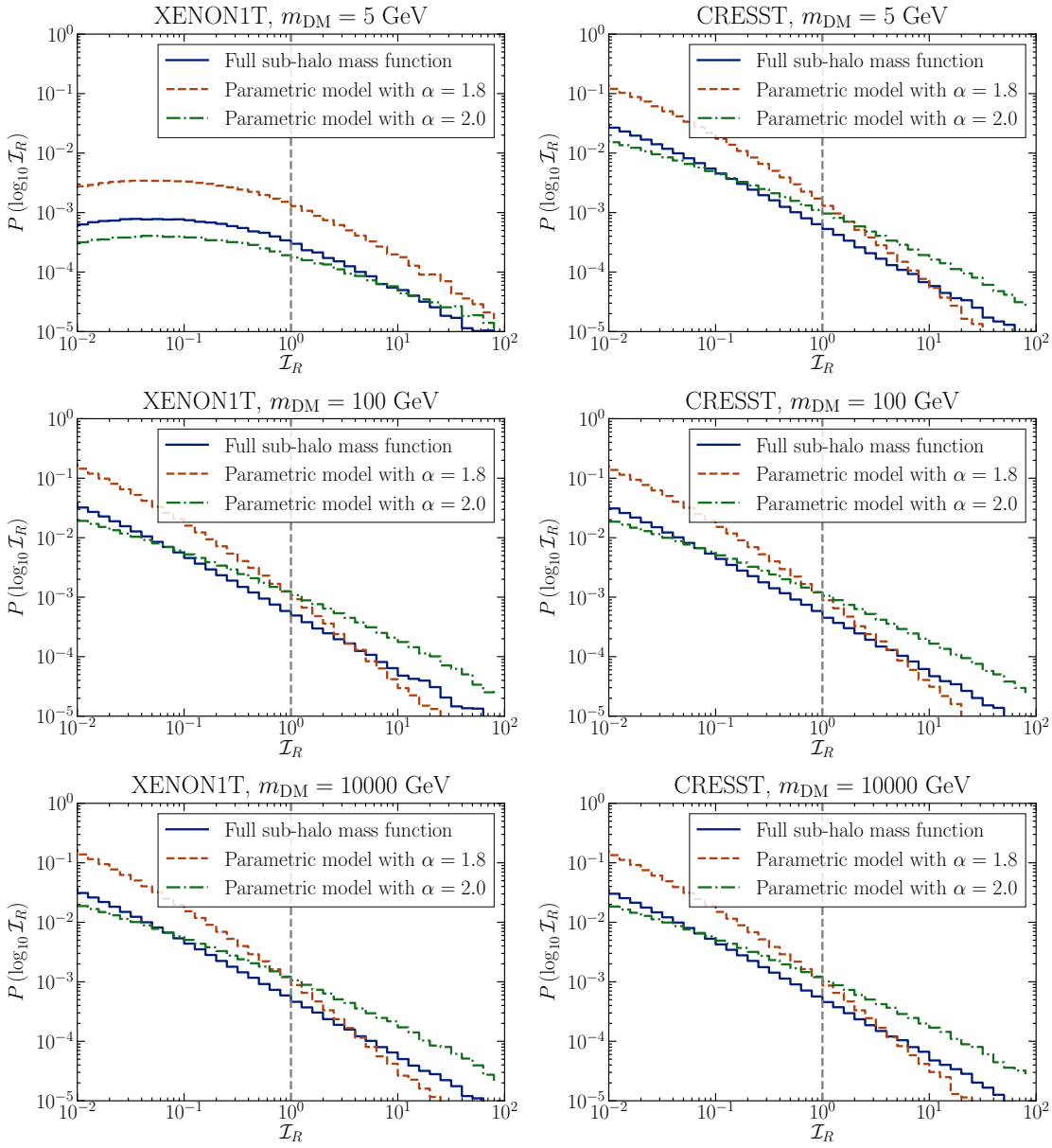

Figure 30.: Probability distributions for the increment $\mathcal{I}_R$ assuming dark matter masses of 5 GeV, 100 GeV and 10000 GeV. The left column of plots shows $P(\mathcal{I}_R)$ for XENON1T [221] and the right column for CRESST [228]. In all plots, we use the `DDCalc` [326, 327] package to compute the detector responses. A gray dashed line indicates the probability for an $\mathcal{O}(1)$ enhancement of the scattering rate. These plots were taken from [5].

function, we also analyze two parametric models where $\mathrm{d}N/\mathrm{d}M$ follows a power law $\propto M^{-1.8}$ respectively $\propto M^{-2.0}$. The choices of the power law indices are motivated by the upper and lower limits of the parameter $\alpha(M)$ from [135]. We show this in the right plot of Fig. 26. When considering those parametric models, we find that the probability to have an $\mathcal{O}(1)$ ($\mathcal{O}(10)$) enhancement of the scattering rate can be a factor of ~ 3 (~ 4) larger than obtained with the full sub-halo mass function from Fig. 26.

8.2. Enhancement of the neutrino signal from the Sun

The idea that dark matter substructure might influence the capture of dark matter in celestial bodies like the Sun was first introduced in [361]. As discussed in detail in section 3.3.2, dark matter particles that traverse the Sun lose energy via scatterings with nuclei in the Sun. If the energy loss is large enough, the dark matter particle is captured gravitationally by the Sun. Here, we write the capture rate of dark matter particles in the Sun, confer equation (3.57), in a time-dependent way by defining it in terms of the flux of dark matter particles at the position of the Sun from Eq. (8.4):

$$C(t) = \sum_i \int_0^{R_\odot} 4\pi\, r^2\, \mathrm{d}r\, \eta_i(r) \int_{v \leq v_{\mathrm{max},i}^{(\mathrm{Sun})}(r)} \mathrm{d}^3 v\, \frac{F(\vec{v},t)}{v^2}\, w^2(r) \int_{m_{\mathrm{DM}} v^2/2}^{2\mu_{T_i}^2 w^2(r)/m_{T_i}} \mathrm{d}E_R\, \frac{\mathrm{d}\sigma_i}{\mathrm{d}E_R}(w(r), E_R)\,. \tag{8.18}$$

We determine the number density of the ith nuclear species from the Solar model AGSS09 [254]. Furthermore, we consider spin-independent and spin-dependent interactions for the differential scattering cross section $\mathrm{d}\sigma_i/\mathrm{d}E_R$. Concretely, we assume the Helm form factor [185, 187] for spin-independent interactions and the form factors from Ref. [207] for spin-dependent interactions.

As the number of dark matter particles captured by the Sun changes over time, we describe it by the differential equation

$$\frac{\mathrm{d}N(t)}{\mathrm{d}t} = C(t) - C_A N(t)^2\,, \tag{8.19}$$

as discussed in section 3.3.2. We neglect the evaporation off nuclei in the Sun as we are interested in dark matter particles heavier than 4 GeV [261]. Furthermore, the constant C_A quantifies how efficient dark matter particles are depleted via annihilation. We calculate this following the procedure discussed in Refs. [249, 256] as well as summarized in section 3.3.2. In the case of a smooth and constant Milky Way dark matter distribution described by the SHM, the capture rate is constant over time, i.e. $C(t) = C_{\mathrm{SHM}}$. In the following, we define the time $t = 0$ as the time of the formation of the Sun and therefore $N(t = 0) = 0$. For a time-independent capture rate C_{SHM}, the solution of Eq. (8.19) is

given by

$$N(t) = \sqrt{\frac{C_{\rm SHM}}{C_A}} \tanh\left(\frac{t}{\tau}\right) = N_{\rm SHM} \tanh\left(\frac{t}{\tau}\right) , \tag{8.20}$$

where $\tau = 1/\sqrt{C_{\rm SHM}\, C_A}$ is the equilibration time. If equilibrium between capture and annihilation of dark matter particles is achieved, i.e. $t \gg \tau$, the number of dark matter particles in the Sun becomes constant and is equal to $N_{\rm SHM} \equiv \sqrt{C_{\rm SHM}/C_A}$.

As discussed in section 3.3.2, the annihilation rate today at $t = t_0 \simeq 4.6$ Gyr is given by

$$\Gamma_A = \frac{1}{2}\, C_A\, N(t_0)^2 \,, \tag{8.21}$$

where $N(t_0)$ is the number of dark matter particles captured in the Sun today. In the case of the time-independent capture rate from the constant Milky Way dark matter distribution $C(t) = C_{\rm SHM}$, the annihilation rate is given by the simple formula

$$\Gamma_A = \frac{C_{\rm SHM}}{2}\, \tanh^2\left(\frac{t_0}{\tau}\right) \xrightarrow{t_0 \gg \tau} \frac{C_{\rm SHM}}{2} \,. \tag{8.22}$$

In the limit that equilibrium is achieved until current times, i.e. $t_0 \gg \tau$, there is one annihilation event per two captured particles. This simple relation is often used when converting the capture rate that is predicted by a given dark matter model to the annihilation rate constrained by neutrino telescopes. However, there are cases where equilibrium is not achieved, for example in scenarios in which the annihilation rate is p-wave suppressed [362] or for very small dark matter-nucleus cross sections. As a consequence of this, the annihilation signal is suppressed by a factor $\tanh^2\left(\frac{t_0}{\tau}\right)$ and Eq. (8.22) overestimates the strength of the annihilation signal.

8.2.1. Impact of a single sub-halo encounter

On top of the smooth Milky Way dark matter density, we consider an additional, time-dependent contribution from sub-halos. For one single sub-halo encounter between $t = t_-$ and $t = t_+$, the capture rate of dark matter particles in the Sun is given by

$$C(t) = C_{\rm SHM} + C_{\rm sh}(t)\Theta(t - t_-)\Theta(t_+ - t) \,, \tag{8.23}$$

where $C_{\rm sh}(t)$ denotes the capture rate from the sub-halo. As an approximation, we only deal with complete sub-halo passages of the Sun, i.e. the Sun enters and exits the sub-halo. Therefore, we replace the time-dependent capture rate from the sub-halo $C_{\rm sh}(t)$ by its mean value between $t = t_-$ and $t = t_+$

$$C_{\rm sh}(t) \simeq \langle C_{\rm sh}(t) \rangle \equiv \frac{1}{\Delta t} \int_{t_-}^{t_+} {\rm d}t\, C_{\rm sh}(t) \,. \tag{8.24}$$

That is, we approximate the time-dependent deviations of the capture rate by step functions with height $\langle C_{\rm sh}(t) \rangle$ for $t_- \leq t \leq t_+$.

Under this approximation, we solve Eq. (8.19) analytically which yields

$$N(t) = \begin{cases} \sqrt{\frac{C_{\rm SHM}}{C_A}} \tanh\left(\frac{t}{\tau}\right) & \text{if } t \leq t_- \,, \\ \sqrt{\frac{C_{\rm SHM}}{C_A}} \frac{\tanh\left(\frac{t_-}{\tau}\right) + \sqrt{1+\frac{\langle C_{\rm sh}(t)\rangle}{C_{\rm SHM}}} \tanh\left\{\sqrt{1+\frac{\langle C_{\rm sh}(t)\rangle}{C_{\rm SHM}}} \frac{(t-t_-)}{\tau}\right\}}{1+\left(\sqrt{1+\frac{\langle C_{\rm sh}(t)\rangle}{C_{\rm SHM}}}\right)^{-1} \tanh\left(\frac{t_-}{\tau}\right) \tanh\left\{\sqrt{1+\frac{\langle C_{\rm sh}(t)\rangle}{C_{\rm SHM}}} \frac{(t-t_-)}{\tau}\right\}} & \text{if } t_- < t \leq t_+ \,, \\ \frac{N(t_+) + \sqrt{\frac{C_{\rm SHM}}{C_A}} \tanh\left(\frac{t-t_+}{\tau}\right)}{1+N(t_+)\left(\sqrt{\frac{C_{\rm SHM}}{C_A}}\right)^{-1} \tanh\left(\frac{t-t_+}{\tau}\right)\Big]} & \text{if } t > t_+ \,, \end{cases} \tag{8.25}$$

where $\tau = \sqrt{C_{\rm SHM}\, C_A}$ is the equilibration time expected from the smooth Milky Way dark matter distribution. In this solution, we identify three dimensionless quantities that fully parametrize $N(t)$ after the Sun has left the sub-halo: The duration of the passage relative to the equilibration time $\Delta t/\tau$, the time elapsed after leaving the sub-halo relative to the equilibration time $(t_0 - t_+)/\tau$ and the time averaged capture rate from the sub-halo relative to the capture rate from the smooth background $\langle C_{\rm sh}(t)\rangle / C_{\rm SHM}$. The latter depends on the properties of the sub-halo as well as the dark matter model under consideration and is calculated for each sub-halo individually. The passage time relative to the equilibration time can be estimated independently of the sub-halo properties. Given an impact parameter L and assuming that the Sun crosses the sub-halo following a straight line, the distance the Sun travels inside the sub-halo is $\Delta d = 2\sqrt{r_t^2 - L^2}$. For the Sun moving with velocity $v_{\rm rel}$ with respect to the sub-halo, the time spent within the sub-halo is given by $\Delta t = \Delta d / v_{\rm rel}$. For dark matter models of interest, the equilibration time is of the order of the age of the Sun $\tau \lesssim t_0$ and hence

$$\frac{\Delta t}{\tau} \leq \frac{2\, r_t}{v_{\rm rel}\, \tau} \simeq \frac{2\, r_t}{v_\odot\, t_0} \ll 1 \,, \tag{8.26}$$

where we used that $v_{\rm rel} \simeq v_\odot$. This also holds in the case that capture and annihilation are out of equilibrium as this implies $\tau \gg t_0$. Therefore, the approximation $\Delta t/\tau \ll 1$ is valid unless there are sub-halos whose diameter is larger than the distance the Sun traveled since her formation. This is not the case for the sub-halos predicted by the sub-halo mass function of [135].

In this limit, the number of captured dark matter particles after the Sun leaves the sub-halo is given by

$$\begin{aligned} N(t) &= N_{\rm SHM}\ \tanh\left[\frac{t-t_-}{\tau} + \operatorname{artanh}\left(\frac{N(t_-)+\Delta N}{N_{\rm SHM}}\right)\right] \\ &\simeq N_{\rm SHM}\Big[\frac{(N(t_-)+\Delta N)/N_{\rm SHM} + \tanh\frac{t-t_-}{\tau}}{1+(N(t_-)+\Delta N)/N_{\rm SHM}\tanh\frac{t-t_-}{\tau}}\Big] \,, \end{aligned} \tag{8.27}$$

where $N(t_-)$ is the number of captured particles at the time the Sun entered the sub-halo. Furthermore, ΔN is the number of particles captured from the sub-halo during the passage. This, in turn, is equivalent to the product of the average capture rate from the

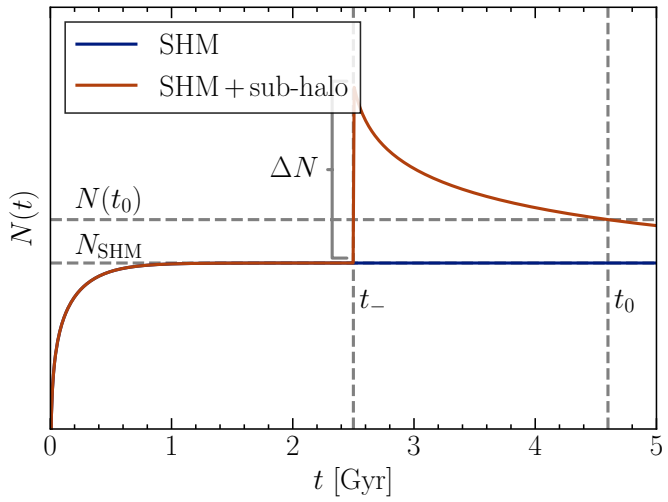

Figure 31.: In this plot, we sketch time evolution of the number of dark matter particles in the Sun. We indicate the time the Sun enters the sub-halo as well as the current time as gray dashed vertical lines. We furthermore denote by gray dashed horizontal lines the number of captured particles from the smooth background dark matter distribution as well as the number of particles captured when additionally assuming a sub-halo encounter. This plot was taken from [5].

sub-halo and the time spent inside the sub-halo, i.e.

$$\Delta N \equiv \langle C_{\rm sh}(t) \rangle \, \Delta t \,. \tag{8.28}$$

In Fig. 31, we show a sketch of the number of captured particles as a function of time. As depicted in this figure, large increments occur when the number of particles captured from the stream is large or in the case of a recent encounter, i.e. $(t_0 - t_+)/\tau \ll 1$.

Under the assumption that the velocity distribution of dark matter particles bound to the sub-halo is well approximated by a stream as given in Eq. (8.3), we rewrite Eq. (8.28) into

$$\Delta N = C^{\rho_{\rm SHM}}_{\delta(\vec{v}+\vec{v}_{\rm rel})} \frac{\langle \rho^{\rm loc}_{\rm sh}[r(t)] \rangle}{\rho_{\rm SHM}} \Delta t \,, \tag{8.29}$$

where $C^{\rho_{\rm SHM}}_{\delta(\vec{v}+\vec{v}_{\rm rel})}$ is the capture rate given a stream with velocity $\vec{v}_{\rm rel}$ and dark matter density $\rho_{\rm SHM}$. We show the dependence of the capture rate on the velocity of the stream in Fig. 32. Furthermore, $\langle \rho^{\rm loc}_{\rm sh}[r(t)] \rangle$ is the dark matter density of the sub-halo averaged along the path of the Sun through the sub-halo. For a constant impact parameter and assuming that the relative velocity between the Sun and the sub-halo is constant over time, we approximate this quantity as

$$\langle \rho^{\rm loc}_{\rm sh}[r(t)] \rangle \simeq \frac{1}{\Delta t} \int_{t_-}^{t_+} {\rm d}t \, \rho^{\rm loc}_{\rm sh}[r(t)] = \frac{1}{2\sqrt{r_t^2 - L^2}} \int_{-\sqrt{r_t^2-L^2}}^{\sqrt{r_t^2-L^2}} {\rm d}x \, \rho^{\rm loc}_{\rm sh}[\sqrt{x^2 + L^2}] \,. \tag{8.30}$$

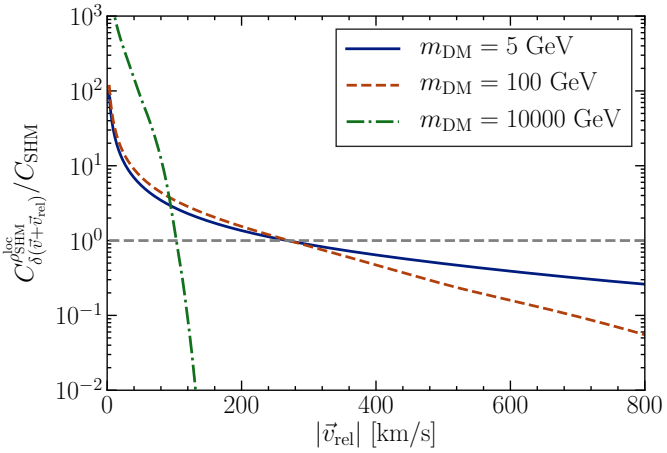

Figure 32.: Capture rate for a stream with velocity $|\vec{v}_{\rm rel}|$ in the rest frame of the Sun and a local dark matter density $\rho^{\rm loc}_{\rm SHM}$. A gray dashed line separates the plot into two regions, where the scattering rate is enhanced (suppressed) with respect to the SHM in the upper (lower) part of the plot. This plot was taken from [5].

Here, we used that the time spent by the Sun inside the sub-halo is given by $\Delta t = 2\sqrt{r_t^2 - L^2}$. Using the NFW profile from Eq. (2.19) and defining $z \equiv L/r_t$, we rewrite this into

$$\langle \rho^{\rm loc}_{\rm sh}[r(t)] \rangle = \frac{\rho_s}{(1-c_V^2 z^2)} \left[\frac{2}{c_V \sqrt{1-z^2}\sqrt{1-c_V^2 z^2}} \operatorname{artanh}\left(\frac{\sqrt{1-z^2}\sqrt{1-c_V^2 z^2}}{(1+z)(1+c_V z)} \right) - \frac{1}{1+c_V} \right] . \tag{8.31}$$

In the limiting cases of $L \ll r_s$ and $L \gg r_s$, we simplify this to be solely dependent on L, c_V and r_t

$$\langle \rho^{\rm loc}_{\rm sh}[r(t)] \rangle \simeq \begin{cases} \dfrac{\rho_s}{c_V(1+c_V)^2}\left[1 + \dfrac{2}{3}\left(\dfrac{1+3c_V}{1+c_V}\right)\left(1 - \dfrac{L}{r_t}\right)\right] & \text{for } r_t > L \gg r_s \\ -\dfrac{\rho_s}{c_V}\left[\log\dfrac{L}{r_s} + \dfrac{c_V}{1+c_V} - \log\dfrac{c_V}{1+c_V} - \log 2\right] & \text{for } L \ll r_s\,. \end{cases} \tag{8.32}$$

As expected for a cuspy profile like the NFW, the mean dark matter density diverges in the limit $L \to \infty$ and the largest enhancement occurs for passages of the Sun close to the sub-halo center.

Following the same rationale as in section 8.1, we define the increment $\mathcal{I}_\Gamma$ of the annihilation rate as

$$\mathcal{I}_\Gamma = \frac{\Gamma(t_0)}{\Gamma_{\rm SHM}(t_0)} - 1 \simeq \left[\frac{(N(t_-) + \Delta N)/N_{\rm SHM} + \tanh\frac{t_0 - t_-}{\tau}}{1 + (N(t_-) + \Delta N)/N_{\rm SHM}\tanh\frac{t_0-t_-}{\tau}}\right]^2 \tanh\left(\frac{t_0}{\tau}\right)^{-2} - 1\,, \tag{8.33}$$

where $\Gamma_{\rm SHM}(t_0) = \frac{1}{2} C_{\rm SHM} \tanh(t_0/\tau)$ is the annihilation rate expected from the smooth Milky Way dark matter distribution. In Fig. 33, we show the increment as a function

of $(t_0 - t_-)/\tau$ and ΔN. For this, we assume that capture and annihilation processes were in equilibrium before the Sun entered the sub-halo and would be in equilibrium when considering solely the smooth Milky Way dark matter distribution. Concretely, this implies $N(t_-) = N_{\rm SHM}$ as well as $\tanh(t_0/\tau) = 1$. As apparent from this figure, large increments occur for large $\Delta N/N_{\rm SHM}$ and when the Sun recently left the sub-halo, i.e. for small $(t_0 - t_-)/\tau$. If equilibrium is not achieved at the time the Sun entered the sub-halo, the increment is even larger since $N(t_-) < N_{\rm SHM}$. This is especially relevant for capture of dark matter in the Earth as equilibration is usually not achieved there.

Similar to section 8.1, we derive the probability distribution for the number ΔN of particles captured from the sub-halo. The probability to find a certain ΔN along with M, c_V and $v_{\rm rel}$ is related to the probability of crossing the sub-halo with an impact parameter L via

$$P(\Delta N, M, c_V, v_{\rm rel}) = P(L, M, c_V, v_{\rm rel}) \left| \frac{\mathrm{d}\Delta N(L, M, c_V, v_{\rm rel})}{\mathrm{d}L} \right|^{-1} \quad \text{for } L < r_t \,. \tag{8.34}$$

As apparent from Eq. (8.29), ΔN depends on L via $\langle \rho_{\rm sh}^{\rm loc}[r(t)] \rangle$ as given in Eq. (8.30) and via the duration of the sub-halo encounter $\Delta t = 2\sqrt{r_t^2 - L^2}/v_{\rm rel}$. The probability $P(L, M, c_V, v_{\rm rel})$ that the Sun encounters a sub-halo characterized by M, c_V and $v_{\rm rel}$ with an impact parameter L is given by

$$P(L, M, c_V, v_{\rm rel}) = P(M) P(c_V|M) P(v_{\rm rel}) P(L|M, c_V, v_{\rm rel}) \,, \tag{8.35}$$

where $P(M)$ and $P(c_V|M)$ are discussed in detail in section 8.1. In addition to this, the probability $P(L|M, c_V, v_{\rm rel})$ that the Sun traverses a sub-halo with impact parameter L given M, c_V and $v_{\rm rel}$ is equal to the probability to find the center of such a sub-halo at a perpendicular distance L from the Sun's path during passage time Δt. This is equal to the number of sub-halos in a cylindrical shell with radius L, length $v_{\rm rel}\Delta t$ and thickness $\mathrm{d}L$ divided by the total number of sub-halos $N_{\rm sh}$. We approximate the amount of sub-halos inside the cylindrical shell as

$$\mathrm{d}N_{\rm sh}(L, M, c_V, v_{\rm rel}) \simeq 2\pi L \mathrm{d}L \, v_{\rm rel} \Delta t \, \bar{n}_{\rm sh}(L) \,. \tag{8.36}$$

With this, we finally obtain the probability for the Sun passing the sub-halo center with impact parameter L as

$$P(L|M, c_V, v_{\rm rel}) \equiv \frac{1}{N_{\rm sh}} \frac{\mathrm{d}N_{\rm sh}(L, M, c_V, v_{\rm rel})}{\mathrm{d}L} \simeq \frac{2\pi L v_{\rm rel} \Delta t \, \bar{n}_{\rm sh}(L)}{N_{\rm sh}} \,. \tag{8.37}$$

Here, $\bar{n}_{\rm sh}(L)$ is the average number of sub-halos at a perpendicular distance L from the trajectory of the Sun

$$\bar{n}_{\rm sh}(L) = \frac{1}{2\pi} \int_0^{2\pi} n_{\rm sh}\left[r(L, \psi)\right] \, \mathrm{d}\psi \,, \tag{8.38}$$

parametrized in terms of the galactocentric radius r.

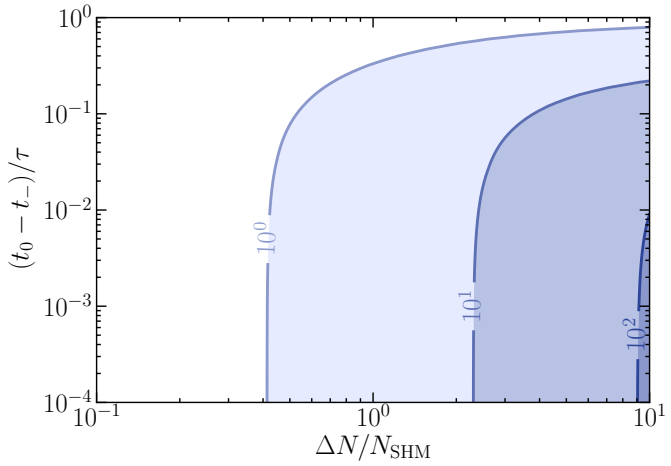

Figure 33.: Increment of the annihilation rate from one sub-halo encounter as a function of $(t_0 - t_-)/\tau$ and $\Delta N/N_{\mathrm{SHM}}$. The white region indicates parameters for which $\mathcal{I}_\Gamma < 1$ while the colored regions indicate larger increments. In this plot, we explicitly assume that capture and annihilation of dark matter particles in the Sun were in equilibrium prior to the encounter with the sub-halo. This plot was taken from [5].

From Eq. (8.35) we finally obtain the probability distribution of the number ΔN of captured particles from any sub-halo by marginalizing M, c_V and v_{rel}

$$P_{\mathrm{single}}(\Delta N) = \int_{M_{\mathrm{min}}}^{M_{\mathrm{max}}} \mathrm{d}M \int_0^\infty \mathrm{d}c_V \int_0^{v_{\mathrm{max}}} \mathrm{d}v_{\mathrm{rel}}\, P(\Delta N, M, c_V, v_{\mathrm{rel}})\,. \tag{8.39}$$

In Fig. 34, we show the probability distributions for $(\Delta N/N_{\mathrm{SHM}}) \cdot (\tau/t_0)$ assuming dark matter masses of 5 GeV, 100 GeV and 10000 GeV. We use this quantity instead of $\Delta N/N_{\mathrm{SHM}}$ in order to highlight the impact of equilibration. If dark matter annihilates efficiently, the equilibrium number of captured particles decreases. Therefore, decreasing τ increases the number of particles captured from the sub-halo relative to the equilibrium number, i.e. $\Delta N/N_{\mathrm{SHM}}$. However, this can be canceled by the factor τ/t_0 which behaves in the opposite way. In each plot of Fig. 34, we show the probability distributions for the sub-halo mass function from Ref. [135] and for two parametric models that approximate the halo mass function by a power law $\mathrm{d}N/\mathrm{d}M \sim M^\alpha$ with $\alpha = 1.8$ as well as $\alpha = 2.0$. We find the largest values of ΔN for $\alpha = 1.8$ as this predicts the most heavy sub-halos, confer Fig. 26. Conversely, we observe the smallest amount of particles captured from the sub-halo in the case of $\alpha = 2.0$ for which the sub-halo mass function is steepest. In addition to this, we find that the distributions for heavy dark matter reach larger values of ΔN and are flatter. This is due to the small maximal velocity at which heavy dark matter particles can be captured by the Sun. Therefore, most of the sub-halo encounters give rise to no additionally captured particles. However, if the velocity of the sub-halo with respect to the Sun is small, the factor $\Delta N/N_{\mathrm{SHM}}$ can be large as the number of particles captured from the smooth Milky Way dark matter halo is small for heavy dark matter. This gives rise to the flat tail of the distributions for heavy dark matter.

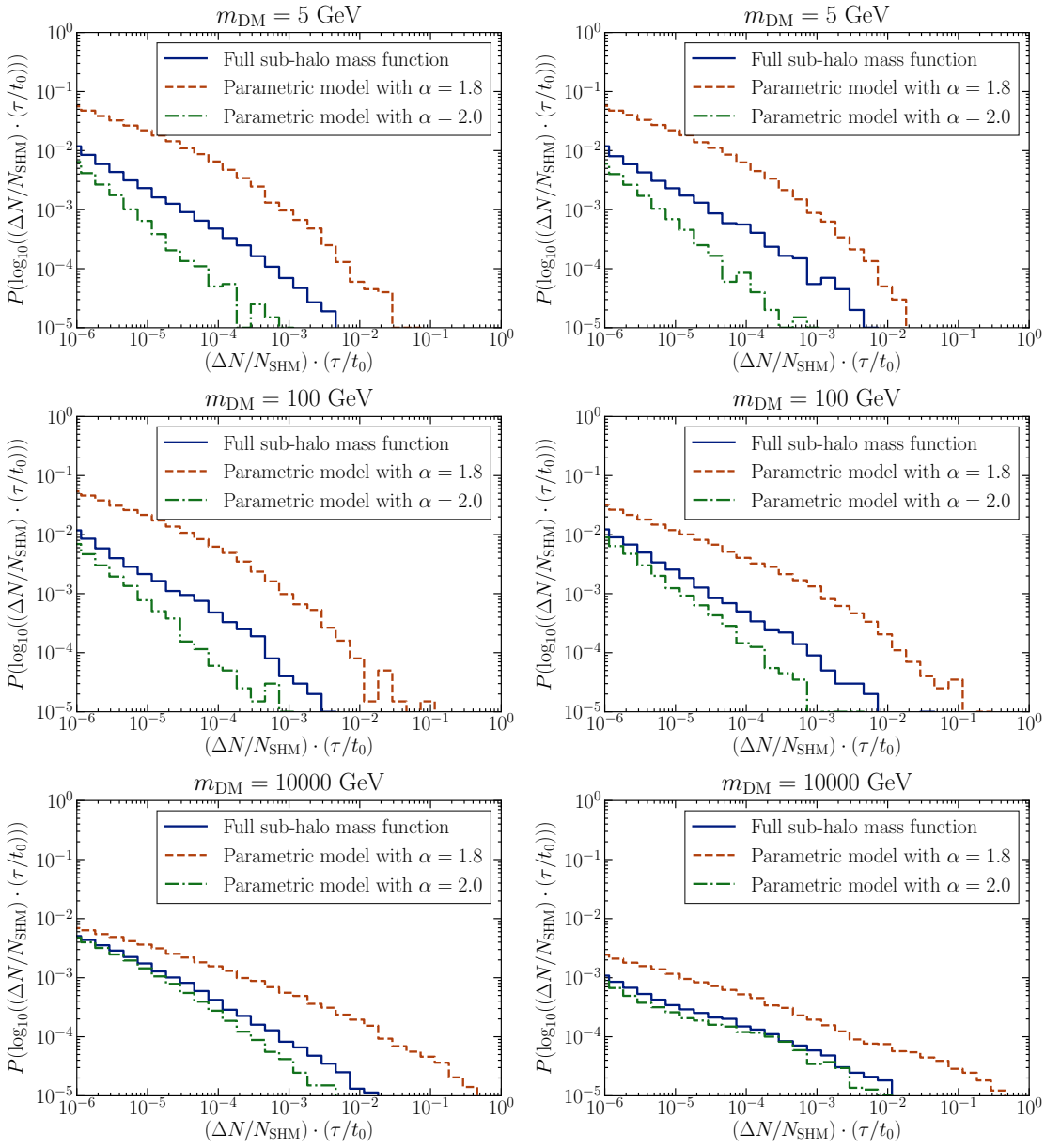

Figure 34.: Impact of a single sub-halo encounter parametrized as $(\Delta N/N_{\mathrm{SHM}}) \cdot (\tau/t_0)$. We include plots for three different dark matter masses and for spin-independent (left) respectively spin-dependent interactions (right). These plots were taken from [5].

8.2.2. Impact of multiple sub-halo encounters

From the large amount of sub-halos predicted by the sub-halo mass functions in Fig. 26, we expect that the Sun traversed multiple sub-halos. In this case, the number of captured particles N(t) and ultimately the annihilation rate could be enhanced further than discussed in the previous section if the Sun encounters a second sub-halo while the number of captured particles still relaxes back into equilibrium. This scenario is shown in Fig. 35

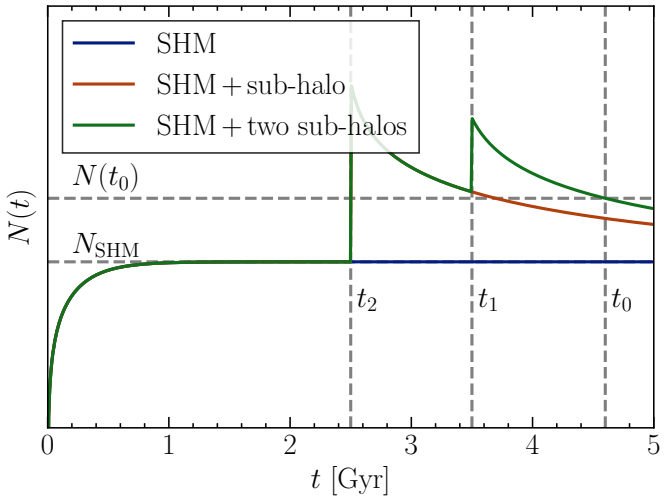

Figure 35.: In this plot, we sketch the time evolution of the number of captured dark matter particles in the Sun for multiple sub-halo encounters. We depict the times the Sun enters a sub-halo as well as the current time as gray dashed vertical lines. We furthermore denote by gray dashed horizontal lines the number of captured particles from solely the smooth background and for the case of two additional sub-halo encounters. This plot was taken from [5].

for two subsequent sub-halo encounters. As a consequence of this, even sub-halo passages which happened far in the past can be relevant today. Since each sub-halo passage could influence the annihilation rate inside the Sun, we expect that we observe a larger increase of the annihilation rate than for the case of single sub-halo encounters.

In order to calculate the increment of the annihilation rate in the sun today, we have to determine the expected number of sub-halo encounters $\mathcal{N}$ of the Sun during her lifetime. We calculate this from Eq. (8.39) via

$$\mathcal{N} = \frac{t_0}{t_{\mathrm{orb}}} N_{\mathrm{sh}} \int_0^\infty \mathrm{d}\Delta N \, P_{\mathrm{single}}(\Delta N) \,, \tag{8.40}$$

where $t_{\mathrm{orb}} = 250\,\mathrm{Myr}$ is the orbital period of the Sun. We show the number of sub-halo passages with an impact parameter smaller than $10^{-3}\,\mathrm{pc}$, $1\,\mathrm{pc}$ respectively $10^{3}\,\mathrm{pc}$ in Fig. 36. As depicted there, the Sun is more likely to cross light sub-halos than heavy ones as expected from the sub-halo mass function in Fig. 26. Furthermore, it is unlikely that the Sun has experienced a close encounter with $L < 10^{-3}$ until present times. In general, we expect that the Sun passed through several sub-halos with mass $M \lesssim 10^{6}\,M_{\odot}$. Despite the fact that heavier sub-halos are larger, it is unlikely that the Sun crossed a

heavy sub-halo until present times, even at large distances, due to their scarcity.

Using this, we determine the number of sub-halo encounters n from a Poisson distribution with mean value $\mathcal{N}$ and generate a large number of realizations to obtain a probability distribution for $\mathcal{I}_\Gamma$. We assume that the encounters happen at times t_i, $i = 1, \ldots, n$, or-

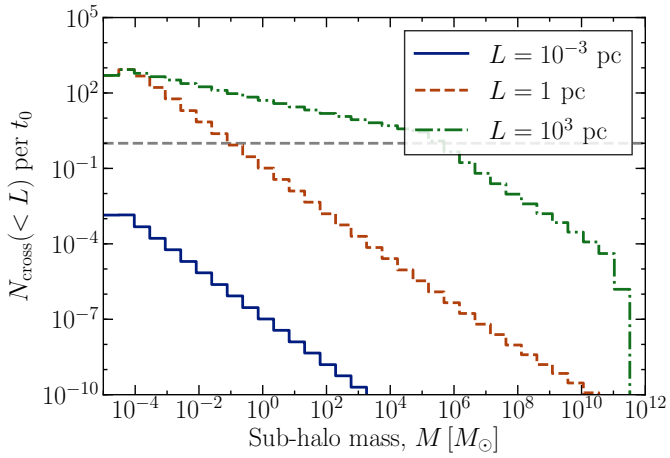

Figure 36.: Number of sub-halo passages with an perpendicular distance L smaller than 10^{-3} pc, 1 pc respectively 10^3 pc. In order to guide the eye, we indicate the value of one sub-halo passage over the lifetime of the Sun with a gray dashed line. This plot was taken from [5].

dered in such a way that $0 < t_n < \cdots < t_0$. Here, t_0 is the age of the Sun and we draw the times of the encounters from a flat distribution on the interval $[0, t_0]$. Assuming, as we did in section 8.2.1, that $\Delta t/\tau \ll 1$ and an initial value $N(t = 0) = 0$, we iteratively solve Eq. (8.19) and obtain the number of particles bound to the Sun today as

$$N(t_0) \simeq N_{\rm SHM}\left[\frac{(N(t_1) + \Delta N_1)/N_{\rm SHM} + \tanh\frac{t_0 - t_1}{\tau}}{1 + (N(t_1) + \Delta N_1)/N_{\rm SHM}\tanh\frac{t_0 - t_1}{\tau}}\right]. \tag{8.41}$$

Here, the number of particles inside the Sun at time t_i before the Sun entered the ith sub-halo is given by

$$N(t_i) \simeq N_{\rm SHM}\left[\frac{(N(t_{i+1}) + \Delta N_{i+1})/N_{\rm SHM} + \tanh\frac{t_i - t_{i+1}}{\tau}}{1 + (N(t_{i+1}) + \Delta N_{i+1})/N_{\rm SHM}\tanh\frac{t_i - t_{i+1}}{\tau}}\right] \quad \text{for } i = 1, \ldots, n\,, \tag{8.42}$$

which, in turn, depends on the previous sub-halo encounter. For a specific dark matter model, we draw the values of ΔN_i from the distributions shown in Fig. 34. Finally, we obtain the increment of the annihilation rate from

$$\mathcal{I}_\Gamma = \frac{\Gamma(t_0)}{\Gamma_{\rm SHM}(t_0)} - 1 \simeq \left(\frac{N(t_0)}{N_{\rm SHM}\,\tanh(t_0/\tau)}\right)^2 - 1\,. \tag{8.43}$$

We show the probability distributions for dark matter masses of 5 GeV, 100 GeV and 10000 GeV in Figs. 37, 38 respectively 39. For each dark matter mass, we determine the probability distributions for three different values of the interaction cross section ranging

down to values that are currently probed by direct detection experiments, confer Fig. 6. In addition to the semi-analytic sub-halo mass function from [135] we show results for two parametric models with $\mathrm{d}N/\mathrm{d}M \sim M^{-\alpha}$.

From Figs. 37, 38 and 39, we observe that large increments $\mathcal{I}_\Gamma$ occur more likely for large cross sections. As apparent from the definition of ΔN in Eq. (8.28), the ratio $(\Delta N/N_{\mathrm{SHM}})$ increases when increasing the scattering cross section. This implies that recent encounters become more important while at the same time the history of sub-halo encounters becomes less important. Therefore, we find that the probability for large increments increases as large values of $\mathcal{I}_\Gamma$ often involve recent encounters. For dark matter-nucleon cross sections smaller than the ones shown here, capture and annihilation processes are far away from equilibration as apparent from Fig. 9. In this case, large increments are possible again as capture from sub-halos can dominate. However, those cross sections cannot be probed even with future upgrades of neutrino telescopes and we do not show results for those here. Finally, we find that the probability to observe large increments is largest for power law sub-halo mass functions with exponent $\alpha = 1.8$ while it is smallest for $\alpha = 2.0$. This is to be expected as the number of heavy sub-halos is larger for a flat sub-halo mass function.

8.3. Discussion and summary

In this chapter, we investigated the impact of dark matter sub-halos on direct detection experiments and neutrino telescopes. We based our calculations on the sub-halo mass function determined in Ref. [135] and used two parametric models with $\mathrm{d}N/\mathrm{d}M \sim M^{-\alpha}$ for $\alpha = 1.8$ and $\alpha = 2.0$ to asses the impact of deviations in the sub-halo mass function. With this, we determined the probability of the Earth being currently immersed in a sub-halo. Furthermore, we investigated the increment of the annihilation rate in the Sun due to sub-halo encounters of the Sun until present days. We did this by drawing a large number of sub-halo passage histories and calculating the annihilation rate by iteratively solving Eq. (8.19).

We found that the impact of dark matter sub-halos can be non-negligible for direct detection experiments, with a probability of 10^{-3} to obtain a $\mathcal{O}(1)$ enhancement of the local dark matter density. We note that our results are consistent with those of previous studies on the impact of sub-halos on direct detection experiments. For example, Ref. [337] estimates that the probability of an $\mathcal{O}(1)$ enhancement in the local density from sub-halos is roughly 1%. Although we found a smaller probability for such an enhancement, uncertainties related to the precise sub-halo mass function could account for that. We calculated the increment of the scattering rate due to sub-halos for two specific direct detection experiments, XENON1T [221] and CRESST [228]. As depicted in Fig. 30, we obtained that the probability for an increment of $\mathcal{O}(1)$ is also roughly 10^{-3} with slightly larger or smaller values possible depending on the dark matter mass and the sub-halo mass function.

For neutrino telescope experiments, we found that the impact of sub-halos is modest. As

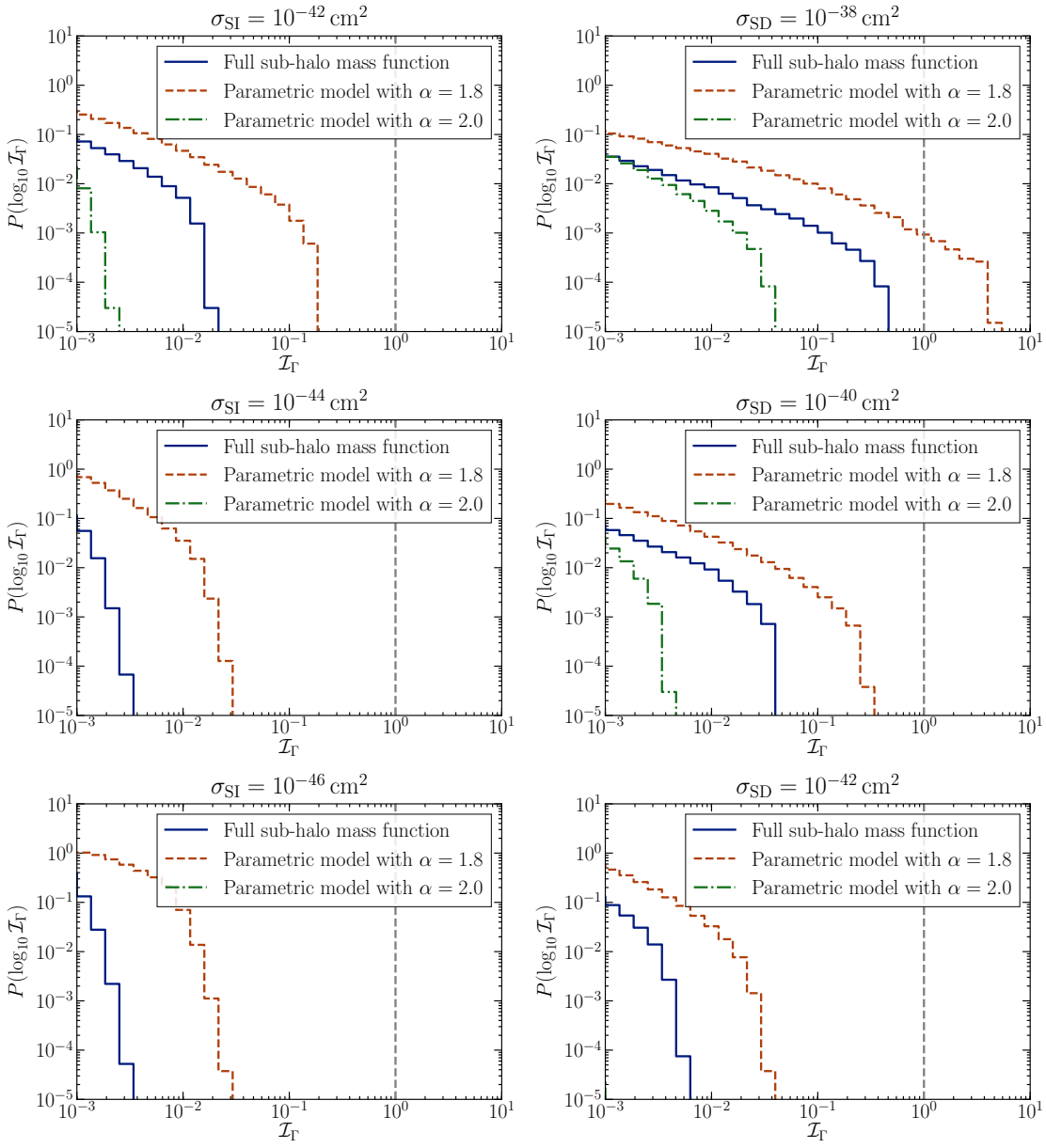

Figure 37.: Probability distributions of $\mathcal{I}_\Gamma$ for spin-independent (left) and for spin-dependent interactions (right) assuming a dark matter mass of 5 GeV. We denote $\mathcal{O}(1)$ increments with a gray dashed line. These plots are taken from [5].

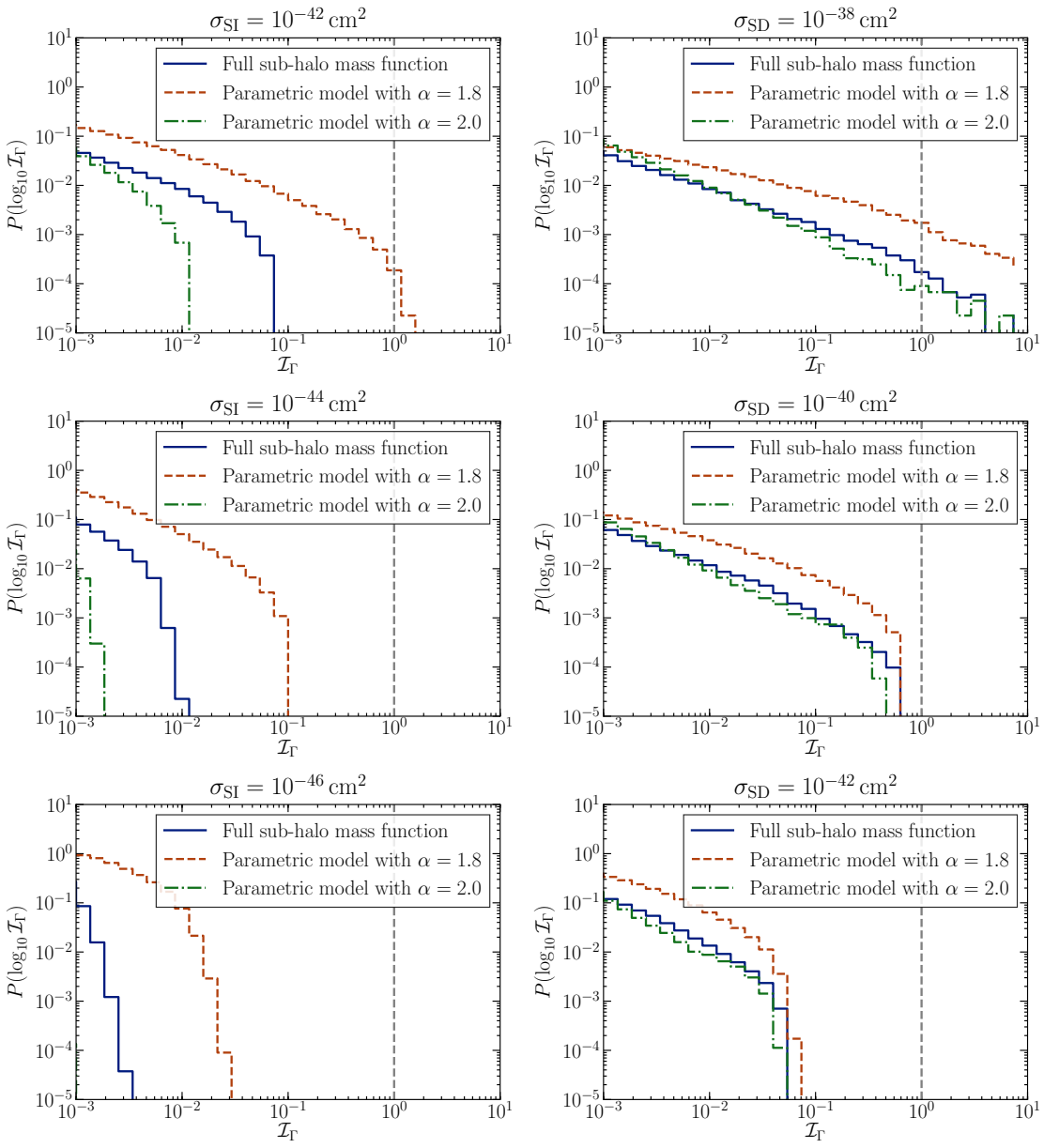

Figure 38.: Same as Fig. 37 but for a dark matter mass of 100 GeV. These plots were taken from [5].

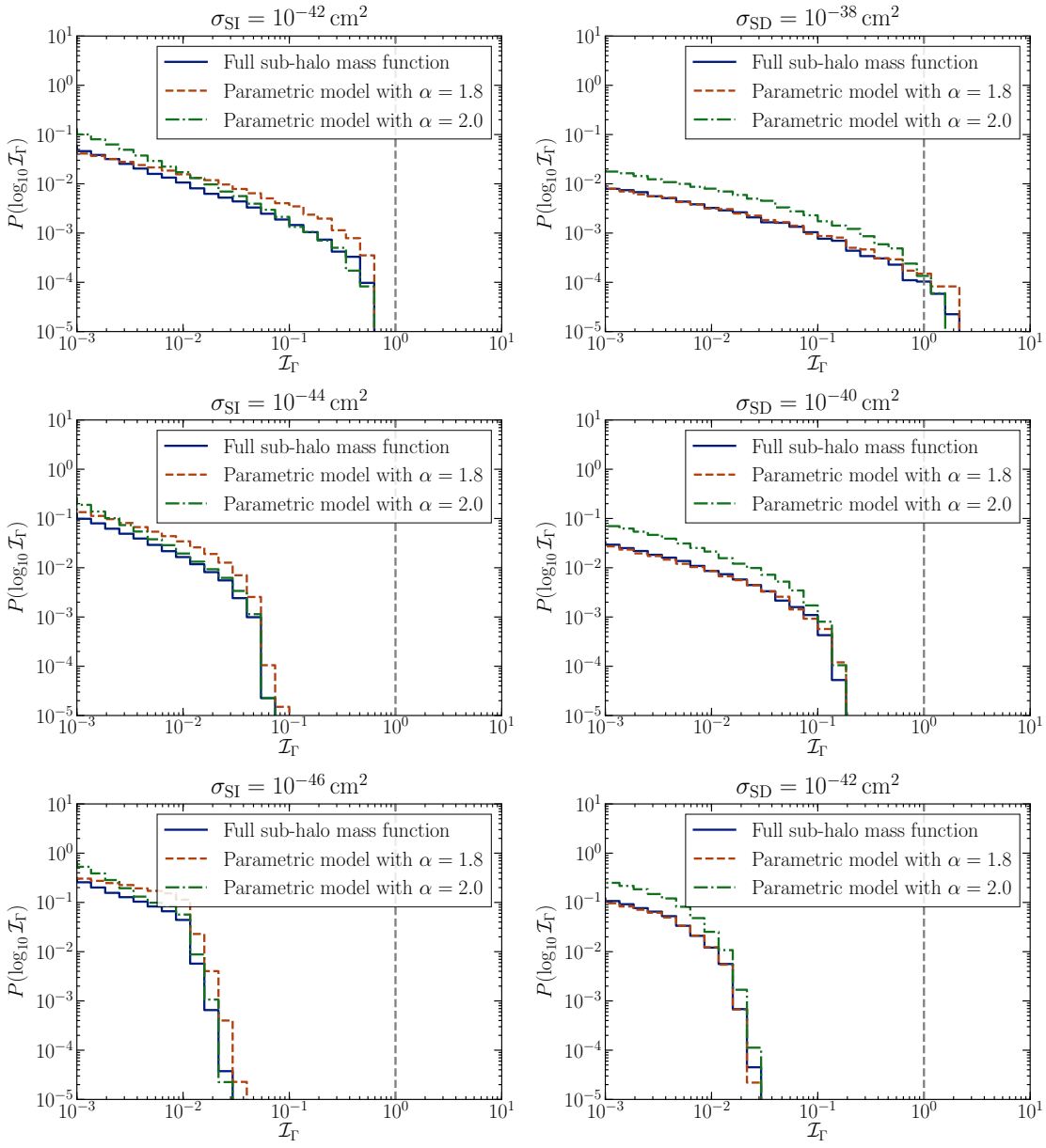

Figure 39.: Same as Fig. 37 but for a dark matter mass of 100 GeV. These plots were taken from [5].

apparent from Figs. 37, 38 respectively 39, $\mathcal{O}(1)$ increments of the neutrino signal from annihilating DM in the Sun have a probability $\lesssim 10^{-5}$. Our results therefore suggest that, for dark matter searches utilizing neutrino telescopes, this source of uncertainty is small in comparison to the astrophysical uncertainties stemming from the local dark matter density and velocity distribution as studied in chapters 4 and 6 respectively in Refs. [363, 364]. Furthermore, Ref. [361] demonstrated that the impact of sub-halos on the neutrino signal from annihilating DM in the Sun can be substantial if the sub-halo is sufficiently dense and the time spent by the Sun inside the sub-halo is sufficiently long. We found that such encounters are rare and that a realistic population of sub-halos is likely to give only a modest enhancement.

In this work, we made several assumptions about the properties of dark matter sub-halos, but the formalism developed here is applicable independent of those assumptions. One major assumption is the NFW dark matter density profile of sub-halos. Recently, Refs. [365,366] claimed that disrupted sub-halos are not well described by an NFW profile but instead suggested an exponential profile $\rho(r) \propto r^{-\gamma} \exp(-r/R_b)$. The parameters γ and R_b are determined from the ELVIS [367] and Via Lactea II simulations [368]. Due to the resolution of those simulations in terms of the sub-halo mass, those parameters can only be determined for sub-halos heavier than $10^7\,M_\odot$. As we observed in Fig. 29 that sub-halos lighter than $10^5\,M_\odot$ contribute to the increment, we did not adopt this density profile in this work. Furthermore, this approach can be applied to other dark matter candidates, different from cold dark matter, that form structures like sub-halos. This includes warm dark matter [369], for which the sub-halo mass function is suppressed for light sub-halos, as well as candidates with special clustering properties [370, 371]. Furthermore, this formalism can be applied to axion searches due to the possibility that axions form mini-clusters [372].

Chapter 9.

Conclusions and outlook

Despite the mounting evidence for dark matter that has accumulated over almost 100 years, dark matter was inferred only through astronomical and cosmological observations. So far, it has not been possible to determine the nature of the dark matter. As the only experiment looking for the distinctive feature of an annual modulation in the recoil rate, DAMA could establish a signal with more than 9σ significance which is compatible with dark matter being constituted by weakly interacting massive particles. However, the WIMP interpretation of this signal is in tension with the null results of other direct dark matter searches. In this thesis, we have therefore investigated the impact of assumptions on the astrophysics of dark matter when interpreting the outcome of two special classes of experiments, direct detection experiments and neutrino telescopes. In particular, we have focused on the class of WIMP dark matter models that predict a signal in both types of experiments. We have also put special emphasis on the complementarity of direct detection experiments and neutrino telescopes highlighting the benefits from combined analyses.

After an introduction to the astro- and particle physics of dark matter as well as to direct dark matter searches, we introduced a method that allows to analyze the results of direct detection experiments and neutrino telescopes completely independent of the halo model. It is based on the decomposition of the dark matter velocity distribution into streams. When using the complementarity of both experimental approaches, we found that the resulting upper limits are remarkably strong and for large masses only one order of magnitude weaker than those obtained with the SHM. Furthermore, we calculated the detection prospects of planned experiments in a halo-independent way considering null results from current experiments and classified the parameter space according to the detection prospects. The region in parameter space that could be tested contains all parameters for which some velocity distribution gives rise to a detectable signal. Similarly, the region that will be tested includes parameters for which the expected signal is large enough to be detected for any velocity distribution. Finally, there is a region that cannot be tested regardless of the velocity distribution.

We then showed that it is possible perform a halo-independent analysis in the context of the non-relativistic effective field theory of dark matter-nucleus interactions. The extended method addresses simultaneously the particle physics uncertainties on the concrete form of the dark matter-nucleon interaction as well as the astrophysical uncertainties on the local dark matter density and velocity distribution. Using the example of the CDMS-

Si signal, we found that this signal is ruled out for any combination of Wilson coefficients except in a small range of dark matter masses between roughly 1 GeV and 8 GeV. However, this region will be tested by next generation experiments, either confirming the signal or ruling it out completely.

In chapter 6, we developed our analysis method further which allows us to calculate the best and the worst signal at an experiment for a given deviation from a reference halo model in a statistically rigorous way. Therefore, we introduced a parameter Δ that parametrizes the deviation from a given reference velocity distribution. The improved method resembles the halo-independent analysis in the limit of very large deviations from the reference distribution. Using this method, we bracketed the effect of a deviation from the SHM on the upper limits derived from direct detection experiments, neutrino telescopes as well as on combined upper limits. Furthermore, we analyzed how the reconstruction of the dark matter mass and the WIMP nucleon cross section is affected by uncertainties in the halo model. In addition to this, we showed that neutrino telescopes improve the reconstruction of dark matter parameters at a direct detection experiment even if no signal is found at a neutrino telescope. Assuming a putative signal at XENON1T, we explicitly calculated the allowed regions in parameters space for various values of the parameter Δ.

As the dark matter interpretation of the DAMA signal is in tension with the null results of other dark matter searches, we analyzed the this signal in-depth in chapter 7. We found that the dark matter interpretation of the annual modulation signal can be excluded in a halo-independent way for spin-independent interactions when using both direct detection experiments and neutrino telescopes. For spin-dependent interactions, it is excluded for dark matter masses smaller than ~ 5 TeV as capture is inefficient for larger dark matter masses. Furthermore, we analyzed the DAMA data of 2018 in a halo-independent and statistically rigorous way. We found that a large region in parameter space is compatible with the modulation signal when being completely agnostic about the velocity distribution. However, we were able to establish lower bounds on the dark matter mass and the scattering cross section. Concretely, we obtained that $m_{\rm DM} \gtrsim 5$ GeV and $\sigma^{\rm p}_{\rm SI} \gtrsim 2 \cdot 10^{-42}\,{\rm cm}^2$ respectively $m_{\rm DM} \gtrsim 5$ GeV and $\sigma^{\rm p}_{\rm SD} \gtrsim 10^{-37}\,{\rm cm}^2$ are required in order to reproduce the modulation signal. We note that the lower bound on the dark matter mass is due to kinematics and the energy threshold $E_{\rm th} \sim 3$ keV of DAMA data released in 2018.

Finally, we investigated a concrete source of astrophysical uncertainties and quantified the effect of dark matter sub-halos on direct detection experiments and neutrino telescopes. Assuming a modern sub-halo mass function that extends to sub-halo masses as light as $10^{-5}\,M_\odot$, we found that $\mathcal{O}(1)$ effects on the recoil rate in direct detection experiments occur with a probability of $\lesssim 7 \cdot 10^{-4}$. Therefore, the influence of dark matter sub-halos on those experiments can be non-negligible. Since direct detection experiments have only been conducted for the last 10 years, the only way to enhance the signal is for Earth to be currently located in a sub-halo. We found that the probability for this is roughly 12%. For neutrino telescopes in contrast, potentially all sub-halo passages of

the Sun could contribute. Therefore, we calculated the probability of an enhancement in the neutrino signal from the Sun by drawing many realizations of the sub-halo crossings of the Sun during her lifetime. We then calculated the increment of the neutrino signal from annihilating DM in the Sun for each individual crossing history. We found that the probability of an $\mathcal{O}(1)$ enhancement is small with a probability of $\lesssim 10^{-5}$. The impact of dark matter sub-halos on the neutrino signal from annihilating DM in the Sun is therefore modest.

Since the analysis methods developed in this work have a broad field of application, we are currently working on some further studies. Concretely, we plan to publish a `Python` module that solves the occuring optimization problems and is built on the `CVXOPT` module [300]. It will be compatible with several external codes like `DDCalc` [326, 327] and `WIMpy_NREFT` [373] that provide the expected recoil rate for direct detection experiments. This makes it possible to analyze the effect of deviations from the SHM on any experiments implemented in external codes or modeled manually by the user. In addition to the distance measure introduced in Eq. 6.1, we are planning to implement additional measures that are motivated by L^p norms or by information theory. Another planned project is to analyze 3 years of IceCube data [250] to set limits on the Wilson coefficients in the non-relativistic effective field theory for dark matter-nucleon scattering presented in section 3.2.3. For this kind of analysis, neutrino telescopes are especially promising as the large number of different target elements in the Sun ensures that all types of dark matter-nucleon interactions can be probed. Finally, CRESST-III data [229] provide an interesting application for the methods developed in this thesis. However, parts of the CRESST background are not fully understood [374], especially the exponential rise of the energy spectrum of the events at low energies. Therefore, the analysis method of choice so far has been the optimum interval method [375] which has never been used in conjunction with halo-independent approaches. In this project, we aim to close this gap and analyze CRESST-III data using the optimum interval method but simultaneously study the impact of deviations from the SHM.

In summary, the hunt for dark matter is one of the most active fields of physics. In the future, planned experiments for all search strategies will help to find dark matter or further narrow down the parameter space. Future direct detection experiments aim to significantly increase the target mass and could even reach the neutrino floor. New data releases and upgrades of neutrino telescopes will further improve the sensitivity to WIMP annihilation in the Sun. However, the analysis of those experiments usually involves simplifying assumptions on the local dark matter halo that might not be justified. In light of the expected progress in direct dark matter searches, it is important to keep track of those uncertainties as this could lead to erroneously ruling out parameter space or significantly affect the reconstruction of WIMP parameters. It is therefore important to develop and refine methods that allow to interpret the data of dark matter searches without being prone to unjustified theoretical assumptions. Furthermore, the identification of astrophysical effects that were not accounted for in the past is important to extract the correct information from direct dark matter searches.

Appendix A.

Response functions for non-relativistic dark matter-nucleus scattering

In this appendix, we give the response functions $R_k^{\tau\tau'}$ that appear in the calculation of the transition probability, confer Eq. (3.41). Here, $v_T^{\perp 2}$ is the transverse velocity defined in Eq. (3.42), $m_N \approx 1\,\text{GeV}$ is the mass of a nucleon, q denotes the momentum transfer and j_{DM} is the spin of the dark matter particle. For dark matter particles with spin 0 or $\frac{1}{2}$, we adopt the response functions from Ref. [206] which are given by

$$
\begin{aligned}
R_M^{\tau\tau'}\left(v_T^{\perp 2}, \frac{q^2}{m_N^2}\right) &= c_1^\tau c_1^{\tau'} + \frac{j_{\text{DM}}(j_{\text{DM}}+1)}{3}\left[\frac{q^2}{m_N^2} v_T^{\perp 2} c_5^\tau c_5^{\tau'} + v_T^{\perp 2} c_8^\tau c_8^{\tau'} + \frac{q^2}{m_N^2} c_{11}^\tau c_{11}^{\tau'}\right] \\
R_{\Phi''}^{\tau\tau'}\left(v_T^{\perp 2}, \frac{q^2}{m_N^2}\right) &= \frac{q^2}{4m_N^2} c_3^\tau c_3^{\tau'} + \frac{j_{\text{DM}}(j_{\text{DM}}+1)}{12}\left(c_{12}^\tau - \frac{q^2}{m_N^2} c_{15}^\tau\right)\left(c_{12}^{\tau'} - \frac{q^2}{m_N^2} c_{15}^{\tau'}\right) \\
R_{\Phi''M}^{\tau\tau'}\left(v_T^{\perp 2}, \frac{q^2}{m_N^2}\right) &= c_3^\tau c_1^{\tau'} + \frac{j_{\text{DM}}(j_{\text{DM}}+1)}{3}\left(c_{12}^\tau - \frac{q^2}{m_N^2} c_{15}^\tau\right) c_{11}^{\tau'} \\
R_{\tilde{\Phi}'}^{\tau\tau'}\left(v_T^{\perp 2}, \frac{q^2}{m_N^2}\right) &= \frac{j_{\text{DM}}(j_{\text{DM}}+1)}{12}\left[c_{12}^\tau c_{12}^{\tau'} + \frac{q^2}{m_N^2} c_{13}^\tau c_{13}^{\tau'}\right] \\
R_{\Sigma''}^{\tau\tau'}\left(v_T^{\perp 2}, \frac{q^2}{m_N^2}\right) &= \frac{q^2}{4m_N^2} c_{10}^\tau c_{10}^{\tau'} + \frac{j_{\text{DM}}(j_{\text{DM}}+1)}{12}\Big[c_4^\tau c_4^{\tau'} + \\
&\quad \frac{q^2}{m_N^2}(c_4^\tau c_6^{\tau'} + c_6^\tau c_4^{\tau'}) + \frac{q^4}{m_N^4} c_6^\tau c_6^{\tau'} + v_T^{\perp 2} c_{12}^\tau c_{12}^{\tau'} + \frac{q^2}{m_N^2} v_T^{\perp 2} c_{13}^\tau c_{13}^{\tau'}\Big] \\
R_{\Sigma'}^{\tau\tau'}\left(v_T^{\perp 2}, \frac{q^2}{m_N^2}\right) &= \frac{1}{8}\left[\frac{q^2}{m_N^2} v_T^{\perp 2} c_3^\tau c_3^{\tau'} + v_T^{\perp 2} c_7^\tau c_7^{\tau'}\right] + \frac{j_{\text{DM}}(j_{\text{DM}}+1)}{12}\Big[c_4^\tau c_4^{\tau'} + \\
&\quad \frac{q^2}{m_N^2} c_9^\tau c_9^{\tau'} + \frac{v_T^{\perp 2}}{2}\left(c_{12}^\tau - \frac{q^2}{m_N^2} c_{15}^\tau\right)\left(c_{12}^{\tau'} - \frac{q^2}{m_N^2} c_{15}^{\tau\prime}\right) + \frac{q^2}{2m_N^2} v_T^{\perp 2} c_{14}^\tau c_{14}^{\tau'}\Big] \\
R_{\Delta}^{\tau\tau'}\left(v_T^{\perp 2}, \frac{q^2}{m_N^2}\right) &= \frac{j_{\text{DM}}(j_{\text{DM}}+1)}{3}\left[\frac{q^2}{m_N^2} c_5^\tau c_5^{\tau'} + c_8^\tau c_8^{\tau'}\right] \\
R_{\Delta\Sigma'}^{\tau\tau'}\left(v_T^{\perp 2}, \frac{q^2}{m_N^2}\right) &= \frac{j_{\text{DM}}(j_{\text{DM}}+1)}{3}\left[c_5^\tau c_4^{\tau'} - c_8^\tau c_9^{\tau'}\right] .
\end{aligned}
\tag{A.1}
$$

Furthermore, the response functions for spin 1 particles are taken from Ref. [208] and read

$$
R_M^{\tau\tau'}\left(v_T^{\perp 2}, \frac{q^2}{m_N^2}\right) = c_1^\tau c_1^{\tau'} + \frac{2}{3}\left[\frac{q^2}{m_N^2} v_T^{\perp 2} c_5^\tau c_5^{\tau'} + v_T^{\perp 2} c_8^\tau c_8^{\tau'} + \frac{q^2}{m_N^2} c_{11}^\tau c_{11}^{\tau'} + \frac{q^2\, v_T^{\perp 2}}{4\, m_N^2} c_{17}^\tau c_{17}^{\tau'}\right]
$$

$$
\begin{aligned}
R_{\Phi''}^{\tau\tau'}\left(v_T^{\perp 2}, \frac{q^2}{m_N^2}\right) &= 0 \\
R_{\Phi''M}^{\tau\tau'}\left(v_T^{\perp 2}, \frac{q^2}{m_N^2}\right) &= 0 \\
R_{\tilde{\Phi}'}^{\tau\tau'}\left(v_T^{\perp 2}, \frac{q^2}{m_N^2}\right) &= 0 \\
R_{\Sigma''}^{\tau\tau'}\left(v_T^{\perp 2}, \frac{q^2}{m_N^2}\right) &= \frac{1}{6} c_4^\tau c_4^{\tau'} + \frac{q^2}{4m_N^2} c_{10}^\tau c_{10}^{\tau'} + \frac{q^2}{12\, m_N^2} c_{18}^\tau c_{18}^{\tau'} \\
R_{\Sigma'}^{\tau\tau'}\left(v_T^{\perp 2}, \frac{q^2}{m_N^2}\right) &= \frac{1}{6}\left[c_4^\tau c_4^{\tau'} + \frac{q^2}{m_N^2} c_9^\tau c_9^{\tau'} + \frac{q^2}{2m_N^2} v_T^{\perp 2} c_{14}^\tau c_{14}^{\tau'} + \frac{q^2}{4m_N^2} c_{18}^\tau c_{18}^{\tau'}\right] \\
R_{\Delta}^{\tau\tau'}\left(v_T^{\perp 2}, \frac{q^2}{m_N^2}\right) &= \frac{2}{3}\left[\frac{q^2}{m_N^2} c_5^\tau c_5^{\tau'} + c_8^\tau c_8^{\tau'} + \frac{q^2}{4m_N^2} c_{17}^\tau c_{17}^{\tau'}\right] \\
R_{\Delta\Sigma'}^{\tau\tau'}\left(v_T^{\perp 2}, \frac{q^2}{m_N^2}\right) &= \frac{2}{3}\left[c_5^\tau c_4^{\tau'} - c_8^\tau c_9^{\tau'}\right] .
\end{aligned}
\tag{A.2}
$$

Appendix B.

Convex optimization

In this appendix, we summarize the key concepts of convex optimization using proper cones and introduce the relevant notation following closely Ref. [323]. Here, we solve convex optimization problems with the `Python` package `CVXOPT` [300] that implements primal-dual path-following interior-points methods. The discussion of those methods is beyond the scope of this work and we refer to Refs. [323, 376] for detailed reviews of interior-point methods. For the special case of linear programming problems, we additionally use the solver implemented in `Mathematica` [299].

In general, a convex optimization problem is defined as

$$\begin{aligned} &\text{minimize:} && f_0(x) \\ &\text{subject to} && f_i(x) \leq 0 \quad \forall i = 1, \ldots, m \\ &&& h_i(x) = 0 \quad \forall i = 1, \ldots, p \end{aligned} \tag{B.1}$$

where $f_i(x) : \mathbb{R}^n \to \mathbb{R}$ and $h_i(x) : \mathbb{R}^n \to \mathbb{R}$ are convex functions. In general, a convex function f has to fulfill the condition

$$f\left(\theta\, y + (1-\theta)\, z\right) \leq \theta\, f(y) + (1-\theta)\, f(z), \tag{B.2}$$

for $y, z \in \mathbb{R}^n$ and $\theta \in [0, 1]$. The vector x contains all primal variables and the function $f_0(x)$ is the objective function. Furthermore, the constraints $f_i(x) \leq 0$ are called inequality constraints while $h_i(x) = 0$ are equality constraints. Finally, a point x that fulfills all constraints is called feasible and the feasible set consists of all those points. If $f_i(x) = 0$ for some feasible x, the constraint is active at x. Conversely, $f_i(x) < 0$ implies that the inequality constraint is inactive.

B.1. Optimality conditions

In the following, we consider only minimization of the objective function. However, a maximization problem can be converted into a minimization problem by multiplying the objective function by a factor of (-1). The minimum of the objective function is called the optimal value $p^\star$ and is defined as

$$p^\star = \inf_x \{ f_0(x) \,|\, f_i(x) \leq 0 \text{ for } i = 1, \ldots, m \;\text{ and }\; h_i(x) = 0 \text{ for } i = 1, \ldots, p \}\,. \tag{B.3}$$

As apparent from this definition of the optimal value, we are interested in the global optimum of the problem presented in Eq. (B.1). However, for the special case of a convex optimization problem, each locally optimal point is also the global optimum which is among the most compelling features of this class of problems. We refer to chapter 4.2.2. of Ref. [323] for a proof of this statement. Furthermore, $x^\star$ is an optimal point if it is feasible and fulfills $f_0(x^\star) = p^\star$. The optimal set is given by

$$X_{\text{opt}} = \{x \,|\, f_i(x) \leq 0 \text{ for } i = 1, \ldots, m \;\text{ and }\; h_i(x) = 0 \text{ for } i = 1, \ldots, p \;\text{ and }\; f_0(x) = p^\star\}\,, \tag{B.4}$$

and contains all optimal points.

The optimal points are subject to several conditions that are an important ingredient for solving the optimization problem. Here, we assume that the optimization problem has a differentiable objective and constraints. In order to derive optimality conditions, it is necessary to define the dual optimization problem first. The Lagrangian of the optimization problem in Eq. (B.1) is given by

$$L(x, \eta, \lambda) = f_0(x) + \sum_{i=1}^{m} \eta_i \, f_i(x) + \sum_{i=1}^{p} \lambda_i \, h_i(x)\,. \tag{B.5}$$

With this, one defines the Lagrange dual function

$$g(\eta, \lambda) = \min_x \, L(x, \eta, \lambda)\,, \tag{B.6}$$

where η and λ are the dual variables. As this function depends linearly on η and λ, it is convex regardless of whether the primal problem is convex or not. The dual problem is then given by

$$\begin{aligned} &\max_{\eta, \lambda} \; g(\eta, \lambda) \\ &\text{Subject to } \eta \geq 0\,, \end{aligned} \tag{B.7}$$

which is always a convex optimization problem. An interesting property of the dual problem is weak duality. This guarantees that the optimal value of the dual problem $g^\star$ is not larger than the optimal value of the primal problem $p^\star$, i.e. $g^\star \leq p^\star$. Under the assumption that the primal problem is convex and that the equality constraints are affine, Slater's condition states that if there is a feasible point x with $f_i(x) < 0$ for $i = 1, \ldots, m$ and $h_i(x) = 0$ for $i = 1, \ldots, p$ then strong duality $g^\star = p^\star$ holds. We refer to section 5.3.2 of Ref. [323] for a proof of this statement. This can also be expressed in terms of the duality gap

$$f_0(x) - g(\eta, \lambda)\,, \tag{B.8}$$

which is zero for the primal and dual optimal points $x^\star, \eta^\star$ and $\lambda^\star$ assuming strong duality.

The duality gap implies

$$f_0(x) - p^\star \leq f_0(x) - g(\eta, \lambda)\,, \tag{B.9}$$

which provides an excellent stopping criterion for algorithms. If there is a solution $x^\star, \eta^\star$ and $\lambda^\star$ that fulfills $f_0(x^\star) = g(\eta^\star, \lambda^\star)$, then these points are guaranteed to be primal respectively dual optimal and the algorithm can be terminated.

Under the assumption of strong duality, the Karush-Kuhn-Tucker (KKT) conditions [294, 295] provide a set of optimality criteria that has to be fulfilled by an optimal solution. As before, we denote a primal optimal point by $x^\star$ and a dual optimal point by $(\eta^\star, \lambda^\star)$. Since $x^\star$ minimizes $L(x, \eta^\star, \lambda^\star)$, the gradient of L with respect to x evaluated at $x^\star$ has to vanish, i.e.

$$\nabla_x L(x, \eta^\star, \lambda^\star)\Big|_{x=x^\star} = \nabla_x f_0(x)\Big|_{x=x^\star} + \sum_{i=1}^{m} \eta_i^\star \, \nabla_x f_i(x)\Big|_{x=x^\star} + \sum_{i=1}^{p} \lambda_i^\star \, \nabla_x h_i(x)\Big|_{x=x^\star} = 0\,, \tag{B.10}$$

which provides one condition for optimality. Following the definition given in Ref. [323], the complete set of KKT conditions is defined as

$$f_i(x^\star) \leq 0 \qquad i = 1, \ldots, m \tag{B.11}$$

$$h_i(x^\star) = 0 \qquad i = 1, \ldots, p \tag{B.12}$$

$$\eta_i^\star \geq 0 \qquad i = 1, \ldots, m \tag{B.13}$$

$$\eta_i^\star \, f_i(x^\star) = 0 \qquad i = 1, \ldots, m \tag{B.14}$$

$$\nabla_x f_0(x)\Big|_{x=x^\star} + \sum_{i=1}^{m} \eta_i^\star \, \nabla_x f_i(x)\Big|_{x=x^\star} + \sum_{i=1}^{p} \lambda_i^\star \, \nabla_x h_i(x)\Big|_{x=x^\star} = 0 \qquad . \tag{B.15}$$

where the first two conditions ensure the feasibility of $x^\star$. The fourth condition is called complementary slackness and implies that $\eta_i^\star$ vanishes if the constraint is not active, i.e. $f_i(x^\star) < 0$. Conversely, $\eta_i^\star$ is non-zero if the ith inequality constraint is active. An optimal solution of Eq. (B.1) has to fulfill this set of equations. Assuming that $x^\star, \eta^\star$ and $\lambda^\star$ fulfill the KKT conditions, the following holds [323]

$$\begin{aligned} g(\eta^\star, \lambda^\star) &= L(x^\star, \eta^\star, \lambda^\star) \\ &= f_0(x^\star) + \sum_{i=1}^{m} \eta_i^\star \, f_i(x^\star) + \sum_{i=1}^{p} \lambda_i^\star \, h_i(x^\star) \\ &= f_0(x^\star)\,, \end{aligned} \tag{B.16}$$

where the first step follows from Eq. (B.10) which implies that $x^\star$ minimizes $L(x, \eta^\star, \lambda^\star)$. In the third step, we used complementary slackness in combination with $h(x^\star) = 0$ as $x^\star$ is feasible. This proves that all points satisfying the KKT conditions are indeed optimal points provided that strong duality holds.

B.2. Generalized inequalities

In this work, we focus on the special case of convex objective functions with generalized inequality constraints. Before discussing generalized inequalities, we introduce the relevant terminology.

A cone $\mathcal{K}$ is defined by the property that for each element $x_1, x_2 \in \mathcal{K}$ and each real number $\theta_1, \theta_2 \geq 0$ the following condition holds

$$\theta_1 x_1 + \theta_2 x_2 \in \mathcal{K}\,. \tag{B.17}$$

This can be extended to the notion of proper cones by demanding that for a cone $\mathcal{K} \subseteq \mathbb{R}^n$ the following additional conditions are satisfied, confer [323]:

- $\mathcal{K}$ is convex, i.e. for each $x_1, x_2 \in \mathcal{K}$ and $\theta \in [0,1]$ we have $\theta x_1 + (1-\theta) x_2 \in \mathcal{K}$.
- $\mathcal{K}$ is closed.
- $\mathcal{K}$ is solid, i.e. it has a nonempty interior.
- $\mathcal{K}$ is pointed, i.e. we have that $x \in \mathcal{K}$ in conjunction with $-x \in \mathcal{K}$ implies $x = 0$.

The partial ordering $P \preceq_{\mathcal{K}} Q$ for $P, Q \in \mathcal{K}$ with respect to the cone $\mathcal{K}$ is defined as

$$P \preceq_{\mathcal{K}} Q \quad \Leftrightarrow \quad P - Q \in \mathcal{K}. \tag{B.18}$$

In a similar way, the strict partial ordering $P \prec_{\mathcal{K}} Q$ for $P, Q \in \mathcal{K}$ is defined as

$$P \prec_{\mathcal{K}} Q \quad \Leftrightarrow \quad P - Q \in \operatorname{int} \mathcal{K}, \tag{B.19}$$

where $\operatorname{int} \mathcal{K}$ denotes the interior of $\mathcal{K}$.

Generalized inequalities extend inequality constraints from standard ordering on $\mathbb{R}^n$, i.e. $G x \leq h$, to partial ordering $G x \preceq_{\mathcal{K}} y$ with respect to a proper cone $\mathcal{K} \subseteq \mathbb{R}^n$. In the following, we additionally assume that the equality constraints $h_i(x)$ are affine functions. Therefore, we extend our definition of the standard minimization problem to generalized inequalities

$$\begin{aligned} \text{minimize:} \quad & f_0(x) \\ \text{subject to} \quad & G x \preceq_{\mathcal{K}} h \\ & A x = b\,. \end{aligned} \tag{B.20}$$

Here, G is a $k \times n$ matrix, h is a $\mathbb{R}^k$ vector, A is a $l \times n$ matrix and b is a $\mathbb{R}^l$ vector. In the following, we drop the subscript $\mathcal{K}$ for convenience.

The most intuitive example of generalized inequality constraints is the non-negative orthant $\mathbb{R}^n_+$. As can be checked with the above conditions, $\mathbb{R}^n_+$ is a proper cone and therefore implies a partial ordering $x \preceq_{\mathbb{R}^n_+} y$. But this partial ordering is nothing but component-wise inequalities of the vectors x and y, i.e. $x_i \leq y_i$ which can be written as matrix-vector inequality $G x \leq h$.

Another familiar proper cone is the set of positive semidefinite matrices $\mathbb{S}_+^n$ that implies the partial ordering $x \preceq_{\mathbb{S}_+^n} y$. Given the set $\mathbb{S}^n$ of symmetric $n \times n$ matrices, the set of positive semidefinite matrices is defined as

$$\mathbb{S}_+^n = \{X \in \mathbb{S}^n \mid v^{\mathrm{T}} X v \geq 0 \quad \forall v \in \mathbb{R}^n\}. \tag{B.21}$$

In order to check that this set is a cone, we first check that it is convex. Assuming that $\theta \in [0,1]$ and $A, B \in \mathbb{S}_+^n$, the linear combination $\theta A + (1-\theta) B$ is indeed a positive semidefinite matrix as

$$v^{\mathrm{T}} \left(\theta A + (1-\theta) B\right) v = \theta v^{\mathrm{T}} A v + (1-\theta) v^{\mathrm{T}} B v \geq 0\,. \tag{B.22}$$

Furthermore, the set is pointed as the only positive semidefinite matrix X for which both X and $-X$ are in $\mathbb{S}_+^n$ is the $n \times n$ matrix made out of only zeros. Finally, $\mathbb{S}_+^n$ is closed and solid. Written down explicitly, the generalized inequalities defined via the set of positive semidefinite matrices are given by

$$A(x) = \sum_{i=1}^{m} A_i x_i \leq B \quad \Leftrightarrow \quad A(x) \preceq_{\mathbb{S}_+^n} B\,, \tag{B.23}$$

where $A_1, \ldots, A_m$ and B are positive semidefinite $n \times n$ matrices and x_i are the primal variables.

Finally, we consider the example of second order cones $\mathcal{Q}^n$. They give rise to the partial ordering $x \preceq_{\mathcal{Q}^n} y$ and are defined as

$$\mathcal{Q}^n = \left\{(x,t) \in \mathbb{R}_+^n | t \geq \|x\|_2\right\}, \tag{B.24}$$

where $\|x\|_2$ denotes the Euclidean norm. In order to show that $\mathcal{Q}^n$ is a proper cone, we first prove that this set is convex. Assuming $\theta \in [0,1]$ and $(t_1, x_1), (t_2, x_2) \in \mathcal{Q}^n$, the linear combination $\theta\,(t_1, x_1) + (1-\theta)\,(t_2, x_2)$ is also in $\mathcal{Q}^n$ as

$$\|\theta\, x_1 + (1-\theta)\, x_2\|_2 \leq \theta \|x_1\|_2 + (1-\theta)\|x_2\|_2 \leq \theta\, t_1 + (1-\theta)\, t_2\,. \tag{B.25}$$

This follows from the fact that the Euclidean norm is subadditive and absolutely homogeneous. Furthermore, the second order cone is pointed as the only vector for which both v and $-v$ are in $\mathcal{Q}^n$ is the vector consisting of only zeros. Finally, $\mathcal{Q}^n$ is closed and solid from which follows that this set is a cone. Written down explicitly, second order cone constraints are given by

$$\|A\, x - b\|_2 \;\leq\; c^{\mathrm{T}} x + d\,, \tag{B.26}$$

where A is a real $k \times n$ matrix, b and c are $\mathbb{R}^k$ respectively $\mathbb{R}^n$ and d is a real number.

B.3. Linear programming

A special class of convex optimization problems are linear programming problems, which feature a linear objective as well as linear constraints. Despite its simple structure, this class of problems has a wide field of application ranging from financial mathematics to the optimization of processes encountered in industry. The first algorithm to solve these problems was presented by George Danzig in 1946 [377], which is known today as the Simplex algorithm.

The standard form of a linear programming problem is given by [323]

$$\begin{aligned} \text{minimize:} \quad & c^{\mathrm{T}} x \\ \text{subject to} \quad & G\,x \leq h \\ & A\,x = b \\ & x_i \geq 0 \quad \forall i\,, \end{aligned} \tag{B.27}$$

where, c is a $\mathbb{R}^n$ vector while h and b are $\mathbb{R}^k$ respectively $\mathbb{R}^l$ vectors. Furthermore, G and A are $k \times n$ respectively $l \times n$ matrices. We emphasize that all the primal variables x_i must be non-negative for linear programming. The reason for this restriction is that problems with unrestricted primal variables can be transformed into the standard form by writing a general primal variable z_i as the difference of two non-negative primal variables, i.e. $z_i = x_i - y_i$. Furthermore, each linear inequality constraint can be converted into an equality constraint by introducing k slack variables s_i. Combining primal and slack variables into one vector $y = (x_1, \ldots, x_n, s_1, \ldots, s_k)$, the problem in Eq. (B.27) can be transformed into

$$\begin{aligned} \text{minimize:} \quad & c^{\mathrm{T}} x \\ \text{subject to} \quad & A\,y = b \\ & y_i \geq 0 \quad \forall i\,, \end{aligned} \tag{B.28}$$

where A is now a $(k + l) \times (n + k)$ matrix. Note, that we do not count the condition that primal variables must be non-negative as inequality constraints in the case of linear programming. Concretely, we solve those problems numerically using the simplex algorithm [377] as implemented in `Mathematica` [299] or the interior points solver from `CVXOPT` [300].

As shown in chapter 8 of Ref. [378], the rows a_i of the matrix A that are members of the set $\{a_i | A\,y^\star = b,\, y_i^\star \neq 0\}$ must be linearly independent for the optimal solution $y^\star$ of this problem. As a $i \times j$ matrix can have at most $\min\{i, j\}$ linearly independent rows, there are exactly $\min\{n + k, l + k\}$ entries of $y^\star$ that are larger than zero. As at most k slack variables could be larger than zero, the number of positive primal variables is given by

$$\min\{n + k, l + k\} - k \;\leq\; \text{Number of } x_i \neq 0 \;\leq\; \min\{n + k, l + k\}\,. \tag{B.29}$$

In practice, the number of primal variables n is much larger than the number of constraints, i.e. $n \gg k, l$ which implies

$$l \;\leq\; \text{Number of } x_i \neq 0 \;\leq\; l + k\,. \tag{B.30}$$

Therefore, the number of positive primal variables is at least equal to the number of equality constraints and can be as large as the total number of constraints. This observation is especially useful to get analytic insight into the solutions and for some objective functions, this can be used to determine the solution.

B.4. Quadratically constrained quadratic problems

Another convex optimization problem that occurs frequently is a quadratic objective function with quadratic constraints (QCQP). However, quadratic constraints are not directly covered by the generalized inequalities discussed in section B.2 and therefore the problem has to be transformed.

In the following, we show that QCQPs are equivalent to second order cone problems (SOCP), confer Eq. (B.26). In general, a QCQP is given by

$$\begin{aligned} \text{minimize:} \quad & x^{\mathrm{T}} Q\, x + v^{\mathrm{T}}\, x \\ \text{subject to:} \quad & x^{\mathrm{T}} P\, x + w^{\mathrm{T}}\, x \leq k \\ & G\, x \preceq h \\ & A\, x = b \end{aligned} \tag{B.31}$$

with real and positive definite matrices Q and P as well as $\mathbb{R}^n$ vectors v and w. The generalization to multiple quadratic constraints is straight forward. By introducing new variables t_0, t_1, the constraints of the optimization problem are transformed into affine respectively solely quadratic constraints. The transformed problem reads

$$\begin{aligned} \text{minimize:} \quad & t_0 + v^{\mathrm{T}}\, x \\ \text{subject to:} \quad & t_1 + w^{\mathrm{T}}\, x \leq k \\ & G\, x \preceq h \\ & A\, x = b \\ & x^{\mathrm{T}} Q\, x \leq t_0 \\ & x^{\mathrm{T}} P\, x \leq t_1, \\ & t_0, t_1 \geq 0\,. \end{aligned} \tag{B.32}$$

A useful relation to transform solely quadratic constraints into conic form is described in Ref. [323] (see problem 4.26). It relates a solely quadratic constraint to a second order

cone constraint, confer Eq. (B.26), via

$$u^{\mathrm{T}}u \;\leq\; y\,z \;\Leftrightarrow\; \left\| \begin{pmatrix} 2u \\ y-z \end{pmatrix} \right\|_2 \;\leq\; y+z, \tag{B.33}$$

where y and z are non-negative real numbers and u is a $\mathbb{R}^n$ vector. Using the Cholesky factorization for positive definite matrices, the matrices Q and P decompose into a product of a matrix and its transpose, i.e. $Q = q\,q^{\mathrm{T}}$ and $P = p\,p^{\mathrm{T}}$. With this, we define

$$u \;= q^{\mathrm{T}}x \tag{B.34}$$

$$y \;= 1 \tag{B.35}$$

$$z \;= t_0\,. \tag{B.36}$$

By combining these definitions with Eq. (B.33), we finally state the QCQP in conic form

$$\begin{aligned} \text{minimize:}\quad & t_0 + v^{\mathrm{T}}\,x \\ \text{subject to:}\quad & t_1 + w^{\mathrm{T}}\,x \leq k \\ & G\,x \preceq h \\ & A\,x = b \\ & \left\| \begin{pmatrix} 2\,q^{\mathrm{T}}x \\ 1-t_0 \end{pmatrix} \right\|_2 \leq 1+t_0 \\ & \left\| \begin{pmatrix} 2\,p^{\mathrm{T}}x \\ 1-t_1 \end{pmatrix} \right\|_2 \leq 1+t_1. \\ & t_0, t_1 \geq 0\,, \end{aligned} \tag{B.37}$$

where all constraints are now generalized linear inequalities.

Appendix C.

Analysis of direct dark matter searches

In the following, we summarize the assumptions we made when analyzing direct dark matter searches in this work. We note that we used the `DDCalc` [326, 327] package to compute the detector responses of the CRESST [228] and XENON1T [221] (2018 data release) experiments and refer to those references for further information. The following information were published in Refs. [2–4].

CDMS-Si The CDMS-Si results presented in Ref. [225] are based on an exposure of 140.2 kg $\times$ days and three events have been observed with reconstructed recoil energies of 8.2 keV, 9.5 keV and 12.3 keV. As we aim to explain those events by dark matter recoil events, we restrict the region of interest to the energy range [7.6 keV, 12.9 keV], where we take into account energy fluctuations of up to $2\sigma_E$ and we assume an energy resolution of $\sigma_E = 0.3$ keV as suggested in [275, 379]. Finally, we extract the efficiency to detect nuclear recoils from the blue solid curve shown in Fig. 1 of Ref. [225].

DAMA The DAMA experiment [332] searches for the annual modulation of the recoil rate due to the changing alignment of the motion of the Sun and the Earth over the course of the year. The data released in 2013 [22] and 2018 [23] favor an annihilation signal with more than $9\,\sigma$ confidence [22, 23] in the lowest energy bins of the data as expected from dark matter. We extract the the energy resolution from figure 20b of Ref. [332] which can be parametrized as follows [247]

$$\sigma(E_{\text{ee}}) = (0.448\ \text{keVee}) \cdot \sqrt{\frac{E_{\text{ee}}}{\text{keVee}}} + 0.0091 \cdot E_{\text{ee}}\,, \tag{C.1}$$

where E_{ee} is the electron equivalent recoil energy in keVee which is related to the recoil energy E_R via $E_{\text{ee}} = Q_i\, E_R$. Here, Q_i is the quenching factor for a specific target nucleus. Concretely, we adopt the quenching factors $\text{Q}_{\text{Na}} = 0.30$ and $\text{Q}_{\text{I}} = 0.09$ as determined by the DAMA collaboration [333]. Furthermore, we assume that the probability to detect a nuclear recoil in the energy bin $[E_-, E_+]$ is given by $\epsilon_i(E_R) = \Phi\left(Q_i E_R, E_-, E_+\right)$. Following Ref. [247] and assuming that it is Gaussian, this probability is given by

$$\Phi(E_{\text{ee}}, E_-, E_+) = \frac{1}{2}\left[\text{erf}\left(\frac{E_+ - E_{\text{ee}}}{\sqrt{2}\cdot\sigma(E_{\text{ee}})}\right) - \text{erf}\left(\frac{E_- - E_{\text{ee}}}{\sqrt{2}\cdot\sigma(E_{\text{ee}})}\right)\right], \tag{C.2}$$

where $\mathrm{erf}(x)$ denotes the error function. For some applications, we additionally take into account the channeling effect studied in Ref. [335].

LUX-ZEPLIN The LUX-ZEPLIN (LZ) [303] experiment is a future experiment and the successor of LUX [380] and ZEPLIN [381]. The goal of LZ is to further increase the fiducial mass from 145 kg to 5.6 tonnes and to refine the xenon based direct detection technology. With a projected exposure time of 1000 days, LZ will gather an unprecedented exposure of 5600 tonnes $\times$ day. As the detector technology is similar to LUX and PandaX, we use the efficiency determined for LUX which we extract from figure 2 of [216] and a nuclear recoil acceptance of 50%.

PandaX During Run 8 [217] and Run 9 [218] with an combined exposure of $3.3 \cdot 10^4$ kg$\times$ days, the PandaX collaboration observed three candidates for nuclear recoils. Therefore, the upper limit on the expected number events is 6.7 at a confidence level of 90%. We calculate the expected number of events by extracting the detection efficiency from figure 2 of [218] and assuming an energy threshold of $E_{\mathrm{th}} = 1.1$ keVnr. Furthermore, we take into account the fact that only half of the nuclear recoil band is used by multiplying the event rate by an additional factor of 0.5 .

PICO-60 (2017 data release) The PICO-60 experiment [237] employs a C_3F_8 target and gathered an exposure of 1167 kg $\times$ days. In this work, we use the data released in 2017 [237]. As the PICO collaboration hasn't observed any events, this leads to an upper limit of 3.00 expected events at a confidence level of 95% when assuming no background events. When deriving the p-value for the PICO-60 experiment in chapter 6, we take into account a background of 0.331 events. We extract the energy dependent efficiency from the black and red dashed curves in Fig. 4 of Ref. [236] and shift them by 0.1 keV towards larger recoil energies to account for the slightly increased detection threshold in Ref. [237] compared to Ref. [236].

SuperCDMS The SuperCDMS experiment [226] observed 11 candidate events with a total exposure of 577 kg$\times$days. This leads to an upper limit of 16.6 expected events at a confidence level of 90%. We extract the energy dependent efficiency from figure 1 of [226] and define the region of interest between 1.6 keVnr and 10 keVnr as suggested by Ref. [226].

XENON1T (2017 data release) The XENON1T data released in 2017 [220] include no candidates for nuclear recoil events despite an exposure of 35.6 tonnes $\times$ days. In chapter 4, we conservatively set the number of expected background events to zero which results in an upper limit of 3.00 signal events at a confidence level of 95% while we assume a background of 0.36 events when constructing the p-value in chapter 6. Furthermore, we adopt the efficiency to detect nuclear recoils provided by the `DDCalc` package [326]. It has been obtained by simulating fluctuations of the $S1$ and $S2$ signal and using the appropriate scintillation and ionization yields. From those simulations, the analysis cuts

as given in [220] were then used to determine the efficiency to detect nuclear recoils. For further information, we refer to Ref. [326].

Neutrino telescopes In order to determine the capture rate of dark matter particles in the Sun, we adopt the solar model AGSS09 [254]. For spin-independent interactions, we include the 29 most abundant nuclei in the Sun while we take into account the scattering off hydrogen and ^{14}N for spin-dependent interactions. For the former, we assume the Helm form factor [187] and for the latter the form factors provided in Ref. [207]. In this work, we use the latest results on the neutrino flux from the Sun due to dark matter annihilation from IceCube [250] and Super-Kamiokande [252]. For Super-Kamiokande, we use `DarkSUSY` [265] to convert the upper limits on the neutrino flux from dark matter annihilation into upper limits on the annihilation rate.

Appendix D.

Optimized velocity distributions for a halo-independent analysis in the effective theory of dark matter-nucleon interactions

In this appendix, we explicitly determine the optimal velocity distributions for a halo-independent analysis in the effective theory of dark matter-nucleon interactions, confer chapter 5. We note that the following discussion was published in Ref. [2]. Working in the detector rest frame, we decompose the velocity distribution as a linear superposition of n streams with fixed velocity:

$$f(\vec{v}) = \sum_{i=1}^{n} a_{\vec{v}_i}^2 \delta(\vec{v} - \vec{v}_i)\,, \tag{D.1}$$

where $a_{\vec{v}_i}^2$ is the (non-negative) weight of the stream with velocity $\vec{v}_i$. Using this, the number of events at the direct detection experiment $\mathcal{E}$ can be decomposed as:

$$N_{f(\vec{v})}^{(\mathcal{E})}(\mathbf{c}) = \sum_{i=1}^{n} a_{\vec{v}_i}^2 N_{\vec{v}_i}^{(\mathcal{E})}(\mathbf{c}) = \sum_{i=1}^{n} \sum_{p,q=1}^{D} a_{\vec{v}_i}^2 c_p \left(\mathbb{N}_{\vec{v}_i}^{(\mathcal{E})}\right)_{pq} c_q\,, \tag{D.2}$$

where $N_{\vec{v}_i}^{(\mathcal{E})}(\mathbf{c})$ denotes the number of expected signal events for a given set of coupling constants $\mathbf{c} = \{c_p\}$, $p = 1, ..., D$, in case that the velocity distribution is a stream with fixed velocity $\vec{v}_i$.

Assuming constraints from two experiments $\mathcal{E}_1$ and $\mathcal{E}_2$, the optimization problem reads:

$$\begin{aligned}
\text{maximize} \quad & \sum_{i=1}^{n} \sum_{p,q=1}^{D} a_{\vec{v}_i}^2 c_p \left(N_{\vec{v}_i}^{(\mathcal{E}_0)}\right)_{pq} c_q\,, \\
\text{subject to} \quad & \sum_{i=1}^{n} \sum_{p,q=1}^{D} a_{\vec{v}_i}^2 c_p \left(N_{\vec{v}_i}^{(\mathcal{E}_1)}\right)_{pq} c_q \leq N_{\text{u.l.}}^{(\mathcal{E}_1)}\,, \\
\text{and} \quad & \sum_{i=1}^{n} \sum_{p,q=1}^{D} a_{\vec{v}_i}^2 c_p \left(N_{\vec{v}_i}^{(\mathcal{E}_2)}\right)_{pq} c_q \leq N_{\text{u.l.}}^{(\mathcal{E}_2)}\,,
\end{aligned} \tag{D.3}$$

$$\text{and} \quad \sum_{i=1}^{n} a_{\vec{v}_i}^2 = 1 \; .$$

We maximize the objective function with respect to the constraints by introducing the Lagrangian

$$\begin{aligned} L(\{a_{\vec{v}_i}\},\{\vec{v}_i\},\{c_p\},s_1,s_2,\lambda_1,\lambda_2,\lambda_3) = & \sum_{i=1}^{n}\sum_{p,q=1}^{D} a_{\vec{v}_i}^2 c_p (N_{\vec{v}_i}^{(\mathcal{E}_0)})_{pq} c_q \\ & - \lambda_1 \Big(\sum_{i=1}^{n}\sum_{p,q=1}^{D} a_{\vec{v}_i}^2 c_p (N_{\vec{v}_i}^{(\mathcal{E}_1)})_{pq} c_q + s_1^2 - N_{\text{u.l.}}^{(\mathcal{E}_1)} \Big) \\ & - \lambda_2 \Big(\sum_{i=1}^{n}\sum_{p,q=1}^{D} a_{\vec{v}_i}^2 c_p (N_{\vec{v}_i}^{(\mathcal{E}_2)})_{pq} c_q + s_2^2 - N_{\text{u.l.}}^{(\mathcal{E}_2)} \Big) \\ & - \lambda_3 \Big(\sum_{i=1}^{n} a_{\vec{v}_i}^2 - 1 \Big) \, , \end{aligned} \tag{D.4}$$

where $\{\vec{v}_i\} \equiv \{\vec{v}_1, ...\vec{v}_n\}$ and $\{a_{\vec{v}_i}\} \equiv \{a_{\vec{v}_1}, ..., a_{\vec{v}_n}\}$ are the velocities and weights of the n streams used in the decomposition of the velocity distribution and $\{c_p\} \equiv \{c_1, ..., c_D\}$ denotes the Wilson coefficients of the D effective operators used in our effective theory approach. Furthermore, λ_1, λ_2 as well as λ_3 are Lagrange multipliers and s_1^2 and s_2^2 are (non-negative) slack variables, introduced to recast the upper inequality constraints into equality constraints. Using the Karush-Kuhn-Tucker conditions discussed in appendix B.1, the maximization conditions are:

$$\frac{\partial L}{\partial a_{\vec{v}_j}} = 2 a_{\vec{v}_j} \left\{ \sum_{p,q=1}^{D} c_p \Big[N_{\vec{v}_j}^{(\mathcal{E}_0)} - \lambda_1 N_{\vec{v}_j}^{(\mathcal{E}_1)} - \lambda_2 N_{\vec{v}_j}^{(\mathcal{E}_2)} \Big]_{pq} c_q - \lambda_3 \right\} = 0, \tag{D.5}$$

$$j = 1, ..., n \; ,$$

$$\frac{\partial L}{\partial \vec{v}_j} = a_{\vec{v}_j}^2 \sum_{p,q=1}^{D} c_p \left[\left(\frac{\partial N_{\vec{v}_j}^{(\mathcal{E}_0)}}{\partial \vec{v}_j} \right) - \lambda_1 \left(\frac{\partial N_{\vec{v}_j}^{(\mathcal{E}_1)}}{\partial \vec{v}_j} \right) - \lambda_2 \left(\frac{\partial N_{\vec{v}_j}^{(\mathcal{E}_2)}}{\partial \vec{v}_j} \right) \right]_{pq} c_q = 0, \tag{D.6}$$

$$j = 1, ..., n \; ,$$

$$\frac{\partial L}{\partial s_1} = 2 \lambda_1 s_1 = 0 \; , \tag{D.7}$$

$$\frac{\partial L}{\partial s_2} = 2 \lambda_2 s_2 = 0 \; , \tag{D.8}$$

$$\frac{\partial L}{\partial \lambda_1} = \sum_{i=1}^{n}\sum_{p,q=1}^{D} a_{\vec{v}_i}^2 c_p (N_{\vec{v}_i}^{(\mathcal{E}_1)})_{pq} c_q + s_1^2 - N_{\text{u.l.}}^{(\mathcal{E}_1)} = 0 \; , \tag{D.9}$$

$$\frac{\partial L}{\partial \lambda_2} = \sum_{i=1}^{n}\sum_{p,q=1}^{D} a_{\vec{v}_i}^2 c_p (N_{\vec{v}_i}^{(\mathcal{E}_2)})_{pq} c_q + s_2^2 - N_{\text{u.l.}}^{(\mathcal{E}_2)} = 0 \; , \tag{D.10}$$

$$\frac{\partial L}{\partial \lambda_3} = \sum_{i=1}^{n} a_{\vec{v}_i}^2 - 1 = 0 \; , \tag{D.11}$$

$$\frac{\partial L}{\partial c_p} = \sum_{i=1}^{n}\sum_{q=1}^{D} 2a_{\vec{v}_i}^2 \left[N_{\vec{v}_i}^{(\mathcal{E}_0)} - \lambda_1 N_{\vec{v}_i}^{(\mathcal{E}_1)} - \lambda_2 N_{\vec{v}_i}^{(\mathcal{E}_2)}\right]_{pq} c_q = 0, \quad p = 1..., D\,. \tag{D.12}$$

We note that the optimal points fulfill the following condition

$$\sum_{j=1}^{n} a_{\vec{v}_j} \frac{\partial L}{\partial a_{\vec{v}_j}} - \sum_{p=1}^{D} c_p \frac{\partial L}{\partial c_p} = 0\,. \tag{D.13}$$

Substituting Eq. (D.5) and Eq. (D.12) as well as using Eq. (D.11) we obtain

$$0 = -2\lambda_3 \left(\sum_{i=1}^{n} a_{\vec{v}_i}^2\right) = -2\lambda_3\,, \tag{D.14}$$

from where we conclude that $\lambda_3 = 0$.

In addition to this, Eq. (D.7) is satisfied either when $s_1 = 0$ or when $\lambda_1 = 0$, and Eq. (D.8) is satisfied either when $s_2 = 0$ or when $\lambda_2 = 0$. A vanishing slack variable implies that the upper limit is saturated. Therefore, $\lambda_1 \neq 0$ ($\lambda_2 \neq 0$) implies that, for the parameters that maximize the number of signal events at $\mathcal{E}_0$, the upper bounds from $\mathcal{E}_1$ ($\mathcal{E}_2$) are saturated. Similarly, $\lambda_1 \neq 0$ and $\lambda_2 \neq 0$ at the same time imply that the upper bounds from $\mathcal{E}_1$ and $\mathcal{E}_2$ are simultaneously saturated.

In the case that both λ_1 and λ_2 do not vanish, Eq. (D.5) reads

$$a_{\vec{v}_j}\left(\langle N_{\vec{v}_j}^{(\mathcal{E}_0)}\rangle - \lambda_1 \langle N_{\vec{v}_j}^{(\mathcal{E}_1)}\rangle - \lambda_2 \langle N_{\vec{v}_j}^{(\mathcal{E}_2)}\rangle\right) = 0, \quad j = 1..., n\,, \tag{D.15}$$

with $\langle ...\rangle \equiv \langle \mathbf{c}|...|\mathbf{c}\rangle$. Since there are only two non-vanishing Lagrange multipliers, it follows that these equations can only be satisfied if

$$\langle N_{\vec{v}_1}^{(\mathcal{E}_0)}\rangle - \lambda_1 \langle N_{\vec{v}_1}^{(\mathcal{E}_1)}\rangle - \lambda_2 \langle N_{\vec{v}_1}^{(\mathcal{E}_2)}\rangle = 0\,, \tag{D.16}$$

$$\langle N_{\vec{v}_2}^{(\mathcal{E}_0)}\rangle - \lambda_1 \langle N_{\vec{v}_2}^{(\mathcal{E}_1)}\rangle - \lambda_2 \langle N_{\vec{v}_2}^{(\mathcal{E}_2)}\rangle = 0\,, \tag{D.17}$$

$$a_{\vec{v}_j} = 0\,, \qquad j = 3, ...n\,, \tag{D.18}$$

for some stream velocities $\vec{v}_1$, $\vec{v}_2$[1]. We conclude that the optimized velocity distribution corresponds to a superposition of two streams with weights $a_{\vec{v}_1}$ and $a_{\vec{v}_2}$ satisfying the normalization condition $a_{\vec{v}_1}^2 + a_{\vec{v}_2}^2 = 1$. It can be cast as

$$f(\vec{v}) = \alpha\delta(\vec{v} - \vec{v}_1) + (1-\alpha)\delta(\vec{v} - \vec{v}_2) \tag{D.19}$$

with $0 \leq \alpha \leq 1$. In the case where the upper limit on the number of events at either $\mathcal{E}_1$ or $\mathcal{E}_2$ is not saturated, one of the Lagrange multipliers vanishes and a similar calculation reveals that the optimized velocity distribution consists of just one stream. This case is also described by Eq. (D.19) when fixing $\alpha = 0$ or 1.

[1] If some of the equations (D.15) are linearly dependent, there are also solutions with three or more non-zero $a_{\vec{v}_j}$. However, it is straightforward to show that in such a scenario there is always a solution with two non-zero $a_{\vec{v}_j}$ giving rise to the same number of expected events in all three experiments.

Acknowledgements

This research was supported by the collaborative research center "Neutrinos and Dark Matter in Astro- and Particle Physics" (SFB 1258). First and foremost, I want to thank my supervisor Professor A. Ibarra for countless discussions and patient explanations that made this work possible. Also, I'm particularly thankful for introducing me to so many interesting ideas making my time at T30d truly inspiring and instructive. Many thanks also to Karin Ramm for help with all during all my time at T30d.

Furthermore, I want to thank all the people I had and have the pleasure collaborating with. Especial thanks to Bradley Kavanagh for the many discussions about dark matter sub-halos and for extending my knowledge on statistics. I also want to thank Ricardo Catena and Sebastian Wild for fruitful discussions about non-relativistic effective field theories of dark matter-nucleus interactions as well as on the velocity distribution of dark matter. Many thanks to Anja Brenner and Gonzalo Herrera-Moreno for interesting discussions and for valuable comments on this manuscript. Furthermore, I want to thank Shin'ichiro Ando for sharing the numerical results. Finally, I want to thank Stephan Meighen-Berger, Elisa Resconi, Stefano Scopel, Gaurav Tomar and Martin Wolf for valuable discussions and collaboration in projects that are not finished yet.

Many thanks also to all my colleagues from the theory department and from SFB 1258 for the great working atmosphere, support and the great times we had. Especial thanks to Johannes Herms, Stephan Meighen-Berger, Max Ruhdorfer and Stefan Weber for being great office mates.

Last but not least, I want to thank my family for their constant support during this my PhD and for making this all possible. Many thanks also to my brother for proofreading parts of my thesis. Thanks to all my friends from university and outside for the support and the good times we had.

Bibliography

[1] A. Rappelt, *A halo independent comparison of direct dark matter searches*, Master's thesis, Technische Universität München, 2016.

[2] A. Ibarra and A. Rappelt, *Optimized velocity distributions for direct dark matter detection*, *JCAP* **1708** (2017), no. 08 039, [arXiv:1703.09168].

[3] R. Catena, A. Ibarra, A. Rappelt, and S. Wild, *Halo-independent comparison of direct detection experiments in the effective theory of dark matter-nucleon interactions*, *JCAP* **1807** (2018), no. 07 028, [arXiv:1801.08466].

[4] A. Ibarra, B. J. Kavanagh, and A. Rappelt, *Bracketing the impact of astrophysical uncertainties on local dark matter searches*, *JCAP* **1812** (2018), no. 12 018, [arXiv:1806.08714].

[5] A. Ibarra, B. J. Kavanagh, and A. Rappelt, *Impact of substructure on local dark matter searches*, arXiv:1908.00747.

[6] L. Bergström, *Nonbaryonic dark matter: Observational evidence and detection methods*, *Rept. Prog. Phys.* **63** (2000) 793, [hep-ph/0002126].

[7] G. Bertone, D. Hooper, and J. Silk, *Particle dark matter: Evidence, candidates and constraints*, *Phys. Rept.* **405** (2005) 279–390, [hep-ph/0404175].

[8] P. Gorenstein and W. Tucker, *Astronomical Signatures of Dark Matter*, *Advances in High Energy Physics* **2014** (June, 2014) 878203.

[9] G. Bertone and D. Hooper, *History of dark matter*, *Rev. Mod. Phys.* **90** (2018), no. 4 045002, [arXiv:1605.04909].

[10] W. Thomson, Baron Kelvin, *Baltimore Lectures on Molecular Dynamics and the Wave Theory of Light*. Cambridge Library Collection - Physical Sciences. Cambridge University Press, 2010.

[11] E. Öpik, *Selective absorption of light in space, and the dynamics of the universe*, *Bull. de la Soc. Astr. de Russie* **21** (1915) 150–158.

[12] J. C. Kapteyn, *First Attempt at a Theory of the Arrangement and Motion of the Sidereal System*, *ApJ* **55** (May, 1922) 302.

[13] J. H. Oort, *The force exerted by the stellar system in the direction perpendicular to the galactic plane and some related problems*, *Bull. Astron. Inst. Netherlands* **6** (Aug., 1932) 249.

[14] F. Zwicky, *On the Masses of Nebulae and of Clusters of Nebulae*, *ApJ* **86** (Oct., 1937) 217.

[15] V. C. Rubin and W. K. Ford, Jr., *Rotation of the Andromeda Nebula from a Spectroscopic Survey of Emission Regions*, *ApJ* **159** (Feb., 1970) 379.

[16] D. Clowe, M. Bradac, A. H. Gonzalez, M. Markevitch, S. W. Randall, C. Jones, and D. Zaritsky, *A direct empirical proof of the existence of dark matter*, *Astrophys. J.* **648** (2006) L109–L113, [astro-ph/0608407].

[17] **Planck**, N. Aghanim *et. al.*, *Planck 2018 results. VI. Cosmological parameters*, arXiv:1807.06209.

[18] **WMAP**, M. R. Nolta *et. al.*, *Five-Year Wilkinson Microwave Anisotropy Probe (WMAP) Observations: Angular Power Spectra*, *Astrophys. J. Suppl.* **180** (2009) 296–305, [arXiv:0803.0593].

[19] J. L. Feng, *Dark Matter Candidates from Particle Physics and Methods of Detection*, *Ann. Rev. Astron. Astrophys.* **48** (2010) 495–545, [arXiv:1003.0904].

[20] G. Jungman, M. Kamionkowski, and K. Griest, *Supersymmetric dark matter*, *Phys. Rept.* **267** (1996) 195–373, [hep-ph/9506380].

[21] E. W. Kolb and M. S. Turner, *The Early Universe*, *Front. Phys.* **69** (1990) 1–547.

[22] R. Bernabei *et. al.*, *Final model independent result of DAMA/LIBRA-phase1*, *Eur. Phys. J.* **C73** (2013) 2648, [arXiv:1308.5109].

[23] R. Bernabei *et. al.*, *First Model Independent Results from DAMA/LIBRA–Phase2*, *Universe* **4** (2018), no. 11 116, [arXiv:1805.10486]. [Nucl. Phys. Atom. Energy19,no.4,307(2018)].

[24] **AMS**, M. Aguilar *et. al.*, *Antiproton Flux, Antiproton-to-Proton Flux Ratio, and Properties of Elementary Particle Fluxes in Primary Cosmic Rays Measured with the Alpha Magnetic Spectrometer on the International Space Station*, *Phys. Rev. Lett.* **117** (2016), no. 9 091103.

[25] M.-Y. Cui, Q. Yuan, Y.-L. S. Tsai, and Y.-Z. Fan, *Possible dark matter annihilation signal in the AMS-02 antiproton data*, *Phys. Rev. Lett.* **118** (2017), no. 19 191101, [arXiv:1610.03840].

[26] A. Cuoco, M. Krämer, and M. Korsmeier, *Novel Dark Matter Constraints from Antiprotons in Light of AMS-02*, *Phys. Rev. Lett.* **118** (2017), no. 19 191102, [arXiv:1610.03071].

[27] A. Cuoco, J. Heisig, L. Klamt, M. Korsmeier, and M. Krämer, *Scrutinizing the evidence for dark matter in cosmic-ray antiprotons*, *Phys. Rev.* **D99** (2019), no. 10 103014, [arXiv:1903.01472].

[28] M. Boudaud, Y. Génolini, L. Derome, J. Lavalle, D. Maurin, P. Salati, and P. D. Serpico, *AMS-02 antiprotons are consistent with a secondary astrophysical origin*, arXiv:1906.07119.

[29] F. Zwicky, *Die Rotverschiebung von extragalaktischen Nebeln*, *Helvetica Physica Acta* **6** (1933) 110–127.

[30] E. Hubble and M. L. Humason, *The Velocity-Distance Relation among Extra-Galactic Nebulae*, *ApJ* **74** (July, 1931) 43.

[31] V. C. Rubin, W. K. Ford, Jr., and N. Thonnard, *Extended rotation curves of high-luminosity spiral galaxies. IV - Systematic dynamical properties, SA through SC*, *ApJ* **225** (Nov., 1978) L107–L111.

[32] V. C. Rubin, W. K. Ford, Jr., and N. Thonnard, *Rotational properties of 21 SC galaxies with a large range of luminosities and radii, from NGC 4605 /R = 4kpc/ to UGC 2885 /R = 122 kpc/*, *ApJ* **238** (June, 1980) 471–487.

[33] K. G. Begeman, A. H. Broeils, and R. H. Sanders, *Extended rotation curves of spiral galaxies: Dark haloes and modified dynamics*, *Mon. Not. Roy. Astron. Soc.* **249** (1991) 523.

[34] M. Milgrom, *A modification of the Newtonian dynamics as a possible alternative to the hidden mass hypothesis*, *ApJ* **270** (July, 1983) 365–370.

[35] B. Famaey and S. McGaugh, *Modified Newtonian Dynamics (MOND): Observational Phenomenology and Relativistic Extensions*, *Living Rev. Rel.* **15** (2012) 10, [arXiv:1112.3960].

[36] G. W. Angus, H. Shan, H. Zhao, and B. Famaey, *On the Law of Gravity, the Mass of Neutrinos and the Proof of Dark Matter*, *Astrophys. J.* **654** (2007) L13–L16, [astro-ph/0609125].

[37] G. W. Angus and S. S. McGaugh, *The collision velocity of the bullet cluster in conventional and modified dynamics*, *Mon. Not. Roy. Astron. Soc.* **383** (2008) 417, [arXiv:0704.0381].

[38] W. Hu and S. Dodelson, *Cosmic Microwave Background Anisotropies*, *Ann. Rev. Astron. Astrophys.* **40** (2002) 171–216, [astro-ph/0110414].

[39] W. Hu, N. Sugiyama, and J. Silk, *The Physics of microwave background anisotropies*, *Nature* **386** (1997) 37–43, [astro-ph/9604166].

[40] M. Trodden and S. M. Carroll, *TASI lectures: Introduction to cosmology*, in *Progress in string theory. Proceedings, Summer School, TASI 2003, Boulder, USA, June 2-27, 2003*, pp. 703–793, 2004. astro-ph/0401547. [,703(2004)].

[41] G. Gamow, *The Origin of Elements and the Separation of Galaxies*, *Physical Review* **74** (Aug., 1948) 505–506.

[42] G. Gamow, *The Evolution of the Universe*, *Nature* **162** (Oct, 1948) 680–682.

[43] R. A. Alpher and R. C. Herman, *On the Relative Abundance of the Elements*, *Physical Review* **74** (Dec, 1948) 1737–1742.

[44] R. A. Alpher and R. Herman, *Evolution of the Universe*, *Nature* **162** (Nov, 1948) 774–775.

[45] A. A. Penzias and R. W. Wilson, *A Measurement of Excess Antenna Temperature at 4080 Mc/s.*, *ApJ* **142** (July, 1965) 419–421.

[46] R. H. Cyburt, B. D. Fields, K. A. Olive, and T.-H. Yeh, *Big Bang Nucleosynthesis: 2015*, *Rev. Mod. Phys.* **88** (2016) 015004, [arXiv:1505.01076].

[47] **Particle Data Group**, M. Tanabashi *et. al.*, *Review of particle physics*, *Phys. Rev. D* **98** (Aug, 2018) 030001.

[48] J. Zavala and C. S. Frenk, *Dark matter haloes and subhaloes*, *Galaxies* **7** (Sep, 2019) 81, [arXiv:1907.11775].

[49] P. Meszaros, *The behaviour of point masses in an expanding cosmological substratum*, *Astron. Astrophys.* **37** (1974) 225–228.

[50] T. Bringmann, *Particle Models and the Small-Scale Structure of Dark Matter*, *New J. Phys.* **11** (2009) 105027, [arXiv:0903.0189].

[51] C. Boehm, A. Riazuelo, S. H. Hansen, and R. Schaeffer, *Interacting dark matter disguised as warm dark matter*, *Phys. Rev.* **D66** (2002) 083505, [astro-ph/0112522].

[52] C. Boehm, J. A. Schewtschenko, R. J. Wilkinson, C. M. Baugh, and S. Pascoli, *Using the Milky Way satellites to study interactions between cold dark matter and radiation*, *Mon. Not. Roy. Astron. Soc.* **445** (2014) L31–L35, [arXiv:1404.7012].

[53] M. R. Buckley, J. Zavala, F.-Y. Cyr-Racine, K. Sigurdson, and M. Vogelsberger, *Scattering, Damping, and Acoustic Oscillations: Simulating the Structure of Dark Matter Halos with Relativistic Force Carriers*, *Phys. Rev.* **D90** (2014), no. 4 043524, [arXiv:1405.2075].

[54] F.-Y. Cyr-Racine, K. Sigurdson, J. Zavala, T. Bringmann, M. Vogelsberger, and C. Pfrommer, *ETHOS—an effective theory of structure formation: From dark particle physics to the matter distribution of the Universe*, *Phys. Rev.* **D93** (2016), no. 12 123527, [arXiv:1512.05344].

[55] **2dFGRS**, S. Cole *et. al.*, *The 2dF Galaxy Redshift Survey: Power-spectrum analysis of the final dataset and cosmological implications*, *Mon. Not. Roy. Astron. Soc.* **362** (2005) 505–534, [astro-ph/0501174].

[56] W. J. Percival *et. al.*, *The shape of the SDSS DR5 galaxy power spectrum*, *Astrophys. J.* **657** (2007) 645–663, [astro-ph/0608636].

[57] M. Viel, G. D. Becker, J. S. Bolton, and M. G. Haehnelt, *Warm dark matter as a solution to the small scale crisis: New constraints from high redshift Lyman-α forest data*, *Phys. Rev.* **D88** (2013) 043502, [arXiv:1306.2314].

[58] G. Efstathiou, M. Davis, S. D. M. White, and C. S. Frenk, *Numerical techniques for large cosmological N-body simulations*, *ApJS* **57** (Feb., 1985) 241–260.

[59] M. Davis, G. Efstathiou, C. S. Frenk, and S. D. M. White, *The evolution of large-scale structure in a universe dominated by cold dark matter*, *ApJ* **292** (May, 1985) 371–394.

[60] Y. B. Zel'dovich, *Gravitational instability: An approximate theory for large density perturbations.*, *A&A* **5** (Mar., 1970) 84–89.

[61] A. Jenkins, *Second-order Lagrangian perturbation theory initial conditions for resimulations*, *Mon. Not. Roy. Astron. Soc.* **403** (2010) 1859, [arXiv:0910.0258].

[62] J. F. Navarro, C. S. Frenk, and S. D. M. White, *The Structure of cold dark matter halos*, *Astrophys. J.* **462** (1996) 563–575, [astro-ph/9508025].

[63] J. F. Navarro, C. S. Frenk, and S. D. M. White, *A Universal density profile from hierarchical clustering*, *Astrophys. J.* **490** (1997) 493–508, [astro-ph/9611107].

[64] F. Nesti and P. Salucci, *The Dark Matter halo of the Milky Way, AD 2013*, *JCAP* **1307** (2013) 016, [arXiv:1304.5127].

[65] J. Einasto, *On the Construction of a Composite Model for the Galaxy and on the Determination of the System of Galactic Parameters*, *Trudy Astrofizicheskogo Instituta Alma-Ata* **5** (1965) 87–100.

[66] A. W. Graham, D. Merritt, B. Moore, J. Diemand, and B. Terzic, *Empirical models for Dark Matter Halos. I. Nonparametric Construction of Density Profiles and Comparison with Parametric Models*, *Astron. J.* **132** (2006) 2685–2700, [astro-ph/0509417].

[67] E. Hayashi and S. D. M. White, *Understanding the shape of the halo-mass and galaxy-mass cross-correlation functions*, *Mon. Not. Roy. Astron. Soc.* **388** (2008) 2, [arXiv:0709.3933].

[68] J. F. Navarro, E. Hayashi, C. Power, A. Jenkins, C. S. Frenk, S. D. M. White, V. Springel, J. Stadel, and T. R. Quinn, *The Inner structure of Lambda-CDM halos 3: Universality and asymptotic slopes*, *Mon. Not. Roy. Astron. Soc.* **349** (2004) 1039, [astro-ph/0311231].

[69] J. F. Navarro, A. Ludlow, V. Springel, J. Wang, M. Vogelsberger, S. D. M. White, A. Jenkins, C. S. Frenk, and A. Helmi, *The Diversity and Similarity of Cold Dark Matter Halos*, *Mon. Not. Roy. Astron. Soc.* **402** (2010) 21, [arXiv:0810.1522].

[70] A. Burkert, *The Structure of dark matter halos in dwarf galaxies*, *IAU Symp.* **171** (1996) 175, [astro-ph/9504041]. [Astrophys. J.447,L25(1995)].

[71] W. J. G. de Blok, *The Core-Cusp Problem*, *Advances in Astronomy* **2010** (Jan, 2010) 789293, [arXiv:0910.3538].

[72] A. M. Green, *Astrophysical uncertainties on direct detection experiments*, *Mod. Phys. Lett.* **A27** (2012) 1230004, [arXiv:1112.0524].

[73] J. I. Read, *The Local Dark Matter Density*, *J. Phys.* **G41** (2014) 063101, [arXiv:1404.1938].

[74] R. Catena and P. Ullio, *A novel determination of the local dark matter density*, *JCAP* **1008** (2010) 004, [arXiv:0907.0018].

[75] M. Weber and W. de Boer, *Determination of the Local Dark Matter Density in our Galaxy*, *Astron. Astrophys.* **509** (2010) A25, [arXiv:0910.4272].

[76] P. Salucci, F. Nesti, G. Gentile, and C. F. Martins, *The dark matter density at the Sun's location*, *Astron. Astrophys.* **523** (2010) A83, [arXiv:1003.3101].

[77] P. J. McMillan, *Mass models of the Milky Way*, *Mon. Not. Roy. Astron. Soc.* **414** (2011) 2446–2457, [arXiv:1102.4340].

[78] F. Iocco, M. Pato, G. Bertone, and P. Jetzer, *Dark Matter distribution in the Milky Way: microlensing and dynamical constraints*, *JCAP* **1111** (2011) 029, [arXiv:1107.5810].

[79] M. Pato, F. Iocco, and G. Bertone, *Dynamical constraints on the dark matter distribution in the Milky Way*, *JCAP* **1512** (2015), no. 12 001, [arXiv:1504.06324].

[80] Y. Huang, X. W. Liu, H. B. Yuan, M. S. Xiang, H. W. Zhang, B. Q. Chen, J. J. Ren, C. Wang, Y. Zhang, Y. H. Hou, Y. F. Wang, and Z. H. Cao, *The Milky Way's rotation curve out to 100 kpc and its constraint on the Galactic mass distribution*, *MNRAS* **463** (Dec, 2016) 2623–2639, [arXiv:1604.01216].

[81] P. J. McMillan, *The mass distribution and gravitational potential of the Milky Way*, *MNRAS* **465** (Feb, 2017) 76–94, [arXiv:1608.00971].

[82] M. C. Smith, S. H. Whiteoak, and N. W. Evans, *Slicing and dicing the Milky Way disk in SDSS*, *Astrophys. J.* **746** (2012) 181, [arXiv:1111.6920].

[83] C. M. Bidin, G. Carraro, R. A. Mendez, and R. Smith, *Kinematical and chemical vertical structure of the Galactic thick disk II. A lack of dark matter in the solar neighborhood*, *Astrophys. J.* **751** (2012) 30, [arXiv:1204.3924].

[84] J. Bovy and S. Tremaine, *On the local dark matter density*, *Astrophys. J.* **756** (2012) 89, [arXiv:1205.4033].

[85] S. Garbari, C. Liu, J. I. Read, and G. Lake, *A new determination of the local dark matter density from the kinematics of K dwarfs*, *Mon. Not. Roy. Astron. Soc.* **425** (2012) 1445, [arXiv:1206.0015].

[86] L. Zhang, H.-W. Rix, G. van de Ven, J. Bovy, C. Liu, and G. Zhao, *The Gravitational Potential Near the Sun From SEGUE K-dwarf Kinematics*, *Astrophys. J.* **772** (2013) 108, [arXiv:1209.0256].

[87] J. Bovy and H.-W. Rix, *A Direct Dynamical Measurement of the Milky Way's Disk Surface Density Profile, Disk Scale Length, and Dark Matter Profile at 4 kpc* $\lesssim R \lesssim$ *9 kpc*, *Astrophys. J.* **779** (2013) 115, [arXiv:1309.0809].

[88] O. Bienaymé *et. al.*, *Weighing the local dark matter with RAVE red clump stars*, *Astron. Astrophys.* **571** (2014) A92, [arXiv:1406.6896].

[89] C. F. McKee, A. Parravano, and D. J. Hollenbach, *Stars, Gas, and Dark Matter in the Solar Neighborhood*, *Astrophys. J.* **814** (2015), no. 1 13, [arXiv:1509.05334].

[90] Q. Xia, C. Liu, S. Mao, Y. Song, L. Zhang, R. J. Long, Y. Zhang, Y. Hou, Y. Wang, and Y. Wu, *Determining the local dark matter density with LAMOST data*, *Mon. Not. Roy. Astron. Soc.* **458** (2016), no. 4 3839–3850, [arXiv:1510.06810].

[91] S. Sivertsson, H. Silverwood, J. I. Read, G. Bertone, and P. Steger, *The localdark matter density from SDSS-SEGUE G-dwarfs*, *Mon. Not. Roy. Astron. Soc.* **478** (2018), no. 2 1677–1693, [arXiv:1708.07836].

[92] M. Vogelsberger, A. Helmi, V. Springel, S. D. M. White, J. Wang, C. S. Frenk, A. Jenkins, A. D. Ludlow, and J. F. Navarro, *Phase-space structure in the local dark matter distribution and its signature in direct detection experiments*, *Mon. Not. Roy. Astron. Soc.* **395** (2009) 797–811, [arXiv:0812.0362].

[93] A. S. Eddington, *The distribution of stars in globular clusters*, *MNRAS* **76** (May, 1916) 572–585.

[94] J. Binney and S. Tremaine, *Galactic Dynamics: Second Edition*. Princeton University Press, 2008.

[95] T. Lacroix, M. Stref, and J. Lavalle, *Anatomy of Eddington-like inversion methods in the context of dark matter searches*, *JCAP* **1809** (2018), no. 09 040, [arXiv:1805.02403].

[96] P. Ullio and M. Kamionkowski, *Velocity distributions and annual modulation signatures of weakly interacting massive particles*, *JHEP* **03** (2001) 049, [hep-ph/0006183].

[97] J. D. Vergados and D. Owen, *New Velocity Distribution for Cold Dark Matter in the Context of the Eddington Theory*, *ApJ* **589** (May, 2003) 17–28, [astro-ph/0203293].

[98] F. Ferrer and D. R. Hunter, *The impact of the phase-space density on the indirect detection of dark matter*, *JCAP* **1309** (2013) 005, [arXiv:1306.6586].

[99] M. Petac and P. Ullio, *Two-integral distribution functions in axisymmetric galaxies: implications for dark matter searches*, *Phys. Rev.* **D99** (2019), no. 4 043003, [arXiv:1812.01531].

[100] S. Mandal, S. Majumdar, V. Rentala, and R. Basu Thakur, *Observationally inferred dark matter phase-space distribution and direct detection experiments*, *Phys. Rev.* **D100** (2019), no. 2 023002, [arXiv:1806.06872].

[101] J. Herzog-Arbeitman, M. Lisanti, and L. Necib, *The Metal-Poor Stellar Halo in RAVE-TGAS and its Implications for the Velocity Distribution of Dark Matter*, *JCAP* **1804** (2018), no. 04 052, [arXiv:1708.03635].

[102] L. Necib, M. Lisanti, and V. Belokurov, *Dark Matter in Disequilibrium: The Local Velocity Distribution from SDSS-Gaia*, *ApJ* **874** (Mar, 2019) 3, [arXiv:1807.02519].

[103] L. Necib, M. Lisanti, S. Garrison-Kimmel, A. Wetzel, R. Sanderson, P. F. Hopkins, C.-A. Faucher-Giguère, and D. Kereš, *Under the Firelight: Stellar Tracers of the Local Dark Matter Velocity Distribution in the Milky Way*, *ApJ* **883** (Sep, 2019) 27, [arXiv:1810.12301].

[104] J. Herzog-Arbeitman, M. Lisanti, P. Madau, and L. Necib, *Empirical Determination of Dark Matter Velocities using Metal-Poor Stars*, *Phys. Rev. Lett.* **120** (2018), no. 4 041102, [arXiv:1704.04499].

[105] M. Valentini, C. Chiappini, D. Bossini, A. Miglio, G. R. Davies, B. Mosser, Y. P. Elsworth, S. Mathur, R. A. García, L. Girardi, T. S. Rodrigues, M. Steinmetz, and A. Vallenari, *Masses and ages for metal-poor stars. A pilot programme combining asteroseismology and high-resolution spectroscopic follow-up of RAVE halo stars*, *A&A* **627** (Jul, 2019) A173, [arXiv:1808.08569].

[106] J. Guedes, S. Callegari, P. Madau, and L. Mayer, *Forming Realistic Late-type Spirals in a ΛCDM Universe: The Eris Simulation*, *ApJ* **742** (Dec, 2011) 76, [arXiv:1103.6030].

[107] L. Lindegren, U. Lammers, U. Bastian, J. Hernández, S. Klioner, D. Hobbs, A. Bombrun, D. Michalik, M. Ramos-Lerate, A. Butkevich, G. Comoretto, E. Joliet, B. Holl, A. Hutton, P. Parsons, H. Steidelmüller, U. Abbas, M. Altmann, A. Andrei, S. Anton, N. Bach, C. Barache, U. Becciani, J. Berthier, L. Bianchi, M. Biermann, S. Bouquillon, G. Bourda, T. Brüsemeister, B. Bucciarelli, D. Busonero, T. Carlucci, J. Castañeda, P. Charlot, M. Clotet, M. Crosta, M. Davidson, F. de Felice, R. Drimmel, C. Fabricius, A. Fienga, F. Figueras, E. Fraile, M. Gai, N. Garralda, R. Geyer, J. J. González-Vidal, R. Guerra, N. C. Hambly, M. Hauser, S. Jordan, M. G. Lattanzi, H. Lenhardt,

S. Liao, W. Löffler, P. J. McMillan, F. Mignard, A. Mora, R. Morbidelli, J. Portell, A. Riva, M. Sarasso, I. Serraller, H. Siddiqui, R. Smart, A. Spagna, U. Stampa, I. Steele, F. Taris, J. Torra, W. van Reeven, A. Vecchiato, S. Zschocke, J. de Bruijne, G. Gracia, F. Raison, T. Lister, J. Marchant, R. Messineo, M. Soffel, J. Osorio, A. de Torres, and W. O'Mullane, *Gaia Data Release 1. Astrometry: one billion positions, two million proper motions and parallaxes*, *A&A* **595** (Nov., 2016) A4, [arXiv:1609.04303].

[108] Gaia Collaboration, A. G. A. Brown, A. Vallenari, T. Prusti, J. H. J. de Bruijne, C. Babusiaux, C. A. L. Bailer-Jones, M. Biermann, D. W. Evans, L. Eyer, and et al., *Gaia Data Release 2. Summary of the contents and survey properties*, *A&A* **616** (Aug., 2018) A1, [arXiv:1804.09365].

[109] C. P. Ahn, R. Alexandroff, C. Allende Prieto, S. F. Anderson, T. Anderton, B. H. Andrews, É. Aubourg, S. Bailey, E. Balbinot, R. Barnes, and et al., *The Ninth Data Release of the Sloan Digital Sky Survey: First Spectroscopic Data from the SDSS-III Baryon Oscillation Spectroscopic Survey*, *ApJS* **203** (Dec., 2012) 21, [arXiv:1207.7137].

[110] N. Bozorgnia, A. Fattahi, D. G. Cerdeno, C. S. Frenk, F. A. Gómez, R. J. J. Grand, F. Marinacci, and R. Pakmor, *On the correlation between the local dark matter and stellar velocities*, *JCAP* **1906** (2019), no. 06 045, [arXiv:1811.11763].

[111] R. J. J. Grand, F. A. Gómez, F. Marinacci, R. Pakmor, V. Springel, D. J. R. Campbell, C. S. Frenk, A. Jenkins, and S. D. M. White, *The Auriga Project: the properties and formation mechanisms of disc galaxies across cosmic time*, *Mon. Not. Roy. Astron. Soc.* **467** (2017), no. 1 179–207, [arXiv:1610.01159].

[112] D. G. Cerdeno and A. M. Green, *Direct detection of WIMPs*, arXiv:1002.1912.

[113] M. Lisanti, *Lectures on Dark Matter Physics*, in *Proceedings, Theoretical Advanced Study Institute in Elementary Particle Physics: New Frontiers in Fields and Strings (TASI 2015): Boulder, CO, USA, June 1-26, 2015*, pp. 399–446, 2017. arXiv:1603.03797.

[114] F. J. Kerr and D. Lynden-Bell, *Review of galactic constants*, *Mon. Not. Roy. Astron. Soc.* **221** (1986) 1023.

[115] A. M. Green, *Astrophysical uncertainties on the local dark matter distribution and direct detection experiments*, *J. Phys.* **G44** (2017), no. 8 084001, [arXiv:1703.10102].

[116] T. Piffl *et. al.*, *The RAVE survey: the Galactic escape speed and the mass of the Milky Way*, *Astron. Astrophys.* **562** (2014) A91, [arXiv:1309.4293].

[117] J. Diemand and B. Moore, *The Structure and Evolution of Cold Dark Matter Halos*, *Advanced Science Letters* **4** (Feb, 2011) 297–310, [arXiv:0906.4340].

[118] C. S. Frenk and S. D. M. White, *Dark matter and cosmic structure*, *Annalen Phys.* **524** (2012) 507–534, [arXiv:1210.0544].

[119] D. Erkal, V. Belokurov, C. F. P. Laporte, S. E. Koposov, T. S. Li, C. J. Grillmair, N. Kallivayalil, A. M. Price-Whelan, N. W. Evans, K. Hawkins, D. Hendel, C. Mateu, J. F. Navarro, A. del Pino, C. T. Slater, S. T. Sohn, and Orphan Aspen Treasury Collaboration, *The total mass of the Large Magellanic Cloud from its perturbation on the Orphan stream*, *MNRAS* **487** (Aug, 2019) 2685–2700, [arXiv:1812.08192].

[120] L. E. Strigari, J. S. Bullock, M. Kaplinghat, J. D. Simon, M. Geha, B. Willman, and M. G. Walker, *A common mass scale for satellite galaxies of the Milky Way*, *Nature* **454** (Aug, 2008) 1096–1097, [arXiv:0808.3772].

[121] A. A. Thoul and D. H. Weinberg, *Hydrodynamic Simulations of Galaxy Formation. II. Photoionization and the Formation of Low-Mass Galaxies*, *ApJ* **465** (Jul, 1996) 608, [astro-ph/9510154].

[122] J. S. Bullock, A. V. Kravtsov, and D. H. Weinberg, *Reionization and the Abundance of Galactic Satellites*, *ApJ* **539** (Aug, 2000) 517–521, [astro-ph/0002214].

[123] R. S. Somerville, *Can Photoionization Squelching Resolve the Substructure Crisis?*, *ApJ* **572** (Jun, 2002) L23–L26, [astro-ph/0107507].

[124] K. V. Johnston, D. N. Spergel, and C. Haydn, *How lumpy is the milky way's dark matter halo?*, *Astrophys. J.* **570** (2002) 656, [astro-ph/0111196].

[125] J. Diemand, M. Kuhlen, and P. Madau, *Early supersymmetric cold dark matter substructure*, *Astrophys. J.* **649** (2006) 1–13, [astro-ph/0603250].

[126] V. Springel, J. Wang, M. Vogelsberger, A. Ludlow, A. Jenkins, A. Helmi, J. F. Navarro, C. S. Frenk, and S. D. M. White, *The Aquarius Project: the subhalos of galactic halos*, *Mon. Not. Roy. Astron. Soc.* **391** (2008) 1685–1711, [arXiv:0809.0898].

[127] M. Boylan-Kolchin, V. Springel, S. D. M. White, and A. Jenkins, *There's no place like home? Statistics of Milky Way-mass dark matter halos*, *Mon. Not. Roy. Astron. Soc.* **406** (2010) 896, [arXiv:0911.4484].

[128] C. Giocoli, G. Tormen, R. K. Sheth, and F. C. van den Bosch, *The Substructure Hierarchy in Dark Matter Haloes*, *Mon. Not. Roy. Astron. Soc.* **404** (2010) 502–517, [arXiv:0911.0436].

[129] L. Gao, C. S. Frenk, M. Boylan-Kolchin, A. Jenkins, V. Springel, and S. D. M. White, *The statistics of the subhalo abundance of dark matter haloes*, *Mon. Not. Roy. Astron. Soc.* **410** (2011) 2309, [arXiv:1006.2882].

[130] M. Kamionkowski, S. M. Koushiappas, and M. Kuhlen, *Galactic Substructure and Dark Matter Annihilation in the Milky Way Halo*, *Phys. Rev.* **D81** (2010) 043532, [arXiv:1001.3144].

[131] T. Ishiyama, J. Makino, S. Portegies Zwart, D. Groen, K. Nitadori, S. Rieder, C. de Laat, S. McMillan, K. Hiraki, and S. Harfst, *The Cosmogrid Simulation: Statistical Properties of Small Dark Matter Halos*, *Astrophys. J.* **767** (2013) 146, [arXiv:1101.2020].

[132] M. A. Sánchez-Conde and F. Prada, *The flattening of the concentration–mass relation towards low halo masses and its implications for the annihilation signal boost*, *Mon. Not. Roy. Astron. Soc.* **442** (2014), no. 3 2271–2277, [arXiv:1312.1729].

[133] M. Stref and J. Lavalle, *Modeling dark matter subhalos in a constrained galaxy: Global mass and boosted annihilation profiles*, *Phys. Rev.* **D95** (2017), no. 6 063003, [arXiv:1610.02233].

[134] C. Okoli, J. E. Taylor, and N. Afshordi, *Searching for dark matter annihilation from individual halos: uncertainties, scatter and signal-to-noise ratios*, *JCAP* **1808** (2018), no. 08 019, [arXiv:1711.05271].

[135] N. Hiroshima, S. Ando, and T. Ishiyama, *Modeling evolution of dark matter substructure and annihilation boost*, *Phys. Rev.* **D97** (2018), no. 12 123002, [arXiv:1803.07691].

[136] D. Lynden-Bell and R. M. Lynden-Bell, *Ghostly streams from the formation of the Galaxy's halo*, *MNRAS* **275** (Jul, 1995) 429–442.

[137] **SDSS**, H. J. Newberg *et. al.*, *The Ghost of Sagittarius and Lumps in the Halo of the Milky Way*, *Astrophys. J.* **569** (2002) 245–274, [astro-ph/0111095].

[138] K. Freese, P. Gondolo, H. J. Newberg, and M. Lewis, *The effects of the Sagittarius dwarf tidal stream on dark matter detectors*, *Phys. Rev. Lett.* **92** (2004) 111301, [astro-ph/0310334].

[139] C. A. O'Hare, C. McCabe, N. W. Evans, G. Myeong, and V. Belokurov, *Dark matter hurricane: Measuring the S1 stream with dark matter detectors*, *Phys. Rev.* **D98** (2018), no. 10 103006, [arXiv:1807.09004].

[140] J. M. M. Lane, J. F. Navarro, A. Fattahi, K. A. Oman, and J. Bovy, *The Ophiuchus stream progenitor: a new type of globular cluster and its possible Sagittarius connection*, *arXiv e-prints* (May, 2019) arXiv:1905.12633, [arXiv:1905.12633].

[141] Z. Yuan, M. C. Smith, X.-X. Xue, J. Li, C. Liu, Y. Wang, L. Li, and J. Chang, *Revealing the Complicated Story of the Cetus Stream with StarGO*, *ApJ* **881** (Aug, 2019) 164, [arXiv:1902.05248].

[142] R. G. Carlberg, *The Density Structure of Simulated Stellar Streams*, *arXiv e-prints* (Nov, 2018) arXiv:1811.10084, [arXiv:1811.10084].

[143] M. R. Buckley, G. Mohlabeng, and C. W. Murphy, *Direct Detection Anomalies in light of Gaia Data*, *Phys. Rev.* **D100** (2019) 055039, [arXiv:1905.05189].

[144] B. Allgood, R. A. Flores, J. R. Primack, A. V. Kravtsov, R. H. Wechsler, A. Faltenbacher, and J. S. Bullock, *The shape of dark matter halos: dependence on mass, redshift, radius, and formation*, *Mon. Not. Roy. Astron. Soc.* **367** (2006) 1781–1796, [astro-ph/0508497].

[145] A. Kravtsov and S. Borgani, *Formation of Galaxy Clusters*, *Ann. Rev. Astron. Astrophys.* **50** (2012) 353–409, [arXiv:1205.5556].

[146] N. E. Drakos, J. E. Taylor, and A. J. Benson, *The phase-space structure of tidally stripped haloes*, *Mon. Not. Roy. Astron. Soc.* **468** (2017), no. 2 2345–2358, [arXiv:1703.07836].

[147] O. N. Snaith, J. Bailin, A. Knebe, G. Stinson, J. Wadsley, and H. Couchman, *Haloes at the ragged edge: the importance of the splashback radius*, *MNRAS* **472** (Dec, 2017) 2694–2712, [arXiv:1708.06181].

[148] L. Gao, C. S. Frenk, M. Boylan-Kolchin, A. Jenkins, V. Springel, and S. D. M. White, *The statistics of the subhalo abundance of dark matter haloes*, *MNRAS* **410** (Feb, 2011) 2309–2314, [arXiv:1006.2882].

[149] J. Penarrubia, A. J. Benson, M. G. Walker, G. Gilmore, A. McConnachie, and L. Mayer, *The impact of dark matter cusps and cores on the satellite galaxy population around spiral galaxies*, *Mon. Not. Roy. Astron. Soc.* **406** (2010) 1290, [arXiv:1002.3376].

[150] C. A. Correa, J. S. B. Wyithe, J. Schaye, and A. R. Duffy, *The accretion history of dark matter haloes - III. A physical model for the concentration-mass relation*, *Mon. Not. Roy. Astron. Soc.* **452** (2015), no. 2 1217–1232, [arXiv:1502.00391].

[151] J. S. Bullock, T. S. Kolatt, Y. Sigad, R. S. Somerville, A. V. Kravtsov, A. A. Klypin, J. R. Primack, and A. Dekel, *Profiles of dark haloes. Evolution, scatter, and environment*, *Mon. Not. Roy. Astron. Soc.* **321** (2001) 559–575, [astro-ph/9908159].

[152] R. H. Wechsler, J. S. Bullock, J. R. Primack, A. V. Kravtsov, and A. Dekel, *Concentrations of dark halos from their assembly histories*, *Astrophys. J.* **568** (2002) 52–70, [astro-ph/0108151].

[153] **Particle Data Group**, C. Patrignani *et. al.*, *Review of Particle Physics*, *Chin. Phys.* **C40** (2016), no. 10 100001.

[154] Q. Zhu, F. Marinacci, M. Maji, Y. Li, V. Springel, and L. Hernquist, *Baryonic impact on the dark matter distribution in Milky Way-sized galaxies and their satellites*, *Mon. Not. Roy. Astron. Soc.* **458** (2016), no. 2 1559–1580, [arXiv:1506.05537].

[155] W. Dehnen, D. E. McLaughlin, and J. Sachania, *The velocity dispersion and mass profile of the Milky Way*, *MNRAS* **369** (July, 2006) 1688–1692, [astro-ph/0603825].

[156] A.-C. Eilers, D. W. Hogg, H.-W. Rix, and M. K. Ness, *The Circular Velocity Curve of the Milky Way from 5 to 25 kpc*, *ApJ* **871** (Jan, 2019) 120, [arXiv:1810.09466].

[157] P. Madau, J. Diemand, and M. Kuhlen, *Dark matter subhalos and the dwarf satellites of the Milky Way*, *Astrophys. J.* **679** (2008) 1260, [arXiv:0802.2265].

[158] G. Despali and S. Vegetti, *The impact of baryonic physics on the subhalo mass function and implications for gravitational lensing*, *Mon. Not. Roy. Astron. Soc.* **469** (2017), no. 2 1997–2010, [arXiv:1608.06938].

[159] R. E. Angulo and S. D. M. White, *The Birth and Growth of Neutralino Haloes*, *Mon. Not. Roy. Astron. Soc.* **401** (2010) 1796, [arXiv:0906.1730].

[160] J. Onions *et. al.*, *SubHaloes going Notts: The SubHalo-Finder Comparison Project*, *Mon. Not. Roy. Astron. Soc.* **423** (2012) 1200–1214, [arXiv:1203.3695].

[161] T. Sawala, C. S. Frenk, R. A. Crain, A. Jenkins, J. Schaye, T. Theuns, and J. Zavala, *The abundance of (not just) dark matter haloes*, *Mon. Not. Roy. Astron. Soc.* **431** (2013) 1366–1382, [arXiv:1206.6495].

[162] M. Vogelsberger, S. Genel, V. Springel, P. Torrey, D. Sijacki, D. Xu, G. Snyder, D. Nelson, and L. Hernquist, *Introducing the Illustris Project: simulating the coevolution of dark and visible matter in the Universe*, *MNRAS* **444** (Oct., 2014) 1518–1547, [arXiv:1405.2921].

[163] M. Schaller, C. S. Frenk, R. G. Bower, T. Theuns, A. Jenkins, J. Schaye, R. A. Crain, M. Furlong, C. Dalla Vecchia, and I. G. McCarthy, *Baryon effects on the internal structure of ΛCDM haloes in the EAGLE simulations*, *MNRAS* **451** (Aug., 2015) 1247–1267, [arXiv:1409.8617].

[164] T. Kelley, J. S. Bullock, S. Garrison-Kimmel, M. Boylan-Kolchin, M. S. Pawlowski, and A. S. Graus, *Phat ELVIS: The inevitable effect of the Milky Way's disk on its dark matter subhaloes*, *MNRAS* **487** (Aug, 2019) 4409–4423, [arXiv:1811.12413].

[165] J. Richings, C. Frenk, A. Jenkins, and A. Robertson, *Subhalo destruction in the Apostle and Auriga simulations*, *arXiv e-prints* (Nov, 2018) arXiv:1811.12437, [arXiv:1811.12437].

[166] K. Kadota, T. Sekiguchi, and H. Tashiro, *A new constraint on millicharged dark matter from galaxy clusters*, arXiv:1602.04009.

[167] A. Stebbins and G. Krnjaic, *New Limits on Charged Dark Matter from Large-Scale Coherent Magnetic Fields*, arXiv:1908.05275.

[168] **KATRIN**, M. Aker *et. al.*, *An improved upper limit on the neutrino mass from a direct kinematic method by KATRIN*, arXiv:1909.06048.

[169] D. N. Schramm and G. Steigman, *Relic Neutrinos and the Density of the Universe*, *ApJ* **243** (Jan., 1981) 1.

[170] P. J. E. Peebles, *Primeval adiabatic perturbations - Effect of massive neutrinos*, *ApJ* **258** (July, 1982) 415–424.

[171] S. D. M. White, C. S. Frenk, and M. Davis, *Clustering in a neutrino-dominated universe*, *ApJ* **274** (Nov., 1983) L1–L5.

[172] E. W. Kolb and R. Slansky, *Dimensional Reduction in the Early Universe: Where Have the Massive Particles Gone?*, *Phys. Lett.* **135B** (1984) 378.

[173] H.-C. Cheng, K. T. Matchev, and M. Schmaltz, *Radiative corrections to Kaluza-Klein masses*, *Phys. Rev.* **D66** (2002) 036005, [hep-ph/0204342].

[174] G. Servant and T. M. P. Tait, *Is the lightest Kaluza-Klein particle a viable dark matter candidate?*, *Nucl. Phys.* **B650** (2003) 391–419, [hep-ph/0206071].

[175] S. Dodelson and L. M. Widrow, *Sterile-neutrinos as dark matter*, *Phys. Rev. Lett.* **72** (1994) 17–20, [hep-ph/9303287].

[176] L. J. Rosenberg and K. A. van Bibber, *Searches for invisible axions.*, *Phys. Rep.* **325** (Feb., 2000) 1–39.

[177] G. Bertone, *The moment of truth for WIMP Dark Matter*, *Nature* **468** (2010) 389–393, [arXiv:1011.3532].

[178] P. Hut, *Limits on Masses and Number of Neutral Weakly Interacting Particles*, *Phys. Lett.* **69B** (1977) 85. [,179(1977)].

[179] B. W. Lee and S. Weinberg, *Cosmological Lower Bound on Heavy Neutrino Masses*, *Phys. Rev. Lett.* **39** (1977) 165–168. [,183(1977)].

[180] M. I. Vysotskiĭ, A. D. Dolgov, and Y. B. Zel'Dovich, *Cosmological limits on the masses of neutral leptons*, *Soviet Journal of Experimental and Theoretical Physics Letters* **26** (Aug, 1977) 188–190.

[181] J. E. Gunn, B. W. Lee, I. Lerche, D. N. Schramm, and G. Steigman, *Some astrophysical consequences of the existence of a heavy stable neutral lepton*, *ApJ* **223** (Aug., 1978) 1015–1031.

[182] P. Gondolo and G. Gelmini, *Cosmic abundances of stable particles: Improved analysis*, *Nucl. Phys.* **B360** (1991) 145–179.

[183] J. R. Ellis, A. Ferstl, and K. A. Olive, *Reevaluation of the elastic scattering of supersymmetric dark matter*, *Phys. Lett.* **B481** (2000) 304–314, [hep-ph/0001005].

[184] P. Salati, *Indirect and direct dark matter detection*, *PoS* **CARGESE2007** (2007) 009.

[185] R. H. Helm, *Inelastic and Elastic Scattering of 187-Mev Electrons from Selected Even-Even Nuclei*, *Phys. Rev.* **104** (1956) 1466–1475.

[186] J. Engel, *Nuclear form-factors for the scattering of weakly interacting massive particles*, *Phys. Lett.* **B264** (1991) 114–119.

[187] J. D. Lewin and P. F. Smith, *Review of mathematics, numerical factors, and corrections for dark matter experiments based on elastic nuclear recoil*, *Astropart. Phys.* **6** (1996) 87–112.

[188] F. Iachello, L. M. Krauss, and G. Maino, *Spin Dependent Scattering of Weakly Interacting Massive Particles in Heavy Nuclei*, *Phys. Lett.* **B254** (1991) 220–224.

[189] J. Engel, S. Pittel, E. Ormand, and P. Vogel, *Scattering of neutralinos from niobium*, *Phys. Lett.* **B275** (1992) 119–123.

[190] J. Engel, S. Pittel, and P. Vogel, *Nuclear physics of dark matter detection*, *Int. J. Mod. Phys.* **E1** (1992) 1–37.

[191] M. T. Ressell, M. B. Aufderheide, S. D. Bloom, K. Griest, G. J. Mathews, and D. A. Resler, *Nuclear shell model calculations of neutralino - nucleus cross-sections for Si-29 and Ge-73*, *Phys. Rev.* **D48** (1993) 5519–5535, [hep-ph/9307228].

[192] V. Dimitrov, J. Engel, and S. Pittel, *Scattering of weakly interacting massive particles from Ge-73*, *Phys. Rev.* **D51** (1995) 291–295, [hep-ph/9408246].

[193] J. Engel, M. T. Ressell, I. S. Towner, and W. E. Ormand, *Response of mica to weakly interacting massive particles*, *Phys. Rev.* **C52** (1995) 2216–2221, [hep-ph/9504322].

[194] **European Muon**, J. Ashman *et. al.*, *A Measurement of the Spin Asymmetry and Determination of the Structure Function g(1) in Deep Inelastic Muon-Proton Scattering*, *Phys. Lett.* **B206** (1988) 364. [,340(1987)].

[195] R. L. Jaffe and A. Manohar, *The G(1) Problem: Fact and Fantasy on the Spin of the Proton*, *Nucl. Phys.* **B337** (1990) 509–546.

[196] **Spin Muon (SMC)**, D. Adams *et. al.*, *Measurement of the spin dependent structure function $g_1(x)$ of the proton*, *Phys. Lett.* **B329** (1994) 399–406, [hep-ph/9404270]. [Erratum: Phys. Lett.B339,332(1994)].

[197] **HERMES**, A. Airapetian *et. al.*, *Precise determination of the spin structure function g(1) of the proton, deuteron and neutron*, *Phys. Rev.* **D75** (2007) 012007, [hep-ex/0609039].

[198] V. Barger, W.-Y. Keung, and G. Shaughnessy, *Spin dependence of dark matter scattering*, *Phys. Rev. D* **78** (Sep, 2008) 056007.

[199] M. T. Ressell and D. J. Dean, *Spin dependent neutralino - nucleus scattering for A approximately 127 nuclei*, *Phys. Rev.* **C56** (1997) 535–546, [hep-ph/9702290].

[200] V. A. Bednyakov and F. Simkovic, *Nuclear spin structure in dark matter search: The Finite momentum transfer limit*, *Phys. Part. Nucl.* **37** (2006) S106–S128, [hep-ph/0608097].

[201] P. Klos, J. Menéndez, D. Gazit, and A. Schwenk, *Large-scale nuclear structure calculations for spin-dependent WIMP scattering with chiral effective field theory currents*, *Phys. Rev.* **D88** (2013), no. 8 083516, [arXiv:1304.7684]. [Erratum: Phys. Rev.D89,no.2,029901(2014)].

[202] **LUX**, D. S. Akerib *et. al.*, *Results on the Spin-Dependent Scattering of Weakly Interacting Massive Particles on Nucleons from the Run 3 Data of the LUX Experiment*, *Phys. Rev. Lett.* **116** (2016), no. 16 161302, [arXiv:1602.03489].

[203] V. A. Bednyakov, H. V. Klapdor-Kleingrothaus, and S. G. Kovalenko, *Direct detection of supersymmetric dark matter and the role of the target nucleus spin*, *Phys. Rev. D* **50** (Dec, 1994) 7128–7143.

[204] J. Fan, M. Reece, and L.-T. Wang, *Non-relativistic effective theory of dark matter direct detection*, *JCAP* **1011** (2010) 042, [arXiv:1008.1591].

[205] A. L. Fitzpatrick, W. Haxton, E. Katz, N. Lubbers, and Y. Xu, *The Effective Field Theory of Dark Matter Direct Detection*, *JCAP* **1302** (2013) 004, [arXiv:1203.3542].

[206] N. Anand, A. L. Fitzpatrick, and W. C. Haxton, *Weakly interacting massive particle-nucleus elastic scattering response*, *Phys. Rev.* **C89** (2014), no. 6 065501, [arXiv:1308.6288].

[207] R. Catena and B. Schwabe, *Form factors for dark matter capture by the Sun in effective theories*, *JCAP* **1504** (2015), no. 04 042, [arXiv:1501.03729].

[208] J. B. Dent, L. M. Krauss, J. L. Newstead, and S. Sabharwal, *General analysis of direct dark matter detection: From microphysics to observational signatures*, *Phys. Rev.* **D92** (2015), no. 6 063515, [arXiv:1505.03117].

[209] S. D. McDermott, H.-B. Yu, and K. M. Zurek, *Turning off the Lights: How Dark is Dark Matter?*, *Phys. Rev.* **D83** (2011) 063509, [arXiv:1011.2907].

[210] M. Cirelli, E. Del Nobile, and P. Panci, *Tools for model-independent bounds in direct dark matter searches*, *JCAP* **1310** (2013) 019, [arXiv:1307.5955].

[211] T. D. P. Edwards, B. J. Kavanagh, and C. Weniger, *Assessing Near-Future Direct Dark Matter Searches with Benchmark-Free Forecasting*, *Phys. Rev. Lett.* **121** (2018), no. 18 181101, [arXiv:1805.04117].

[212] A. L. Fitzpatrick and K. M. Zurek, *Dark Moments and the DAMA-CoGeNT Puzzle*, *Phys. Rev.* **D82** (2010) 075004, [arXiv:1007.5325].

[213] E. Del Nobile, G. B. Gelmini, P. Gondolo, and J.-H. Huh, *Direct detection of Light Anapole and Magnetic Dipole DM*, *JCAP* **1406** (2014) 002, [arXiv:1401.4508].

[214] F. Bishara, J. Brod, B. Grinstein, and J. Zupan, *From quarks to nucleons in dark matter direct detection*, *JHEP* **11** (2017) 059, [arXiv:1707.06998].

[215] F. Bishara, J. Brod, B. Grinstein, and J. Zupan, *DirectDM: a tool for dark matter direct detection*, arXiv:1708.02678.

[216] **LUX**, D. S. Akerib *et. al.*, *Results from a search for dark matter in the complete LUX exposure*, *Phys. Rev. Lett.* **118** (2017), no. 2 021303, [arXiv:1608.07648].

[217] **PandaX**, A. Tan *et. al.*, *Dark Matter Search Results from the Commissioning Run of PandaX-II*, *Phys. Rev.* **D93** (2016), no. 12 122009, [arXiv:1602.06563].

[218] **PandaX-II**, A. Tan *et. al.*, *Dark Matter Results from First 98.7 Days of Data from the PandaX-II Experiment*, *Phys. Rev. Lett.* **117** (2016), no. 12 121303, [arXiv:1607.07400].

[219] **PandaX-II**, X. Cui *et. al.*, *Dark Matter Results From 54-Ton-Day Exposure of PandaX-II Experiment*, *Phys. Rev. Lett.* **119** (2017), no. 18 181302, [arXiv:1708.06917].

[220] **XENON**, E. Aprile *et. al.*, *First Dark Matter Search Results from the XENON1T Experiment*, *Phys. Rev. Lett.* **119** (2017), no. 18 181301, [arXiv:1705.06655].

[221] **XENON**, E. Aprile *et. al.*, *Dark Matter Search Results from a One Ton-Year Exposure of XENON1T*, *Phys. Rev. Lett.* **121** (2018), no. 11 111302, [arXiv:1805.12562].

[222] **DEAP-3600**, P. A. Amaudruz *et. al.*, *First results from the DEAP-3600 dark matter search with argon at SNOLAB*, arXiv:1707.08042.

[223] **DEAP**, R. Ajaj *et. al.*, *Search for dark matter with a 231-day exposure of liquid argon using DEAP-3600 at SNOLAB*, *Phys. Rev. D* **100** (Jul, 2019) 022004, [arXiv:1902.04048].

[224] **DarkSide**, P. Agnes *et. al.*, *DarkSide-50 532-day Dark Matter Search with Low-Radioactivity Argon*, *Phys. Rev.* **D98** (2018), no. 10 102006, [arXiv:1802.07198].

[225] **CDMS**, R. Agnese *et. al.*, *Silicon Detector Dark Matter Results from the Final Exposure of CDMS II*, *Phys. Rev. Lett.* **111** (2013), no. 25 251301, [arXiv:1304.4279].

[226] **SuperCDMS**, R. Agnese *et. al.*, *Search for Low-Mass Weakly Interacting Massive Particles with SuperCDMS*, *Phys. Rev. Lett.* **112** (2014), no. 24 241302, [arXiv:1402.7137].

[227] **SuperCDMS**, R. Agnese *et. al.*, *Results from the Super Cryogenic Dark Matter Search Experiment at Soudan*, *Phys. Rev. Lett.* **120** (2018), no. 6 061802, [arXiv:1708.08869].

[228] **CRESST**, G. Angloher *et. al.*, *Results on light dark matter particles with a low-threshold CRESST-II detector*, *Eur. Phys. J.* **C76** (2016), no. 1 25, [arXiv:1509.01515].

[229] **CRESST**, A. H. Abdelhameed *et. al.*, *Description of CRESST-III Data*, *arXiv e-prints* (May, 2019) arXiv:1905.07335, [arXiv:1905.07335].

[230] E. Aprile *et. al.*, *Constraining the spin-dependent WIMP-nucleon cross sections with XENON1T*, *Phys. Rev. Lett.* **122** (2019), no. 14 141301, [arXiv:1902.03234].

[231] **PandaX-II**, C. Fu *et. al.*, *Spin-Dependent Weakly-Interacting-Massive-Particle–Nucleon Cross Section Limits from First Data of PandaX-II Experiment*, *Phys. Rev. Lett.* **118** (2017), no. 7 071301, [arXiv:1611.06553]. [Erratum: Phys. Rev. Lett.120,no.4,049902(2018)].

[232] **PICO**, C. Amole *et. al.*, *Dark Matter Search Results from the Complete Exposure of the PICO-60 C_3F_8 Bubble Chamber*, *Phys. Rev.* **D100** (2019), no. 2 022001, [arXiv:1902.04031].

[233] J. Xu *et. al.*, *Scintillation Efficiency Measurement of Na Recoils in NaI(Tl) Below the DAMA/LIBRA Energy Threshold*, *Phys. Rev.* **C92** (2015), no. 1 015807, [arXiv:1503.07212].

[234] E. Del Nobile, G. B. Gelmini, A. Georgescu, and J.-H. Huh, *Reevaluation of spin-dependent WIMP-proton interactions as an explanation of the DAMA data*, *JCAP* **1508** (2015), no. 08 046, [arXiv:1502.07682].

[235] S. Baum, K. Freese, and C. Kelso, *Dark Matter implications of DAMA/LIBRA-phase2 results*, *Physics Letters B* **789** (Feb, 2019) 262–269, [arXiv:1804.01231].

[236] **PICO**, C. Amole *et. al.*, *Dark Matter Search Results from the PICO-2L C_3F_8 Bubble Chamber*, *Phys. Rev. Lett.* **114** (2015), no. 23 231302, [arXiv:1503.00008].

[237] **PICO**, C. Amole *et. al.*, *Dark Matter Search Results from the PICO-60 C_3F_8 Bubble Chamber*, *Phys. Rev. Lett.* **118** (2017), no. 25 251301, [arXiv:1702.07666].

[238] C. McCabe, *The Earth's velocity for direct detection experiments*, *JCAP* **1402** (2014) 027, [arXiv:1312.1355].

[239] R. Schönrich, J. Binney, and W. Dehnen, *Local kinematics and the local standard of rest*, *MNRAS* **403** (Apr, 2010) 1829–1833, [arXiv:0912.3693].

[240] K. Freese, M. Lisanti, and C. Savage, *Colloquium: Annual modulation of dark matter*, *Rev. Mod. Phys.* **85** (2013) 1561–1581, [arXiv:1209.3339].

[241] J. Amaré *et. al.*, *First Results on Dark Matter Annual Modulation from the ANAIS-112 Experiment*, *Phys. Rev. Lett.* **123** (2019), no. 3 031301, [arXiv:1903.03973].

[242] G. Adhikari *et. al.*, *An experiment to search for dark-matter interactions using sodium iodide detectors*, *Nature* **564** (2018), no. 7734 83–86, [arXiv:1906.01791]. [erratum: Nature566,no.7742,E2(2019)].

[243] **COSINE-100**, G. Adhikari *et. al.*, *Search for a Dark Matter-Induced Annual Modulation Signal in NaI(Tl) with the COSINE-100 Experiment*, *Phys. Rev. Lett.* **123** (2019), no. 3 031302, [arXiv:1903.10098].

[244] G. Angloher *et. al.*, *The COSINUS project - perspectives of a NaI scintillating calorimeter for dark matter search*, *Eur. Phys. J.* **C76** (2016), no. 8 441, [arXiv:1603.02214].

[245] **DM-Ice**, E. Barbosa de Souza *et. al.*, *First search for a dark matter annual modulation signal with NaI(Tl) in the Southern Hemisphere by DM-Ice17*, *Phys. Rev.* **D95** (2017), no. 3 032006, [arXiv:1602.05939].

[246] **SABRE**, M. Antonello *et. al.*, *The SABRE project and the SABRE Proof-of-Principle*, *Eur. Phys. J.* **C79** (2019), no. 4 363, [arXiv:1806.09340].

[247] C. Savage, G. Gelmini, P. Gondolo, and K. Freese, *Compatibility of DAMA/LIBRA dark matter detection with other searches*, *JCAP* **0904** (2009) 010, [arXiv:0808.3607].

[248] J. Silk, K. A. Olive, and M. Srednicki, *The Photino, the Sun and High-Energy Neutrinos*, *Phys. Rev. Lett.* **55** (1985) 257–259. [,283(1985)].

[249] A. Gould, *Resonant Enhancements in WIMP Capture by the Earth*, *Astrophys. J.* **321** (1987) 571.

[250] **IceCube**, M. G. Aartsen *et. al.*, *Search for annihilating dark matter in the Sun with 3 years of IceCube data*, *Eur. Phys. J.* **C77** (2017), no. 3 146, [arXiv:1612.05949]. [Erratum: Eur. Phys. J.C79,no.3,214(2019)].

[251] **ANTARES**, S. Adrian-Martinez *et. al.*, *Limits on Dark Matter Annihilation in the Sun using the ANTARES Neutrino Telescope*, *Phys. Lett.* **B759** (2016) 69–74, [arXiv:1603.02228].

[252] **Super-Kamiokande**, K. Choi *et. al.*, *Search for neutrinos from annihilation of captured low-mass dark matter particles in the Sun by Super-Kamiokande*, *Phys. Rev. Lett.* **114** (2015), no. 14 141301, [arXiv:1503.04858].

[253] L. M. Krauss, K. Freese, D. N. Spergel, and W. H. Press, *Cold dark matter candidates and the solar neutrino problem*, *ApJ* **299** (Dec., 1985) 1001–1006.

[254] A. M. Serenelli, S. Basu, J. W. Ferguson, and M. Asplund, *New Solar Composition: The Problem with Solar Models Revisited*, *Astrophys. J.* **705** (Nov., 2009) L123–L127, [arXiv:0909.2668].

[255] A. Gould, *Cosmological density of WIMPs from solar and terrestrial annihilations*, *Astrophys. J.* **388** (1992) 338–344.

[256] K. Griest and D. Seckel, *Cosmic Asymmetry, Neutrinos and the Sun*, *Nucl. Phys.* **B283** (1987) 681–705. [Erratum: Nucl. Phys.B296,1034(1988)].

[257] A. Gould, *Weakly interacting massive particle distribution in and evaporation from the sun*, *ApJ* **321** (Oct., 1987) 560–570.

[258] G. Busoni, A. De Simone, and W.-C. Huang, *On the Minimum Dark Matter Mass Testable by Neutrinos from the Sun*, *JCAP* **1307** (2013) 010, [arXiv:1305.1817].

[259] Z.-L. Liang, Y.-L. Wu, Z.-Q. Yang, and Y.-F. Zhou, *On the evaporation of solar dark matter: spin-independent effective operators*, *JCAP* **1609** (2016), no. 09 018, [arXiv:1606.02157].

[260] R. Garani and S. Palomares-Ruiz, *Dark matter in the Sun: scattering off electrons vs nucleons*, *JCAP* **1705** (2017), no. 05 007, [arXiv:1702.02768].

[261] G. Busoni, A. De Simone, P. Scott, and A. C. Vincent, *Evaporation and scattering of momentum- and velocity-dependent dark matter in the Sun*, *JCAP* **1710** (2017), no. 10 037, [arXiv:1703.07784].

[262] L. Bergstrom, J. Edsjo, and P. Gondolo, *Indirect detection of dark matter in km size neutrino telescopes*, *Phys. Rev.* **D58** (1998) 103519, [hep-ph/9806293].

[263] V. D. Barger, F. Halzen, D. Hooper, and C. Kao, *Indirect search for neutralino dark matter with high-energy neutrinos*, *Phys. Rev.* **D65** (2002) 075022, [hep-ph/0105182].

[264] M. Blennow, J. Edsjo, and T. Ohlsson, *Neutrinos from WIMP annihilations using a full three-flavor Monte Carlo*, *JCAP* **0801** (2008) 021, [arXiv:0709.3898].

[265] T. Bringmann, J. Edsjo, P. Gondolo, P. Ullio, and L. Bergstrom, *DarkSUSY 6 : An Advanced Tool to Compute Dark Matter Properties Numerically*, *JCAP* **1807** (2018), no. 07 033, [arXiv:1802.03399].

[266] M. Fairbairn, T. Douce, and J. Swift, *Quantifying Astrophysical Uncertainties on Dark Matter Direct Detection Results*, *Astropart. Phys.* **47** (2013) 45–53, [arXiv:1206.2693].

[267] N. Bozorgnia, R. Catena, and T. Schwetz, *Anisotropic dark matter distribution functions and impact on WIMP direct detection*, *JCAP* **1312** (2013) 050, [arXiv:1310.0468].

[268] M. Benito, N. Bernal, N. Bozorgnia, F. Calore, and F. Iocco, *Particle Dark Matter Constraints: the Effect of Galactic Uncertainties*, *JCAP* **1702** (2017), no. 02 007, [arXiv:1612.02010]. [Erratum: JCAP1806,no.06,E01(2018)].

[269] P. J. Fox, J. Liu, and N. Weiner, *Integrating Out Astrophysical Uncertainties*, *Phys. Rev.* **D83** (2011) 103514, [arXiv:1011.1915].

[270] P. J. Fox, G. D. Kribs, and T. M. P. Tait, *Interpreting Dark Matter Direct Detection Independently of the Local Velocity and Density Distribution*, *Phys. Rev.* **D83** (2011) 034007, [arXiv:1011.1910].

[271] C. McCabe, *DAMA and CoGeNT without astrophysical uncertainties*, *Phys. Rev.* **D84** (2011) 043525, [arXiv:1107.0741].

[272] M. T. Frandsen, F. Kahlhoefer, C. McCabe, S. Sarkar, and K. Schmidt-Hoberg, *Resolving astrophysical uncertainties in dark matter direct detection*, *JCAP* **1201** (2012) 024, [arXiv:1111.0292].

[273] J. Herrero-Garcia, T. Schwetz, and J. Zupan, *On the annual modulation signal in dark matter direct detection*, *JCAP* **1203** (2012) 005, [arXiv:1112.1627].

[274] P. Gondolo and G. B. Gelmini, *Halo independent comparison of direct dark matter detection data*, *JCAP* **1212** (2012) 015, [arXiv:1202.6359].

[275] M. T. Frandsen, F. Kahlhoefer, C. McCabe, S. Sarkar, and K. Schmidt-Hoberg, *The unbearable lightness of being: CDMS versus XENON*, *JCAP* **1307** (2013) 023, [arXiv:1304.6066].

[276] E. Del Nobile, G. B. Gelmini, P. Gondolo, and J.-H. Huh, *Halo-independent analysis of direct detection data for light WIMPs*, *JCAP* **1310** (2013) 026, [arXiv:1304.6183].

[277] E. Del Nobile, G. Gelmini, P. Gondolo, and J.-H. Huh, *Generalized Halo Independent Comparison of Direct Dark Matter Detection Data*, *JCAP* **1310** (2013) 048, [arXiv:1306.5273].

[278] P. J. Fox, Y. Kahn, and M. McCullough, *Taking Halo-Independent Dark Matter Methods Out of the Bin*, *JCAP* **1410** (2014), no. 10 076, [arXiv:1403.6830].

[279] J. F. Cherry, M. T. Frandsen, and I. M. Shoemaker, *Halo Independent Direct Detection of Momentum-Dependent Dark Matter*, *JCAP* **1410** (2014), no. 10 022, [arXiv:1405.1420].

[280] S. Scopel and K. Yoon, *A systematic halo-independent analysis of direct detection data within the framework of Inelastic Dark Matter*, *JCAP* **1408** (2014) 060, [arXiv:1405.0364].

[281] B. Feldstein and F. Kahlhoefer, *Quantifying (dis)agreement between direct detection experiments in a halo-independent way*, *JCAP* **1412** (2014), no. 12 052, [arXiv:1409.5446].

[282] N. Bozorgnia and T. Schwetz, *What is the probability that direct detection experiments have observed Dark Matter?*, *JCAP* **1412** (2014), no. 12 015, [arXiv:1410.6160].

[283] A. J. Anderson, P. J. Fox, Y. Kahn, and M. McCullough, *Halo-Independent Direct Detection Analyses Without Mass Assumptions*, *JCAP* **1510** (2015), no. 10 012, [arXiv:1504.03333].

[284] G. B. Gelmini, A. Georgescu, P. Gondolo, and J.-H. Huh, *Extended Maximum Likelihood Halo-independent Analysis of Dark Matter Direct Detection Data*, *JCAP* **1511** (2015), no. 11 038, [arXiv:1507.03902].

[285] F. Ferrer, A. Ibarra, and S. Wild, *A novel approach to derive halo-independent limits on dark matter properties*, *JCAP* **1509** (2015), no. 09 052, [arXiv:1506.03386].

[286] G. B. Gelmini, J.-H. Huh, and S. J. Witte, *Assessing Compatibility of Direct Detection Data: Halo-Independent Global Likelihood Analyses*, *JCAP* **1610** (2016), no. 10 029, [arXiv:1607.02445].

[287] F. Kahlhoefer and S. Wild, *Studying generalised dark matter interactions with extended halo-independent methods*, *JCAP* **1610** (2016), no. 10 032, [arXiv:1607.04418].

[288] P. Gondolo and S. Scopel, *Halo-independent determination of the unmodulated WIMP signal in DAMA: the isotropic case*, *JCAP* **1709** (2017), no. 09 032, [arXiv:1703.08942].

[289] G. B. Gelmini, J.-H. Huh, and S. J. Witte, *Unified Halo-Independent Formalism From Convex Hulls for Direct Dark Matter Searches*, *JCAP* **1712** (2017), no. 12 039, [arXiv:1707.07019].

[290] A. Fowlie, *Halo-independence with quantified maximum entropy at DAMA/LIBRA*, *JCAP* **1710** (2017), no. 10 002, [arXiv:1708.00181].

[291] F. Kahlhoefer, F. Reindl, K. Schäffner, K. Schmidt-Hoberg, and S. Wild, *Model-independent comparison of annual modulation and total rate with direct detection experiments*, *JCAP* **1805** (2018), no. 05 074, [arXiv:1802.10175].

[292] A. Fowlie, *Non-parametric uncertainties in the dark matter velocity distribution*, *JCAP* **1901** (2019), no. 01 006, [arXiv:1809.02323].

[293] **IceCube, PICO**, M. G. Aartsen *et. al.*, *Velocity independent constraints on spin-dependent DM-nucleon interactions from IceCube and PICO*, arXiv:1907.12509.

[294] W. Karush, *Minima of functions of several variables with inequalities as side constraints*, *M. Sc. Dissertation. Dept. of Mathematics, Univ. of Chicago* (1939).

[295] H. W. Kuhn and A. W. Tucker, *Nonlinear Programming*, in *Second Berkeley Symposium on Mathematical Statistics and Probability* (J. Neyman, ed.), pp. 481–492, 1951.

[296] W. Fenchel, *Convex cones, sets and functions.* Department of Mathematics, Princeton University, 1953.

[297] H. Eggleston, *Convexity (Cambridge Tracts in Mathematics and Mathematical Physics. No.47).* Cambridge University Press, 1958.

[298] G. Choquet, *Existence et unicité des représentations intégrales au moyen des points extrémaux dans les cônes convexes*, vol. 4, pp. 33–47, Séminaire Bourbaki, 1956.

[299] W. R. Inc., "Mathematica, Version 10.4." Champaign, IL, 2019.

[300] M. S. Andersen, J. Dahl, and L. Vandenberghe, "CVXOPT - Python software for convex optimization." https://cvxopt.org. Accessed: 2019-08-07.

[301] B. J. Kavanagh, M. Fornasa, and A. M. Green, *Probing WIMP particle physics and astrophysics with direct detection and neutrino telescope data*, *Phys. Rev.* **D91** (2015), no. 10 103533, [arXiv:1410.8051].

[302] M. Blennow, J. Herrero-Garcia, and T. Schwetz, *A halo-independent lower bound on the dark matter capture rate in the Sun from a direct detection signal*, *JCAP* **1505** (2015), no. 05 036, [arXiv:1502.03342].

[303] **LZ**, D. S. Akerib *et. al.*, *LUX-ZEPLIN (LZ) Conceptual Design Report*, arXiv:1509.02910.

[304] R. Catena, A. Ibarra, and S. Wild, *DAMA confronts null searches in the effective theory of dark matter-nucleon interactions*, *JCAP* **1605** (2016), no. 05 039, [arXiv:1602.04074].

[305] MATLAB, *version 8.3.0.532 (R2014a).* The MathWorks Inc., Natick, Massachusetts, 2014.

[306] S. J. Witte and G. B. Gelmini, *Updated Constraints on the Dark Matter Interpretation of CDMS-II-Si Data*, *JCAP* **1705** (2017), no. 05 026, [arXiv:1703.06892].

[307] A. H. G. Peter, *WIMP astronomy and particle physics with liquid-noble and cryogenic direct-detection experiments*, *Phys. Rev.* **D83** (2011) 125029, [arXiv:1103.5145].

[308] B. J. Kavanagh and A. M. Green, *Improved determination of the WIMP mass from direct detection data*, *Phys. Rev.* **D86** (2012) 065027, [arXiv:1207.2039].

[309] B. Feldstein and F. Kahlhoefer, *A new halo-independent approach to dark matter direct detection analysis*, *JCAP* **1408** (2014) 065, [arXiv:1403.4606].

[310] B. J. Kavanagh and A. M. Green, *Model independent determination of the dark matter mass from direct detection experiments*, *Phys. Rev. Lett.* **111** (2013), no. 3 031302, [arXiv:1303.6868].

[311] B. J. Kavanagh, *Parametrizing the local dark matter speed distribution: a detailed analysis*, *Phys. Rev.* **D89** (2014), no. 8 085026, [arXiv:1312.1852].

[312] J. I. Read, V. Debattista, O. Agertz, L. Mayer, A. M. Brooks, F. Governato, and G. Lake, *A dark matter disc in the Milky Way*, *PoS* **IDM2008** (2008) 048, [arXiv:0901.2938]. [AIP Conf. Proc.1240,no.1,391(2010)].

[313] J. I. Read, L. Mayer, A. M. Brooks, F. Governato, and G. Lake, *A dark matter disc in three cosmological simulations of Milky Way mass galaxies*, *Mon. Not. Roy. Astron. Soc.* **397** (2009) 44, [arXiv:0902.0009].

[314] M. Kuhlen, N. Weiner, J. Diemand, P. Madau, B. Moore, D. Potter, J. Stadel, and M. Zemp, *Dark Matter Direct Detection with Non-Maxwellian Velocity Structure*, *JCAP* **1002** (2010) 030, [arXiv:0912.2358].

[315] M. Kuhlen, M. Lisanti, and D. N. Spergel, *Direct Detection of Dark Matter Debris Flows*, *Phys. Rev.* **D86** (2012) 063505, [arXiv:1202.0007].

[316] Y.-Y. Mao, L. E. Strigari, R. H. Wechsler, H.-Y. Wu, and O. Hahn, *Halo-to-Halo Similarity and Scatter in the Velocity Distribution of Dark Matter*, *Astrophys. J.* **764** (2013) 35, [arXiv:1210.2721].

[317] M. Kuhlen, A. Pillepich, J. Guedes, and P. Madau, *The Distribution of Dark Matter in the Milky Way's Disk*, *Astrophys. J.* **784** (2014) 161, [arXiv:1308.1703].

[318] I. Butsky, A. V. Macciò, A. A. Dutton, L. Wang, A. Obreja, G. S. Stinson, C. Penzo, X. Kang, B. W. Keller, and J. Wadsley, *NIHAO project II: Halo shape, phase-space density and velocity distribution of dark matter in galaxy formation simulations*, *Mon. Not. Roy. Astron. Soc.* **462** (2016), no. 1 663–680, [arXiv:1503.04814].

[319] N. Bozorgnia, F. Calore, M. Schaller, M. Lovell, G. Bertone, C. S. Frenk, R. A. Crain, J. F. Navarro, J. Schaye, and T. Theuns, *Simulated Milky Way analogues: implications for dark matter direct searches*, *JCAP* **1605** (2016), no. 05 024, [arXiv:1601.04707].

[320] N. Bozorgnia and G. Bertone, *Implications of hydrodynamical simulations for the interpretation of direct dark matter searches*, *Int. J. Mod. Phys.* **A32** (2017), no. 21 1730016, [arXiv:1705.05853].

[321] P. Bhattacharjee, S. Chaudhury, S. Kundu, and S. Majumdar, *Sizing-up the WIMPs of Milky Way : Deriving the velocity distribution of Galactic Dark Matter particles from the rotation curve data*, *Phys. Rev.* **D87** (2013) 083525, [arXiv:1210.2328].

[322] M. Fornasa and A. M. Green, *Self-consistent phase-space distribution function for the anisotropic dark matter halo of the Milky Way*, *Phys. Rev.* **D89** (2014), no. 6 063531, [arXiv:1311.5477].

[323] S. Boyd and L. Vandenberghe, *Convex Optimization*. Cambridge University Press, 2004.

[324] S. E. Koposov, H.-W. Rix, and D. W. Hogg, *Constraining the Milky Way potential with a 6-D phase-space map of the GD-1 stellar stream*, *Astrophys. J.* **712** (2010) 260–273, [arXiv:0907.1085].

[325] J. Bovy, C. Allende Prieto, T. C. Beers, D. Bizyaev, L. N. da Costa, K. Cunha, G. L. Ebelke, D. J. Eisenstein, P. M. Frinchaboy, A. E. García Pérez, L. Girardi, F. R. Hearty, D. W. Hogg, J. Holtzman, M. A. G. Maia, S. R. Majewski, E. Malanushenko, V. Malanushenko, S. Mészáros, D. L. Nidever, R. W. O'Connell, C. O'Donnell, A. Oravetz, K. Pan, H. J. Rocha-Pinto, R. P. Schiavon, D. P. Schneider, M. Schultheis, M. Skrutskie, V. V. Smith, D. H. Weinberg, J. C. Wilson, and G. Zasowski, *The Milky Way's Circular-velocity Curve between 4 and 14 kpc from APOGEE data*, *ApJ* **759** (Nov, 2012) 131, [arXiv:1209.0759].

[326] **The GAMBIT Dark Matter Workgroup**, T. Bringmann *et. al.*, *DarkBit: A GAMBIT module for computing dark matter observables and likelihoods*, *Eur. Phys. J.* **C77** (2017), no. 12 831, [arXiv:1705.07920].

[327] **GAMBIT**, P. Athron *et. al.*, *Global analyses of Higgs portal singlet dark matter models using GAMBIT*, *Eur. Phys. J.* **C79** (2019), no. 1 38, [arXiv:1808.10465].

[328] **IceCube**, M. G. Aartsen *et. al.*, *Improved limits on dark matter annihilation in the Sun with the 79-string IceCube detector and implications for supersymmetry*, *JCAP* **1604** (2016), no. 04 022, [arXiv:1601.00653].

[329] G. Cowan, K. Cranmer, E. Gross, and O. Vitells, *Asymptotic formulae for likelihood-based tests of new physics*, *Eur. Phys. J.* **C71** (2011) 1554, [arXiv:1007.1727]. [Erratum: Eur. Phys. J.C73,2501(2013)].

[330] A. Wald, *Tests of statistical hypotheses concerning several parameters when the number of observations is large*, *Transactions of the American Mathematical society* **54** (1943), no. 3 426–482.

[331] S. S. Wilks, *The Large-Sample Distribution of the Likelihood Ratio for Testing Composite Hypotheses*, *Annals Math. Statist.* **9** (1938), no. 1 60–62.

[332] **DAMA**, R. Bernabei *et. al.*, *The DAMA/LIBRA apparatus*, *Nucl. Instrum. Meth.* **A592** (2008) 297–315, [arXiv:0804.2738].

[333] R. Bernabei *et. al.*, *New limits on WIMP search with large-mass low-radioactivity NaI(Tl) set-up at Gran Sasso*, *Phys. Lett.* **B389** (1996) 757–766.

[334] K. Fushimi, H. Ejiri, H. Kinoshita, N. Kudomi, K. Kume, K. Nagata, H. Ohsumi, K. Okada, H. Sano, and J. Tanaka, *Application of a large-volume NaI scintillator to search for dark matter*, *Phys. Rev. C* **47** (Feb., 1993) R425–R428.

[335] N. Bozorgnia, G. B. Gelmini, and P. Gondolo, *Channeling in direct dark matter detection I: channeling fraction in NaI (Tl) crystals*, *JCAP* **1011** (2010) 019, [arXiv:1006.3110].

[336] K. Griest and M. Kamionkowski, *Unitarity Limits on the Mass and Radius of Dark Matter Particles*, *Phys. Rev. Lett.* **64** (1990) 615.

[337] D. Stiff, L. M. Widrow, and J. Frieman, *Signatures of hierarchical clustering in dark matter detection experiments*, *Phys. Rev.* **D64** (2001) 083516, [astro-ph/0106048].

[338] A. Helmi, S. D. M. White, and V. Springel, *The Phase space structure of a dark matter halo: Implications for dark matter direct detection experiments*, *Phys. Rev.* **D66** (2002) 063502, [astro-ph/0201289].

[339] A. M. Green, *WIMP direct detection and halo structure*, astro-ph/0310215. [IAU Symp.220,483(2004)].

[340] M. Vogelsberger, S. D. M. White, A. Helmi, and V. Springel, *The fine-grained phase-space structure of Cold Dark Matter halos*, *Mon. Not. Roy. Astron. Soc.* **385** (2008) 236, [arXiv:0711.1105].

[341] M. Kamionkowski and S. M. Koushiappas, *Galactic substructure and direct detection of dark matter*, *Phys. Rev.* **D77** (2008) 103509, [arXiv:0801.3269].

[342] J. Diemand, M. Kuhlen, and P. Madau, *Dark matter substructure and gamma-ray annihilation in the Milky Way halo*, *Astrophys. J.* **657** (2007) 262–270, [astro-ph/0611370].

[343] L. E. Strigari, S. M. Koushiappas, J. S. Bullock, and M. Kaplinghat, *Precise constraints on the dark matter content of Milky Way dwarf galaxies for gamma-ray experiments*, *Phys. Rev.* **D75** (2007) 083526, [astro-ph/0611925].

[344] L. Pieri, G. Bertone, and E. Branchini, *Dark Matter Annihilation in Substructures Revised*, *Mon. Not. Roy. Astron. Soc.* **384** (2008) 1627, [arXiv:0706.2101].

[345] T. E. Jeltema and S. Profumo, *Searching for Dark Matter with X-ray Observations of Local Dwarf Galaxies*, *Astrophys. J.* **686** (2008) 1045, [arXiv:0805.1054].

[346] T. Ishiyama, *Hierarchical Formation of Dark Matter Halos and the Free Streaming Scale*, *Astrophys. J.* **788** (2014) 27, [arXiv:1404.1650].

[347] R. Bartels and S. Ando, *Boosting the annihilation boost: Tidal effects on dark matter subhalos and consistent luminosity modeling*, *Phys. Rev.* **D92** (2015), no. 12 123508, [arXiv:1507.08656].

[348] **Fermi-LAT**, M. Ackermann *et. al.*, *Dark matter constraints from observations of 25 Milky Way satellite galaxies with the Fermi Large Area Telescope*, *Phys. Rev.* **D89** (2014) 042001, [arXiv:1310.0828].

[349] **Fermi-LAT**, M. Ackermann *et. al.*, *Searching for Dark Matter Annihilation from Milky Way Dwarf Spheroidal Galaxies with Six Years of Fermi Large Area Telescope Data*, *Phys. Rev. Lett.* **115** (2015), no. 23 231301, [arXiv:1503.02641].

[350] D. Hooper and T. Linden, *On The Gamma-Ray Emission From Reticulum II and Other Dwarf Galaxies*, *JCAP* **1509** (2015), no. 09 016, [arXiv:1503.06209].

[351] A. Geringer-Sameth, M. G. Walker, S. M. Koushiappas, S. E. Koposov, V. Belokurov, G. Torrealba, and N. W. Evans, *Indication of Gamma-ray Emission from the Newly Discovered Dwarf Galaxy Reticulum II*, *Phys. Rev. Lett.* **115** (2015), no. 8 081101, [arXiv:1503.02320].

[352] **Fermi-LAT, DES**, A. Drlica-Wagner *et. al.*, *Search for Gamma-Ray Emission from DES Dwarf Spheroidal Galaxy Candidates with Fermi-LAT Data*, *Astrophys. J.* **809** (2015), no. 1 L4, [arXiv:1503.02632].

[353] **MAGIC, Fermi-LAT**, M. L. Ahnen *et. al.*, *Limits to Dark Matter Annihilation Cross-Section from a Combined Analysis of MAGIC and Fermi-LAT Observations of Dwarf Satellite Galaxies*, *JCAP* **1602** (2016), no. 02 039, [arXiv:1601.06590].

[354] **Fermi-LAT, DES**, A. Albert *et. al.*, *Searching for Dark Matter Annihilation in Recently Discovered Milky Way Satellites with Fermi-LAT*, *Astrophys. J.* **834** (2017), no. 2 110, [arXiv:1611.03184].

[355] S. Hoof, A. Geringer-Sameth, and R. Trotta, *A Global Analysis of Dark Matter Signals from 27 Dwarf Spheroidal Galaxies using Ten Years of Fermi-LAT Observations*, arXiv:1812.06986.

[356] D. Erkal and V. Belokurov, *Properties of Dark Subhaloes from Gaps in Tidal Streams*, *Mon. Not. Roy. Astron. Soc.* **454** (2015), no. 4 3542–3558, [arXiv:1507.05625].

[357] J. Bovy, D. Erkal, and J. L. Sanders, *Linear perturbation theory for tidal streams and the small-scale CDM power spectrum*, *Mon. Not. Roy. Astron. Soc.* **466** (2017), no. 1 628–668, [arXiv:1606.03470].

[358] N. Banik, G. Bertone, J. Bovy, and N. Bozorgnia, *Probing the nature of dark matter particles with stellar streams*, *JCAP* **1807** (2018), no. 07 061, [arXiv:1804.04384].

[359] N. Banik and J. Bovy, *Effects of baryonic and dark matter substructure on the Pal 5 stream*, *Mon. Not. Roy. Astron. Soc.* **484** (2019), no. 2 2009–2020, [arXiv:1809.09640].

[360] A. Bonaca, D. W. Hogg, A. M. Price-Whelan, and C. Conroy, *The Spur and the Gap in GD-1: Dynamical evidence for a dark substructure in the Milky Way halo*, arXiv:1811.03631.

[361] S. M. Koushiappas and M. Kamionkowski, *Galactic Substructure and Energetic Neutrinos from the Sun and the Earth*, *Phys. Rev. Lett.* **103** (2009) 121301, [arXiv:0907.4778].

[362] A. Ibarra, M. Totzauer, and S. Wild, *High-energy neutrino signals from the Sun in dark matter scenarios with internal bremsstrahlung*, *JCAP* **1312** (2013) 043, [arXiv:1311.1418].

[363] K. Choi, C. Rott, and Y. Itow, *Impact of the dark matter velocity distribution on capture rates in the Sun*, *JCAP* **1405** (2014) 049, [arXiv:1312.0273].

[364] A. Nuñez-Castiñeyra, E. Nezri, and V. Bertin, *Dark matter capture by the Sun: revisiting velocity distribution uncertainties*, arXiv:1906.11674.

[365] D. Hooper and S. J. Witte, *Gamma Rays From Dark Matter Subhalos Revisited: Refining the Predictions and Constraints*, *JCAP* **1704** (2017), no. 04 018, [arXiv:1610.07587].

[366] S. Kazantzidis, L. Mayer, C. Mastropietro, J. Diemand, J. Stadel, and B. Moore, *Density profiles of cold dark matter substructure: Implications for the missing satellites problem*, *Astrophys. J.* **608** (2004) 663–3679, [astro-ph/0312194].

[367] S. Garrison-Kimmel, M. Boylan-Kolchin, J. Bullock, and K. Lee, *ELVIS: Exploring the Local Volume in Simulations*, *Mon. Not. Roy. Astron. Soc.* **438** (2014), no. 3 2578–2596, [arXiv:1310.6746].

[368] J. Diemand, M. Kuhlen, P. Madau, M. Zemp, B. Moore, D. Potter, and J. Stadel, *Clumps and streams in the local dark matter distribution*, *Nature* **454** (2008) 735–738, [arXiv:0805.1244].

[369] M. R. Lovell, C. S. Frenk, V. R. Eke, A. Jenkins, L. Gao, and T. Theuns, *The properties of warm dark matter haloes*, *Mon. Not. Roy. Astron. Soc.* **439** (2014) 300–317, [arXiv:1308.1399].

[370] S. Nussinov and Y. Zhang, *What If Dark Matter Clusters?*, arXiv:1807.00846.

[371] D. M. Grabowska, T. Melia, and S. Rajendran, *Detecting Dark Blobs*, *Phys. Rev.* **D98** (2018), no. 11 115020, [arXiv:1807.03788].

[372] P. Tinyakov, I. Tkachev, and K. Zioutas, *Tidal streams from axion miniclusters and direct axion searches*, *JCAP* **1601** (2016), no. 01 035, [arXiv:1512.02884].

[373] B. J. Kavanagh and T. Edwards, "WIMpy_NREFT v1.0 [ComputerSoftware]." Available at https://github.com/bradkav/WIMpy_NREFT, May, 2018.

[374] **CRESST**, A. H. Abdelhameed *et. al.*, *Geant4-based electromagnetic background model for the CRESST dark matter experiment*, *arXiv e-prints* (Aug, 2019) arXiv:1908.06755, [arXiv:1908.06755].

[375] S. Yellin, *Finding an upper limit in the presence of an unknown background*, *Phys. Rev. D* **66** (Aug, 2002) 032005, [physics/0203002].

[376] F. A. Potra and S. J. Wright, *Interior-point methods*, *Journal of Computational and Applied Mathematics* **124** (Dec., 2000) 281–302.

[377] G. B. Dantzig, *Programming in a linear structure, Comptroller USAF Washington, DC, February* (1948) 479–495.

[378] A. Schrijver, *Theory of linear and integer programming*. John Wiley & Sons, 1998.

[379] **CDMS**, D. S. Akerib *et. al.*, *A Low-Threshold Analysis of CDMS Shallow-Site Data*, *Phys. Rev.* **D82** (2010) 122004, [arXiv:1010.4290].

[380] **LUX**, D. S. Akerib *et. al.*, *The Large Underground Xenon (LUX) Experiment*, *Nucl. Instrum. Meth.* **A704** (2013) 111–126, [arXiv:1211.3788].

[381] D. Yu. Akimov *et. al.*, *The ZEPLIN-III dark matter detector: instrument design, manufacture and commissioning*, *Astropart. Phys.* **27** (2007) 46–60, [astro-ph/0605500].